MF Radar Interferometry

A THESIS
SUBMITTED IN PARTIAL FULFILMENT
OF THE REQUIREMENTS FOR THE DEGREE

OF

DOCTOR OF PHILOSOPHY,
DEPARTMENT OF PHYSICS AND ASTRONOMY
UNIVERSITY OF CANTERBURY.

BY

William O. J. Brown.

University of Canterbury

1992

MF Radar Interferometry

Abstract

This thesis describes the development, operation and observations of interferometry experiments on two medium frequency spaced antennae radar operated by the Department of Physics and Astronomy of the University of Canterbury; the 2.4 MHz radar at Birdlings Flat near Christchurch, New Zealand, and the 2.9 MHz radar at Scott Base on Ross Island in the Antarctic. These radars are of a standard design and detect scattering from the D and lower E regions of the ionosphere in the mesosphere and lower thermosphere.

The interferometry techniques used were those of temporal, spatial and frequency domain interferometry which provide information on Doppler shifting and the directional and radial distribution of backscattered signals received by the radars. This project represents the first time that these techniques have been operated together on radars of the type used in this project. The techniques were also carried out in conjunction with the standard procedures used on these radars, that of Spaced Antennae Drifts with Full Correlation Analysis (FCA).

Various forms of interferometric analyses were carried out and comparisons were made between the results of interferometric analyses and those of more conventional techniques. For example a study was made of the relationship between interferometric and FCA velocities in which it was found that there was good agreement between the two methods, particularly when the scattering region does not change rapidly as it moves. Other analysis techniques investigated included examination of the angular distribution of scattering and aspect sensitivity, the statistical distributions of scattered signals, postbeam steering, vertical velocities and momentum fluxes.

Frequency domain interferometry provided enhanced measurement of range and the scattering depth or distribution of range of scattered signals. Measurements of scattering depth clearly identified examples of thin layers or localized scatter. These localized scattering events appeared to be associated with either steady flow or long period variations in steady flow, for example with the semidiurnal solar tide. Aside from these events much of the scatter was observed to be anisotropic and also appeared to originate from a number of distributed scattering centres spread horizontally and vertically in a manner consistent with Fresnel scattering models.

Contents

1 Introduction 1

1.1 The Middle Atmosphere 1

1.2 The Lower Ionosphere 4

1.2.1 Magnetoionic Theory and Refractive Index 5

1.2.2 Geomagnetic Storms and the Polar Ionosphere 8

1.3 Scattering Processes in the Middle Atmosphere 8

1.3.1 Diffraction Considerations 10

1.3.2 Bragg Scatter 11

1.3.3 Fresnel Reflection 11

1.3.4 Fresnel Scattering 12

1.4 Middle Atmosphere Radars 13

1.4.1 Radar Concepts 14

1.4.2 Spaced Antennae Radars 16

1.4.3 Doppler Beam Swinging Radar 18

1.4.4 Comparing Spaced Antennae Drifts and Doppler Beam Swinging . . 19

1.4.5 Frequency Shift Techniques 20

2 The Radars 21

2.0.1 The Spaced Antennae Drifts Programmes 21

2.0.2 The Interferometry Experiment 22

2.1 The Birdlings Flat Radar 24

2.1.1 Transmitting Equipment 27

2.1.2 Antennae 28

2.1.3 Oscillators 32

2.1.4 Receivers 33

2.1.5 Phase Locking 38

2.1.6 Birdlings Flat Computer 40

2.1.7 Data Collection 42
2.2 The Scott Base Radar 47
2.2.1 The Scott Base Transmitter 49
2.2.2 The Arrival Heights Receiving site 51
2.2.3 Phase Locking the Scott Base Radar 55
2.2.4 Arrival Heights data logging 58
2.3 Calibration 62
2.3.1 Gain Calibration 63
2.3.2 Phase Calibration 63

3 Gravity Waves, Turbulence and Scattering Scales 77
3.1 Atmospheric Gravity Waves 78
3.1.1 Gravity Wave Saturation 81
3.1.2 Tides 85
3.2 Turbulence 85
3.2.1 Measuring the Intensity of Turbulence on Radar 88
3.3 Scattering Scales : Aspect Sensitivity 91
3.3.1 Measuring Scattering Scales and Aspect Sensitivity 93
3.4 Signal Distributions 96
3.4.1 Applying Signal Distributions 98

4 Time Series Analysis 101
4.1 Correlation Functions 101
4.1.1 Auto Correlation 103
4.1.2 Cross Receiver Correlation 104
4.1.3 Frequency Correlation 105
4.1.4 Uncertainities in Correlation Functions 106
4.2 Spectral Analysis 107
4.2.1 Introduction 107
4.2.2 Fourier Analysis 108
4.2.3 Other Spectral Analysis Techniques. 117
4.2.4 Spectral Identification of Scattering Centres 122

5 Interferometry 125
5.1 Time Domain Interferometry 126
5.2 Spatial Domain Interferometry 127

5.3 Frequency Domain Interferometry 130
5.3.1 Pulse Compression 131
5.3.2 Frequency Stepping 131
5.3.3 Frequency Domain Interferometry Estimation of Range and Depth . 137
5.4 Cross Spectral Analysis for Interferometry 141
5.5 Interferometric Velocities 144
5.5.1 Determining Interferometric Velocity 145
5.6 Postbeam Steering 148

6 Spaced Antennae Drifts **153**
6.1 Background 153
6.1.1 Comparison Studies 155
6.2 Full Correlation Analysis 156
6.2.1 The Full Correlation Analysis Procedure 157
6.2.2 Acceptance Criteria 164
6.2.3 Full Correlation Analysis as used here 166

7 Results **169**
7.1 Auto Correlation Functions 170
7.1.1 Signal Power 171
7.1.2 Fading Time 172
7.1.3 Mean Doppler Shifts 172
7.2 Cross Correlation Functions 173
7.3 Frequency Correlation Functions 174
7.4 Doppler Spectra 176
7.5 Full Correlation Analysis 179
7.5.1 FCA observations of tides 184
7.6 Comparisons with the Drifts Experiment 186
7.6.1 Coherent, Incoherent Comparison 186
7.6.2 FCA Results Comparisons 188
7.7 Spatial Interferometry 194
7.7.1 Spatial Interferometry from Correlation functions 195
7.7.2 Vertical Velocities 196
7.7.3 Spatial Interferometry from Spectral Analysis 198
7.8 Interferometric Velocity Results 199
7.8.1 Comparing results 200

7.8.2 Interferometric Velocity Comparison with FCA 203
7.8.3 Discussion 208
7.9 Scattering Measurements 211
7.9.1 Aspect Sensitivity 211
7.9.2 Turbulent Eddy Dissipation 216
7.9.3 Signal Distributions 218
7.10 Frequency Domain Interferometry 220
7.10.1 Distributions of FDI range 225
7.10.2 FDI and Aspect sensitivity 227
7.10.3 Comparing FDI and Doppler radial velocities 228
7.10.4 FDI from Cross Spectral Analysis 228
7.11 Postbeam steering 230
7.12 Gravity Wave Activity 233
7.12.1 Momentum Flux Measurements 236
7.13 Uncertainties 239
7.13.1 FCA uncertainties 239
7.13.2 Uncertainties in phase 241

8 Conclusion **243**

Appendices

A Antarctic Reports **251**
A.1 Logistic Report 252
A.2 Science Report 262

B The Data Files **267**

C Additional Results, Scott Base **273**

D Additional Results, Birdlings Flat **279**

References **285**

Acknowledgements **303**

Index **305**
Citation Index 305
Subject Index 309

List of Figures

1.1 The Structure of the Atmosphere 3
1.2 Reference atmosphere zonal wind at 45°S 4
1.3 Components of a radar 15

2.1 Location map of Birdlings Flat 25
2.2 Plan of the Birdlings Flat site 26
2.3 Radiation patterns of the Birdlings Flat antennae 30
2.4 Impedance of the Birdlings Flat antennae and feeders. 31
2.5 The phase sensitive receivers 34
2.6 Frequency response of the Birdlings Flat receivers 36
2.7 Phase locking synchronizer unit 39
2.8 Location map of Scott Base and Arrival Heights, Ross Island 48
2.9 Modifications to the Scott Base transmitter 50
2.10 Plan of Arrival Heights 53
2.11 Impedance of Arrival Heights antennae 54
2.12 Frequency response of the Arrival Heights receivers 55
2.13 Oscillator controller at Arrival Heights 57
2.14 Cross receiver phase distributions, 6 Oct 90 66
2.15 Cross receiver phase distributions with altitude, 8 Dec 90 67
2.16 Cross receiver phase distributions with frequency, 8 Dec 90 68
2.17 Cross receiver phase distributions with frequency, 18 Aug 90 69
2.18 Cross receiver phase distributions at Scott Base 70
2.19 Distribution of cross frequency phase differences (18 kHz), 25 Sep 90 72
2.20 Distribution of cross frequency phase differences, 6 Oct 90 73
2.21 Distribution of cross frequency phase differences at Scott Base 74

3.1 Cross section of a gravity wave 79
3.2 Orographic lee waves 81

3.3 A model of gravity wave saturation 82
3.4 Power spectrum of wind fluctuations 84
3.5 The turbulence spectrum 87
3.6 Spectral broadening effects 90
3.7 Aspect ratio 92
3.8 Determining the Rice parameter 97

4.1 Spectral analysis of a synthesized data set. 112
4.2 Examples of raw data spectra 114
4.3 Examples of averaged spectra 116
4.4 Final Prediction Error filter lengths 121

5.1 Spatial interferometry path difference between two antennae 128
5.2 Example of FDI on the Urbana MF radar 136
5.3 Frequency correlation functions for two methods of analysis 140
5.4 Cross spectral analysis of synthesized data 142
5.5 Example of cross spectral analysis, Scott Base 18 Dec 88 143
5.6 Spatial Domain Interferometry from cross spectral analysis. 144
5.7 Postbeam antenna diagram for the Birdlings Flat radar 149
5.8 Example of postbeam steering, viewing angle and Doppler shift 150
5.9 Example of postbeam steering, FDI range 151

6.1 Idealized auto and cross correlation functions 158
6.2 Apparent velocity as projected from spaced antenna pair time delays 158
6.3 Anisotropic drifting diffraction pattern 159
6.4 Spatial Correlation Function 160
6.5 Correlation Ellipsoid 161

7.1 Example of auto covariance and auto correlation functions 170
7.2 Signal Power Birdlings Flat 8 Dec 90 171
7.3 Fading Time Birdlings Flat 8 Dec 90 172
7.4 Radial velocity, Birdlings Flat, 8 Dec 90 173
7.5 Example of a cross correlation function 174
7.6 Example of a frequency correlation function 174
7.7 Sequence of frequency correlation functions 176
7.8 Frequency correlation amplitude at 20 kHz, 6 Oct 90 177
7.9 Sample spectra at Scott Base 178

7.10 Sample spectra at Birdlings Flat 179
7.11 FCA results summary diagram 181
7.12 FCA true velocity, 8 Dec 90 182
7.13 Correlation ellipse axial ratio and minor axis orientation 183
7.14 FCA true velocity, 6 Oct 90 185
7.15 FCA $T_{\frac{1}{2}}$, 6 Oct 90 185
7.16 Comparisons of FCA results between coherent and incoherent receivers . . . 187
7.17 Velocity vectors on incoherent and coherent receivers 189
7.18 Drifts mean velocity vectors around 6 October 1990 190
7.19 Mean profiles of drifts and FCA results around 8 Dec 90 191
7.20 Drifts mean velocity vectors at Scott Base, December 88 192
7.21 Interferometry FCA velocity vectors at Scott Base 193
7.22 Mean midday profiles of drifts and FCA results at Scott Base 194
7.23 Mean scattering centre location, 8 Dec 90 195
7.24 Variation in mean angel of arrival vs Signal, 8 Dec 90 196
7.25 Vertical velocities, 6 Oct 90 197
7.26 Spatial interferometry of scattering centres 199
7.27 Examples of mean FCA and interferometric velocity profiles 200
7.28 Ten minute means of FCA and interferometric velocity vectors 201
7.29 FCA apparent and interferometric velocity components at Scott Base . . . 202
7.30 Rate of Interferometric/FCA velocity agreement/disagreement with $\sigma_{v_{\text{rad}}}$. 207
7.31 Rate of Interferometric/FCA velocity agreement/disagreement with $T_{\frac{1}{2}}$ . . . 208
7.32 Rate of Interferometric/FCA velocity agreement/disagreement axial ratio . 209
7.33 FCA and interferometric velocities and angular distribution 209
7.34 Comparisons between different methods of finding aspect sensitivity 213
7.35 Variation of scattered power against angular separation 214
7.36 Aspect sensitivity 6 Oct 90 215
7.37 Eddy dissipation and aspect sensitivity profiles at Scott Base 216
7.38 Eddy dissipation and aspect sensitivity profiles at Birdlings Flat 217
7.39 Mean(amp) / std.dev. (ip,qd) 6 Oct 91 219
7.40 Distributions of the Nakagami parameter 219
7.41 Relationship between Nakagami and kurtosis 220
7.42 FDI range and scattering depth, 8 Dec 90 221
7.43 FDI altitude and scattering depth, 6 Oct 90 223
7.44 FDI altitude and scattering depth, 15 & 17 Dec 88, Scott Base 224

7.45 Profiles of FDI scattering depth and range standard deviation 224
7.46 Distributions of FDI range at Birdlings Flat 225
7.47 Distributions of FDI range at Scott Base 226
7.48 Aspect sensitivity and scattering depth 228
7.49 FDI and Doppler shift radial velocities compared 229
7.50 FDI range from cross spectral analysis, 6 Oct 90 229
7.51 Example of postbeam steering, signal 230
7.52 Sequence of postbeam steering images 232
7.53 Spatial interferometry results for postbeam sequence 233
7.54 Power spectra of 8 Dec 90 winds 234
7.55 Power spectra of 6 Oct 90 winds 235
7.56 Profiles of angle of arrival, 8 Dec 90 235
7.57 Momentum flux measurements, 8 Dec 90 237
7.58 Momentum flux measurements at Scott Base 238
7.59 Correlation functions uncertainty, FCA winds 240
7.60 Correlation functions, phase uncertainties 241
7.61 Spatial and frequency domain interferometry uncertainties 242

C.1 FCA results BIL221 data 274
C.2 FCA results BNLL10 data 275
C.3 FCA results BNNK47 data 276
C.4 Spatial interferometry BNLL10 data 277
C.5 Spatial interferometry BNNK47 data 277
C.6 Spatial interferometry BIL221 data 278
C.7 FDI range and scattering depth, BNNA19, BNNK47 278

D.1 FDI altitude and scattering depth, 28 July 90 280
D.2 Sample FFT spectra, 18 Aug 90 280
D.3 FCA true velocity, 18 Aug 90 281
D.4 FDI range and scattering depth, 18 Aug 90 281
D.5 Rice parameters for 6 Oct 90 282
D.6 Momentum flux measurements, 6 Oct 90 282
D.7 Vertical velocities, 8 Dec 90 283
D.8 Sample MEM spectra, 6 Oct 90 283
D.9 Fading Time, 6 Oct 90 284
D.10 FCA $T_{\frac{1}{2}}$, 8 Dec 90 284

List of Tables

2.1 Power variation between frequencies and antennae, Birdlings Flat 37
2.2 Pulse length and average power of Scott Base transmitter 51
2.3 Power variation between frequencies and antennae, Scott Base 56
2.4 Birdlings Flat, cross receiver phase calibration 64
2.5 Scott Base radar, cross receiver phase calibration 64

6.1 Methods of averaging correlation functions 166

7.1 Agreement rates between randomly generated velocity series 203
7.2 Agreement between Interferometric and FCA winds 204
7.3 Agreement between Interferometric and FCA winds at various conditions . 205

B.1 Contents of the header block 269
B.2 Scott Base data sets 271
B.3 Birdlings Flat data sets 272

List of Abbreviations

Abbreviation	Definition
A/D	Analogue to Digital (converters)
DEC	Digital Equipment Corporation
D, E, F	regions of the ionosphere
DMA	Direct Memory Access
FCA	Full Correlation Analysis
FDI	Frequency Domain Interferometry
FFT	Fast Fourier Transform
FPE	Final Prediction Error (MEM)
HPFW	Half Power Full Width
IDI	Imaging Doppler Interferometer
kB	kiloByte
MAD	Multiple Analogue to Digital (converters)
MB	MegaByte
MEM	Maximum Entropy Method (spectral analysis)
MF	Medium Frequency (0.3-3 MHz)
MST	Mesospheric, Stratospheric, Tropospheric (radar)
NTD	Normalized Time Discrepancy
PDP-11	(model of computer)
PLL	Phase Locked Loop
PRO350	Professional 350 (computer)
PSD	Power Spectral Density
RF	Radio Frequency
RMS	Root Mean Square (deviation)
SAD	Spaced Antennae Drifts
SNR	Signal to Noise Ratio
ST	Stratospheric, Tropospheric (radar)
VHF	Very High Frequency (30-300 MHz)
UHF	Ultra High Frequency (300-3000 MHz)

Definitions of many of the abbreviations used in this work.

List of Symbols

Symbol	Definition
α	azimuth angle, clockwise from north (also Rice parameter)
A, B, C, F, G, H, K	used in FCA (correlation ellipsoid parameters)
c	speed of light
$d_{\frac{1}{2}}, T_{\frac{1}{2}}$	spatial and temporal FCA scales
ϵ	spatial lag (vector)
ε, η	eastward and northward components of spatial lag
f	frequency, also Coriolis parameter
i	$\sqrt{-1}$ (imaginary part of complex numbers)
k	wavenumber ($k = \frac{2\pi}{\lambda}$)
λ	wavelength
p	path length
ϕ	phase
ρ	correlation function
r	range
σ	standard deviation
σ_r	scattering depth, (also for Rayleigh distribution)
t	time
$\tau, \delta t$	time lag
τ_{fad}	fading time
θ	zenith angle (from vertical)
θ_s	aspect sensitivity (e^{-1} half width)
θ_b	antenna beam width (-6 dB full width)
θ_{sb}	aspect sensitivity convolved with antenna beam width
u, v, w	eastward (zonal), northward (meridional), vertical velocity
$\overline{u'w'}, \overline{v'w'}$	upward fluxes of zonal and meridional momentum
V	velocity vector
v_{rad}	radial velocity
ω	angular frequency ($2\pi\times$ frequency in Hz)
ω_D	Doppler frequency
ω_T	transmitter frequency

Definitions of many of the mathematical symbols used in this work.

Chapter 1

Introduction

This work describes the development of interferometry techniques and the integration of those techniques with the spaced antennae class of radar which are commonly used to study the middle atmosphere.

The radars used here were Medium Frequency (MF) radars specifically designed to probe the upper mesosphere and lower thermosphere and the interferometry experiments carried out here concentrated on that region. However these techniques can be readily applied to radars that probe any part of the middle atmosphere or indeed any part of the entire atmosphere. In general terms the emphasis here shall be on the middle atmosphere and the first part of the introduction, section 1.1, backgrounds this region.

MF radars rely on the presence of free electrons in that part of the ionosphere, the D-region and lower E-region, that resides in the mesosphere and lower thermosphere to provide backscattering targets. Section 1.2 then considers properties of the lower ionosphere, including some of the complicating factors that arise in this region.

Section 1.3 discusses some of the scattering processes considered important to radar studies of the middle atmosphere. The last section in the introduction, section 1.4, introduces basic radar concepts and the various techniques that are used in radar probing of the middle atmosphere.

1.1 The Middle Atmosphere

The atmosphere can be classified into a number of regions on the basis of either temperature structure, mixing properties or ionization. Some of these classifications are illustrated in figure 1.1. The troposphere, stratosphere and mesosphere are characterized by their temperature structure and the upper boundaries of these regions are known as the

tropopause, stratopause and mesopause respectively.

The middle atmosphere is the region above the tropopause and below the turbopause and includes the stratosphere, mesosphere and lower thermosphere. The turbopause delineates the atmosphere on the basis of mixing. Below the turbopause (or homopause) in the homosphere turbulent processes keep the constituent gases well mixed whereas above this level the composition varies as the constituent gases diffuse out depending on their relative molecular masses to form the heterosphere.

The term "middle atmosphere" is a term that has come into regular use as techniques have developed to readily probe the region. Formerly the entire atmosphere above the troposphere was known as the upper atmosphere, and the difficult-to-probe region above the troposphere and below the thermosphere was referred to by some as the ignorosphere! Fortunately the situation has changed and there are now many research programmes using a variety of techniques to make measurements of the region. An example of these is the international venture the "Middle Atmosphere Program" (MAP) of which the *MAP Handbooks* are a product and these are often referred to in this work. The dynamics of the middle atmosphere is the topic of the text [Andrews et al., 1987] and a number of collections, such as [Hocking et al., 1990] and [Plumb and Vincent, 1989], discuss research into the middle atmosphere.

Observations by many workers at different locations are collected together to produce "model" or "reference" atmospheres. "Mean" temperature profiles from the most recent of these, the *COSPAR International Reference Atmosphere, 1986*, [CIRA, 86], are shown in figure 1.1 for latitudes 45°S and 80°S (close to the latitudes of the Birdlings Flat and Scott Base radars). This model also has profiles of mean zonal (eastward) wind and a contour plot of these for latitude 45°S appears in figure 1.2. The dominant features in this figure are the westward flow below about 90 km and eastward above in the summer, and the reverse eastward below and westward above about 90 km in winter. A similar reversal is seen in mean wind observations made on the Birdlings Flat radar, [Fraser, 1989].

This project was primarily interested in short term activity in the upper mesosphere and lower thermosphere since the time scales of most of the experiments ranged from minutes to several hours. The main activity in the middle atmosphere corresponding to these time scales is that of "atmospheric gravity waves" and this topic is discussed further in section 3.1.

Two regions in figure 1.1, the stratosphere and the thermosphere, show an increase in temperature with altitude because of the significant absorption of solar radiation that occurs in those regions. In the stratosphere the ozone layer absorbs ultraviolet radiation

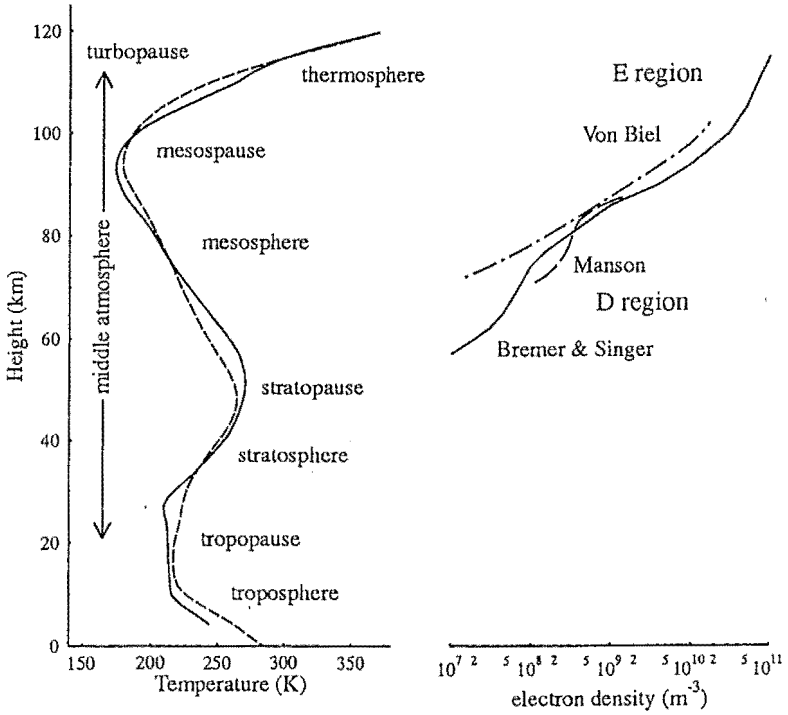

Figure 1.1: **The Structure of the Atmosphere.** The temperature profiles are from the reference atmosphere [CIRA, 86]. The solid line indicates the annual mean profile at latitude 45°S and the dashed line at 80°S. The electron density profiles are a mean mid-latitude profile, from [Bremer and Singer, 1973], a typical profile from the Scott Base radar using the techniques of [Von Biel, 1989], (collected at 09:00 on 1 Jan 1991) [von Biel, pers.comm.] and a profile from [Manson, 1965] who used differential absorption techniques at Christchurch.

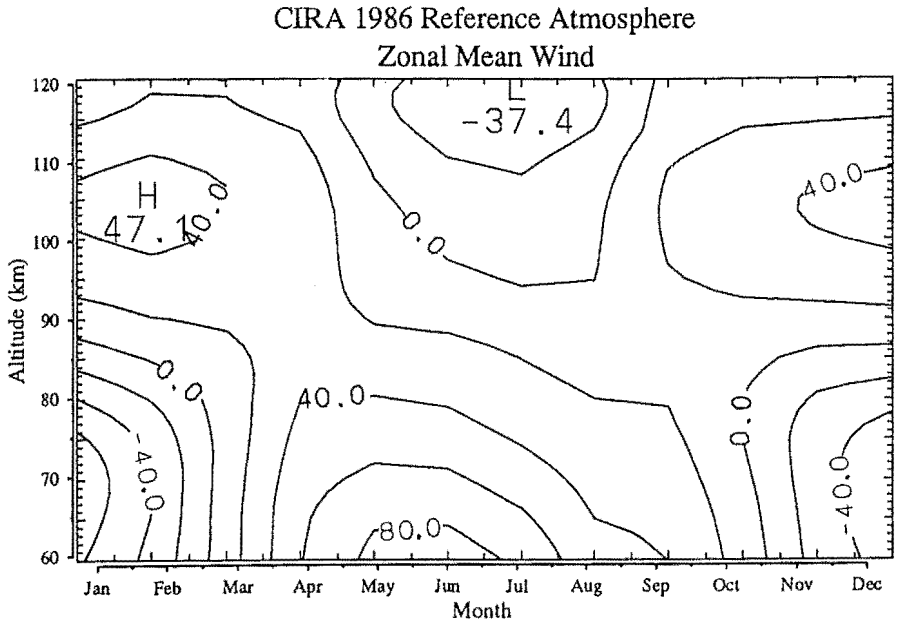

Figure 1.2: **Reference atmosphere zonal wind at** 45°S, monthly means, [CIRA, 86]. (The contours are at 20 ms^{-1} intervals.)

and in the thermosphere atomic and molecular oxygen in particular absorb ultraviolet and other radiation. In the thermosphere, this absorption results in ionization of the region into ions and free electrons and thus the formation of the ionosphere. There is also absorption of radiation in the mesosphere leading to some ionization there; however this absorption is not as significant in the heating of the region as the absorption in the stratosphere and in the thermosphere. The ionospheric regions included in the middle atmosphere are the D-region and the lower part of the E-region.

1.2 The Lower Ionosphere

The lower ionosphere consists of the D-region and the lower part of the E-region. Beyond the E-region there is the F-region and the magnetosphere; however these regions are beyond the scope of this project. The main sources of ionization in the D-region are solar far ultraviolet radiation, hard X-rays and cosmic rays. In the E-region, solar far ultraviolet and soft X-rays are the main ionization sources. With the removal of the ionizing sources at night time the ionization in the D and E regions declines greatly. Typical day time free electron density profiles in the D and E regions are given in figure 1.1. At night time the E region electron density is approximately two orders of magnitude lower; the D region

electron density is also lower although the magnitude of the decline is more variable than in the E region. The electron density of the E region and particularly the D region vary greatly from day to day and from location to location as is indicated by the variability between the profiles of this figure. Variations in solar activity have a considerable affect on ionization in the D and E regions, with enhanced activity producing typically an order of magnitude increase in electron density. Also at times an extra layer of intense ionization, known as sporadic-E, occurs. This layer often appears as thin sheets at altitudes of between 90 to 120 km.

The reason for the uneven electron density profile leading to the division of the ionosphere into various regions relates to the variation in chemical composition with altitude, particularly above the turbopause where molecular diffusion leads to some segregation of various components. In the D-region nitric oxide (NO) is ionized and in the E region molecular oxygen (O_2) is ionized. However the distinction between the D and E regions in the ionization profile is often not very strong; the D region just being a slight indentation in the profile and at times is completely indistinguishable from the E region.

1.2.1 Magnetoionic Theory and Refractive Index

A considerable body of knowledge has built up regarding the interaction of radio waves and the electron plasma in the ionosphere and standard texts in this work are [Davies, 1966, Davies, 1990] and [Budden, 1985].

The free electrons in the ionosphere interact with an electric field (such as the electric field of a radio wave). A natural frequency of oscillation is the "plasma frequency", ω_N. The plasma frequency is given by

$$\omega_N^2 = \frac{Ne^2}{\epsilon_o m_e}. \tag{1.1}$$

where N is the electron number density (electrons per cubic metre), e and m_e are the charge and mass of an electron respectively and ϵ_o is the permittivity of free space, (ω_N here is the angular plasma frequency.) For the profiles of figure 1.1, the plasma frequency is about 1 MHz at 95-100 km and 3 MHz at around 120 km, although in practice these values vary considerably as the electron density varies.

The refractive index of the plasma in the ionosphere is given by the Appleton equation (sometimes known as the Appleton-Hartree or Appleton-Lassen equation) based on a series of works such as [Appleton, 1928]. This equation has several forms, (for example [Davies, 1966]), depending on factors such as whether a magnetic field or collisions between electrons and molecules of the neutral atmosphere are considered. For the purposes of this work the effect of the earth's magnetic field in the D region can be taken to be negligible;

however collisions between electrons and the neutral atmosphere are important. The Appleton equation here then is,

$$n^2 = 1 - \frac{\omega_N^2}{\omega^2} \frac{1}{(1 - i\frac{\nu}{\omega})} \tag{1.2}$$

where i is $\sqrt{-1}$, ω is the probing frequency and ν is the electron collisional frequency (collisions per second). The refractive index here is complex and this can lead to absorption which maximizes when the collisional frequency approaches the probing frequency.

Since it is related to the electron density as well as the density of the neutral atmosphere, the collisional frequency varies considerably with time and declines rapidly with altitude. Typically it might be of the order of 3 MHz at around 80 km and have fallen to less than 100 kHz at around 100 km, [Budden, 1985].

Higher into the ionosphere, for example the lower E-region, the collisional frequency can be ignored and the refractive index becomes real; however geomagnetic field effects become important. If the geomagnetic field is ignored, the refractive index can be approximated by

$$\mu^2 = 1 - \frac{\omega_N^2}{\omega^2}; \tag{1.3}$$

however when the geomagnetic field is considered the equation becomes much more complicated with the inclusion of terms involving the transverse and longitudinal components of the field with respect to the direction of propagation of the radio wave.

By Snell's law, when a wave encounters a region where the refractive index is zero the wave is reflected. Here then, a radio wave traveling up into the ionosphere is "totally" reflected when it encounters a region where the frequency of the wave equals the plasma frequency of the region. In the case of equation 1.2, the real part of the refractive index never reaches zero so total reflection never occurs, however strong reflection can occur as the refractive index gets very small.

The electron density of the ionosphere increases with altitude as seen in figure 1.1 and so the plasma frequency, and thus the frequency at which radio waves get totally reflected, increases as well. At night time, the electron density of the whole ionosphere declines and so radio waves of a given frequency travel higher before being reflected. (For example MF radio waves are generally totally reflected at around 110 - 120 km during the day time and often above 150 km at night.)

The electron density profile is somewhat layered and the maximum plasma frequency for each layer is known as the "critical" frequency for the layer. If a radio wave has a higher frequency than the critical frequency of a layer it will penetrate that particular

layer. The E region critical frequency at mid-latitudes varies from around 4 MHz during the middle of the day down to around 2 MHz before dawn and after dusk.

Radio waves can also be returned from the atmosphere when fluctuations in refractive index occur. Then just a portion of the energy in the wave is backscattered so the wave is said to be "partially reflected". Partial reflections are a very important scattering process for radar probing of the D-region although the amount of signal returned in this manner can vary greatly.

The degree of scattering via partial reflection mechanisms is related to the intensity of the refractive index fluctuations which in turn is related to the intensity of fluctuations in electron density. These relationships are non-trivial without making great simplifications. For example following [Woodman and Guillen, 1974] (who were working at VHF wavelengths) and ignoring the collisions between electrons and the neutral atmosphere and by assuming the radio wave frequency is much greater than the plasma frequency, differentiating the refractive index (equation 1.3) with respect to the electron density gives

$$\delta n = \frac{\omega_N^2 \delta N}{2\omega^2 N}. \tag{1.4}$$

Expressions based on this form are often used to relate atmospheric fluctuations (for example turbulence) to scattered signal strength. In general the greater the fluctuations, and thus fluctuations in δN, the greater the strength of the scattered signal. However in formulating these relationships there are many complicating factors to consider such as variations in the volume of these fluctuations in view at one time and the relationship between δn and scattered signal strength, (see for example [Gage, 1990]). At MF wavelengths where collisional and plasma frequencies are of greater importance, the situation is further complicated so there will not be a more quantitative attempt to relate scattered signal strength to intensity of atmospheric fluctuations here.

As a radio wave approaches a region where the refractive index for the wave is near zero, the group and phase velocities of the wave begin to have different magnitudes. The group velocity slows down so if the range is determined by recording the time between transmission of a wave and reception of its echo and it was assumed to travel at the speed of light, then the inferred range can be too great. The range determined solely from timing in this way is the "virtual" or "group" height of reflection. The "real" height of reflection can be estimated from the virtual height using factors such as the electron-density profile and the geomagnetic field. The difference between the virtual height and the real height is sometimes referred to as the "pulse retardation". [Fraser and Kochanski, 1970] determined the pulse retardation for the Birdlings Flat radar under various conditions and

found that typically it was less than one kilometre for reflections at around 100 km and less than this for lower altitudes.

1.2.2 Geomagnetic Storms and the Polar Ionosphere

Occasional solar storms produce streams of charged energetic particles that interact with the earth's geomagnetic field and the upper atmosphere. These interactions disrupt the ionosphere and the geomagnetic field producing geomagnetic storms. Geomagnetic storms have a variety of effects on radio wave propagation. The high latitude ionosphere, being close to the magnetic pole and thus the "auroral zone", can become particularly disturbed.

During geomagnetic storms bursts of energetic electrons penetrate the earth's atmosphere (known as "precipitation"). "D-region absorption" often results in which radio waves travelling in the region can be totally absorbed. The Scott Base radar is well within the southern auroral zone and during severe absorption events receives no signals at all from any part of the ionosphere. At other times ionization to levels as low as 40 km altitude can occur, [Von Biel, 1992], apparently due to influxes of electrons that have relativistic energies. [Manson and Meek, 1991] at Saskatoon (52°N) in Canada observed that particle precipitation has an effect on winds and tidal oscillations in the mesosphere, although the magnitude of the effect is fairly weak ($\sim$ 10%).

Other geomagnetic effects and electric field effects can become important in the upper mesosphere in polar regions. During storms, the influence of these fields on the motion of electrons can be significant. [Reid, 1983], working on the Alaskan Poker Flat VHF radar (65°N), considered that there it was possible for the electrons to have induced velocities of around 1 ms^{-1} at 90 km and 10 ms^{-1} at 100 km as a result of geomagnetic and electric field interactions during disturbed conditions. Radar observations of this motion could be easily misinterpreted as movement of the neutral atmosphere. Reid notes that even during relatively quiet geomagnetic conditions, vertical wind observations may be in error because of this effect.

1.3 Scattering Processes in the Middle Atmosphere

This section introduces the main radio wave scattering processes in the middle atmosphere. Recent reviews on this topic include [Reid, 1990], [Gage, 1990] and [Hocking, 1989].

It was apparent in early MF radar observations of the mesosphere that partial reflection processes are important in the mesosphere. For example [Gardner and Pawsey, 1953] in Australia reported partial reflections apparently from layers around 70 km. [Gregory, 1956]

observed stratified layers and reported their diurnal variations. It was found that such preferred reflecting layers in the mesosphere appeared globally, [Titheridge, 1962]. Also at VHF wavelengths reflections from the mesosphere were reported which were of a greater strength than that anticipated from the assumed electron density or turbulence structure of the region, (for example [Flock and Balsley, 1967]).

As was discussed above, if radio waves traveling up into the atmosphere encounter a region where either the refractive index of the medium drops to near zero or there are variations in the refractive index then they are either totally or partially backscattered. There seem to be two extremes to the backscattering processes, these being seemingly random backscatter or relatively strong, mirror-like, "specular" reflections as well as processes in between. The signals from these scattering processes are sometimes described as being incoherent and coherent because of the way their amplitude and phase does or does not fluctuate rapidly. Variations in refractive index are generally associated with turbulence or with some form of stratification, leading to either the random backscatter or specular reflections respectively. Total reflections tend be fairly specular because the electron density only becomes sufficiently high for MF total reflection in the E-region which is in the more stable thermosphere. Sporadic-E layers in particular result in very strong specular reflections on MF radar. Specular reflections can become seemingly random-like if the reflecting layer becomes distorted leading to multiple specular reflecting paths which interfere. Alternatively there can be several specularly reflecting layers in view at one time which also lead to interfering reflections. Both of these cases can be difficult to distinguish from random backscatter.

Backscatter can be isotropic, that is scatter evenly in all directions, or can be more anisotropic displaying directionality, limited "angular spread" or "aspect sensitivity". Single specular reflections are, of course, very aspect sensitive, although multiple specular reflections tend to be less so. Aspect sensitivity is an important indicator of the nature of the scattering process being observed and many studies have examined this topic. Most studies have found that there is a variation in aspect sensitivity with altitude. Generally below about 80 km scattering appears to more aspect sensitive (that is more directional) than above this level, (for example [Fraser and Vincent, 1970] and [Lindner, 1975b]). The topic of aspect sensitivity and its measurement in this project is discussed further in sections 3.3 and 7.9.1.

Note that in this work (and in middle atmosphere radar work in general) the term scatter or backscatter will be often used when describing any scattering or reflection process

irrespective of these two extremes. Also the term scattering region will be used to indicate a region in the atmosphere where either random backscatter or some sort of specular reflections occur. Another term that will be used is "scattering centre" (or "scatterer") which generally refers to fairly localized scatter but is not necessarily constrained to any particular scattering model.

1.3.1 Diffraction Considerations

Early studies in scattering, or "diffraction", theory applied to the ionosphere include [Bramley, 1951] and the review of [Ratcliffe, 1956]. These workers laid some of the ground work for analyses that use scatter from the atmosphere to make measurements of motion in the scattering region and estimate the temporal and spatial scales of the scattering.

The scattering region is modelled as a diffraction screen which can be dominated by "irregularities" leading to random scatter, or specular reflection can be more important. An observer on the ground sees a diffraction pattern of signals on the ground that forms as a result of scattering in the screen.

Bramley examined how the scale of the diffraction pattern observed on the ground relates to the scale of structures causing the scattering in the atmosphere. His results show that if the diffraction screen is "deep", that is it leads to large variations in the scattered signal, the diffraction pattern scale on the ground is considerably smaller than the scales of irregularity in the diffraction screen. This reduction in scale occurs because the many components of the deep scattering interfere with each other. On the other hand, if the screen is "shallow" resulting in a steady or specular component to the scattered signals, the diffraction pattern has scales similar to those in the diffraction screen. These effects can be parameterized in terms of the standard deviation ϕ_m of the random phase changes imposed on the scattered signals as they leave the diffraction screen. A shallow screen is one which imposes phase changes of $\phi_m < 1$. A deep screen for which the phase changes $\phi_m \gg 1$ results in diffraction scales on the ground being smaller by $\frac{1}{\phi_m}$ than the scales in the screen. Experiments that measure the spatial scale of the diffraction pattern on the ground cannot, from these observations alone, determine whether the scattering is undergoing deep or shallow scattering so cannot relate the scales directly to scales in the scattering region.

When examining scattering from the atmosphere, it becomes apparent that the scattering can be modelled using either Bragg scatter or Fresnel diffraction principles, for example [Doviak and Zrnic, 1984]. Bragg scatter refers to the preferential scatter that occurs from structures of the scale of half the wavelength of the probing radio waves.

Fresnel diffraction becomes important as the horizontal scale of the scattering structures increase to around the scale of the Fresnel zone, (the radius of the first Fresnel zone is $\sqrt{\frac{r\lambda}{2}}$, r being the range and λ the wavelength). The Fresnel zone for MF scattering from the mesosphere is of the order of two kilometres. Fresnel diffraction is used because the spherical (rather than planar) form of the wavefront is found to be significant for scattering from structures of around this scale or larger.

There are three main classifications used to describe scattering processes seen in radar studies of the middle atmosphere. These are Bragg scatter, and two forms of Fresnel processes, Fresnel reflections and Fresnel scatter. (There is also Thomson scatter but this is only important at high VHF or at UHF wavelengths so will not be considered here).

1.3.2 Bragg Scatter

Bragg scatter originates from structures much smaller than the Fresnel zone and is strongest from structures of a depth about half the probing wavelength. The only structures with such small scales in the mesosphere are thought to be various forms of turbulence and so this scatter is also often known as "turbulent scatter". Bragg scatter is characterised by its random confused nature, the amplitude and phase of the backscattered signals tend vary continuously in an irregular manner. This behaviour has lead some to term the structures causing this scatter, "irregularities".

As will be seen in section 3.2, the structure of turbulence can be isotropic leading to isotropic scatter or can be somewhat elongated leading to more anisotropic, although still random scatter. Since turbulence involves random motion in many directions, the backscattered signals have a broad range of different Doppler shifts. If the scattered signals are spectrally analysed, the amplitude spectra tend to have a broad Gaussian like envelope and the phase varies randomly between $\pm\pi$ radians. Because turbulence is in general fairly extensive, increasing the viewing area of the radar increases the scattered power.

1.3.3 Fresnel Reflection

Fresnel reflection includes the specular reflections mentioned above. Originating from much larger structures the reflected signals are much more steady or "coherent" than Bragg scattered signals. The reflected signals can also be considerably stronger than Bragg scattered signals.

These reflections appear to be associated with some form of stratified layer or sheet

which for some reason have large discontinuities in refractive index. Some of these discontinuities are simply the result of ionization effects, the ionizing radiation penetrating to certain depths and forming ledges in electron density which reflect the radar pulses. At times however there are thought to be more complicated processes involved. Some of these processes have been linked to conditions such as temperature inversions or to certain turbulent conditions such as extremely anisotropic turbulence in the presence of an electron density gradient, [Bolgiano, 1968].

The sheets, which generally appear to extend for a few kilometres or more, occur occasionally in the mesosphere and in the lower thermosphere, where they may take the form of sporadic E. In its simplest form, Fresnel reflecting sheets have just one reflection point and thus a single steady component to the scattered signal. The sheets can become distorted by other effects in the atmosphere such as atmospheric gravity waves and there may then be more than one reflection point in which case the reflected signals interfere with each other and the observations of the scattered signals become more confused.

In the situation of three or fewer components, spectral analysis of the reflected signals results in an amplitude spectrum with strong spikes corresponding to each component at spectral frequencies depending on the Doppler shift of each component and a phase spectrum with steady behaviour around each spike. Provided the pulse power does not vary and the layer and reflecting points remain inside the volume of view of the radar, altering the viewing volume does not alter the received signal power.

1.3.4 Fresnel Scattering

Fresnel scatter is a variation on Fresnel reflection, in that it models scattering as being the result of multiple Fresnel reflecting layers occurring within the viewing volume of the radar at one time. The specular reflections from each layer interfere with each other to produce quasi-randomly varying signals. Spectral analysis of the signals shows a number of strong spikes in the amplitude spectrum and a somewhat irregular phase spectrum. Unlike the Fresnel reflection model (with, say, just one reflecting point), Fresnel scattered signals increase their intensity as the viewing volume of the radar is increased because more reflection points come into view.

The concept of multiple localized Fresnel reflecting structures was advanced by [Austin and Manson, 1969] to explain observations on the MF radar at Birdlings Flat. The model has advanced considerably with the development VHF radar probing of the middle atmosphere beginning with [Gage et al., 1981], with updates by studies such as [Hocking and Röttger, 1983] and [Gage et al., 1985], and now is considered very important

in radar observations of the middle atmosphere. (The term "Fresnel scatter" originated in VHF work.)

Like Fresnel reflections, Fresnel scattering is influenced by motions such as atmospheric gravity waves. In the mesosphere, longer period gravity waves in particular seem to generate Fresnel scattering as the waves produce fluctuations in the refractive index of the region, for example [VanZandt and Vincent, 1983] and [Muraoka et al., 1989].

1.4 Middle Atmosphere Radars

This section introduces the radar techniques that are used in the study of the middle atmosphere. The collections of [Fukao, 1988] and [Atlas, 1990] provide comprehensive reviews of these radar techniques and current aspects of research into these techniques include the collections of [Liu et al., 1990] and [Edwards, 1991].

Radars that probe the middle atmosphere usually operate either around 2-3 MHz in the Medium Frequency (MF) band, in the Very High Frequency (VHF) band, typically around 50 MHz or in the Ultra High Frequency (UHF) band. Radio scattering from mesospheric heights in particular is very weak. Even at MF wavelengths where the backscatter is strongest radars have to have peak powers of typically a few tens to about a hundred kilowatts to get reliable backscatter. At VHF wavelengths higher powers and/or considerable averaging of the scattering signals is required, and even then most VHF radars only obtain adequate scattering during daylight hours. Better coverage is obtained with VHF radars if scattering from meteor ionization trails is used, although this scattering is normally limited to an altitudes of 90 - 100 km. UHF radars normally only operate in troposphere and stratosphere although there are a few very powerful UHF radars, known as Incoherent Scatter Radars (ISR), which use very weak Thomson scatter from free electrons to obtain scattering from the upper mesosphere and beyond.

The regions of the atmosphere that a radar probes are often used to describe the radar. For example radars (particularly UHF and VHF radars) that probe the Stratosphere and Troposphere are often called *ST* radars and those that probe the Mesosphere, Stratosphere and Troposphere are often called *MST* radars. These acronyms are not normally applied to MF radars, although sometimes these radars are referred to as D-region radars.

The emphasis in this section will be on the type of radars used in this project, Medium Frequency, Spaced Antennae[1] radars although at various points higher frequency radars will be mentioned.

[1]The plural *antennae* will be employed here, although *antennas* and the term *Spaced Antenna* find common usage in the literature.

1.4.1 Radar Concepts

This section outlines the components and operation of typical spaced antennae radars and introduces some of the terminology used on these and middle atmosphere radars in general.

Figure 1.3 illustrates many of the points discussed in this section. A transmitter linked to an antenna generates short high powered pulses of radio waves. The waves travel upwards into the atmosphere and, as has been discussed above, if they encounter a region where the refractive index drops to near zero or a region where there are fluctuations in the refractive index, they are either totally or partially backscattered. In general the scattering has more than one component so the different scattered signals interfere with each other. If the scattering region has components of motion along the line of sight of the radar, then the signals can be Doppler shifted to slightly different frequencies.

On the ground there are typically three receivers each linked to separated antennae (hence "spaced antennae"). These receivers detect the transmitted radio pulse directly from the transmitter (the "ground pulse") and, a short time later, backscattered signals from the atmosphere. An image of the signal level produced by a receiver during reception of the ground pulse and the scattered signals, known as an "A-scan", is given in the figure.

The range of the backscatter can be estimated by simply recording the time delay between reception of the ground pulse and reception of the backscattered signals. Because the pulse issued has some finite length, typically tens of microseconds, there is an uncertainty to the exact range which is the "resolution" of the radar. The resolution of the radar also depends on factors such as the bandwidth of the transmitter and receivers which, if not sufficiently broad, can smear the signals and degrade the resolution.

The viewing area of the radar, that is the area of the scattering region probed by the radar, depends on the directivity or "polar diagram" of the radar's antennae. The polar diagram describes the variation in power as a function of direction; the "beam width" of the antenna is the angle between the half power points of the antenna's polar diagram.

The A-scan is sampled by data logging equipment which records the voltage level at small intervals along the scan using Analogue to Digital (A/D) converters. The length of these intervals, or "range gates", can also have a bearing on the range resolution of the data. The sample at a range gate then is a composite of signals backscattered from a spread of ranges corresponding to the resolution of the radar, and from an area in the scattering region corresponding to the beam width of the radar's antennae. In the scattering region this area times depth of resolution is often referred to as the "radar volume".

Usually a series of A-scans are made and the samples at particular range gate are

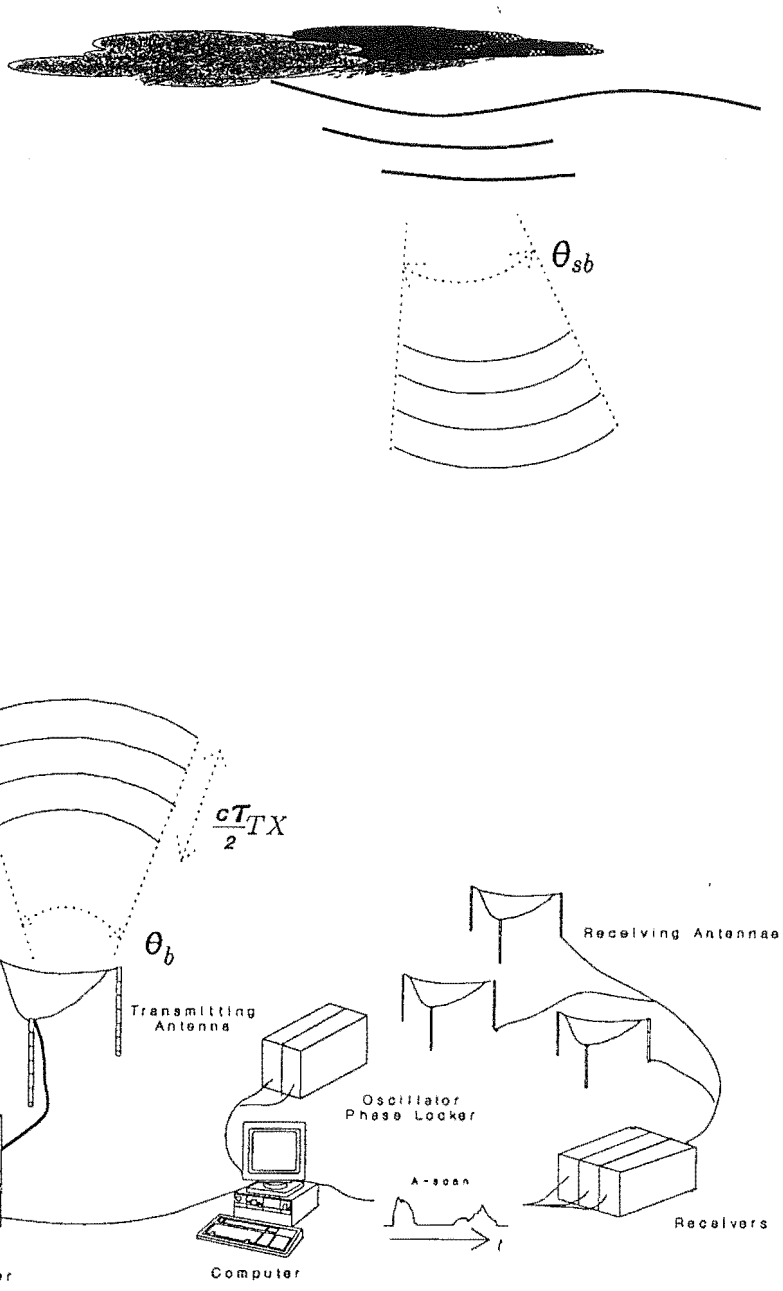

Figure 1.3: **Components of a radar,** based loosely on the Scott Base MF radar. A "pulse" of radio waves (indicated by the four arcs) is transmitted into the atmosphere and is partially reflected, perhaps from diffuse turbulent structures or perhaps from thin specularly reflecting layers. (Note that normally only one pulse would be in flight at one time.) The length of the transmitted pulse (τ_{TX} in time or $\frac{c\tau_{TX}}{2}$ in range) and angular width of the pulse (θ_b, determined by the antenna beamwidth), define the "radar volume". The angular distribution (θ_{sb}) of the backscattered signals may be wider or narrower than that of the transmitted pulse depending on whether the scattering is diffuse or specular. In this radar, three spaced antennae receive the scattered signals which are demodulated by three receivers. An image of the amplitude of the demodulated signal as a function of time is labelled the "A-scan". The signal is converted to digital form and stored in the computer. As well as collecting data, the computer controls the radar, instructing the transmitter when to pulse, and, for this project, selecting the operating frequency of the radar.

collated together to build up a time series of samples. Generally, depending on the capabilities of the data recording equipment, there are several such time series recorded each corresponding to a different range gate. These time series are then analysed to determine information about the behaviour of the scattering region. An example of this analysis is the examination of the series by time series analysis techniques to look for periodic behaviour in the signal level of the series.

The amplitude of the signals received by the radar receivers is displayed in the A-scan of figure 1.3. Receivers that just detect the amplitude of signals are "incoherent receivers". The radars used in this project were adapted to be "phase coherent" so that phase as well as amplitude information was available. (As noted above the terms incoherent and coherent are also sometimes used to describe the signals from random scatter and specular reflections and is also used to describe UHF Thomson scatter radars.) Phase coherent receivers compare the phase of the signals they receive with the waveform from which the transmitted pulse was originally generated. The outputs of a typical phase coherent receiver consists of "inphase" and "quadrature" channels, which can essentially be treated as the cosine and sine parts, or real and imaginary parts, of a complex function. If the received signals are at a different frequency to that of the transmitted pulse because of Doppler shifting in the scattering region, then the inphase and quadrature outputs include an oscillating component to their signals at the difference frequency, or in this case the Doppler frequency.

Other advantages of phase coherency used in this project are the ability to compare the phase of signals received on different antenna and thus determine the direction the scattering came from. Also it is possible to observe how the phase of the scattered signals change as the wavelength of the radar is changed. As will be shown, this can allow a finer measurement of range than is possible using timing methods.

1.4.2 Spaced Antennae Radars

This is the type of radar used in this project. These radars use three or more receiving antennae that are separated on the ground by typically one or two wavelengths of the radar. The signals received on each of the antennae are compared to derive information on the characteristics of the scattering region. Most MF radar use spaced antennae techniques, and a number of VHF radars have recently introduced spaced antennae techniques as well.

Spaced antennae radars generally use broad beam antennae so that a large area in the sky is probed. Being able to use broad antennae is a significant advantage on MF radar because the antenna systems can be kept fairly simple. Each antenna can consist of as few

as one or two half wavelength elements, a bonus when the wavelength is about a hundred metres.

Using broad antennae means that parameters found on spaced antennae radars tend to be an average of a broad scattering region although if there are strong scatterers in the radar volume these will dominate the received signals. The scattering from a range of structures in the broad radar volume lead to a seemingly irregular diffraction pattern of backscattered signals at the ground. There are two main approaches to the analysis of the signals received on spaced antennae radar :

Spaced Antennae Drifts

If the scattering structures are moving due to wind or oscillations in the scattering region then the diffraction pattern on the ground moves (or "drifts") as well, [Mitra, 1949]. If the fluctuations in signal received at one antenna are compared with the fluctuating signals received at a separated antenna there appears to be a time delay between the sets of signals that can be related to the motion of the diffraction pattern. The signals on two antennae are usually compared by means of correlation functions, whereby the signals at each antenna are cross correlated with each other at a series of different timing offsets or "lags". By using correlation functions on three spaced antenna, and finding the time lag of maximum correlation between each pair of antennae, a velocity vector can be determined. This technique forms the basis of the "Spaced Antenna Drifts" (SAD) technique and the analysis procedure often used in technique is known as "Full Correlation Analysis" (FCA), [Briggs et al., 1950]. The development of SAD and FCA will be discussed more fully in chapter 6, where complications such as evolution and elongation in the diffraction pattern are considered. As will be seen in that section, FCA can supply measures such as the degree of evolution and elongation in the scattering and can estimate the scale of scattering.

Spaced antennae drifts is the principal form of mode of operation used on the two radars used in this project and is commonly applied to MF spaced antennae radar. The receivers need not be phase coherent and the Birdlings Flat and Scott Base radars are normally operated in incoherent mode.

Interferometry Techniques

These techniques primarily use phase information and therefore the radar must have phase coherent receivers to run in interferometry mode. The techniques find the direction of arrival of the backscattered signals and measure the Doppler shift of those

signals, [Pfister, 1971]. (In this work the techniques that measure the Doppler shift and direction of arrival of signals will be termed *time domain* and *spatial domain* interferometry respectively.) If there are several distinct signals in differing directions, and each possess distinct line of sight velocities then the signals can be separated or "sorted" using their Doppler spectra. If the direction of arrival and the Doppler shift of each signal is known, a picture of the motion of the scattering region can be built up, [Farley et al., 1981]. Information such as the directional distribution of scattering can also be found. If there are too many scattering centres, particularly if they are moving somewhat independently of each other, signals from differing directions can have indistinguishable Doppler shifts resulting in a misleading interpretation of their motion. Diffuse or intermittent scattering can also confuse interferometry techniques.

There are several different variations to the application of interferometry techniques and the method used in this project will be discussed further in section 5.5. Interferometry techniques are being increasing applied to spaced antennae radars in conjunction with spaced antennae drifts because of the extra information they can supply about the distribution of scattering.

The experiments of this project collected phase and amplitude information on three spaced antennae which allows both spaced antennae drifts and interferometry analyses to be carried out and a comparison study to be made. Several other studies have also compared the results of both techniques for example [Adams et al., 1985] and [Meek and Manson, 1987]. In general the two techniques have been found to give fairly similar results and these comparison studies and comparisons of results from this study will be discussed in section 7.8.1. Comparison studies between spaced antennae drifts and non-radar techniques will be discussed in section 6.1.1.

1.4.3 Doppler Beam Swinging Radar

Doppler Beam Swinging (DBS) radars, (sometimes referred to as Doppler radars) point a narrow beam in typically three or more directions into the atmosphere, (for example [Woodman and Guillen, 1974]). These direction might be zenith and several degrees off zenith towards say the east, and several degrees towards the north. The Doppler shift of signals received in each direction is measured and the resulting radial velocity estimates are used to determine the wind in the scattering region. Estimates of turbulence in the scattering region can also be made using the width of the spread in Doppler shifting along each beam.

The Doppler beam swinging method assumes that the wind field is the same in each direction that the radar looks along, even though these the scattering volumes can be tens of kilometers apart. The radar volumes of each of the directed beams are much narrower than those used in spaced antennae drifts; however they still do include a significant area of the scattering region. Information about the distribution of scatterers in the radar volumes is not available. If there are strong scatterers unevenly distributed in the radar volumes, for example towards one edge of a volume, the inferred direction of signal can be in error, leading to significant errors in the resulting velocity, [Röttger, 1981] and [Fukao et al., 1988a]. Also there can be variations in the line of sight component of the wind in the radar volumes (for example see figure 3.6 in section 3.2.1) which must be allowed for when measuring parameters such as turbulence, [Hocking, 1983b].

A narrow antenna beam is required which requires antenna arrays consisting of a large number of elements. Therefore the technique is normally only used on VHF or UHF radars where the wavelength, and thus the antenna elements, are of scales of metres or less. VHF and UHF radars also require arrays of many elements for signal level reasons because the backscattered signals from the middle atmosphere are comparatively much weaker at VHF and UHF than MF. To carry out Doppler beam swinging at the longer wavelengths of MF radars, a very extensive array is necessary to obtain a sufficiently narrow antenna beam. One MF radar, the Buckland Park radar run by the University of Adelaide in South Australia does use Doppler beam swinging techniques with an antenna array that is approximately one kilometre across, [Briggs et al., 1969].

1.4.4 Comparing Spaced Antennae Drifts and Doppler Beam Swinging

Many comparison studies of the Doppler beam swinging and the spaced antennae drifts methods have been made. The principles behind the methods have been examined by [Briggs, 1980] and [May, 1990]. Briggs showed that fundamentally both methods make the same measurement; the Doppler shifting that is observed directly in the Doppler beam swinging method is equivalent to that observed indirectly in the motion of the diffraction pattern on the ground in the spaced antennae method. May and [Röttger, 1981] considered the aspect sensitivity of scattering, showing how spaced antennae methods have an advantage if the scattering is aspect sensitive.

A number of sites have operated Doppler beam swinging and spaced antennae techniques either simultaneously or nearly simultaneously. For example at the South Australian Buckland Park site, on the HF system observing the mesosphere, [Hocking, 1983a], and on the VHF system in an extensive tropospheric study that included comparisons with

radiosonde (balloon) wind measurements, [Vincent et al., 1987]. Also on the Japanese MU radar (run by the Radio Atmospheric Science Center of Kyoto University) both spaced antennae and Doppler beam swinging measurements can be carried out and in another tropospheric study [Van Baelen et al., 1990] compared both techniques. All of these studies found good agreement between the two methods.

1.4.5 Frequency Shift Techniques

Techniques that shift the operating frequency of radars are increasingly being developed on middle atmosphere radars. These various frequency shifting techniques generally attempt to enhance the range resolution of the radar.

In this project a frequency shift technique here referred to as frequency stepping was employed which involved pulsing the radar at frequencies that differ by up to about 1% ($\sim$ 30 kHz) from the normal operating frequency. Frequency stepping techniques are a very recent development on MF radars and are also fairly new to other middle atmosphere radars, although the concepts were raised sometime ago by [Briggs, 1951].

The backscattered signals at each of the different frequencies are compared. As will be seen in section 5.3 the variation in the phase of the signals as the frequency is varied can be directly related to the range of the scattering. The coherence between signals of different frequency depends on how well defined the scattering is. If the scattering originates from a sharp layer (for example a single Fresnel reflection) then the signals are highly correlated as the frequency of the radar is changed, however if there is scattering from a spread of scattering centres, then the coherence is much lower. The coherence of signals as the frequency is stepped then, provides a measure of the "scattering depth" of the reflecting structures.

The method of analysis used in the frequency stepping experiments of this work has become known as *frequency domain interferometry*, [Kudeki and Stitt, 1987]. Most of the experiments in this project included frequency stepping, typically switching between five different frequencies. This project one of the first to implement frequency domain interferometry on MF radar and the first to incorporate spaced antennae drifts, temporal, spatial and frequency domain interferometry techniques on MF radar.

Chapter 2

The Radars

Two radars were used in this project. These are at Birdlings Flat near Christchurch and at Arrival Heights near Scott Base on Ross Island in the Antarctic. Both radars run on-going partial reflection spaced antennae drift programmes for measuring winds in the mesosphere and lower thermosphere, [Fraser, 1989], and much of the equipment used in this project is associated with these programmes.

Before the radars themselves are discussed the operation of the partial reflection drifts programmes will be commented on in section 2.0.1. Section 2.0.2 mentions some aspects of the operation of this project that are common to both radars. Sections 2.1 and 2.2 discuss the two radars and the running of this project's interferometry experiments and these sections are followed by an outline of the calibration procedures. section 2.3.

2.0.1 The Spaced Antennae Drifts Programmes

The two spaced antennae drifts programmes are operated as similarly as possible to allow ready interchange of procedures and comparison of results between the two programmes.

The two radars have many features in common, for example they both have separate transmitter and receiving antennae arrays and operate at comparable frequencies (2.4 MHz and 2.9 MHz). Both programmes use three incoherent receivers so that only the amplitude of signal received by the radar are normally available. Logarithmic amplifiers are included on the receiver outputs to increase dynamic range.

The data collection routines are also similar. The transmitter is pulsed at 4 Hz for 256 samples so that the sampling time is 64 seconds. Data is collected from the receivers using three A/D converters which sample the A-scans at 64 points and store the data in computer memory for processing at the end of the pulsing run. Full Correlation Analysis is then carried out on the data at each range bin using the procedure of [Brown and Chapman, 1972].

The routine takes between three and ten minutes to run, depending on the quality of the data; the data is not fully analysed if, for example, the signal to noise ratio of the data is deemed to be too low. A summary of the results, which includes average signal, 'fading time', 'apparent' and 'true' FCA winds and correlation ellipse parameters (see section 6.2), is stored on magnetic media for further later analysis. The raw data is then discarded and the sampling processes restarts.

2.0.2 The Interferometry Experiment

The experiments of the current project were designed to be able to carry out time, spatial and frequency domain interferometry.

Time and spatial domain interferometry requires the radars to be phase coherent. This means that the receivers must be capable of measuring the phase of the signals they receive compared to some stable reference. The output these receivers produce is an oscillating signal at the difference frequency between the reference and the received signals. The outputs consist of two channels, labelled *in-phase* and *quadrature* channels which can be modelled by the complex form $Ae^{i\phi(t)} = A(\cos\phi + i\sin\phi)$; the in-phase channel being the cosine channel and the quadrature being the sine channel. The amplitude of the difference signal is the square of the sum of the channels and the phase is the arctangent of the quadrature channel divided by the in-phase channels.

The reference used here was the signal the transmitted pulse was generated from. The oscillations of the output signals must result from phase changes imposed from the time the signals leave the oscillator on their way to the transmitter and to them being received by the receivers after scattering in the atmosphere. As will be discussed in chapter 5, time variations of the phase of the received signals can be related to motion in the scattering region leading to Doppler shifting of the backscattered signals. The phase differences between the output signals from the different receivers are used to determine the direction of arrival at the radar of the backscattered signals in spatial domain interferometry analysis. There are other phase changes induced by the transmitter, antennae and the receivers themselves the effects of which are estimated here by the calibration techniques of section 2.3 and removed from the received signals.

To use the signal the transmitted pulse was generated from as a reference for the receivers, there must be a link capable of carrying this signal between the transmitter and the receivers. As will be seen, this requirement was readily met on the Birdlings Flat radar; however it proved more difficult to achieve on the Scott Base radar.

Frequency domain interferometry involves shifting the operating frequency of the radar

for each pulse. This was done here on both radars by using controllable oscillators at the receiving sites and carrying the signals to the transmitters along high speed lines.

Like the drifts programmes, the sampling period used in this project was one minute. This period seems to be a reasonable compromise between obtaining sufficient data points to be able to make reliable inferences about the collected data and avoiding changes in the characteristics of the data over longer sampling periods. The highest frequency of natural oscillations (over the scales measured by this type of radars) is the Brunt-Väisälä frequency which is about five minutes in the mesosphere. In general then the scattering region is not expected to change significantly over one minute and it has been found by experience that sampling over this period does give self consistent results.

Also like the drifts programmes, the sampling rate used during this period was approximately 4 Hz. The time scale of fluctuation in scattered signals (known as the fading time of the signals) is typically of the order of one to five or more seconds so the sampling rate was sufficiently fast to observe the characteristics of the fluctuating signals.

For frequency domain interferometry the frequency of the radar was cycled typically through five different frequencies. The signals received at each frequency were compared to the signals at the other frequencies so the radar had to be stepped through these frequencies at a rate considerably faster than the fading time to able to identify changes in the signal due to the frequency steps. Here there was generally 20 or 30 milliseconds between each frequency step. Each frequency was repeated a quarter of a second later to give the 4 Hz sampling rate for the signals of each frequency.

2.1 The Birdlings Flat Radar

The Department of Physics and Astronomy of the University of Canterbury operates a field station at Birdlings Flat (43°50′S, 172°40′E) at the base of Kaitorete Spit approximately 40 km south of Christchurch. A map of the area is shown in figure 2.1. The hills of Banks Peninsula, with peaks ranging between about 300 and 600 metres, separate the site from Christchurch reducing much of the higher frequency radio noise originating in the city. There are, however powerful A.M. transmitters at Gebbie's pass (15 km north of Birdlings Flat) that do at times produce considerable interference at the field station. The field station site is fairly flat and coastal, in the main being less than ten metres above sea level. A plan of the site appears in figure 2.2.

Two pulse radars are sited at Birdlings Flat, an MF radar, the main radar used for this experiment, which normally operates at 2.4 MHz, and an HF radar operating at 26 MHz. The 26 MHz radar is chiefly used for detecting meteors as they interact with the earth's upper atmosphere in order to determine the interplanetary orbits of the meteors, [Taylor, 1991]. Studies has been made into using these meteor trail observations to measure atmospheric parameters such as wind shears along the meteor path, (for example [Howick, 1991]). This radar has also been used as part of an oceanography experiment, [McGregor, 1985].

The 2.4 MHz radar has recently mainly been used for partial reflection drifts observations of mesospheric and lower thermospheric winds and turbulence. Dr. Grahame Fraser is the principal investigator for the drifts experiment, [Smith, 1981, Fraser, 1989], and the procedures used in the drifts experiment are discussed further in sections 2.0.1 and 7.6. The radar has also been used for D-region electron density measurements (for example [Manson, 1965]), although these measurements are not currently made, as well as being part of McGregor's oceanographic experiment. Some higher range resolution measurements of D-region partial reflections than are normally possible have been made on the radar. [Austin et al., 1969] demonstrated a method of enhancing the range resolution of A-scans using phase measurements. [Fraser and Vincent, 1970] made a series of phase height measurements in a seasonal study of scattering structures. A limited number of high range resolution observations were made by [Krenek, 1977] using pulse compression, or "chirp", of the transmitter pulse. [Brown, 1986] attempted vertical velocity measurements of the mesosphere using Doppler and angle of arrival techniques.

This project used the transmitter, antennae and the computer hardware of the drifts experiment. The receivers were developed for previous experiments, but currently are only used for the interferometry experiment. The phase locking arrangement, oscillators and

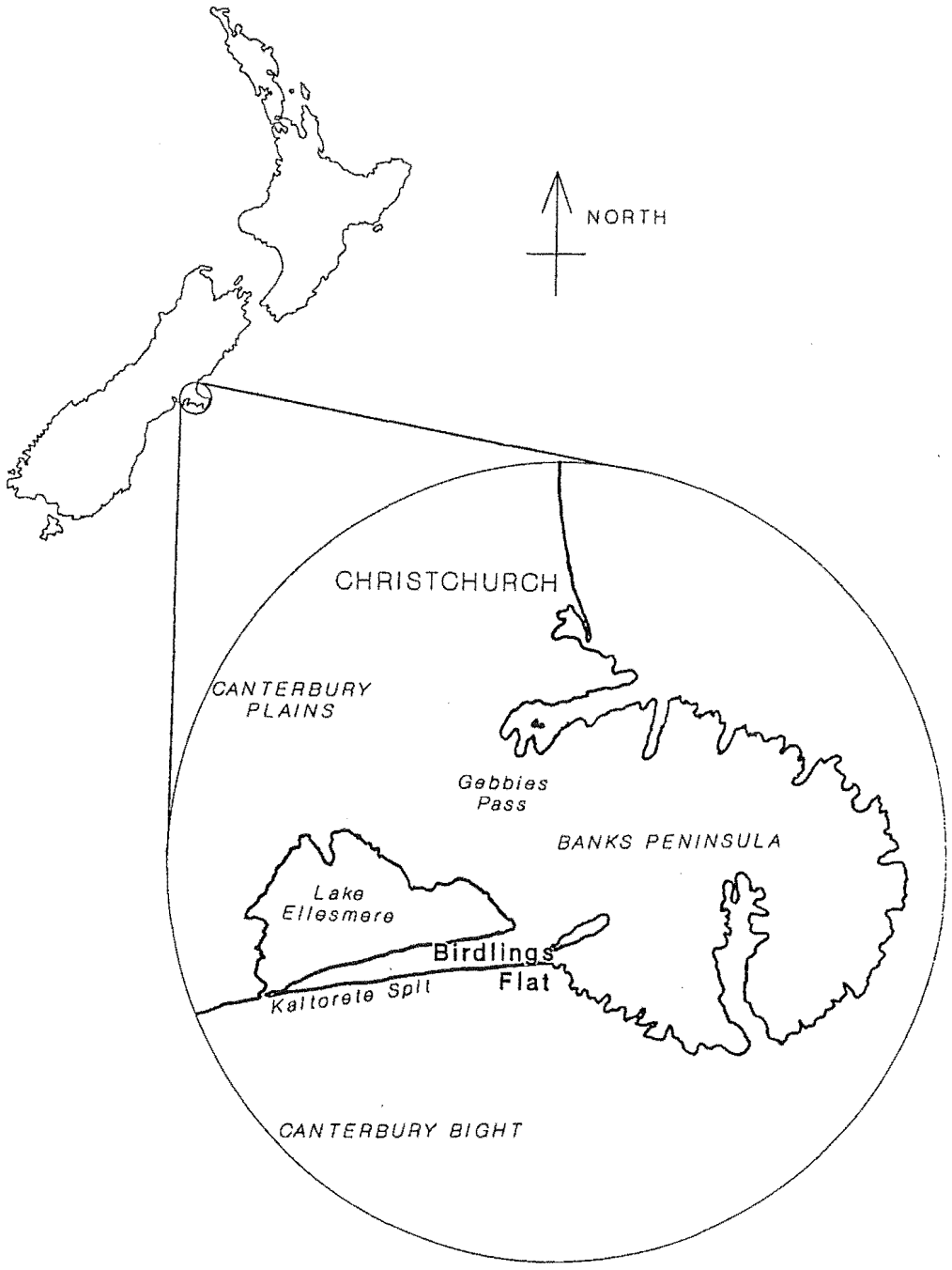

Figure 2.1: **Location map of Birdlings Flat.** Birdlings Flat is on level ground on the eastern edge of the Canterbury Plains which stretch from the hills of Banks Peninsula and the surrounding sea, to the Southern Alps, about 80 km to the west. The inset includes an area approximately 75 km across.

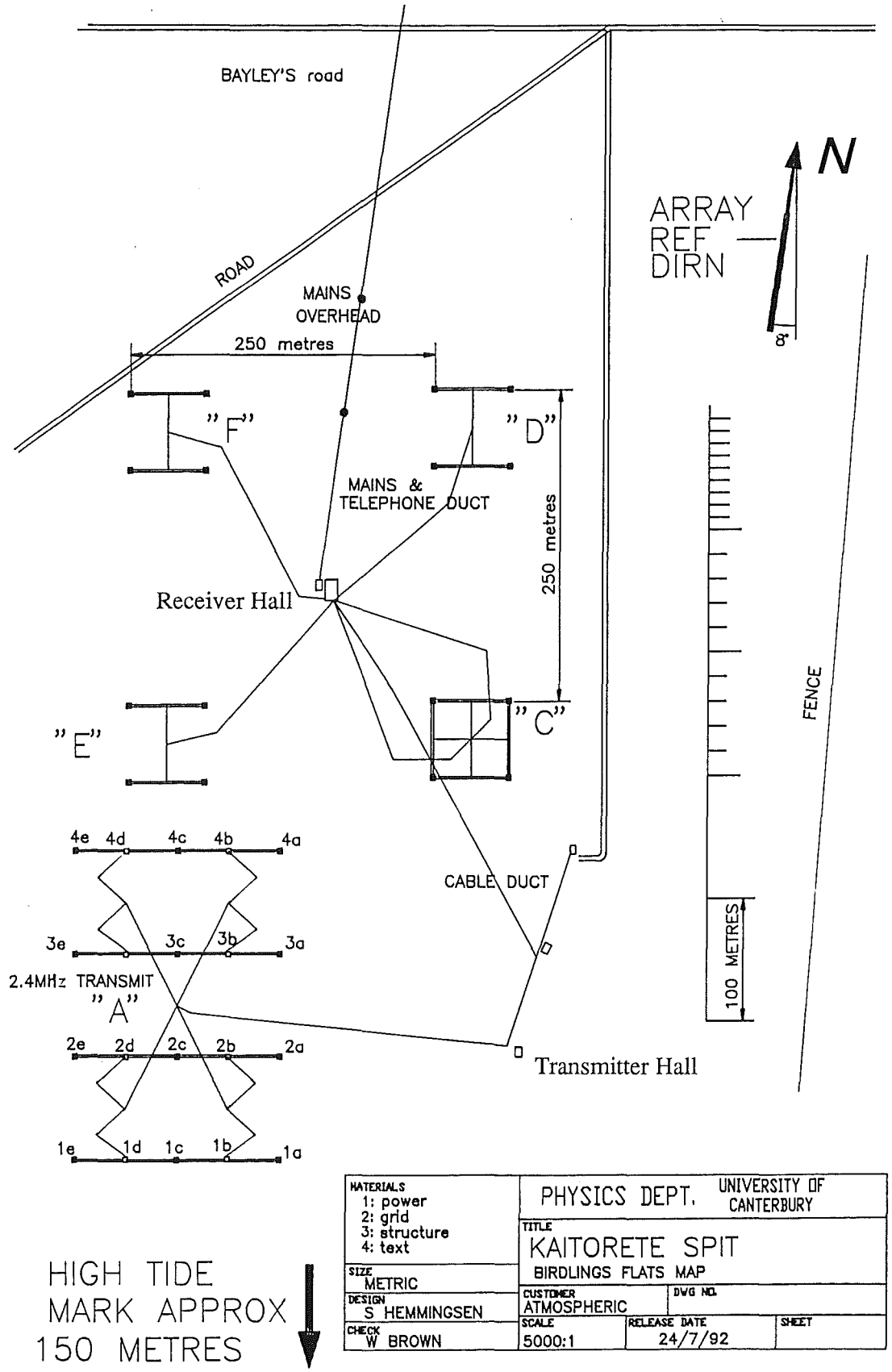

Figure 2.2: **Plan of the Birdlings Flat site,** showing the relative positions and separation of the transmitting and receiving antennae. The receiving antennae used in the interferometry experiment are the arrays labelled (for historial reasons) **F**, **C** and **D**. Note that the direction of true north.

much of the computer software was developed especially for the interferometry experiment. Extra A/D (Analogue to Digital) converter channels were also installed for this project.

There are three buildings on the site, the transmitter hall, and the receiver hall and an equipment shed. The transmitter and receivers are, naturally, housed in the transmitter and receiver halls respectively. The control and data logging computer, as well as the phase locking equipment and oscillators are also housed in the receiver hall.

The site is fairly isolated which made security a problem and unfortunately the station was the target of some criminal activity during the course of this project. The receiver hall was broken into, and important items were removed on several occasions and some equipment was vandalized. These problems lead to delays and the adoption of inconvenient procedures, such as the carrying of some equipment essential to this project back and forth between the university and the site whenever the interferometry experiment was run.

2.1.1 Transmitting Equipment

The transmitter modulates and amplifies a carrier wave from an external source, producing a short, high powered burst of signal which is fed into the transmitting antenna where it is radiated into the atmosphere. The 2.4 MHz transmitter feeds into the transmitter array to the west of the transmitter hall (figure 2.2). The transmitter is connected to the receiver hall via underground cables which supply electricity as well as the transmitter trigger signal and the carrier wave from oscillators in the receiver hall.

The final amplifier of the transmitter consists a push-pull tetrode amplifier operating with peak voltages of up to 10 kV and a nominal peak power of 100 kW. The class C operation of the final amplifier means that the output power of this stage is fairly independent of variations in its input. The pulse compression study of [Krenek, 1977] found that overall response of the transmitter was very flat. The frequency of the carrier in Krenek's chirp pulse varied over the range 2.35 - 2.45 MHz and the output power produced by the transmitter varied by less than 0.5 dB over this range.

The pulse shape is to some extent adjustable and is set to provide a fairly even powered pulse with rounded leading and trailing edges to reduce unwanted harmonics. The length of the pulse is also adjustable and was set to approximately 30 microseconds (half power full width, corresponding to $4\frac{1}{2}$ kilometres in range). This pulse length is that used for the drifts experiment and was chosen as a compromise between the higher resolution of shorter pulse lengths and the increased signal-to-noise ratio obtained with longer pulses.

Although the peak power is very high, the pulse length is short and the duty cycle is very low, so the average power is low. The pulse rate for the drifts experiment is 4 Hz.

The maximum pulse rate the transmitter can handle is 50 Hz and for the interferometry experiment, the average pulse rate was 21 Hz.

2.1.2 Antennae

The transmitting antenna is a narrow beam, broadband array designed by [Krenek, 1977]. To obtain a broadband response with a narrow antenna beam and yet fit in with existing masts, a fairly complicated array and feeder system was developed. The feeders are mainly of four line open wire type (arranged as corners of a square in the cross-section), linked to quarter wave transformer lines then to the dipoles. There are eight dipoles, all being three wire folded dipoles 59 metres long. The dipoles are driven in four sets of parallel pairs, although for analysis purposes can be considered to be four rows, of two collinear dipoles (figure 2.2). The separation between adjacent dipoles, both between the rows and between the collinear dipoles, is 84 metres. The dipoles are all fed in phase with each other (to make a broadside array), and with the water table about five metres below the surface of the ground acting as a reflector the direction of greatest radiation is vertical. The radio waves transmitted from the the array are linearly polarized approximately east-west. As can be seen in figure 2.2, the dipoles are actually aligned 8° off an east - west line so that looking along the dipoles to the east, a bearing of 82° (clockwise from north) is seen.

Three antennae were used for reception in this project, being the same antennae as used by the drifts experiment. These are the antennae labeled **F**, **C** and **D** forming a right angled triangle in figure 2.2. Each consists of two parallel half wavelength (nominally $\frac{1}{2} \times 125$ m) folded dipoles mounted 20 metres above the ground, half a wavelength apart. The dipoles are aligned with the dipoles of the transmitter array. These antennae are also broadside arrays, (the dipoles are fed in phase) so with the ground plane of the order of a quarter wavelength below (depending on the level of the water table) their primary direction of reception is vertical. The feeders from the receiving antennae are mainly open wire transmission lines (of nominal impedance 600 ohm) aside from 20 metres of twin core (nominally 300 ohm impedance) line from the dipoles down to the lines and lengths of coaxial cable inside the receiver hall. Baluns connect the dipoles to the feeders and matching transformers link the open wire lines to the coaxial cables. Coaxial cables are not used outside the buildings because of past difficulties experienced with weathering and with tracing and repairing faults, [Mr. G. Lees pers.comm.].

A computer program was written by the author to calculate the far field radiation patterns of the transmitting and receiving arrays, as well as the combined pattern of the transmitter and a receiving array acting together. The calculated radiation patterns

for the arrays as a function of zenith angle, both parallel to and across the dipoles, are shown in figure 2.3. A perfectly conducting ground plane five metres below the surface of the ground was assumed and allowances were made for the finite length of the dipoles (following [Kraus, 1988]). The combined transmitter-receiver array has a polar diagram of half power full beam width of 18° along the dipoles and 32° across the dipoles, with a gain towards zenith of about 10 dB. The transmitter array radiation pattern across the dipoles is very similar to a plot given by [Krenek, 1977].

Being an exposed coastal site, sea spray and occasional strong winds lead to occasional breakages or weakened connections in the transmission lines and antennae, particularly in the transmitter array which is closest to the sea. For example there was often a break or loose patch in one of the dipoles closest to the sea which would have altered the beam pattern (and impedance) of the array. Another common problem was tangling of the four wire transmission line to the transmitter array which reduced the power of the transmitted signal.

The radiation pattern program was used to investigate various aspects of the antenna system. For example, there was uncertainty about the conductivity of the water table and its ability to act as a reflector. If the ground plane is ignored then the overall beam widths increase by only about $\frac{1}{2}^\circ$ and 2° along and across the dipoles respectively. If a dipole was removed from the transmitter array, mimicking a break in a dipole, the overall beam widths were found to increase by about 1° and the gain of the transmitting array falls by about 1 dB, (although in reality the effect may be greater because the impedance of the array would also change). The radiation pattern when the outputs of the receiving antennae are coherently added together producing a combined array was found and is presented in section 5.6 on postbeam steering.

The "look-in" impedance of the transmitter and one of the receiving antennae and feeders as seen by the transmitter and receivers as measured on various occasions is shown in figure 2.4. (The transmitter impedance includes the final tuning plates and so is the impedance seen by the final amplifier.) As can be seen, there is some variation between measurements made at different times on the transmitting array. Some of the larger fluctuations are probably related to the weathering problems mentioned above. Other environmental factors also contributed to the variation in impedance. [Kwa, 1977] made a study of the impedance of the receiving antennae to examine variations due to tides. The site is on loose, very stony ground lying between Lake Ellesmere with its surrounding wetlands 1-2 km to the north and the sea 200 metres to the south. It was expected that there would be a strong tidal variation to the impedance as the water table (effectively

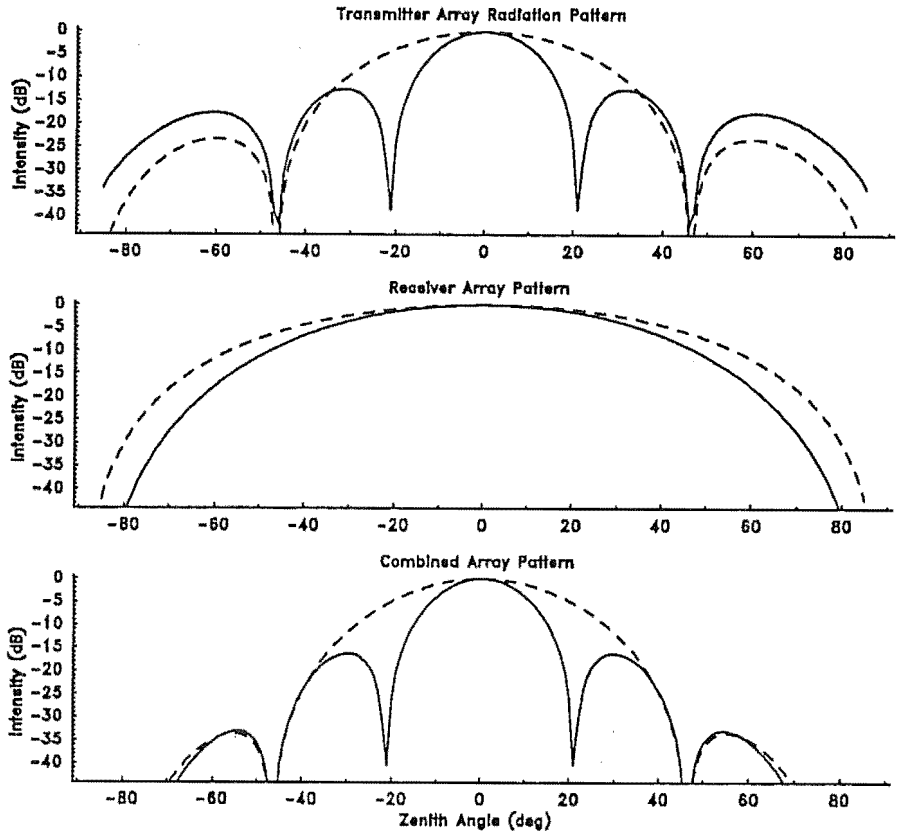

Figure 2.3: **Radiation patterns of the Birdlings Flat antennae.** The panels show the intensity of the far field radiation patterns for the transmitter array, a receiver array, and the transmitter and a receiver array acting together as a function of zenith angle. The solid line indicates the intensity perpendicular to the direction of the dipoles (approximately north-south) and the dashed line along the direction of the dipoles (approximately east-west).

the reflector behind the dipoles) moved up and down with the ocean tides. In fact at the tidal frequency, no significant reactive variation and a resistive variation of less than about 6 ohms (5%) were observed. However at other periodicities there were found to be considerable fluctuations in impedance that Kwa traced to other environmental factors. Rain was observed to increase the impedance in both the resistance and reactance by up to about 10 ohms during and just after rainfall, and wind produced variations in resistance and reactance over short time scales by up to 30 ohms. These factors produced most of their effect in the feeders, which are of different lengths for each array and so the impedance change for each array can be expected to be different. Kwa also observed variations of up to 20 ohms over several days which he considered to be a result of drifts in the equipment

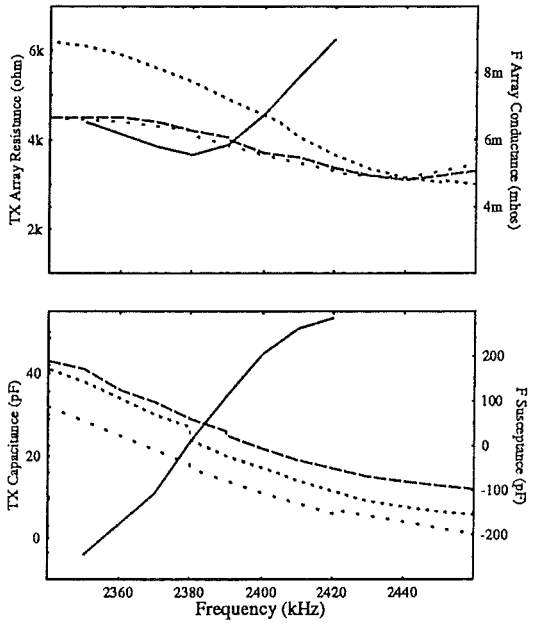

Figure 2.4: **The impedance of the Birdlings Flat antennae and feeders.** The impedance of the transmitter antennae, feeder and tuning plates on three occasions is indicated by the dashed lines. The solid line indicates the parallel impedance for receiving array F and its feeder.

he used, although they could be due to other environmental factors such as changes in the moisture content of the soil below the arrays.

The variations in impedance will affect the signal level of the observations made in this project, and also will affect the phase of received signals as compared to a stable reference, mainly by producing variations in the phase velocity of the signals as they travel along the transmission lines. The effects of longer term variations, such as the weak tidal affect or changes due to faults (provided they don't occur during the course of the experiments), are reduced because of the calibration techniques discussed in section 2.3 which effectively removes mean levels or fixed offsets from the data. This study derives most of its results from estimates of fluctuations in the variance and co-variance quantities at periodicities ranging from the sampling rate out to several seconds. Some of the strongest variations in impedance occur over these same time scales. As mentioned in section 2.3, it was found that the mean levels did not vary significantly during the course of each experiment, although it is possible some samples in each experiment may be affected by the short period variations.

2.1.3 Oscillators

The standard operating frequency of the radar is 2.4 MHz. A "master oscillator" of 9.6 MHz (4×2.4 MHz) is used by the drifts experiment to generate the carrier wave and was used by previous experiments that required phase locking of the radar. The frequency shift portion of this project called for an ability to alter the operating frequency of the radar. During the intial stages of this project, there was some uncertainty about the form of the frequency shift experiments in terms of the size and number of steps in frequency. A programmable oscillator was required that could automatically rapidly change frequency precisely and accurately.

An oscillator was developed to produce a wide range of frequencies under computer control. The oscillator was based on a Phase Locked Loop (PLL) and it was designed to operate over the range 9.2 - 10 MHz in 2 kHz steps (corresponding to 500 Hz steps over 2.3 - 2.5 MHz at the carrier frequency). The PLL generates a waveform and constantly compares it to a reference signal (here the master 9.6 MHz reference), making adjustments accordingly. With this arrangement there is a trade-off between stability and stepping speed. The unit was required to be stable to approximately 0.01 Hz over the time it takes for transmitted pulses to travel to and back from the mesosphere (about 700 μs for scattering from 100 km altitude). Upon the return of the signals, their frequency is compared with the carrier frequency to measure Doppler shifts to a resolution of approximately 0.015 Hz. To get this level of stability, the stepping speed was adjusted to approximately 1 kHz per millisecond, which corresponds to 5 kHz in the carrier frequency over the 20 ms typically available to make a frequency change.

The PLL oscillator was useful for the preliminary experiments, but as the project developed it was found that the PLL unit was not sufficiently stable, nor sufficiently fast at changing frequency. A simpler "multiple-oscillator" was constructed, which consisted of up to eight crystal based oscillators whose outputs could be selected at random. The crystal oscillators were each mounted on small plug in boards that could be readily replaced should alternate frequencies be required. External signals could be fed in to replace any crystal and in this manner the 9.6 MHz master signal and output from the PLL oscillator (which while not being stepped is very stable) were available.

The main frequencies used for most of the experiments reported in this project ranged from about 2.375 MHz to 2.42 MHz which was found to be sufficient for the interferometry measurements carried out. This range is somewhat narrower than the range of the PLL unit so it may have been possible to obtain fast enough switching with the PLL had the more limited range been originally specified. The multiple oscillator, however, provided

more than sufficient selectivity for this project. The actual frequencies generally used are indicated in table 2.1 which shows the typical average variation of received power with frequency and antennae.

2.1.4 Receivers

The receivers used in this project were phase sensitive receivers. They provide a measure of the amplitude of the signal they receive and of the phase of the signal with respect to a reference signal which is usually phase locked to the transmitter carrier signal. The receivers were originally designed by [Krenek, 1977], with modifications by [McGregor, 1985] and for this project. The main components and operation of the receivers are outlined in figure 2.5.

The receiver inputs are matched to the antenna feeders and have diodes placed across them to protect the receivers from static that can build up to high levels on the antennae. The four main stages of the analogue part of the receivers are :

RF amplifier in a tuned circuit providing approximately 45 dB gain with a bandwidth of 200 kHz (half power full width) centred on 2.4 MHz.

The output of this stage is split in two and the following stages are duplicated in parallel, one side being termed the *in-phase* (or cosine) channel, the other the *quadrature* (or sine) channel. The two channels both consist of

Multiplier, multiplying the RF amplifier output and the reference signal at the transmitter frequency. The reference wave being fed into the quadrature channel lags the in-phase channel reference by 90° in phase. The product of the multiplier has components at two frequencies, at the sum of the reference and RF amplifier output frequencies and at the difference between the two frequencies, (figure 2.5).

Low Pass Filter which filters out the RF amplifier output and reference frequency sum components, leaving just the frequency difference component. These filters have roll-off (-3 dB at 50 kHz), giving an output with a bandwidth of 100 kHz (half power full width) centred on 0 Hz.

Video Amplifier amplifies the demodulated signal and shifts the range of the output to match the range of the A/D converters (this did have to be adjusted for the requirements of the interferometry experiment).

The reference signal originated externally from the oscillator which nominally operates at 9.6 MHz (four times the transmitter frequency). In the receiver it passes into a

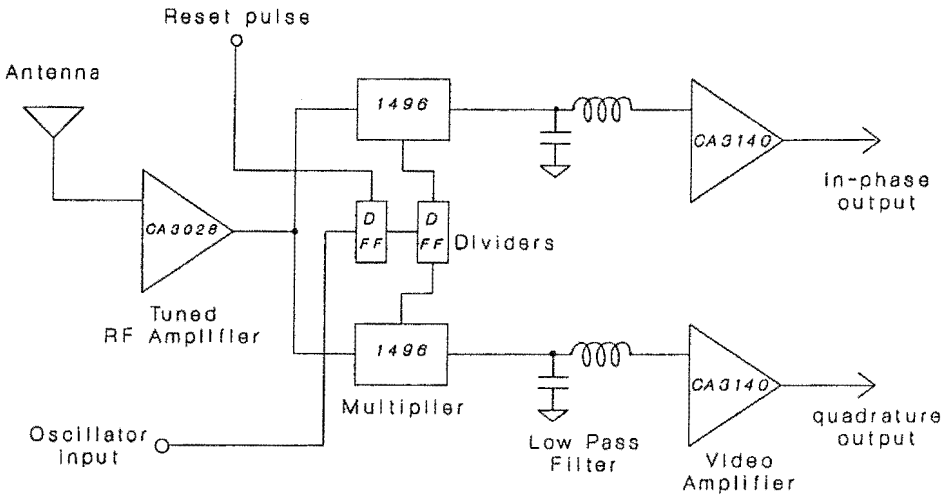

Phase receiver coherent detection

Let the received signal be modelled as a single component, $A_r \cos \omega_r t$, of amplitude A_r and frequency ω_r which can be considered to be the transmitter frequency shifted by, say, Doppler shifting imposed during scattering. (Here we are ignoring constant phase factors and components such as those introduced by the transmitter pulse shape and the transmitter and receiver bandwidths.)

The receiver multipliers find the product of this signal and a reference signal (usually the carrier signal) of frequency ω_c. The reference signals (the outputs of the D-flip flop dividers above) on the in-phase and quadrature channels can be represented by $\cos \omega_c t$ and $\sin \omega_c t$. Using standard trigonometric substitutions, the in-phase channel multiplier output is then

$$A_r G \cos \omega_r t \cos \omega_c t = \frac{A_r G}{2} \left[\cos(\omega_r t + \omega_c t) + \cos(\omega_r t - \omega_c t)\right]$$

and the quadrature channel multiplier output is

$$A_r G \cos \omega_r t \sin \omega_c t = \frac{A_r G}{2} \left[\sin(\omega_r t + \omega_c t) - \sin(\omega_r t - \omega_c t)\right],$$

(where G is represents the RF amplifier gain). The multiplier outputs therefore have components at the sum and difference of the reference and input signal frequencies. The sum components are filtered out by the low pass filters leaving the difference frequency components, (that is the frequency of the Doppler shifting imposed during scattering).

Figure 2.5: **The phase sensitive receivers**, simplified circuit diagram and outline of the operation of the multipliers and low pass filters.

Digital Section where the oscillator signal feeds two D type flip-flops which divide the signal by four to produce two reference waves at the transmitter frequency but at 90° out of phase with respect to each other. This section is housed in a separate sealed copper compartment designed to shield the analogue part of the receivers from signals at the transmitter frequency that could interfere with the backscattered signals the receiver is trying to detect. Modifications were made for the interferometry experiment to allow a reset pulse to be fed from the synchronizer box (discussed below and in figure 2.7) to clear the flip-flops. This pulse could be simultaneously fed into all of the receivers and thus start (or "lock") the divide by four cycles in each of them together. This ensured that the reference signals at the transmitter frequency were in phase with each other in all of the receivers. Without synchronization, occasional random phase changes between the different receiver outputs occurred when the oscillator frequency changed.

The video amplifier stage offsets the outputs to match the range of the A/D converters (0–10 volts) so that a zero level input produces outputs of ideally close to 5 volts allowing "positive" and "negative" levels in the two channels. The actual output level corresponding to no input, known as the DC offset of the receivers, was determined by monitoring the outputs at times when no pulse was transmitted or at times when no significant echoes were expected to be picked up by the receivers. The DC levels of the receivers was found to vary somewhat, typically up to 10-20 mV over several seconds and so was constantly monitored and later removed during data processing. The main source of the DC variation was thought to be an intermittent earth loop problem and it was significantly reduced when a set of isolating buffers was installed between the receiver outputs and A/D converters during the course of this project.

The modulus of the in-phase and quadrature channel outputs (the square root of the sum of the squares of the two outputs) is proportional to the amplitude of the received signal by the gain of the receivers. The phase or frequency difference between the received signal and the reference signal can be found by taking the arctangent of the quadrature (or sine) output divided by the in-phase (or cosine) output, and taking note of the sign of the outputs to obtain the quadrant of the phase.

The frequency response of each of the receiver channels at each of the five main carrier frequencies used is shown in figure 2.6. As can be seen, the response of each channel is very similar for each frequency, although the response does vary somewhat between receivers and is not as even about 2.4 MHz as would be ideal. In general the overall bandwidth is about 100 kHz centred on the reference frequency, provided the reference frequency being

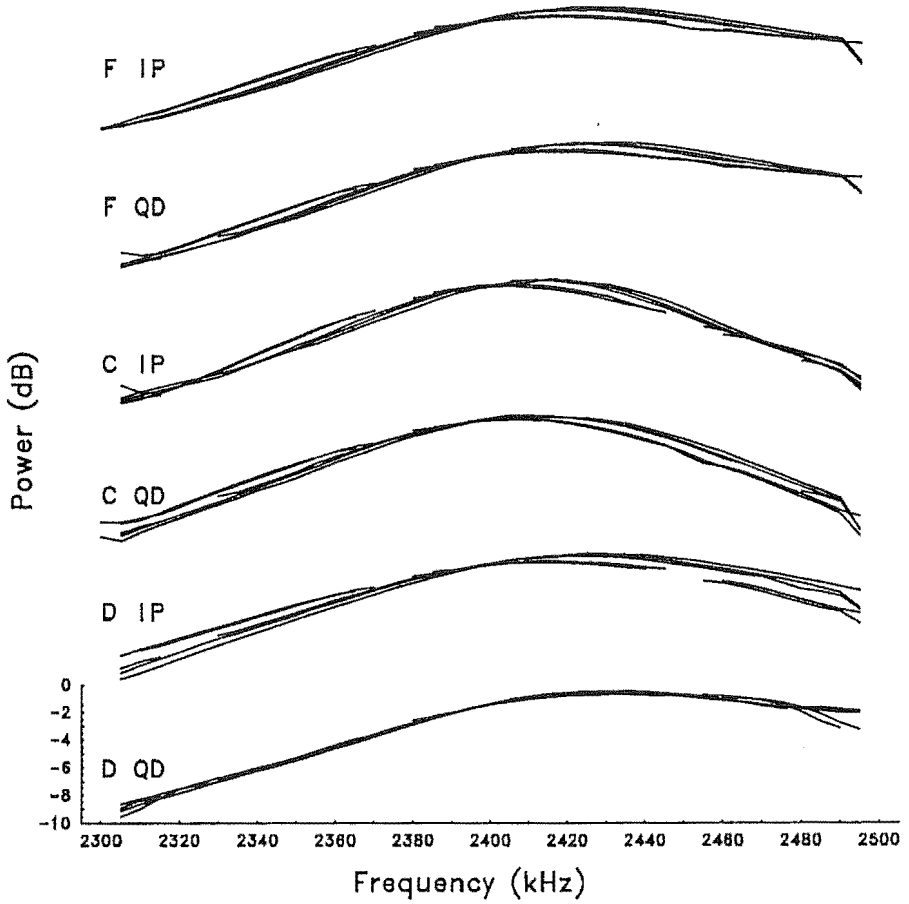

Figure 2.6: **Frequency response of the Birdlings Flat receiver** channels used in the interferometry experiment. **F IP** and **F QD** indicates the in-phase and quadrature channels of the receiver on antenna F, etc. A 1 mV peak-to-peak signal was fed into the receivers at the frequencies along the bottom axis. The response of each channel at each of the five reference frequencies indicated in table 2.1 is shown.

used is not further than approximately 45 kHz from 2.4 MHz (not shown here), beyond which the RF amplifier tuning attenuates the signal. The maximum range resolution achievable using this bandwidth is 1.5 km although the length of the transmitter pulse used (30 μs) reduced this resolution to 4.5 km. Ideally the bandwidth of the receivers should have been reduced to match the transmitter pulse and minimize external noise picked up by the receivers, although there were plans at various times to decrease the pulse width for higher resolution experiments.

The internal noise of the receiver is approximately 0.1 μV (RMS), which is much less than the external noise picked up on the antennae, generally a minimum of about 1-2 μV. With the typical noise output of 5 mV (RMS) and the maximum swing from DC of the

Frequency (MHz)				
2.4 (0 kHz)	2.375 (-25 kHz)	2.407 (7 kHz)	2.380 (-20 kHz)	2.418 (18 kHz)
0 dB	-0.14 dB	0.11 dB	-0.15 dB	0.02 dB

Receiver/Antenna		
F	C	D
0 dB	-0.50 dB	-1.71 dB

Table 2.1: **Typical power variation of received signals between frequencies and antennae** with respect to 2.4 MHz and antenna F. The order of the frequencies is that used during the interferometry experiments and the frequencies in brackets indicate the offsets from 2.4 MHz. Determined using the calibration methods of section 2.3.1.

output of 5 volts, the dynamic range of the receivers is about 55 dB. The overall gain of the receivers is approximately 70 dB, although this figure varied from receiver to receiver by up to about 1.5 dB. The gain of the in-phase and quadrature channels differed from each other by up to approximately 0.3 dB, which if unaccounted for would lead to an error in phase of about 1°. In addition a similar error in phase was observed in bench tests when a signal differing from the reference by 25 kHz was fed into the receivers. 25 kHz, corresponds to 40 μs and is approximately the bandwidth required to encompass the transmitter pulse.

Both the varying gain between receivers and the differing gain between the in-phase and quadrature channels were corrected for by procedures outlined in the calibration section, section 2.3. Typical results of the gain calibration are shown in table 2.1.

The receivers were separated from the A/D converters and the computer by about four metres to cut down on noise originating in the computer. The receiver outputs were fed by coaxial cable to the A/Ds. Isolating buffers were installed at the A/D end part way through this project to reduce an intermittent earth loop problem that often produced a mains hum of up to half a volt and noise of tens of millivolts at other frequencies. These buffers are (approximately) unity gain amplifiers with differential inputs which isolated the computer and receiver earths greatly reducing the problem. (The reduction in noise when this isolator unit was installed is apparent in the results of chapter 7).

2.1.5 Phase Locking

The drifts experiment uses incoherent receivers and requires no phase reference between the receiving and transmitting components of the radar. However there is provision for phase locking which was used in the studies by [Krenek, 1977, McGregor, 1985, Brown, 1986]. These studies locked the transmitter and receivers using a signal from a master oscillator which operates at four times the carrier frequency of the transmitter. This master signal was used rather than directly feeding the carrier around the radar site directly to avoid interference problems in the sensitive receivers used by the radar (such interference would swamp the weak signals the receivers detect). The receivers and the transmitter use separate circuits to divide the master signal down to the carrier frequency. There was no facility to ensure that these circuits divided in time with each other, although if the master signal is constant (and there isn't excessive pick-up from other equipment and the power supply is stable) the circuits do seem to stay reasonably stable with respect to each other.

For the studies of Krenek and McGregor (who made Doppler observations of ocean wave backscatter) this locking was sufficient since they were concerned with comparing the variation in phase of scattered signals observed by one receiver with time. (The compressed pulse of Krenek's experiment was locked to the master oscillator signal and the received echos were compared with this master signal.)

The phase locking requirements of this experiment were somewhat more rigorous because not only were variations in phase of scattered signals with time observed, differences in the phase of signals observed by separate receivers and at unrelated transmitter frequencies were to be measured.

The study by [Brown, 1986] also compared the phase of separate receivers and experienced some difficulty with occasional changes in phase between the separate divider circuits in each receiver. The replacement of the master oscillator with a switchable oscillator in the frequency shifting experiments of this thesis produced many more phase jumps between receivers as the oscillator frequency changed.

A "synchronizer" unit was developed for this experiment to synchronize the divider circuits in the receivers and lock these to the carrier and transmitter pulse. The operation of this unit is outlined in figure 2.7. The main inputs to this unit were the multiple-oscillator output and the transmitter trigger pulse from the controlling computer. The unit divided the oscillator signal by four to produce the carrier signal and send it across to the transmitter, replacing the divider and line driver circuits that previously did this. The unit also delayed the transmitter trigger pulse to synchronize it with the carrier signal.

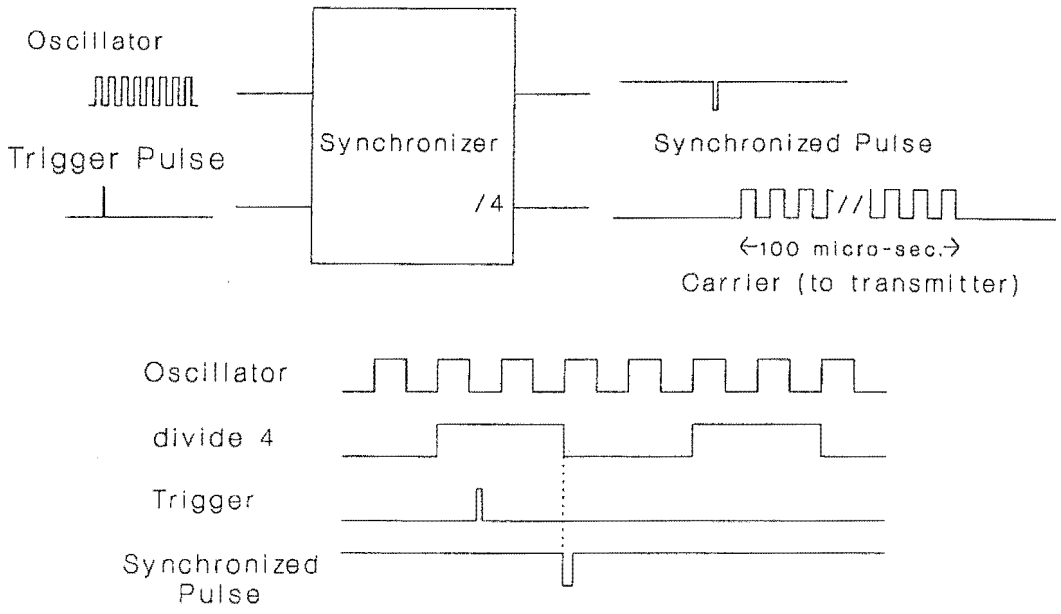

Figure 2.7: **The synchronizer unit** developed to carry out phase locking for this project. The **oscillator** and **trigger pulse** are the input signals and the **synchronized pulse** and the **carrier** are the outputs. The timing of the signals is indicated in the lower part of the figure.

Once this occurred, the unit sent the reset pulse to all of the receiver dividers to lock together the reference signals in each receiver. To reduce interference from the carrier signal the unit suppressed transmission of the carrier signal across to the transmitter for the millisecond or so period in which the scattered signals arrive back at the radar. The unit also replaced the functions of a previous simpler synchronizer unit that synchronized the transmitter trigger pulse with the timing circuits of the A/D converters and provided trigger signals for test gear such as oscilloscopes.

The timing of the various reset pulses is critical. For example the divider circuits had to receive their reset pulses at times not coincident with the arrival of edges in the oscillator signal, otherwise ambiguities may have arisen as different receivers might treat the signals differently leading to phase jumps between the receivers. Also the A/D converters require an initiation pulse from the unit, and the computer pauses until the A/Ds have finished their sampling. Occasional glitches caused timing mis-matches and the whole system hung until time-outs occurred or a manual reset was done. The unit did, however, result

in true phase locking and greatly improved the phase stability of signals observed for the interferometry experiment.

2.1.6 Birdlings Flat Computer

The data logging and experiment control was done using a DEC[1] LSI-11 mini-computer (closely related to the PDP-11 series machines). This computer has an 16-bit LSI-11/23 microprocessor and a 22-bit Q-bus which provides slots for installation of peripherals such as interfaces to control external equipment, and devices such as a magnetic tape drive and a hard disk. The system has 512 kB memory of which about 28 kB is directly addressable by user programs, 2 kB is used by the operating system, with the remainder available as a virtual disk.

The computer is attached to a magnetic tape drive which uses ANSI standard 9-track, $\frac{1}{2}$ inch, 1600 bpi tape. The computer also has a dual floppy disk drive, of DEC RX50 type which uses 400 kB $5\frac{1}{4}$ inch floppy disks (not IBM format however). A 40 MB hard disk is available, although because an earlier disk was stolen from the hall, it was decided this disk could not be left unattended and was transported to the site whenever it was required. (The drifts experiment operates unattended using the floppy drives and the magnetic tape drive.) A terminal to control the computer was also carried back and forth as required after an earlier terminal was stolen.

The equipment interface device (the "station control register") on the Q-bus sends instructions to a rack of equipment that houses the receivers and oscillators and transmitter triggering equipment. The data lines that control this rack are isolated using optical coupling to reduce electrical noise to the receivers. The rack currently holds a series of 21 equipment slots. Each slot on the rack can be individually selected and six bits of data can be sent to control the equipment in that slot. The main items controlled in this way for this project were the multi-oscillator and PLL units.

The operating system used on the PDP-11 is RT-11SJ. The radar control and data logging programs were written in ROGALGOL, [Abbott, 1980], a ALGOL-60 based language that provides for calls to user written MACRO-11 assembly language subroutines and uses a minimum of memory. Although assembly language routines are considerably more complicated to program than high level languages such as ROGALGOL, they allow faster operation and direct interfacing to peripherals, for example the station control register or the A/Ds. Much of the time critical part of the software was written in assembly language to achieve operating maximum speed. Most of the ROGALGOL programs and the data

[1] Digital Equipment Corporation

collection assembly language routines used in this project were written by the author. (The extensive magnetic tape handling routines were written by Mr. John Welch).

An independent clock system attached to the PDP-11 supplies the date and time. A one millisecond counter (derived from the 9.6 MHz master oscillator) is used for timing on scales less than a second, such as pulse repetition. The counter was originally also used for synchronization, locking together the transmitter trigger and the A/D converters but for this project the synchronization aspects were taken over by the controllable oscillator via the synchronizer box.

Analogue to Digital Data Converters

There are two Analogue to Digital (A/D) converter systems attached to the PDP-11.

The first contains a single A/D converter (a 12-bit DATEL EH12B1 A/D) connected directly to the computer's memory via "Direct Memory Access" (DMA) mode. When the transmitter is triggered, this A/D converter samples its analogue input once every $6\frac{2}{3}$ μs. $6\frac{2}{3}$ μs is the time required for a radio wave to travel to, and return from, a scattering target that is one kilometre away in range. (This timing is also derived from the 9.6 MHz master oscillator.) By sampling every $6\frac{2}{3}$ μs a series of samples, or a "scan", at successive one kilometre intervals in range or altitude (one kilometre "range gates" or "range bins") is built up. A predetermined number of range bin samples are taken and the digital output of each sample is written directly into the computer's memory.

Only one device at a time can directly access the computer's memory like this and there is insufficient time between range bin samples to switch between devices. To simultaneously sample other signals a more independent system, the Multiple A/D (MAD) system, is used. The MAD system consists of eight parallel A/D channels and data can be collected all channels simultaneously. Each channel has an A/D converter (a 12-bit DATEL EH12B3) and its own 2 kB of memory. When the transmitter is triggered, each A/D channel samples its analogue input at one kilometre ranges (that is $6\frac{2}{3}$ μs) and stores the digital output in its own buffer memory. After the predetermined number of range bins have been sampled, the computer can transfer the collected data from each channel to the computer's memory and then to the hard disk or magnetic tape. After that the system is free to collect another scan.

The input sensitivity range of all of the A/Ds is 0–10 volts, and with the 12 bit conversion, the smallest detectable voltage variation (or "quantization step") was 2.4 mV or 0.024% (-72 dB) of the full range. The A/Ds were stable to approximately this quantization level, although the typical noise level of the receiver outputs from external sources

was generally at least two or three times the quantization level.

The drifts experiment uses three of the A/D of the MAD unit for its amplitude receivers. The remaining five channels were commissioned for the interferometry experiment making available a total of nine A/D channels with the DMA device. This made possible simultaneous collection of samples from the drifts and phase receivers and a limited number of data runs were collected like this, although most of the data collected consisted of the six outputs of the phase receivers using six channels of the MAD system.

2.1.7 Data Collection

The number of range bins, frequency steps, receiver channels, the sampling rate and the quantity of data collected was a compromise between the amount of data storage area available and the rates at which data could be transferred between the various stages. The main limitations are :

- The rate at which data can be transferred from the MAD buffer memory to the computer memory (about 30 μs per range bin sample).
- The size of computer memory available for direct transfer of data, (about 20 kB or 10 000 samples), which meant the data had to be then stored on some other media.
- The rate at which the data can be written to hard disk (about 80 μs per sample).
- The amount of hard disk available for storage, typically 20 MB.

The hard disk was not an option for storage of the data until it could be analysed as the computer was used for other experiments and so could not be tied up for analysis or even later transfer of data to another machine, (the hard disk was available for temporarily holding data however). Therefore the data was written to magnetic tape, the limitations of which were :

- The write speed of the tape drive, approximately 5 kB per second (about half a millisecond per sample).
- The storage capacity of the tapes, which for the drive being used, was typically 20 MB on a standard 2400 foot tape (considerably lower than is possible for these tapes).

The limited write speed would have slowed down the sampling rate if the data had been written directly to tape after collection. Therefore the data was stored temporarily on

hard disk during sampling, then the data collection was paused to write the data to tape, then sampling began again. Once one magnetic tape was full, it could be replaced within a couple of minutes. Data collected in the meantime was stored on hard disk and transferred to magnetic tape at the end of sampling.

When the transmitter is triggered, the A/Ds start sampling immediately, but there is a short delay before the actual transmission of the pulse. This delay time must be determined so that the time between transmission of a pulse and reception of scattered signals from some target, and thus the range of the target, can be found. Before the main data collection sequence began, a single scan was made to determine this transmission delay time. This was done by triggering the transmitter and examining the first 64 range bins of all of the A/D channels for reception of the "ground pulse", the R.F. pulse that travels directly from the transmitter antenna to the receiving antennae. The amplitude of the signal received on each antenna was found (the modulus of the in-phase and quadrature channels), and averaged over all three antennae for each range bin. A parabola was fitted to the signal with respect to the range bin number and the position of the maximum, in units of range bin number, was taken to be the "range" of the ground pulse. This range was recorded to be later subtracted from the apparent range of the samples of backscatter. The ground pulse range was typically 7 km (indicating the transmission delay time was about 50 μs).

The Data

The main data collection procedure consisted of a long sequence of scans. Each scan typically consisted of 15 samples of range bins. Of these, 13 were spread uniformly over the bins corresponding to the altitudes of most interest to this study, generally 80–100 km. The other two bins corresponded to altitudes below those that produced significant scatter to indicate the zero input or DC offset component of the receivers outputs mentioned in section 2.1.4. The range of the bins used for determining the DC offset was usually 60–65 km. It was found that at this range there was no scattering that was detectable by the receivers used in this project. The DC offsets varied by 10-20 mV over 5-10 seconds so running averages were found over both bins over typically five samples for each channel and radar frequency. These running averages were removed from the recorded data. The variation in DC offset decreased after the installation of isolating equipment between the receivers and the A/D converters part way through this project.

Sampling for the frequency shift part of the project was not done on two frequencies simultaneously. There has to be some delay between scans from one frequency to the

next, not only to allow the equipment time to change frequencies, but also to ensure back scattered signals from one frequency are not mixed with signals received on another frequency. The delay should be short to minimize the effects of changes in the scattering targets being probed. The minimum time between scans here is set by the highest pulse rate the transmitter can handle, which is 50 Hz. This is also the time required to shift a reasonable number of samples (about 100 from each channel) from the MAD to memory.

Most of the data was collected using five frequencies so the time between scans on the first and last frequencies was 80 ms which is essentially instantaneous in terms of the expected rate of change of the scattering targets. Five frequencies gives up to ten different frequency steps. The frequencies were chosen to provide a range of step sizes, although some steps were of nearly equal magnitude to check consistency of behaviour. The five main frequencies used are indicated in table 2.1 which shows the typical variation in average power received by the radar.

Only a limited number of scans could be made before the computer memory began to get full and the end of the five frequency pulse sequence was a convenient time to pause to allow the computer to write the collected data to disk. Once this was done, another "burst" of five scans at the same frequencies was made.

The time between successive samples of the same radar frequency should be short enough to ensure unambiguous observation of the most rapid expected changes in the signals. At least two observations must be taken during an oscillation of a signal to be able to distinguish the oscillation from slower variations in the signal (the Nyquist condition). Here the most rapid oscillation can be modelled by the expected Doppler shift observations of an off-vertical target. The greatest velocities observed by the drifts experiment are of the order of 200 ms^{-1} and the greatest zenith angle might be expected to be of the order of 20°, so the line of sight Doppler shift (equation 5.6 in section 5.1) would be 1 Hz in this situation. Under the Nyquist condition a sampling rate of at least 2 Hz is required to unambiguously measure this. In practice, as we shall see in section 7.4 the highest frequency observed was around 0.5 Hz and since the actual sampling rate was about 4 Hz the Nyquist condition was met.

If a higher sampling rate than that required by the Nyquist condition can be achieved, then "coherent integration" be used to reduce random noise in the data. (for example [Tsuda, 1989]). Coherent integration involves averaging the in-phase and quadrature components of successive samples. If a random noise component is present in the samples, it is in the main not correlated from sample to sample - unlike the typical signal component.

On addition, the random components tend to average to zero, whereas the signal components add. Coherent integration is equivalent to passing a low pass filter through the data sets, reducing the uncorrelated or high frequency components of the data.

During the frequency shift operation of the current project, the sampling rate was not considered to be high enough beyond the Nyquist limit to carry out coherent integration. (The data collected at separate radar frequencies could not be coherently averaged together because each frequency carries unique phase information related to the range to the scattering target and this would have been lost during the averaging). However before many of the analyses carried out in this project were performed, a low pass filter in the form of quarter-half-quarter function was passed through the data to reduce some of the high frequency components in the data. This filter acts on the ith point, x_i, of a data series to produce $x_i' = \frac{x_{i-1}}{4} + \frac{x_i}{2} + \frac{x_{i+1}}{4}$ with a 6 dB reduction in power at half the Nyquist frequency.

The time between repeating samples at the same radar frequency was generally 240 ms which corresponds to a sampling rate of $4\frac{1}{6}$ Hz. (This sampling rate means that the quarter-half-quarter filter has a -3 dB cutoff at about 0.73 Hz.) This sampling rate was chosen to be close to that of the drifts experiment but also it was desired to synchronize the sampling with the frequency of the A.C. power supply. The New Zealand mains frequency is 50 Hz, corresponding to a period of 20 ms and here, as with many sensitive experiments, a component of noise at mains frequency was often observed on monitoring equipment. By choosing a sampling period that equals an integer number of mains cycles, contributions by mains to the samples should be similar from sample to sample and should add to the overall mean of the samples (or contribute a zero frequency component) which is generally removed during initial data analysis.

Data collection continued in this manner for 256 bursts, or just over a minute of sampling. At the end of each minute sampling period, the data that has been saved to disk is written to magnetic tape, a process that took just under a minute with the quantity of data that was collected after which time another sampling period could begin. Usually there was a pause for a few seconds, so successive sampling runs would begin on the start of each second minute. Generally this pattern of sampling continued for two to five hours. The intention of collecting data for several hours was to be able to observe short period phenomena such as gravity wave activity which can have periods ranging from ten minutes to several hours. The length of the data runs was mainly limited by considerations of data management. Each one minute sampling run produced a raw data file of about 260 kB so a five hour run totalled nearly 40 MB of data. This quantity was found to be near to

the largest that could be conveniently handled on the computer systems available for data analysis.

The dates, times and range gates sampled of the main data sets collected are listed in table B.3, appendix B, (this table does not include a number of calibration and test runs made at various times).

The data were returned to the University on magnetic tape for analysis. Before analysis could begin, the DC offset of the receivers was removed using a running average of the "quiet" range bins. The range of the ground pulse was removed from the range bin numbers to get the actual range or height of the range bins. Then the data were translated, so that instead of the data files consisting of a series of scans one after each other, each record consists of all of the bin samples at a particular range, collected on one receiver at one radar frequency. Therefore if the time series of samples at a particular range, radar frequency and of a particular receiver channel was required, then that single record could be retrieved rather than retrieving many records and collecting the desired data point from each scan. (The structure of these sorted data files is indicated in appendix B for reference.)

2.2 The Scott Base Radar

Scott Base (77°50′S, 166°45′E) is located on Ross Island (figure 2.8) and is the main New Zealand station in the Antarctic. The New Zealand Antarctic Research Programme is overseen by the the Ross Dependency Research Committee. All logistic and operational support is provided by the Antarctic Division of the New Zealand Department of Scientific and Industrial Research (DSIR). Scott Base was established as part of the New Zealand activities of the International Geophysical Year (1957/58), and MF radar observations of the ionospheric D-region, [Gregory, 1961], were amongst the very early experiments at the base.

The Department of Physics of the University of Canterbury has an MF radar at Scott Base that is similar to, although somewhat more specialized than, the Birdlings Flat radar. The layout of the radar follows that of figure 1.3 (section 1.4.1) which was loosely based on this radar. Two experiments make permanent use of the radar, making more or less continuous observations throughout the year. These experiments are

The Polarimeter Experiment or the Partial Reflection Differential Absorption experiment, described by [Von Biel, 1989, Von Biel. 1992]. This experiment estimates the electron density profile of the ionosphere from approximately 40 km to 120 km altitude. The electron density profile labelled 'Von Biel' in figure 1.1 of section 1.1 was obtained by this experiment. The polarimeter runs for twelve minutes every hour.

The Drifts Experiment or the Partial Reflections Spaced Antennae Winds experiment. This experiment is very similar to the Birdlings Flat drifts experiment and has been described by [Fraser, 1984b, Fraser, 1989]. A one minute sample is taken every five to ten minutes, provided the polarimeter isn't running.

The Physics Department also operates an ionosonde, [Davies, 1966], at Scott Base scanning every fifteen minutes.

This section describes the implementation of the interferometry experiment on the Scott Base radar for an observational campaign in October through to December, 1988. The aim of this part of the project was to demonstrate the generality and portability of the experiment as well as using the experiment to study the nature of scattering structures in the Antarctic lower ionosphere. The resident equipment used for this project was mainly that associated with the drifts experiment.

The original intention was to temporarily install and operate the interferometry experiment for a two to three week period, and then return to New Zealand after restoring the radar to its original configuration. The equipment and procedures to be used were, as

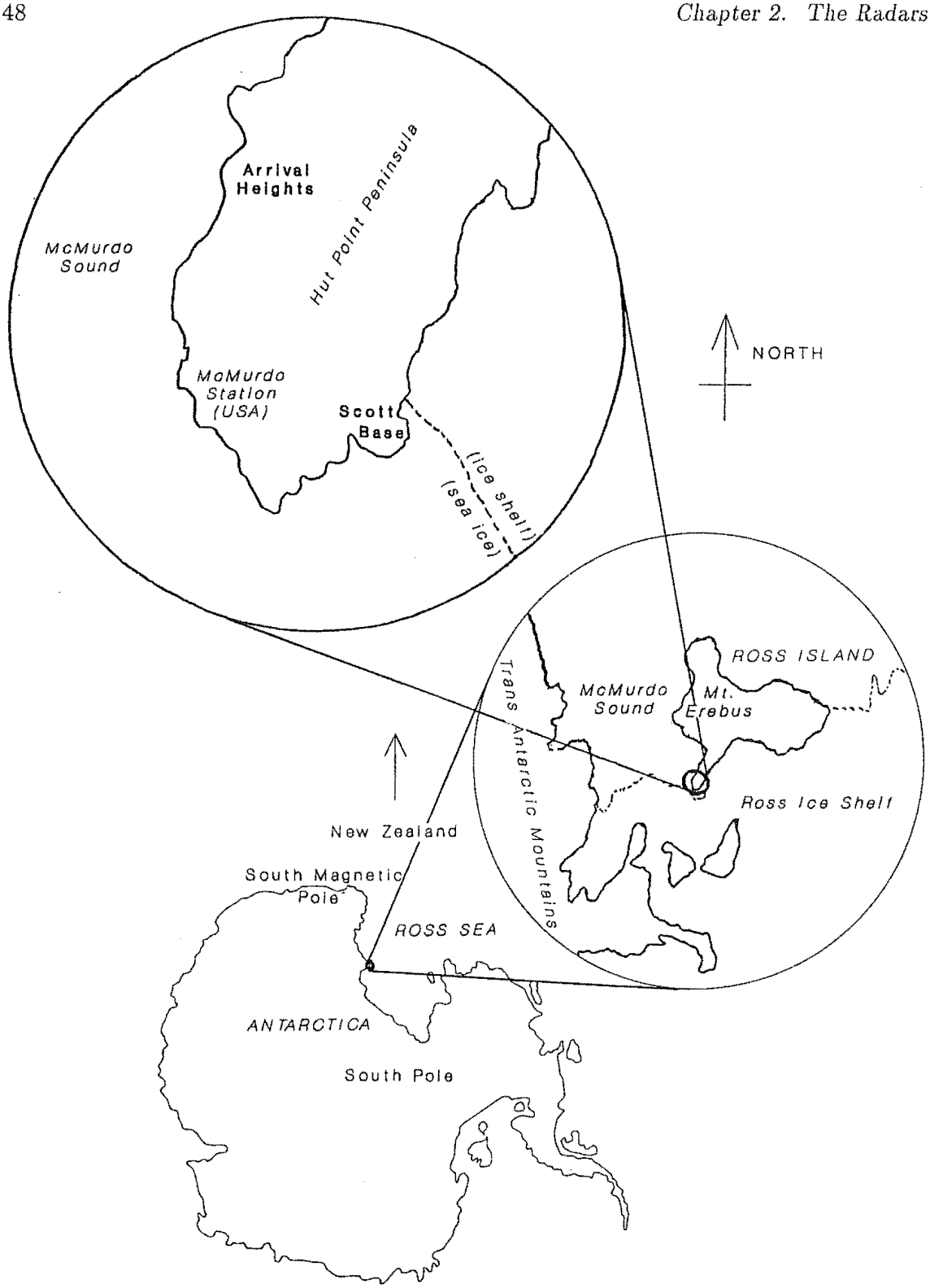

Figure 2.8: **Location map of Scott Base and Arrival Heights.** The two insets indicate the location of Ross Island relative to the Antarctic mainland (this inset includes an area approximately 200 km across, Antarctica itself averages about 4000 km across) and the locations of Scott Base and Arrival Heights (8 km across) on the southern tip of Hut Point Peninsula which projects south westward from Ross Island. The transmitter part of the radar is at Scott Base and the reception part is at Arrival Heights, 8 km by four wheel drive road or 3.3 km to the north as the skua flies.

far as possible, the same as those being used on the Birdlings Flat radar. The modifications made were designed to enable the continued operation of the drifts and polarimeter experiments when the interferometry experiment was not running.

The sequence of events of this undertaking and some of the problems encountered therein are discussed in appendix A.1 which consists of the "Logistic Report" of the programme to the Antarctic Division of DSIR. An associated report, the "Science Report" to the Ross Dependency Research Committee is in appendix A.2, [Brown, 1989].

The experiment was run successfully, although there were some unexpected problems in the setting up stages that lead to a revision of the original schedule.

2.2.1 The Scott Base Transmitter

The radar's transmitter is housed in a small hut (or "wannigan") 50 metres from the Hatherton Geophysical Laboratory at Scott Base. The polarimeter and the drifts experiments use the same transmitter, although the length of the pulse transmitted when under the control of the polarimeter experiment is, at 25 microseconds (half power, full width), shorter than the 35 microsecond pulse of the drifts experiment. The interferometry experiment used the drifts experiment control system, so had a pulse length of 35 microseconds,

The peak power developed by the transmitter is 60 kW, although since the duty cycle is so low the average operating power during the operation of the drifts and polarimeter experiments is approximately 8 W and 2 W respectively. During the interferometry experiment, the transmitter was pulsed 20 times each second (compared with 4 Hz and a burst of 10 pulses, 20 milliseconds apart, every 6 seconds respectively for the drifts and polarimeter experiments) giving an average power of 40 W.

Operation of the radar transmitter can cause interference problems to short wave communications at Scott Base, particularly if the transmitter is being pulsed at a faster than normal rate as occurs while running the interferometry experiment. Short wave radio is the only means of direct communication to remote field sites and back to New Zealand[2]. In an emergency situation, the Scott Base radio operators can disable the radar transmitter and on one occasion this was done for several hours. In consultation with the radio operators, rapid pulsing of the transmitter (either during testing or by the interferometry experiment) was avoided during scheduled short wave link-ups with remote sites.

The carrier frequency of the transmitter is 2.9 MHz, slightly higher than the Birdlings

[2]Since this time a satellite link for communicating with New Zealand has been installed.

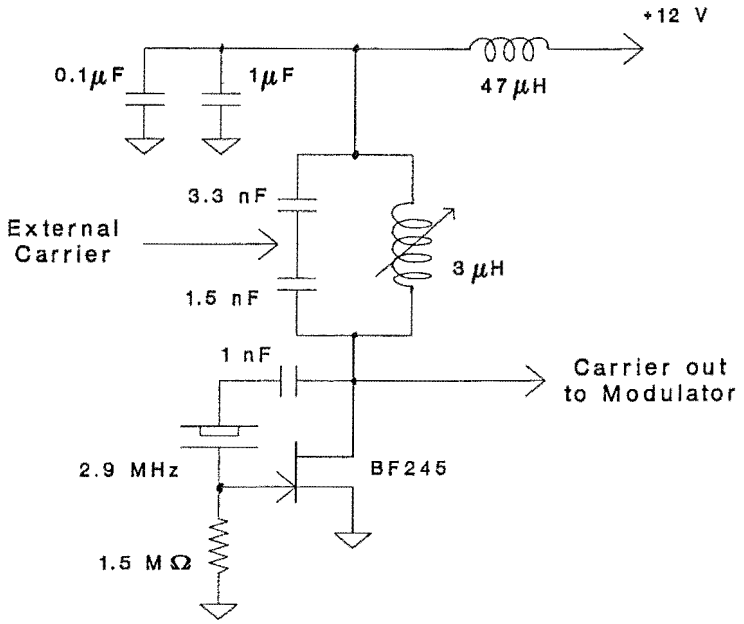

Figure 2.9: **Modifications to the Scott Base transmitter** oscillator circuit. The +12 Volt supply was disconnected and the external carrier signal (originating from Arrival Heights) was fed in at the indicated point. This signal was approximately 5 Volts peak-peak (loaded).

Flat carrier of 2.4 MHz. Unlike the Birdlings Flat radar, the carrier frequency is normally generated within the transmitter, not at the receiving site. An external tap into the oscillator circuits had to be made to feed in an external carrier for the interferometry experiment, (figure 2.9). This feed worked well, however as will be seen in section 2.2.3, problems were experienced in bringing the carrier to the transmitter from the receiving site.

There was some reduction in the power produced by the transmitter when the frequency was altered by the frequency shift part of the interferometry experiment. Also the length and shape of the pulse varied somewhat as the frequency was shifted. The frequency steps chosen were those for which the pulse produced by the transmitter was the most stable. Table 2.2 shows the variation in average power and pulse length with frequency at the main frequency steps used in this experiment.

The triggering of the transmitter is controlled remotely from computers at the receiving site at Arrival Heights. A twin core telephone type line running from Arrival Heights to Scott Base carries the trigger signal. The line runs across exposed rocky ground and two ice fields. Continual winds rub the wire against the coarse volcanic rock and the gradual

Frequency MHz	frequency offset kHz	pulse length μs ($\pm 1\mu$s)	power dB ($\pm$0.1 dB)
2.870	30	32	-1.3
2.880	20	32	-0.6
2.9	0	33	0
2.902	2	33	-0.3
2.912	12	30	-2.2

Table 2.2: **Pulse length and average power of Scott Base transmitter** at different frequency steps. The pulse length is the half power full width time. The average power is quoted relative to the power at 2.9 MHz, the standard operating frequency of the radar.

motion of the ice fields adds extra strain to the wire leading to occasional breakage. During the summer the problem gets worse as patches of snow which shelter the line from the wind melt; also the action of the sun on the wire melts it into the ice fields. Partial breaks and weakening of connections can lead to erratic pulsing of the transmitter. These problems were particularly severe during the setting up stages of this experiment and eventually some of the line had to be replaced.

The transmitter feeds a full-wave triangular loop antenna, mounted horizontally, 20 metres above the ground. More conventional dipoles aren't used because of the wind and ice loading problems they have been found to suffer from. The polarisation is linear and aligned along the side opposite the feeder, running in a north-south direction. Approximating this antenna with a short dipole model gives a half power half beam width of about 40°.

2.2.2 The Arrival Heights Receiving site

The receiving site for the radar is at Arrival Heights, some 3.3 km to the north of Scott Base or 8 km by four wheel drive road. The area is part of a 100 hectare declared *Site of Special Scientific Interest.* The area is described in the 1988 *Antarctic Operations Manual* published by the Antarctic Division of DSIR as

> ... an electromagnetically and natural "quiet site" offering ideal conditions for the installation of sensitive instruments for recording minute signals associated with upper atmosphere programmes.

Access to the site is restricted and the radio noise generated on the site does appear to be fairly minimal. However there is at times considerable radio noise from outside the site,

particularly from the nearby HF communications transmission site attached to the United States Antarctic Program at McMurdo Station.

A sketch plan of the receiving site appears in figure 2.10. The receiving antennae are triangular loops, identical to the transmitting antenna, although they are mounted only three metres above the ground. The ground is permafrosted to the surface and has very low conductivity so that the antennae almost behave as though they are in free space. Insulated wire is used to reduce the considerable static that occurs when snow blows on to the antennae. The drifts experiment uses the three spaced antennae labeled drifts **1,2,3** in figure 2.10 and these were the antennae used by the interferometry experiment. The polarimeter experiment uses the four antennae arranged in the form of a Maltese cross. The lengths of the heavy duty coaxial cables that lead to these antennae are indicated on figure 2.10 and the implication of these lengths of cable on the phase calibration of the radar is discussed in section 2.3. Figure 2.11 shows the impedance of the antennae and feeders "looking" down the feeder cable where the receiver inputs are connected. Antenna 1 had a greater variation in impedance with frequency than the other antennae indicating there may have been a fault either in this antenna or in its feeder.

The hut houses various atmospheric experiments, including the radar receivers, computers and data logging equipment for the drifts and polarimeter experiments. The computer used for the interferometry experiment was the DEC Professional 350, (PRO350), micro-computer normally used for data collection and analysis by the drifts experiment.

The receivers used in the interferometry experiment were the same receivers used by the interferometry experiment at Birdlings Flat (section 2.1). The receiver input stages were retuned to centre on 2.9 MHz. Examples of the frequency response of the retuned receivers in given in figure 2.12. The bandwidth of the receivers was approximately 100 kHz which was, with a transmitter pulse of 35 μsecs, somewhat wider than was necessary, so some avoidable noise was probably picked up. At approximately 70 dB, the gain of the receivers turned out to be a little low. The variance due to noise at the receiver outputs was generally around 40 mV, the minimum level detectable by the A/Ds. Unfortunately the backscattered signal from the mesosphere was often of a similar level and being of the same order as the A/D quantisation step, the signal and noise were difficult to separate. The receivers never came close to saturation (that is the outputs never went beyond the 0-10 volts limit of the A/Ds), so in retrospect an extra amplification stage could have been added.

The results of the gain calibration procedures of section 2.3.1 are shown in table 2.3. The power variation with frequency follows similar trends to that of table 2.2 although

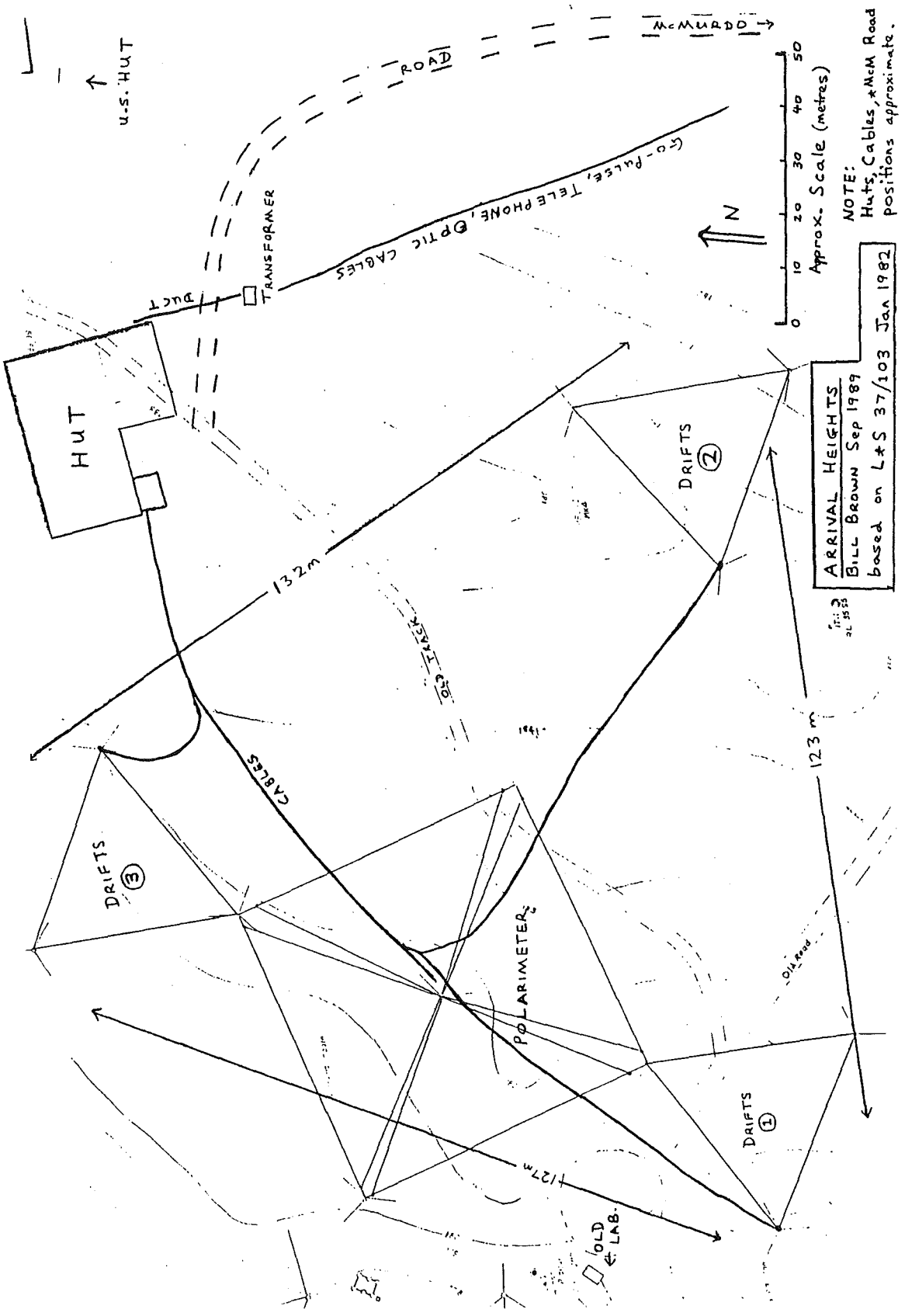

Figure 2.10: **Plan of the Arrival Heights** receiving site. (Adapted from the New Zealand Department of Lands and Survey map 37/103, January 1982, this diagram was prepared for the Scott Base Drifts Experiment operations manual.)

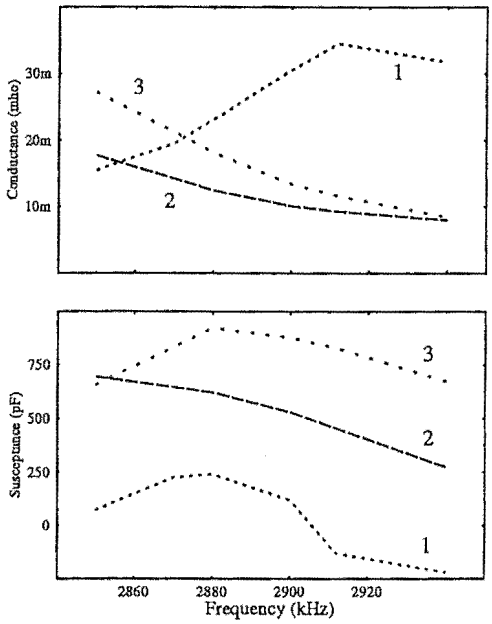

Figure 2.11: **The impedance of the Arrival Heights antennae,** (parallel impedance measured at the output of the feeders). The numbering of the antennae follows that in figure 2.10.

the magnitudes differ somewhat because this table also includes the varying frequency response of the receivers and antennae. The problem in antenna 1 is also apparent in this table.

The oscillators that generate the frequency steps for the experiment were also installed at Arrival Heights. The same multiple oscillator unit used at Birdlings Flat was used here, although the oscillator crystals used here had frequencies of around 11.6 MHz (4×2.9 MHz) rather than 9.6 MHz (4 × 2.4 MHz). A separate oscillator controller had to be built because, as discussed below, the computer used here was not capable of directly controlling extra ancillary equipment such as the oscillator without major modification of the existing hardware. So instead a sequential switching scheme was developed using the transmitter trigger signal to cycle the controller (figure 2.13) through the frequency steps. In practice this scheme was not a handicap although some care had to exercised in resetting the stepping cycle before each sampling run. The controller also carried out the phase-locking functions of the "Synchronizer" unit at Birdlings Flat, resetting the receivers to lock them together. The unit also generated the carrier signal (oscillator frequency divided by four) to send down the fibre optic cable to the transmitter at Scott Base. This signal was blanked during the time the receivers were detecting signals backscattered from the ionosphere to

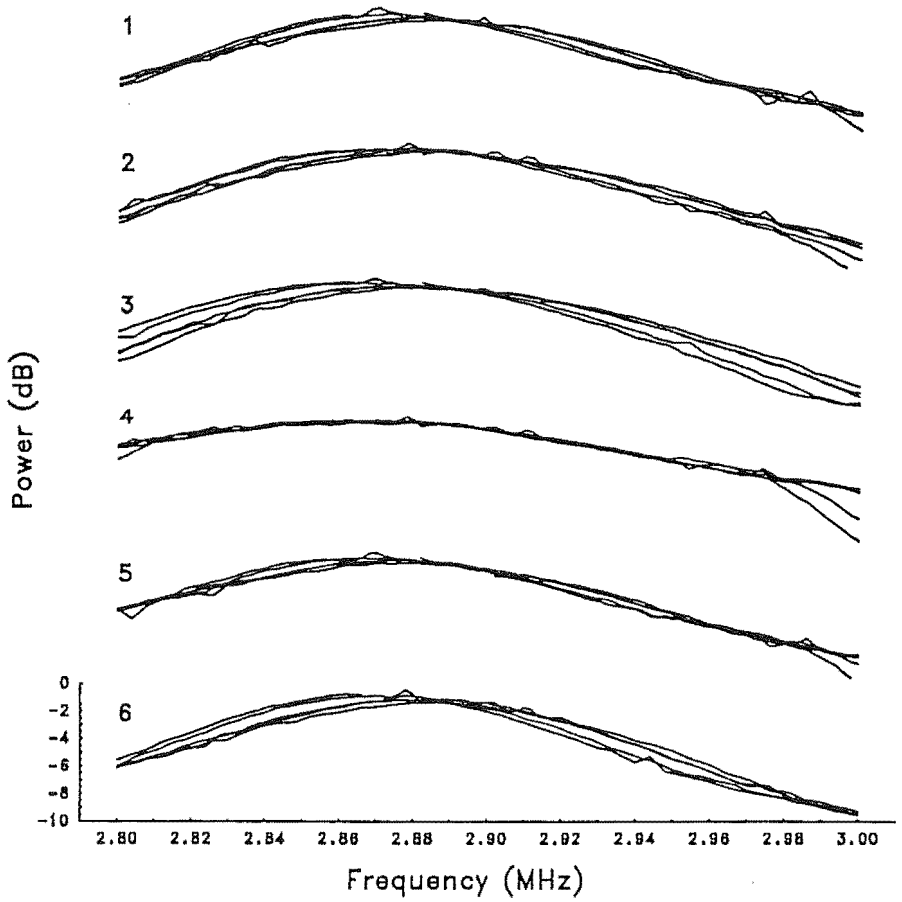

Figure 2.12: **Frequency response of the receiver** channels used in the interferometry experiment, retuned for the Scott Base radar. Plot 1 and 2 are the in-phase and quadrature channels for the receiver on antenna 1, etc. A 1 mV peak-to-peak signal was fed into the receivers at the frequencies along the bottom axis. The response of each channel at each of the five reference frequencies indicated in table 2.2 is shown.

avoid interference.

2.2.3 Phase Locking the Scott Base Radar

Unlike the Birdlings Flat radar, normally the carrier frequency for the radar is generated within the transmitter itself. The drifts and polarimeter experiments use incoherent receivers, so there is no facility for phase locking between the transmitter and the Arrival Heights site. The only link between the transmitter and the Arrival Height site is the twin core transmitter trigger line which has insufficient bandwidth for use in phase locking.

There is a six core fibre optic cable[3] with optical transmitting and receiving equipment

[3]Five cores of this cable were working at the time, unfortunately the whole cable was recently severed

Frequency (MHz)				
2.870 (-30 kHz)	2.880 (-20 kHz)	2.912 (12 kHz)	2.902 (2 kHz)	2.9 (0 kHz)
0.55 dB	0.31 dB	-1.56 dB	-0.24 dB	0 dB

Receiver/Antenna		
1	2	3
0 dB	2.50 dB	3.17 dB

Table 2.3: **Power variation of received signals between frequencies and antennae** with respect to 2.9 MHz and antenna 1. The order of the frequencies is that used during the interferometry experiments and the frequencies in brackets indicate the offsets from 2.9 MHz. Determined using the calibration methods of section 2.3.1.

provided by DSIR running between the Arrival Heights laboratory and the Scott Base Hatherton Geophysical Laboratory. The original plan was to simulate the Birdlings Flat arrangement, generating the carrier frequency at the receiving site and use the fibre optic cable to transport the carrier to Scott Base. A 70 metre coaxial cable would then be used to carry the signal from Scott Base to the transmitter to be patched into the existing oscillator circuit (figure 2.9).

Before travelling to the Antarctic, we were informed (Hatherton Laboratory management, pers. comm.) that the fibre optic cable would be capable of carrying the carrier (an approximately 2.9 MHz TTL type signal) and the equipment for this project was developed with this capability in mind. Upon installation however it was found that the maximum frequency of signal we could successfully send down the fibre optic cable was approximately 500 kHz. We were able to double this by modifying the optical transmit and receive units, but the capacity was still well short of that required.

A tolerable solution was found after considerable effort based on a divider chain and a phase locked loop multiplier. The carrier was divided by four at Arrival Heights (to 725 kHz), fed down the fibre optic cable, then multiplied four times at Scott Base before being fed into the transmitter. One of the major difficulties to overcome was reducing the severe feedback that occurred between the fibre optic receiver and the radar transmitter. The transmitter produces 60 kW pulse at 2.9 MHz and the optical receiver uses high impedance circuits in its amplifiers and power regulators so some feedback problems were to be expected. However an effective shielding scheme proved to be difficult to obtain. in

by a bulldozer and has had to be abandoned.

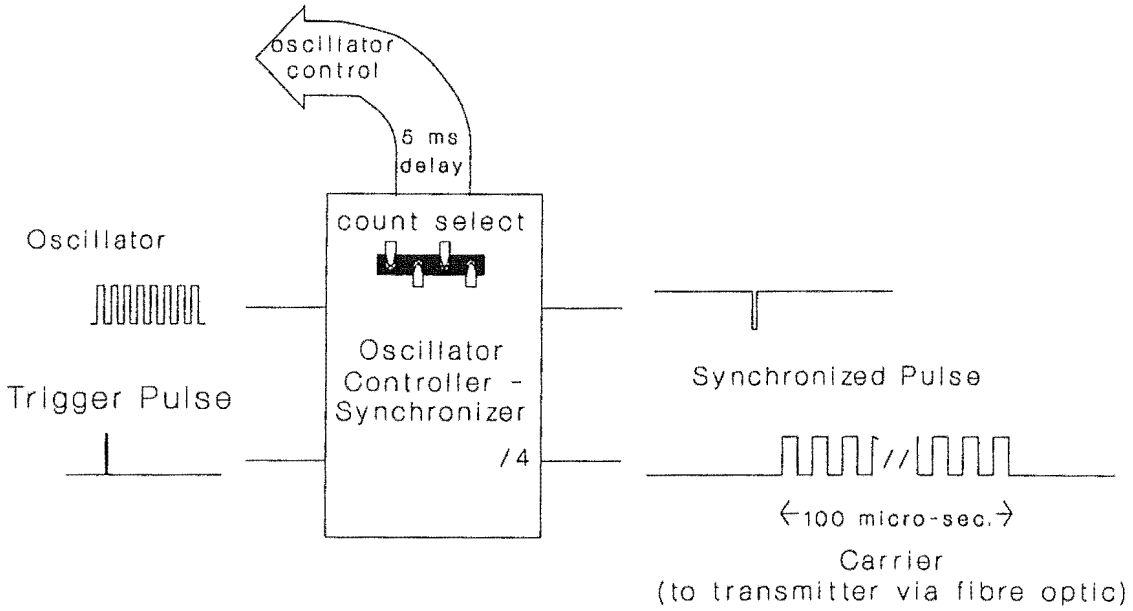

Figure 2.13: **Oscillator controller at Arrival Heights** The controller accepted a transmitter trigger pulse and stepped a 4 bit counter whose output was used to control the multiple oscillator. The counting cycle could be preset with switches, but was generally set to 5. After each trigger pulse, there was a several millisecond delay before the multiple oscillator was set to the next frequency to allow the receivers to demodulate the incoming signals scattered from the ionosphere. The synchronizing operations of this unit are the same as those of the Birdlings Flat synchronizer unit of figure 2.7.

part because of the lack of good earthing in the Scott Base environment due the apparent dielectric properties of ice and permafrost in the RF band. Eventually acceptable stability in the carrier signal and transmitter pulse was achieved[4].

[4]In hindsight a better scheme would have been to place the oscillator unit at Scott Base and feed a phase locking signal up to Arrival Heights, using a second fibre optic line to remotely control the oscillator from Arrival Heights. This scheme would place the fibre optic receiver receiving the carrier signal at Arrival Heights well away from the transmitter. Any feedback that may occur in the optical link should have died away by the time the radio backscatter from the mesosphere returns to the Arrival Heights receivers 100-200 μs later so the carrier signal against which the backscattered signals are compared against should be stable.

2.2.4 Arrival Heights data logging

The CPU of the PRO350 computer, like the Birdlings Flat PDP-11/23 computer, contains an LSI-11 16-bit microprocessor. However the PRO350 CPU only emulates the activities of a PDP-11, therefore the operating speed is somewhat slower than the Birdlings Flat PDP-11/23. The computer has a dual $5\frac{1}{4}$" DEC RX50 400 kB floppy disk drive and a 5 MB DEC RD50 hard disk. No other data storage media was available.

The PRO350 computer has a standard RS-423 type communications port and a network connector port which has been fitted with a DEC real-time interface module. This interface module is fully utilized in communicating with the A/D system, triggering the transmitter and to monitoring the state of the polarimeter experiment. The operating system used (RT-11FB) cannot address the standard communications port. (An alternative operating system, RT-11XM, can use this port, but was found to have insufficient memory available to it and ran too slowly for this project.) Since no control lines were readily available, the radar frequency could not be directly selected by the data collection program as it is at Birdlings Flat. As mentioned above a separate controller was developed to control the multiple oscillator using the transmitter trigger pulse.

The A/D system attached to the PRO350 uses just three channels for the drifts experiment (connected to three amplitude receivers), but fortunately slots for three more channels were incorporated into the original design. These extra channels were installed for the interferometry experiment, which, using three phase sensitive receivers, requires six A/D channels. Each A/D channel has an 8 bit A/D chip with an input range of 0-10 volts (a DATEL EH8B2) and its own 1 kB of memory. As with the Birdlings Flat A/D system, when the computer instructs the transmitter to pulse, a trigger signal initiates sampling of the receiver outputs by the A/Ds. Every $6\frac{2}{3}$ microseconds (corresponding to one kilometre in range) for typically 128 samples, the A/Ds take a measurement storing the digitized measurement in their local memories. (These samples form an A-scan.) These measurements are then transferred from the memories of each of the A/D channels to the computer memory for storage.

The PRO350 has 512 kB of memory although the operating system can only directly address 56 kB. It is possible to set a program up to indirectly address much more memory, but when this is done the real-time interface module cannot be accessed. The approximately 400 kB of memory that is left over from the running the operating system and user programs, is available as a virtual disk device.

The lack of directly addressable memory forced a substantial rearrangement of the programs originally used at Birdlings Flat. The programs were broken up into a series of

smaller programs to optimize use of the memory. As with the Birdlings Flat software, all of the programs were written by the author, although some of the assembly language routines were based on those used by the drifts experiment. Like the Birdlings Flat computer, the high level language used on the PRO350 is ROGALGOL.

The clock system also differs slightly from the Birdlings Flat arrangement, the PRO350's internal clock is based on a 60 Hz counter. Therefore the clock cycle is $16\frac{2}{3}$ millisecond which being substantially longer than the Birdlings Flat clock cycle (one millisecond) lead to some changes in timing procedures, but not to the overall data collection procedure, aside from automatically sychronzing pulses with mains.

Data collection procedure

The data collection procedure was fairly similar to that used at Birdlings Flat. A "burst" of five pulses was transmitted, each at different frequencies. 33 milliseconds apart (two clock cycles). The three receivers with a total of six output channels produced six A-scans for each frequency step. Each of the six A/D channels took 256 samples (or range bins) of these scans and stored the samples temporarily in their on-board memories. Between each step 25 of these samples, corresponding to range bins at which scattering from the mesosphere was expected to be observed in, were transferred from the A/D memories to the computers memory. At the end of each burst there was a longer pause of 118 msec, during which time the data was written to a buffer file. Then the cycle was repeated with another burst of pulses. Each burst of pulses started 250 milliseconds (15 mains or clock cycles) apart. The sampling run continued in this manner for 256 cycles, or 64 seconds. At the end of the sampling run, there was a two minute pause while the buffer file was transferred to more permanent storage for later processing, then a another one minute sampling run would start up again.

The buffer file was on the virtual disk in the PRO350s extended memory which is limited to 400 kB. The data transfer rate to the hard disk would have been unacceptably slow for use during sampling, (approximately 50% slower than the virtual disk). As it was the speed of the data handling procedures (for example the transferring data from the memory on the A/D boards to the PRO350 memory) limited the amount of data that could be collected to about 400 kB anyway. Each buffer file, consisting of 256 samples of five frequency steps on six A/D channels, each having 25 bins, totalling up to 384 kB (192 000 two byte words), plus timing and other information, was 394 kB (769 DEC "blocks") long.

At the end of the sampling period, the data had to be shifted from the virtual disk to provide space for the next run. The limited amount of space on the hard disk meant

that generally only five buffer files could be stored there. When the hard disk was filled, buffer files were stored on floppy disks. It took about a minute to transfer the data to the hard disk and about a minute and a half to transfer the 384 kB buffer files to the floppy disks. With the inclusion of setting up procedures, approximately two minutes was required between sampling periods therefore data was collected every third minute (compared with every second minute at Birdlings Flat).

There was a fairly limited supply of the RX50 floppy disks[5] and coupled with the occasional hiccups and the pauses to run the hourly polarimeter experiment, the longest period the sampling runs could be kept going for was 37 minutes (13 sampling runs).

The floppy disks were the only means of bringing the data back to Christchurch for further processing therefore the data was heavily sifted to save space. Only eight range bins were retained from most data files, although a limited number of runs with the full 25 range bins were kept. Of these eight range bins, only seven have useful scattering information because the first was always selected to be from altitudes for which negligible scattering occurred. This "quiet height" bin served as a reference level or DC level for the receivers.

The Collected Data

105 data runs were taken, of which 85 were full interferometry samples. The other 20 runs were either calibration runs (for example sampling the ground pulse or testing the response of the receivers) or observations taken using the drifts experiment, amplitude only, receivers.

Table B.2, appendix B, lists the times and altitudes sampled of the full interferometry observations runs. (Note that the times are local time which is New Zealand standard time.) It had been intended to sample over at least two weeks, but the delays in setting up the experiment meant this had to be cut back to four days. As mentioned above, the gain of the receivers proved to be somewhat less than desirable. The typical scattered signal from lower mesospheric heights was observed to be of the same order as the noise level and the quantization step of the A/Ds. Since data storage was at a premium, most of the data that was retained was of observations of upper mesospheric / lower thermospheric heights (90-110 km), where the signal to noise ratio was greater.

Even at these heights, there were periods of several hours during which time scattering

[5] No formating program for these disks was available at that time, and so they had to be brought, at a premium, preformatted from DEC. Although the record and directory structure of RX50s differ from quad density (1.2 MB) IBM disks, the track positions seem to be identical, except that only the top side of the disks are used!

appeared to be too weak to make any observations. This weak scattering was due to radio wave "absorption" due to enhanced ionization in the D-region ([Davies, 1966]). At times this absorption can become so intense that the total radio "blackout" can occur for several days. A blackout event did occur during the setting-up stages of this experiment, but fortunately not during the brief period of observations.

As a result of these absorption events and occasional short periods of intense interference, the data runs were not as evenly spread throughout the day as would have been desirable. In fact most of the runs were taken from mid-morning to midday.

2.3 Calibration

When analysing experimental data it is important to be able isolate characteristics in the data that are due to the imperfect response of the equipment from those in the system under study (in this case the mesosphere). In this project it was found that in general the radars were reasonably consistent in their response during the course of each observation run. There were however variations in response from day to day and from channel to channel.

The power of the transmitters along with antenna impedances and the gain and frequency response of the receivers of the Birdlings Flat and Scott Base radars were reported in the sections describing each radar. It was noted in these sections that there was some variability in the operating conditions of the radars from day to day. For example the transmitting antenna of the Birdlings Flat radar often had problems with one of its dipoles and the Scott Base radar had problems with phase locking. Also some factors, such as the antennae impedance, varied unpredictably from day to day.

Some of these variations are significant for different stages of the analyses and some can be ignored. In many sections of the analyses used in this work, the variations in gain between receivers or antennae are not particularly important, (provided the gain does not vary rapidly with time). For example the cross correlation functions used in full correlation analysis are normalized with respect to the covariance of each receiver therefore any gain differences cancel out. However if the gain of the inphase and quadrature channels of the receivers differ from each other there will be an error induced in phase measurements.

Measurements of phase differences of signals received at different antennae or at different frequencies were very important to this project. These phase differences generally included an equipment factor that had to be isolated and removed from the measurements.

The variations in gain and the equipment phase factors can be determined from measurements of the characteristics of each component of the radar. Alternatively, if assumptions are made about the medium term (say, over a few hours) behaviour of the signals seen by the radar, then sufficient calibration can be made by examining the characteristics of the signals themselves. The general philosophy followed in this project was to follow this alternate approach. That is rather than keeping precise track of the response of the radar's components (other than for maintenance purposes), the collected data was examined to determine calibration factors.

2.3.1 Gain Calibration

As mentioned above, much gain calibration was carried out automatically in analyses such as that of correlation functions. Further gain calibration was made by examining the statistics of each A/D channel output. The assumption was made that averaging over the typical periods each data set was recorded over (two to five hours at Birdlings Flat and half an hour at Scott Base) and over the altitude ranges recorded (about 25 and 15 km at Birdlings Flat and Scott Base respectively), each receiver channel and each frequency step should see the same total signal. On time scales less than a minute there may be variations between receivers and between the different frequencies used in the frequency shift experiment. However at the separation of the receiving antennae here (120 - 350 metres) and magnitude of the frequency steps (less than 45 kHz), the variations should not be great enough to see significant differences when averaging over the time scales and altitude ranges of the data sets observed.

The procedure followed was to determine the signal level and Signal to Noise Ratio (SNR) of each one minute series on each receiver channel for all range gates and radar frequencies. (The signal and SNR were found using the auto covariance function as discussed in section 4.1.1). If the SNR was above a certain limit, normally 0.5, the signal was retained. The average of all the signals for each channel and frequency over the whole data set were found and by assuming these should all be equal the gain correction factor for each channel was determined.

Typical results of the gain calibration procedure are shown in tables 2.1 (section 2.1.4) and 2.3 (section 2.2.2) for the Birdlings Flat and Scott Base radars respectively.

2.3.2 Phase Calibration

This project made heavy use of measurements of the variation in the phase of received signals with time and between receivers and across frequency steps. Since in general the oscillators and the phase locking arrangements were found to stable with time to a higher precision than measurable by the resolution of this experiment, no further corrections than the amplitude corrections above were made when measuring variations of phase with time.

However when finding the phase difference between signals from different receivers and when finding the change in phase as the radar frequency is stepped (cross receiver and cross frequency phase respectively), the equipment component of the measured phase difference had to be determined and removed.

antenna	open wire (metres)	coaxial cable (metres)	antenna pair	phase correction (radians)
F	201	9	F - C	-0.05
C	175	25	F - D	1.22
D	213	17	C - D	1.27

Table 2.4: **Birdlings Flat, cross receiver phase calibration**, determined from the feeder lengths and respective altitudes of the antennae.

antenna	feeders (metres)	altitude (metres)	antenna pair	phase correction (radians)
1	134	55.0	1 - 2	-2.30
2	144	56.1	1 - 3	-2.57
3	37	55.2	2 - 3	-0.26

Table 2.5: **Scott Base radar, cross receiver phase calibration**, determined from the feeder lengths and respective altitudes of the antennae.

Cross Receiver Phase Calibration

The problem is best defined as finding "which way is up" and which way the radar is pointing. In principle the pointing direction is largely a function of the difference in the lengths of the transmission lines connecting the receiving antennae to the receivers themselves. The lengths of the various receiving lines on Birdlings Flat radar and on the Scott Base radar (at Arrival Heights) are given in tables 2.4 and 2.5 respectively. The implied phase changes induced by these lengths and the variation in altitudes of the antennae (at Birdlings Flat, C array is approximately two metres lower than F and D arrays) are also given. (Velocity factors, which describe wavelength in the cable over that in free space, of 97% and 66% were used for the open wire and coaxial feeders respectively. Also the number 3 antenna on the Scott Base radar is orientated in the opposite direction to the other antennae thus is π radians out of phase which is included in the corrections.)

Past studies at the Birdlings Flat site however have found that the effective pointing direction can vary considerably from day to day, (for example [Brown, 1986] and on the 26 MHz meteor radar [Taylor, 1991]). These variations appear to be due environmental factors such as moisture content of the air, leading to changes in the impedance of the transmission lines, [Kwa, 1977].

The previous attempts at cross receiver phase calibration on the MF radar had only

limited success. [Brown, 1986] observed what was considered to be gravity wave distortions of a specularly reflecting layer and made assumptions about the expected variations in the direction of scattering from the waves. The phase velocity of the wave was matched to the velocity determined by FCA and using the observed variation in Doppler shift, directions of arrival were surmised. These were related to the observed phase differences on the spaced antennae and to obtain estimates of the phase factors. Clear examples of wave distortions of specularly reflecting layers are rare and require too many assumptions about the scattering process to consider using this method as a primary means of phase calibration in this project.

Another attempt at phase calibration by [Brown, 1986] used tracking of a twice daily airline flight over the site. The altitude of the flight is approximately 10 km and the length of the transmitted pulse had to be halved to completely isolate the aircraft reflections from the ground pulse of the transmitter. There were some difficulties in achieving this and there were also problems interpreting the weak signal made so this method of phase calibration was considered impractical for regular use.

It was decided in this study to carry out phase calibration by examining each data set as a whole in a similar manner to that used for gain calibration. It was assumed that averaging over a few hours and over the range of altitudes observed, the only preferred direction to the scattering should be zenith. There may well be, as studies on other MF radar have found (such as [Murphy, 1984]), a preferred scattering direction around particular altitudes due to the orientation of dominant reflecting structures. However over a broad range of altitudes and over an extended period, many scattering targets of various orientations should travel over the radar. Care should be made that the comparative strength of scattering at each altitude is not used to weight samples against each other and so bias the results towards directions where strong scattering might originate. The scattering can have an angular distribution (that is aspect sensitivity) as long as on average it is directed downwards. Indeed aspect sensitivity is useful because it helps balance out any unevenness in the polar diagrams of the antennae of the radar.

The polar diagrams of the transmitting and receiving antenna beams of the Scott Base radar are very broad, much broader than the typical aspect sensitivity of the scattering. As a result any slight bias in the directions of the antennae polar diagrams should have negligible effect on the average direction of scattering.

Similarly the receiving antennae at Birdlings Flat are much broader than the typical aspect sensitivity of the scattering so small variations in the directivity of their individual polar diagrams should not be significant. However the polar diagram of the transmitting

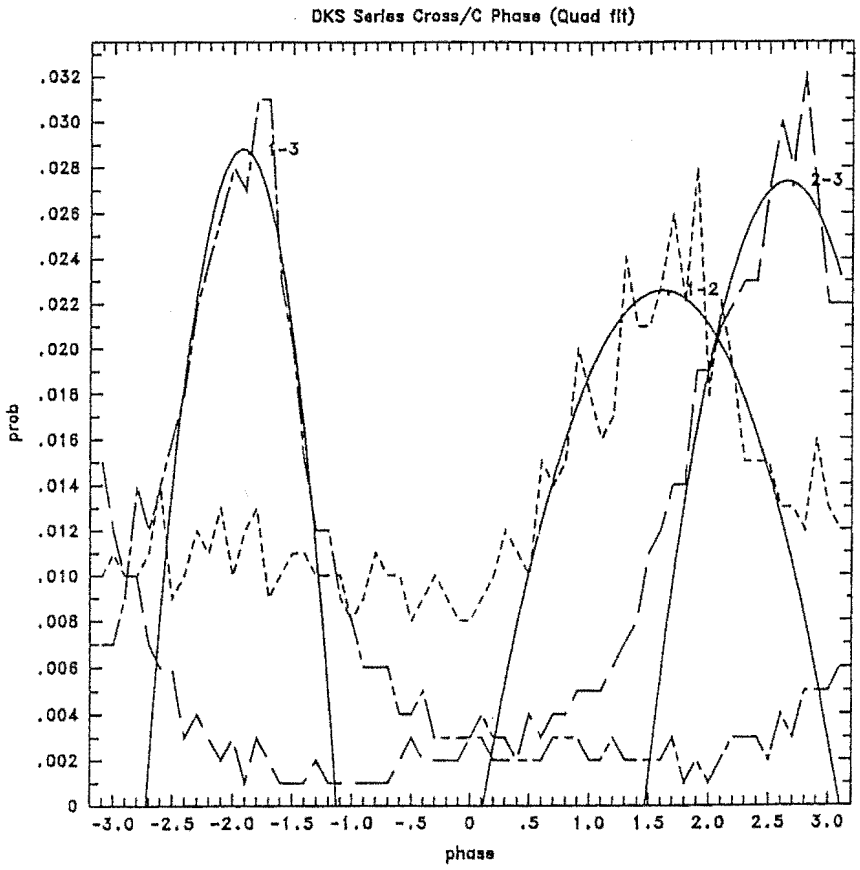

Figure 2.14: **Cross receiver phase distributions, 6 October 1990,** Birdlings Flat. Data collected over 5 hours at 13 range gates, 79-103 km, and at five frequencies. The labeling **1-3**,**1-2** and **2-3** refer antenna pairs F-D, F-C and C-D respectively. The fitted curves have peaks at 1.606, -1.926 and 2.644 radians.

array at Birdlings Flat is of similar order to the scattering aspect sensitivity and a variation of the direction of this array's polar diagram away from zenith could lead to a misleading calibration. As reported in section 2.1.2, the effect of, for example, removing a dipole from the array was tested and the theoretical beam width increased by about 1°. It was also found however that the overall direction of the theoretical polar diagram was not significantly altered in this case.

The phase differences between each of the three receivers for each one minute sample at each range gate and radar frequency was found using the cross correlation methods of section 4.1.2 (checking first that the SNR of the samples was above 0.5). A phase difference of between $-\pi$ and $+\pi$ radians is obtained and the distribution of all the phase differences over each data set is determined. Figure 2.14 gives an example of the distribution of the phase differences between the three receivers collected over all range gates and frequencies. If the equipment phase factor was zero, and on average the scattered signals do arrive from

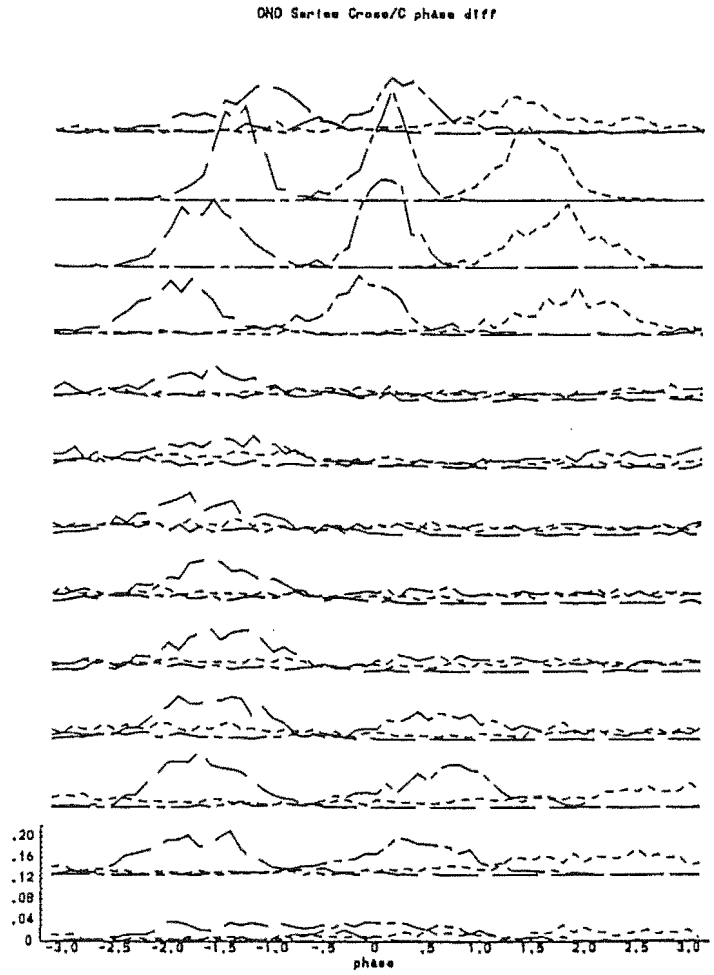

Figure 2.15: **Cross receiver phase distributions with altitude, 8 December 1990**, Birdlings Flat. Data collected over five hours at thirteen range gates, evenly spread from 79 km (bottom distribution) to 103 km (top distribution). The three lines at each level correspond to the three pairs of receivers as for figure 2.14.

zenith, then these distributions would peak at zero radians. As can be seen they do not.

Curves were fitted to find the peaks of the distributions; in the example of figure 2.14 quadratic curves were used although more generally Gaussian functions were used. The phases of the peaks were used as the equipment phase factors. Ideally these phases would sum around the loop of pairs of antennae (F-C,C-D,D-F) to zero or $\pm 2\pi$. In this case they add to 6.176 radians or 0.107 radians short of 2π, and this measure provides some indication of the uncertainty in the method.

An example of the variations in the distributions with altitude is given in figure 2.15 and with different frequencies in figure 2.16. All of the frequencies give very similar distributions. There is some variation in the distributions with altitude suggesting that certain ranges do have different preferred directions to their scattering. However when

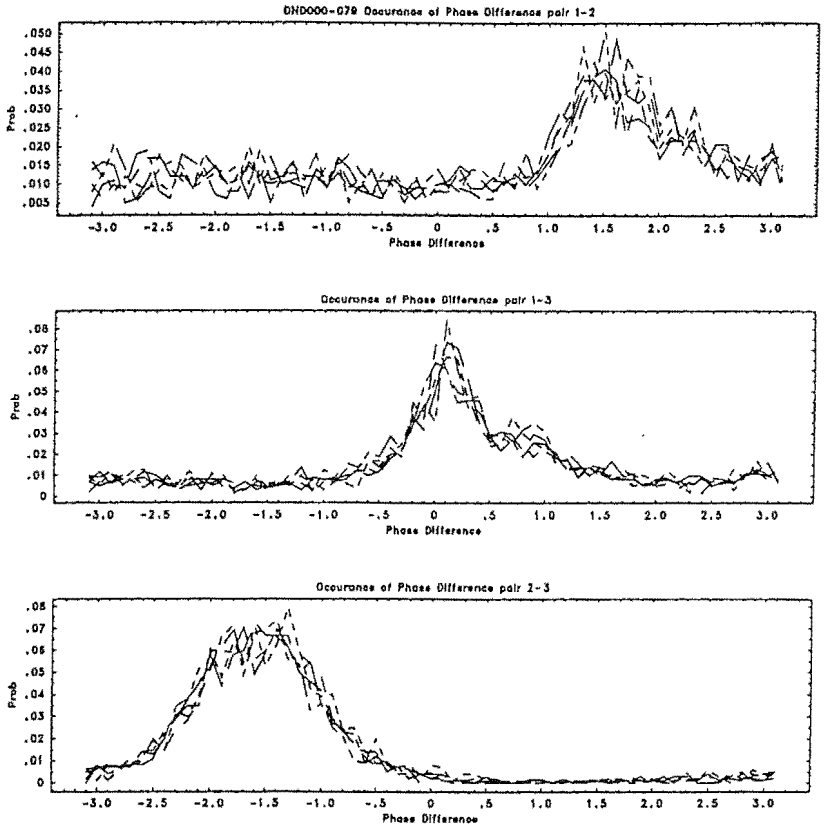

Figure 2.16: **Cross receiver phase distributions with frequency, 8 December 1990.** Data collected over two hours and forty minutes at thirteen range gates as for figure 2.15. The range gates are collected together in this figure. Each dash pattern refers to data collected at each of five different frequencies.

all altitudes are gathered together (as in figure 2.16) the locations of the peaks of the distributions in this data set is fairly clear. (Note that some of the lower range gates in figure 2.15 have lower distributions because fewer samples had sufficient signal to noise ratios to be included.)

Another check on the consistency of the phase difference distributions was to see how the distributions varied using different subsets of the data sets. The distributions in figure 2.16 were compiled from about half of all of the data collected on that day; however the distributions shown are very similar to the distributions for all of that day's data set.

Some of the earlier data collected at Birdlings Flat had less distinct distributions. For example, figure 2.17 displays the distributions of data collected on 18 August 1990. The pairs F-D and C-D (**1-3** and **2-3** in figure 2.17) have fairly clear peaks, but the pair F-C (**1-2**) has a double peaked distribution. If the fitted curves are used, the phases of the peaks sum to -1.119 radians, which indicates a large uncertainty in the distributions. If

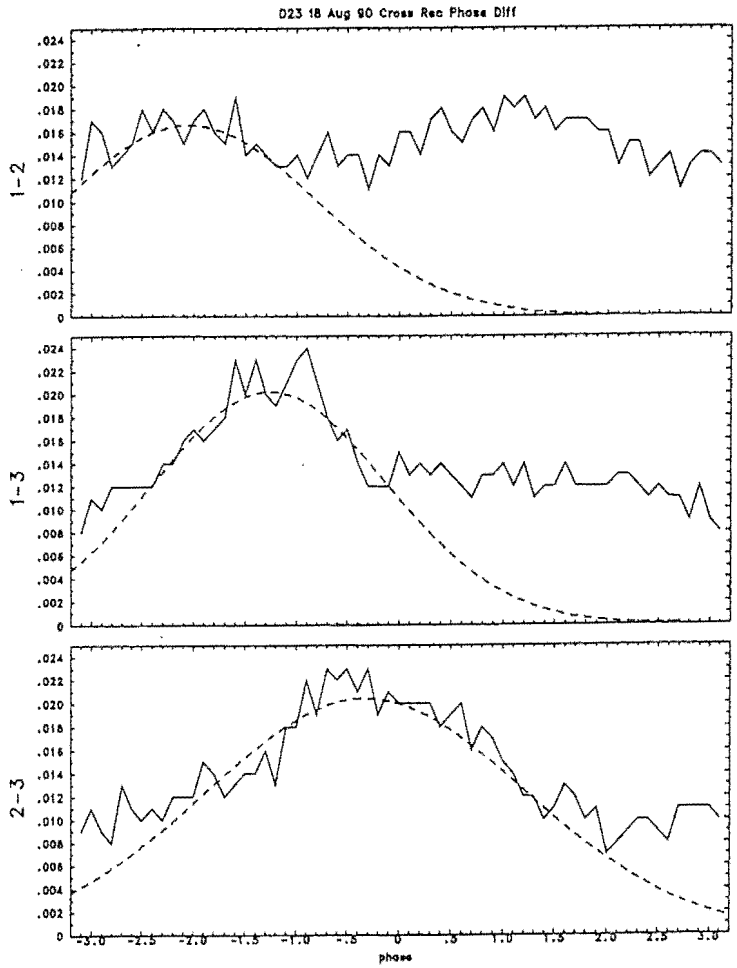

Figure 2.17: **Cross receiver phase distributions, 18 August 1990,** Birdlings Flat. Data collected over five and half hours at thirteen range gates. The dashed lines indicate fitted Gaussian functions and these have peaks at -2.050, -1.259 and -0.328 radians respectively.

the F-D and C-D distributions are used to indicate an ideal peak for F-C, the peak would be -0.931 radians where there is a large dip in the F-C distribution.

As mentioned in section 2.1.7, isolating buffers were installed between the receivers and the A/D system substantially reducing the effects of an earth loop problem. Data collected after this time (here the data sets from 6 October 1990 onwards) gave significantly clearer phase difference distributions than the earlier data.

The phase factors found in these data sets do not seem to bear any relationship those in table 2.4. The differences between these phase factors can be explained in terms of the impedance of the feeders and antennae. [Kwa, 1977] found that the impedance could fluctuate by 10 ohms during rain and 30 ohms due to wind, as well as by up to 20 ohms

due to unknown variations that Kwa considered were drifts in the measuring equipment he used.

At Scott Base there do not appear to be the variations over time in the phase offsets between receivers as there are at Birdlings Flat. Moisture in the air appears to be a significant source of the phase variations at Birdlings Flat. In the Antarctic any moisture in the atmosphere is immediately frozen out so the air is very dry. The feeder lines from the antennae to the receivers are coaxial cables so only the impedance of the antennae can be affected by variations in the air. Also there is no water table (other than permafrost!) so another source of variations is removed. There are low snow banks below the antennae, but these did not vary much during the course of this projects experiments and it is doubtful whether they would have much impact on the characteristics of the antennae.

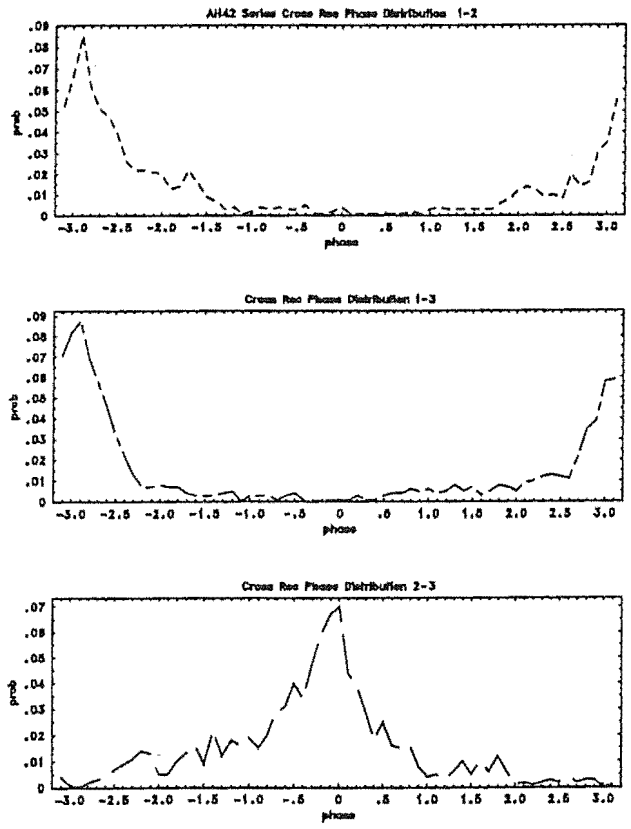

Figure 2.18: **Cross receiver phase distributions at Scott Base.** Peaks determined to be at -2.910, -2.941 and -0.077 radians.

The data sets collected on the Scott Base radar were then concatenated together to find the cross receiver phase offsets. Figure 2.18 shows the distributions of phase differences between the receivers. The phase difference around the loop sum to 0.046 radians, which

is smaller than many of the sums found in the Birdlings Flat data. The phase factors found here are much closer to the theoretical values (table 2.5) than was the case for the Birdlings Flat radar.

Cross Frequency Phase Calibration

A similar approach was used to calibrate the phase differences on changes of the radar frequency. As discussed in the section on frequency domain interferometry (section 5.3.3), the phase difference between signals received on one receiver but with the radar operating at two different frequencies, depends on the difference between the two frequencies and the range on the scattering target being observed.

The phase response of the radar, particularly the transmitter and antennae, varies as the frequency is changed and this adds a phase factor to the phase differences observed. Determining this phase factor from equipment parameters is difficult. In some respects this factor can be ignored, since generally only the variations in the FDI range with time are of interest rather than the absolute FDI range. However it is possible readily to make an estimate of the equipment phase factor for frequency steps.

Without using FDI, the range resolution of the radar due to timing factors such as the transmitter pulse length and the bandwidth of the system, is about four kilometres (much broader than the one kilometre gate separation). The transmitter pulse and the bandwidth of the radar are not boxcar or sharp cut-off functions, but are rounded at the edges and so the response of the system will tend to be strongest towards the centre of each range gate. If, over time, there is a fairly even spread of scattering targets throughout the radar volume the response of the system will lead to a distribution of ranges centred on the centre of the radar volume. Distributions of the phase changes on frequency steps in the FDI experiment do show peaks and for calibration purposes these peaks were assumed to be centred on the range gates.

Figure 2.19 shows an example of the distributions of these phase changes at thirteen different range gates corresponding to a step in radar frequency of 18 kHz. A 2π change in phase (the full width of the plots) corresponds to a range variation of 8.3 km. From range gate to range gate, the peaks are offset by 1.5 radians which corresponds to the two kilometre gap between the range gates shown here. Interestingly the half height full widths of the lower range distributions are about 0.6 radians, equivalent to approximately 800 metres, which is much narrower than the four kilometres pulse length, a point that will be considered further in section 7.10. The phase differences for each receiver are plotted together and are very similar for each receiver; the differences in the lengths of the feeder

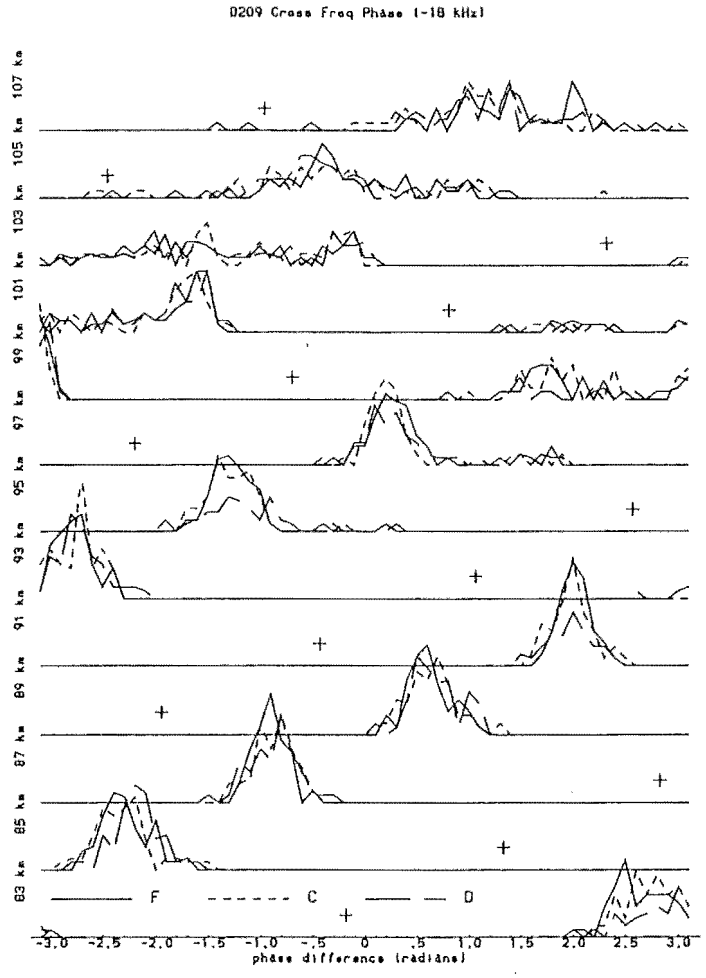

Figure 2.19: **Distribution of cross frequency phase differences, 25 September 1990**, Birdlings Flat. Data collected over two hours. The frequencies used were 2.4 MHz and 2.418 MHz, so the frequency step is 18 kHz. The distributions correspond to range gates from 83 - 107 km and the three lines at each level indicate the distributions of each of the three receivers, F, C and D. The pluses mark the phase difference for each range gate had there been no equipment factor offset.

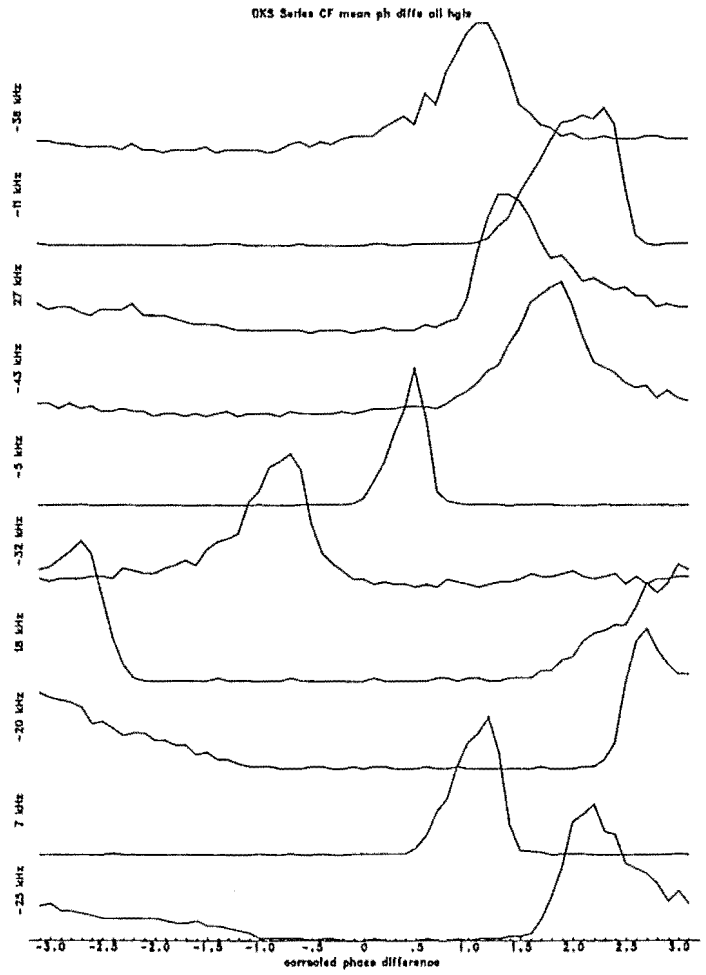

Figure 2.20: **Distribution of cross frequency phase differences, 6 October 1990**, Birdlings Flat. Data collected over five hours at 13 range gates (79-103 km) on three receivers. The distribution of phase differences, with the phase change due to the range as found by timing removed, is shown for all ten frequency steps. The order of the steps in frequency relates to the order of the frequencies themselves.

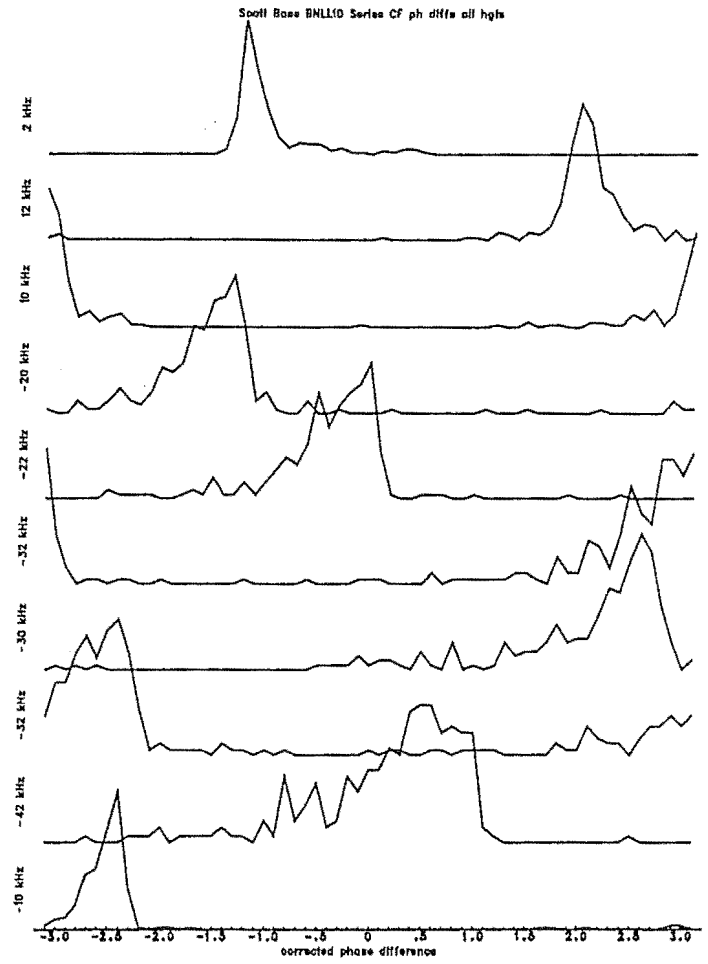

Figure 2.21: **Distribution of cross frequency phase differences at Scott Base.** Collected over 31 minutes at seven range gates (92 - 104 km) at 10:20, 15 December 1988.

lines from the different antennae to the receivers do not produce significant variations in the phase from receiver to receiver.

The pluses at each level in figure 2.19 mark the phase change expected on a frequency step of 18 kHz if no phase changes were introduced by the radar itself. The difference between the expected and the measured phase change is similar for all of the range gates and so the average of these was used as the cross frequency phase factor.

Figure 2.20 gives a distribution of phase for all ten frequency steps each compiled from all range gates and receivers for data collected at Birdlings Flat on 6 October 1990. The phase change due to the range of each gate has been removed so that the remaining phase has a distribution with a spread due the variation of range of the data within each range gate, and a mean due to the equipment offsets at that frequency step. The peaks of these distributions were fitted with Gaussian functions to obtain the offset for each frequency

step. As with the cross receiver phase factor, the cross frequency phase factors were found to be fairly similar if subsets of the full data set was used to determine the factors.

At Scott Base adjustments had to be frequently made to the circuits that fed the carrier signal from the receiving site at Arrival Heights to the transmitter at Scott Base. As a result the phase offset at each frequency step varied from data set to data set, so a calibration could not be made using multiple data sets concatenated together as they were when finding the cross receiver phase offsets. Calibrations had to be found for each of the data sets which typically only lasted half an hour and covered only seven range gates (90-105 km) as compared with two - five hours and thirteen range gates at Birdlings Flat. However even with these smaller data sets, a reasonably clear calibration could be made. An example is given in figure 2.21 which follows the same form as figure 2.20.

This method of calibration can be used to give an absolute range esimate for FDI observations. The method is limited by the form of the distribution of the phase differences. As can be seen in figures 2.20 and 2.21 some of the distributions are uneven and the fitted peaks varied by the order of 0.1 radians ($\sim$ 100 m at 20 kHz) on the Birdlings Flat radar and 0.2 - 0.3 radians on the Scott Base radar depending how the fit was performed. Another limitation is how precisely the range of the range gates is known. This is determined from the range of the ground pulse (section 2.1.7) to the nearest 0.1 km (although the range gates are quoted to the nearest kilometre here). Errors in the calibration add a systematic uncertainty to the FDI range estimates; all of the FDI range estimates at a particular frequency step for a data set may be too high or too low by one or two hundred metres. When the range estimates from different frequency steps are averaged together the different systematic errors at each step will add to the standard deviaion of the mean.

Chapter 3

Gravity Waves, Turbulence and Scattering Scales

The observations made by the interferometry experiment presented in this thesis were a series of one minute samples collected over time scales of up to several hours. Over these time scales, the dominant oscillatory motions in the mesosphere are "atmospheric gravity waves" and this topic is introduced in section 3.1. Over the one minute time scale of each of the samples, phenomena that are generally grouped together under the category of turbulence are important. Turbulence in various forms is important to radar studies because it provides fluctuations in refractive index from which radio waves are backscattered. Turbulence is discussed in section 3.2 as is methods of measuring turbulence intensity. Section 3.3 considers the measurement of the scale of scattering structures, particularly measures of the angular spread or aspect sensitivity of scattering. Examination of the statistical distribution of scattered signals can also provide information on scattering processes and this topic is covered in section 3.4.

There are useful discussions of various atmospheric phenomena in [Houghton, 1977] and [Andrews et al., 1987]. The collections of [Atlas, 1990] and [Fukao, 1988] review radar probing of the middle atmosphere to observe features such as gravity waves and turbulence, discussing the valuable contributions that many workers have made to these topics.

Two other classes of oscillatory motions that occur in the middle atmosphere are "planetary waves" and "acoustic waves". Planetary waves have periods of days and wavelengths of a scales comparable to the circumference of the earth and are important when studying the large scale activity of the middle atmosphere. They require measurements over days or over large distances to make any inferences about their activity and thus are not considered further here. Acoustic waves have periods of a few minutes or less and wavelengths

less than about 300 metres; however they are not generally regarded as being important in the middle atmosphere.

3.1 Atmospheric Gravity Waves

The term "atmospheric gravity waves" (or often just "gravity waves") is used to describe a range of buoyancy type oscillations in the middle atmosphere. Short period (less than a few hours) wave type activity was first observed in the middle and upper atmosphere in ionospheric measurements such as those of [Munro, 1950]. [Hines, 1960] first recognised such observations as being manifestations of atmospheric gravity waves. Since then there have been many observations of oscillatory activity that have been linked to gravity waves. Radars probing the middle atmosphere often observe these oscillatory motions, for example as periodic variations in wind measurements or fluctuations in the angle of arrival of backscattered signals ([Adams et al., 1989] and [Meek and Manson, 1992]). Observations of specular reflections in the ionosphere also sometimes display ripple like perturbations that appear to be associated with the passage of gravity waves, [Pfister, 1971].

There have been a number of review articles on aspects of gravity waves in the middle atmosphere. Recent reviews include [Fritts, 1989] and [Klostermeyer, 1989a], and there are also useful discussions of gravity waves in texts such as [Andrews et al., 1987].

The periods of these oscillations range from several minutes up to the order of a day and they act over horizontal scales ranging from tens of kilometres up to several hundreds of kilometres. An unusual feature of gravity waves is that the group and phase velocities of these waves are perpendicular to each other. That is, the direction of propagation of energy (the group velocity direction) is parallel to the wave crests or lines of constant phase, quite unlike ocean surface waves and acoustic waves. Parcels of air oscillate along the wave fronts, transverse to the direction of phase propagation. As well as the actual motion in the atmosphere as gravity waves pass, there are oscillations in density, pressure and temperature. Figure 3.1 illustrates these perturbations associated with the passage of a gravity wave.

The vertical velocity of an air parcel perturbed by a gravity wave, w', can be related to the horizontal velocity perturbations, u', using one of the "polarization relations".

$$u' = -\frac{\lambda_h}{\lambda_v} w' \tag{3.1}$$

where λ_h and λ_v are the horizontal and vertical wavelengths of the gravity wave. A useful measure of gravity wave activity is the mean of the product of perturbations in vertical and horizontal velocity observations, $\overline{u'w'}$. Measures such as $\overline{u'w'}$, are known as measures

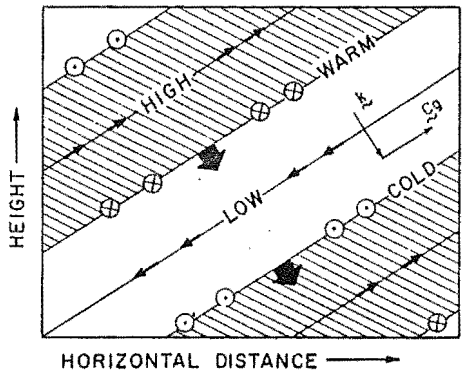

Figure 3.1: **Cross section of a gravity wave,** showing the temperature, pressure and motion perturbations associated with the passages of an inertial gravity wave in the northern hemisphere. Note that the induced motions (small arrows and arrows into and out of the page) are perpendicular to the direction of travel of the phase fronts (thick arrows). For an inertial gravity wave in the southern hemisphere the arrows into and out of the page would be reversed. The group velocity and the wave vector are indicated by Cg and k. The same diagram applies to internal gravity waves if the arrows into and out of the page are omitted. (After [Andrews et al., 1987].)

of "momentum flux", [Vincent and Reid, 1983]. If u is zonal (eastward) velocity, $\overline{u'w'}$ is the "upward flux of zonal momentum".

The upper limit to the frequency of buoyancy oscillations is the Brunt-Väisälä frequency, the natural frequency of stable oscillations of a parcel of air which is displaced in a stratified atmosphere. The Brunt-Väisälä frequency, N, as a function of altitude, z, depends on the variation of the mean temperature $\overline{T}$,

$$N^2(z) = \frac{g}{\overline{T}} \left(\frac{\partial \overline{T}}{\partial z} + \frac{g}{C_p} \right), \tag{3.2}$$

[Fritts, 1984], where C_p is the specific heat at constant pressure and g is gravitational acceleration. In the mesosphere, the Brunt-Väisälä frequency is about five minutes. If there is any wind blowing waves along, the observed frequency of a gravity wave may be Doppler shifted to higher than the Brunt-Väisälä limit. The non-Doppler shifted frequency of a wave, that is in a frame travelling with the wave, is known as the "intrinsic" frequency of the wave.

Gravity waves in which buoyancy alone is the main restoring force are termed "internal gravity waves". The motions of air parcels disturbed by an internal gravity wave are along lines perpendicular to the direction of phase propagation, (figure 3.1).

As the frequency of oscillations drops, the earth's rotation via the Coriolis effect increasingly contributes to the restoring force. Displaced air parcels trace out ellipses in an inclined plane perpendicular to the direction of phase propagation. For a wave with a typical upward component to its propagation, the air parcels move in an anticyclonic direction (anti-clockwise in the southern hemisphere), reversing for a downward wave. Gravity waves for which the Coriolis effect dominates are known as "inertio gravity waves". These waves have periods of several hours or more, and horizontal wavelengths greater than several hundred kilometres. The horizontal wavelengths of inertio gravity waves are much greater than the vertical wavelengths (typically around 10 km), so the motion of air parcels displaced is largely in the horizonal plane. The direction of propagation is also largely horizontal.

The lower frequency limit of inertio gravity waves depends on latitude, ϕ, and is given by the "inertial frequency", or the Coriolis parameter f,

$$f = 2\Omega sin\phi, \tag{3.3}$$

where Ω is the earth's rotation rate. At Birdlings Flat (latitude 45°S) the inertial period is 17 hours and at Scott Base (latitude 78°S) it is $12\frac{1}{4}$ hours. The polarization equation describing the relationship between zonal and meridional (eastward and northward) perturbation for a monochromatic wave is given by

$$v' = \frac{if}{\omega} u' \tag{3.4}$$

(where $i = \sqrt{-1}$), so as the frequency of the wave, ω, decreases, the perturbation velocity vector traces out an increasingly circular motion in the horizontal plane.

The main source of gravity waves in the mesosphere is the lower atmosphere. The greater density of the lower atmosphere means that the energy density of oscillations is greater than in the upper atmosphere and gravity waves are more readily propagated upwards than downwards. Sources are thought to range from storms and fronts to disturbances resulting from air flow over mountains ("orographic lee waves") for example figure 3.2 from [Gerbier and Berenger, 1961]. Note how the lines of constant phase tilt back against the flow so that perturbations due to the wave appear to be traveling downwards, whereas the energy is propagating upwards.

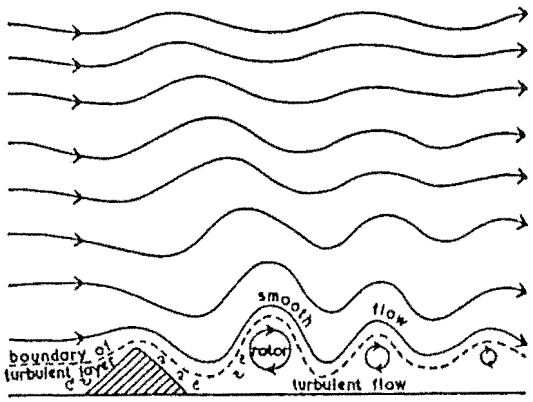

Figure 3.2: **Orographic lee waves** generated by uniform flow over mountains. Note how the phase fronts propagate against the flow. (From [Gerbier and Berenger, 1961]).

3.1.1 Gravity Wave Saturation

As gravity waves originating in the lower atmosphere propagate upwards their energy must be conserved as the atmospheric density ρ_o declines. The energy in the waves includes the terms $\rho_o\overline{u'^2}$ and $\rho_o\overline{v'^2}$; therefore if unchecked the rate of amplitude growth increases as $\frac{1}{\sqrt{\rho_o}}$ or $e^{\frac{z}{2H}}$, where H is scale height. (The momentum flux, $\overline{u'w'}$, would grow as $e^{\frac{z}{H}}$).

However observations have shown that gravity wave activity does not increase with altitude as rapidly as implied by the decline in density, (for example [Reid and Vincent, 1987b] and [Smith et al., 1987]). There appear to be damping processes or "saturation" mechanisms that limit the growth of gravity waves. An important class of these mechanisms are thought to be linear-instabilities whereby the waves "break" as their oscillations become so great that the atmosphere can longer support the motion, a process quantified by [Lindzen, 1981]. This process is often likened to the breaking of ocean waves on a sloping beach, [Andrews et al., 1987]. When the waves break, the energy that they carry is dissipated in effects such as turbulence [Fritts and Rastogi, 1985]. The contribution that gravity waves make to the dynamics of the mesosphere via saturation processes has been recognized as being very significant, for example [Fritts, 1989].

An important feature of gravity wave saturation is the interaction with the background wind. A simplified and idealised example of damping of a monochromatic wave is shown in figure 3.3 from [Fritts, 1984]. In this example, the horizontal perturbation velocity is indicated by the sinusoidal line (temperature perturbations could be similarly modelled),

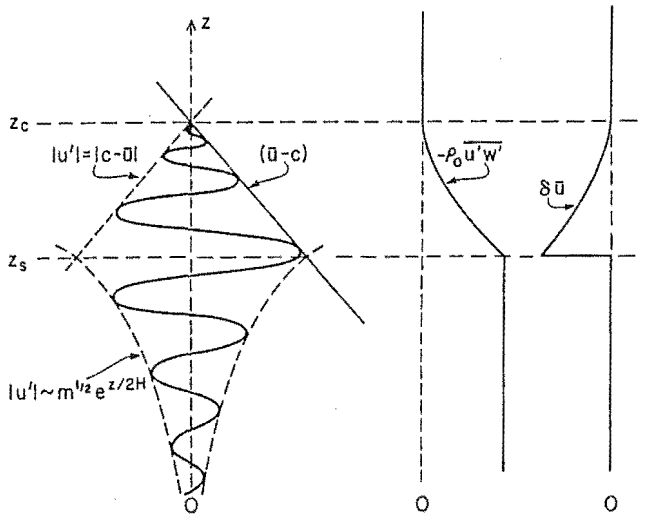

Figure 3.3: **A model of gravity wave saturation.** The wave grows exponentially in amplitude until the velocity perturbations, u′ match the phase velocity of the wave less the background wind $|c - \overline{u}|$ at the saturation level Z_s. The background wind is accelerated (indicated by $\delta\overline{u}$) towards c, until the critical layer is reached Z_c, where $\overline{u} = c$ and the wave is completely damped. The vertical flux of horizontal momentum is also plotted, $-\rho_o\overline{u'w'}$; notice here that it includes density, ρ_o. (After [Fritts, 1984].)

and the growth in amplitude due to declining density is indicated by the exponential line. When a region is entered where the overall velocity of a parcel of perturbed air, $\overline{u} + u'$, (background flow plus perturbation velocity), exceeds the phase velocity c of the wave, convective instability sets in, and the growth in amplitude of the wave is restricted such that $|u'| \leq |c - \overline{u}|$. An effect of this damping mechanism is that the background flow is accelerated (or decelerated depending on which is greater) towards the phase speed of the wave. In the example given here the accelerating flow increasingly restricts the wave amplitude until a level is reached, the "critical" level (z_c), where the wave is completely damped. The vertical flux of horizontal momentum falls off exponentially to zero as the wave is damped and the momentum carried by the wave is transferred into the background wind.

In reality, gravity wave saturation is more complicated. There tend to be multiple waves at different frequencies that can, for example, superimpose and lead to more or less damping than indicated by the simple monochromatic model, [Smith et al., 1987]. There are also other interactions such as "turning" in which a gravity wave can be refracted under certain conditions if it meets a velocity shear in the background wind. Gravity wave turning as well as saturation at critical levels act to filter out certain frequency

waves traveling through lower parts of the atmosphere so that they do not penetrate higher into the atmosphere.

Observations of gravity wave saturation in the upper mesosphere and lower thermosphere by various techniques have been summarized by [Reid, 1986]. Observations on MF radar include [Meek et al., 1985] who noted fewer gravity waves propagating with the background wind than against, suggesting background wind damping of the waves. [Reid and Vincent, 1987b] identified a number of individual wave events, determining the wavelength, phase velocity and momentum flux of the waves. Typical waves had horizontal wavelengths of several tens of kilometres, phase velocities of 20 - 40 ms^{-1} and momentum fluxes of around 1 m^2s^{-2}. They were able to detect damping and flow acceleration in some of the these wave events, although the damping was not as heavy as the simplified model above suggested because there appeared to be some superpositioning of the waves. Extensive measurements of momentum flux in the mesosphere by [Reid and Vincent, 1987a] showed more activity, in terms of a greater variation with altitude, at higher frequencies (periods less than an hour) than at frequencies closer to the inertial frequency. [Murphy, 1990] also reported greater momentum flux at these shorter periods than longer periods, although only in the zonal component, not the meridional. Typically the short period momentum flux was observed to peak at around 20 - 50 m^2s^{-2}. Murphy also reports a greater seasonal variation in shorter period measurements than in longer period. At polar latitudes, the intial study of [Fritts and Yuan, 1989] at Poker Flat observed highly variable short period momentum fluxes, peaking at up to 60 m^2s^{-2}, and concluded that gravity wave activity might be greater in polar regions than at lower latitudes.

The greater variability of short period momentum flux with, for example altitude, as compared with longer period momentum flux, indicates that higher frequency waves particularly are damped by saturation processes. However working in the troposphere and stratosphere on VHF radar, [Fukao et al., 1988b] observed the reverse, a domination of $\overline{u'w'}$ by longer period (greater than 6 hours) fluctuations, and concluded that some caution in interpreting momentum flux measurements is required. [Fukao et al., 1988b] noted that particularly for shorter periods, the averaging methods used can influence momentum flux estimates. They also found that momentum flux estimates can be unduly influenced by the considerable short period variability in vertical velocity measurements they observed which are not necessarily associated with gravity wave activity.

At mid-latitudes there generally appears to be a broad spectrum of gravity waves at any one time in the atmosphere although occasionally observations are dominated

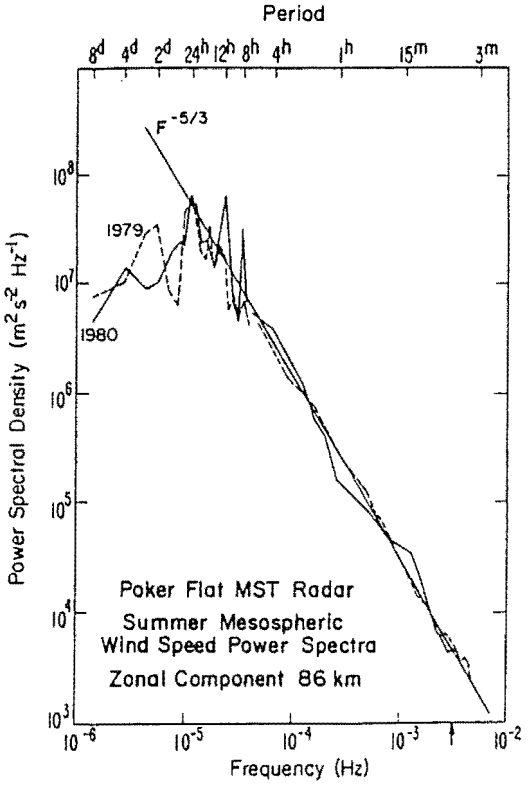

Figure 3.4: **Power spectrum of wind fluctuations** from [Carter and Balsley, 1982]. The measurements were made over two summers (1979 and 1980) on the Poker Flat VHF radar at an altitude of 86 km.

by quasi-monochromatic waves. The spectrum of wave activity is observed to fall off with increasing frequency due to the increased damping by saturation processes of higher frequency waves. The rate of fall-off has been estimated, [VanZandt, 1982], to be $\omega^{-\frac{5}{3}}$ and an example of such a fall off in a spectrum of wind measurement can be seen figure 3.4 from [Carter and Balsley, 1982]. Effects such as damping of activity at different frequencies in different parts of the atmosphere and Doppler shifting of the spectrum by the background wind can however lead to spectra that appear significantly different to this.

Non-linear wave-wave interaction theories offer alternative explanations to the above linear-instability theories for many aspects of gravity wave saturation (also discussed in the review by [Fritts, 1989]). An example of these theories is the recent contribution made by [Hines, 1990 a,b&c] with "Doppler-spread" theory.

3.1.2 Tides

Tides are global scale oscillations that are a special case of inertio gravity waves. The main driving mechanism of tides in the middle atmosphere is the daily solar heating of atmospheric water vapour and ozone to produce "thermal tides" (gravitational tides are by comparison very weak). Tides are then, "forced" waves; they are driven by a periodic excitation mechanism and thus oscillate at the frequency of the forcing mechanism and at harmonics of this frequency. The dominant tidal component in the mesosphere is the "semidiurnal" (12 hour) tide which has a vertical wavelength greater than 100 km. At middle and polar latitudes, the diurnal (24 hour) tide does not readily propagate vertically and so is generally more variable than the semidiurnal tide at mesospheric altitudes. Within about 30° latitude of the equator the diurnal propagates vertically with a vertical wavelength of around 30 km. The physical properties of tides are discussed further in texts such [Andrews et al., 1987].

Tides are very frequently observed in mesospheric radar measurements and summaries of observations made on MF radars have been reported by [Manson et al., 1989], [Fraser et al., 1989] and [Forbes, 1990] amongst others. The power spectrum of figure 3.4 displays tidal features at 8, 12 and 24 hour periods. Typically observations of the tidal variations in wind measurements show a twice daily (for the semidiurnal tide) downwardly propagating rotation in the velocity vector with an amplitude of around 10 - 20 ms^{-1}. The actual amplitude and timing of the rotation vary somewhat with season and latitude. In polar regions tides can be effected by geomagnetic disturbances. [Manson and Meek, 1991] found that on days of high particle precipitation the amplitude of tides are weakened by about 10%.

[Manson and Meek, 1991] also reported that radar backscatter was enhanced on days in which the amplitude of tidal oscillations was strong. Evidence of saturation of tidal gravity waves in observations of turbulence was found by [Fraser and Khan, 1990] and this will be discussed further in the next section.

3.2 Turbulence

The term turbulence in the middle atmosphere work is used describe irregular or random motions such as eddies. As well as physical motion, turbulence is associated with random fluctuations in density, temperature and importantly for radar probing, refractive index. The overall mean of turbulent motion is zero, although if there is a background wind turbulence will be blown along with this wind. The term is generally used fairly loosely

and can change meaning in different circumstances or as the understanding of different phenomena in the atmosphere develops.

Turbulence appears to be somewhat variable in extent and intensity in the mesosphere and lower thermosphere. In the thermosphere there is a cut-off region called the "turbopause", above which kinematic viscosity greatly increases strongly damping any turbulent activity. The height of the turbopause is generally around 110 - 120 km, above the region of interest in this study, although sometimes it can extend down as low as 95 km. Much turbulence in the middle atmosphere appears to particularly associated with the breakdown of gravity waves via the saturation mechanisms mentioned in the last section, [Fritts and Rastogi, 1985].

An important property that separates turbulence from wave type oscillations in the atmosphere is their energy "cascade" from large eddies to small eddies, while non-breaking waves do not show any such energy transfer to smaller scales. The swirling motion in large eddies generates smaller eddies, which in turn generate even smaller eddies. As the eddies get smaller, the velocity shears across the eddies increase and eventually the viscosity of the atmosphere leads to them becoming damped out and their energy goes into heating of the atmosphere.

Even though turbulence is not a wave phenomenon, scales of turbulence are sometimes described in term of "wavelength" λ, (or "wavenumber" $k = \frac{2\pi}{\lambda}$), such a description being useful when describing variations in turbulence scales. Assigning wavenumbers to turbulence scales can be considered as a Fourier decomposition of a noise spectrum rather specifically identifying oscillations in turbulence.

The "spectrum" of turbulence scales in the middle atmosphere has three distinct regions, figure 3.5. The region of largest scales is the "buoyancy subrange". Here turbulence is affected by the buoyancy and the stratification of the atmosphere which tends to lead to eddies that are elongated and anisotropic (the horizontal scales being larger than the vertical scales). The buoyancy subrange is the region where turbulence is generated. The upper limit to the buoyancy subrange is the "buoyancy scale", L_B, which is related to the Brunt-Väisälä frequency, the natural frequency of buoyancy oscillations mentioned in relation to gravity waves in section 3.1. The region of smallest scales is the "viscous subrange", being comprised of eddies which viscous effects break down leading to heating of the atmosphere.

The region in between the buoyancy range and the viscous range is the "inertial subrange". The limits to the inertial subrange, η and L_B, are sometimes referred to as the inner and outer scales to the inertial range. In the mesosphere the inner and outer scales

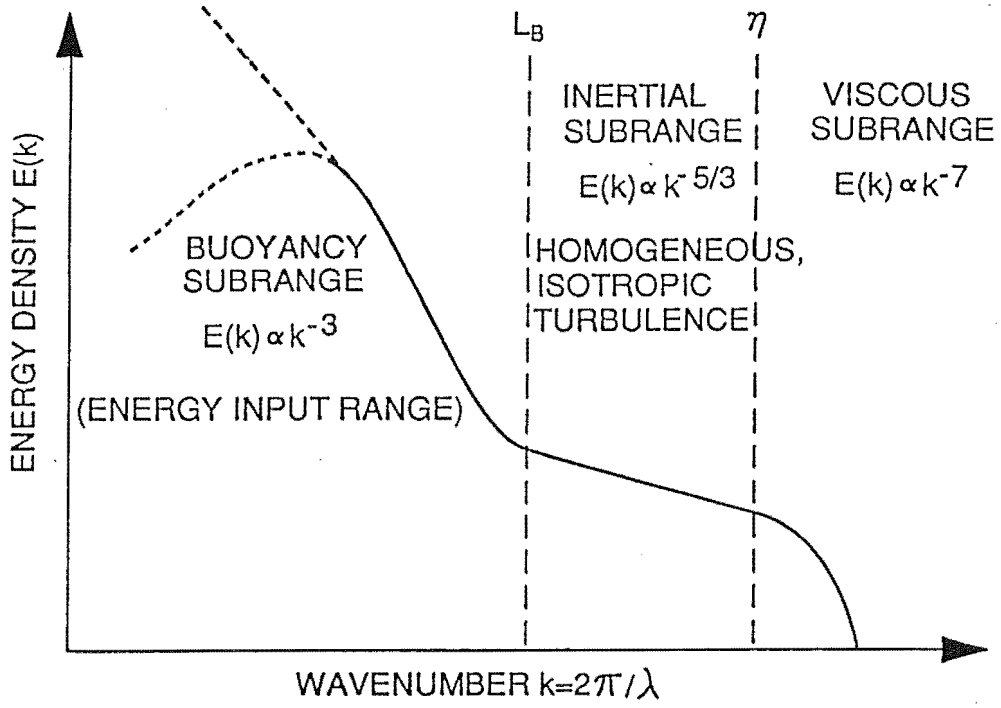

Figure 3.5: **The turbulence spectrum,** indicating the three important ranges of activity. (Adapted from [Murphy, 1990] who attributes the figure to an unpublished report by [Blix, 1988].)

are typically a few tens of metres and several hundreds of metres (up to about two kilometres) respectively, [Hocking, 1985]. As indicated in figure 3.5 eddies in this region are thought to be relatively homogeneous and isotropic. The energy associated with eddies in this range falls off with increasing wavenumber as $k^{-\frac{5}{3}}$, a relationship known as the Kolmogoroff law, [Houghton, 1977].

This region includes eddies that are most easily detected by radars that study the middle atmosphere, that is eddies that have a scales about half the wavelength of typical radars, and so has been the most intensively studied by these radars.

A commonly used measure of inertial range turbulence is the "turbulent energy dissipation rate" or "eddy dissipation rate", ϵ, which provides some measure of the intensity of turbulence although as the name suggests is more properly a measure of the rate energy deposition into the atmosphere. ϵ can be broadly related to the velocity fluctuations of the turbulence using

$$\epsilon \sim \frac{v_{\text{rms}}^3}{\ell} \tag{3.5}$$

(where v_{rms} is the magnitude of the r.m.s. velocity fluctuations and ℓ indicates the scale

of the turbulence) or

$$\epsilon \sim \frac{v_{\text{rms}}^2}{\tau} \tag{3.6}$$

(where τ indicates the "life time" of an eddy).

[Hocking, 1987c] summarizes inertial range turbulence measurements in the upper mesosphere and lower thermosphere made by various methods such as radars and by rocket probes. Hocking reports a mean eddy dissipation rate of the order of 10^{-1} W/kg although individual measurements can range from about 10^{-3} W/kg up to about 1 W/kg.

Observations of turbulence on the radars used by this project were reported by [Khan, 1988] and [Fraser and Khan, 1990]. The Full Correlation Analysis time scale parameter $T_{\frac{1}{2}}$ was used. This parameter provides some measure of stability (or the inverse of turbulence) in the scattering region although as discussed in the next section must be used with some caution, particularly since these studies used the radars in incoherent mode. A strong tidal variation was found by these workers at Scott Base with a decrease in $T_{\frac{1}{2}}$ (implying an increase in turbulence) when the westward wind component of the semidiurnal tide is at its maximum and an increase in $T_{\frac{1}{2}}$ (decrease in turbulence) with maximum eastward wind component. [Fraser and Khan, 1990] suggest that the semidiurnal tide, which is propagating westward, could be saturating and thus generating turbulence when its velocity perturbations are also westward along similar lines to the saturation model of [Fritts, 1984] mentioned in the previous section.

3.2.1 Measuring the Intensity of Turbulence on Radar

The eddy dissipation rate can be estimated from radar observations by using either the backscattered signal strength or the variations in Doppler shift of the backscattered signal, [Hocking, 1985, Hocking, 1989]. A radar is most sensitive to turbulence scales around half the wavelength of the radar, that is the "Bragg scale" of the radar, so measurements of turbulence by radar are biased towards the Bragg scale.

The signal strength approach relates ϵ to C_n^2, a measure of the intensity of refractive index variations due to the turbulence, which in turn can be related to backscattered signal power. As mentioned in section 1.2.1, relating scattered signal power to fluctuations in refractive index and intensity of turbulence is a complicated excerise. One difficulty is the uncertainty as to how much of the radar volume is filled with turbulence during sampling, a particular problem with broad beam radars such as those used in this project. Another is the effect of specularly reflecting sheets that often form in the mesosphere which have very high reflectivity not necessarily directly to turbulence. Also extra caution needs to be exercised in this approach when using MF radars above about 100 km altitude since MF

scattering can also be due the value of the absolute refractive index as well as variations in refractive index (see section 1.2.1).

The Doppler approach to measuring ϵ relates the distribution of observed Doppler shifts of the backscattered signals to the fluctuating velocity in the turbulence. The spread in the distribution of Doppler shifts due to the velocity fluctuations, f_{fluct}, is related to the magnitude of the r.m.s. velocity fluctuations by

$$\overline{v_{\text{rms}}^2} = \left(\frac{\lambda}{2}\right)^2 \frac{f_{fluct}^2}{2\ln 2}, \tag{3.7}$$

(λ being the wavelength of the radar). For a broad beam radar, all scales of inertial turbulence are observed in the radar volume. As indicated by equation 3.5, the largest scales have the greatest velocity fluctuations associated with them. Smaller scale eddies tend to get carried around by larger eddies, so although the radar is preferentially tracing Bragg scale features, the velocity fluctuations observed are more closely related to the fluctuations of the largest eddies. The eddy dissipation rate ϵ can be related to the r.m.s. velocity fluctuations via equation 3.5. The approximation is often made that the buoyancy scale L_B is the largest scale of turbulence, which is more reasonable on narrow beam radars where the main velocity fluctuations contributing to spectral spread are in the vertical. Using L_B as ℓ in equation 3.5, [Hocking, 1983b] found from considerations of the spectrum of fluctuations a constant of proportionality, 3.5, giving

$$\epsilon \approx 3.5 \frac{\overline{v_{\text{rms}}}^3}{L_B}. \tag{3.8}$$

f_{fluct} can be estimated using the spectral width of the Doppler spectrum of the backscattered signals. [Hocking, 1983b] pointed out a number of problems associated with using spectral width, illustrated in figure 3.6, such as variations in the line of sight component of the background wind in the radar volume. Another problem Hocking pointed out is variations in the wind over the sampling time, or through the radar volume, due to effects such as gravity waves, although if the sampling time is of the order of a minute or less, then to some extent the variations due to gravity wave activity should be minimized, [Hocking, 1985]. The spectral broadening problems of figure 3.6 can be particularly severe for broad beam radars such as the radars used in this project.

If there are specularly reflecting layers in the radar volume, the Doppler spectrum can contain large spikes (section 1.3.3) that should be removed. If the wind and wind shear can be measured, the magnitude of the beam broadening and shear broadening effects can be estimated and removed before determining f_{fluct}. If f_{ob} is the observed spectral width and f_b is the frequency variance due to broadening then to a reasonable approximation,

$$f_{ob}^2 \simeq f_b^2 + f_{fluct}^2. \tag{3.9}$$

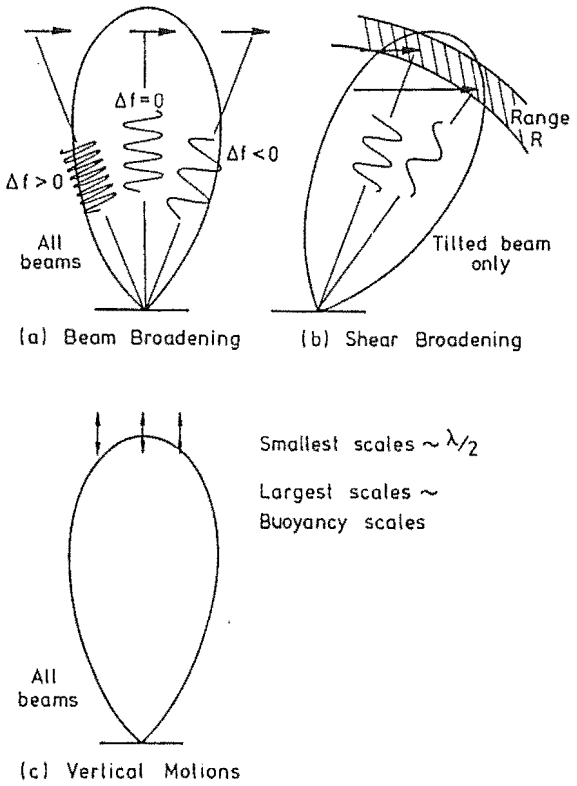

Figure 3.6: **Spectral broadening effects** from [Hocking, 1983b]. **(a) Beam broadening** where a constant wind has varying line of sight components to its velocity in different parts of the radar beam, **(b) shear broadening** where there is a wind shear across the radar volume (the beam is tilted here because [Hocking, 1983b] was illustrating these effects on Doppler beam swinging radar, but they apply equally well to broad beam spaced antennae radar) and **(c) vertical motions** due to gravity waves or turbulence.

On spaced antennae radars it is possible to determine Full Correlation Analysis parameters, ([Briggs, 1984], see section 6.2), that provide possible alternatives to using the width of the Doppler spectrum for finding the distribution of fluctuations due to turbulence. For example the time parameter $T_{\frac{1}{2}}$ (as used by [Khan, 1988] and [Fraser and Khan, 1990] above) which is a measure of the time scale of changes in the backscattered signal, with the effect of advection by the background wind removed (that is the beam broadening effect of figure 3.6(a) removed). Also there is the closely related "random velocity" parameter $(V_c)_v$ which provides some measure of the rate of random change in the scattering region. [Hocking, 1983b] concluded that both of these parameters do give some measure of the fluctuations due to turbulence although on broad beam radar they are susceptible to variations in wind across the radar volume and so provide more of an upper limit to

turbulence rather than an accurate measure of the turbulence itself.

[Hocking, 1989] shows how an estimate of ϵ can be made from $T_{\frac{1}{2}}$, first by assuming that the Doppler spectrum due to turbulent fluctuations is approximately Gaussian in which case the auto-correlation function is also approximately Gaussian (being the Fourier transform pair of the spectrum) so the half power half width of the spectrum can be estimated by

$$f_{\frac{1}{2}} = \frac{0.22}{T_{\frac{1}{2}}}. \tag{3.10}$$

$f_{\frac{1}{2}}$ can be used as f_{fluct} in equation 3.7 to get $v_{\rm rms}$ and thus determine the eddy dissipation rate via equation 3.8.

3.3 Scattering Scales : Aspect Sensitivity

Radar observations of the middle atmosphere often show marked anisotropy, with signals being more strongly scattered from near the zenith than away from zenith. Inertial turbulence is assumed to be isotropic, having very similar scales in all three dimensions. As turbulent scales increase into the buoyancy subrange, the turbulent structures become increasingly anisotropic, flattening out in the horizontal plane as compared with the vertical. The ratio of the horizontal scale to the vertical scale, or the "aspect ratio" of the structures is sometimes used as to parameterize anisotropy. Generally however, the "aspect sensitivity" of the backscatter is found. Aspect sensitivity can be expressed in the form of a function describing the variation of scattered power with zenith angle. More usually the angular quantity, θ_s is found which models the variation of power with zenith angle, θ, according to

$$e^{-\frac{\sin^2\theta}{\sin^2\theta_s}}, \tag{3.11}$$

so that θ_s is the half width at e^{-1} power of the backscatter polar diagram. If the scattering structures are approximated to be of some sort of ellipsoidal shape, then the aspect ratio can be estimated from aspect sensitivity measurements using functions such as those illustrated in figure 3.7, [Hocking, 1987a].

In the extreme, anisotropic structures seem to form flat sheets of turbulence perhaps several kilometres across and one or two kilometres deep, although sometimes sheets as thin as a hundred metres or so become apparent. These sheets of intense turbulence have been put forward as the basis for strong specular reflections frequently observed in the mesosphere by MF and VHF radar, [Bolgiano, 1968]. Wind shears forming intense turbulence such as Kelvin-Helmholtz instabilities may be the source of some of these extended sheets of turbulence. [Reid, 1990] summarizes radar observations of specularly

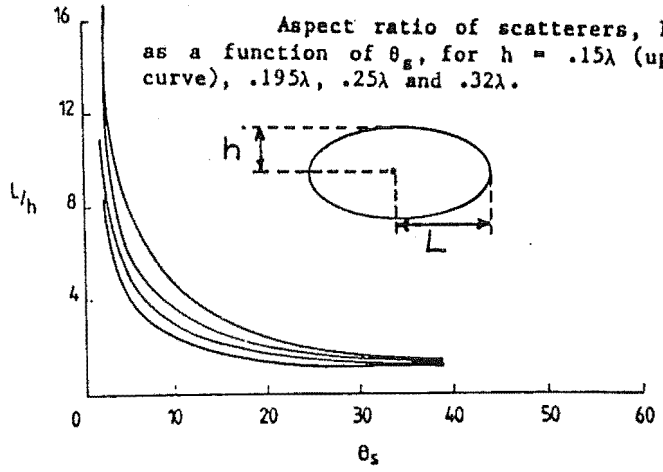

Figure 3.7: **Aspect ratio,** $\frac{L}{h}$, as a function of aspect sensitivity θ_s for various depths, $h = .15\lambda$ (upper curve), $.195\lambda, .25\lambda$ and $.32\lambda$. (After [Hocking, 1989].)

reflecting sheets (or "stratified layers"), concluding that many, although not necessarily all, such layers appear to be the result of gravity wave breakdown into turbulence.

An example of strong anisotropic scatter that has received recent attention is the so-called "Polar Mesopause Summer Echo" (PMSE). PMSE shows up clearly on VHF radar as intense scattering with narrow aspect sensitivity, [Czechowsky et al., 1988], indicating some sort of layered structure, particularly, as the name suggests, in the polar regions during the summer near the altitude of the mesopause (80-90 km). There is also some suggestion of PMSE characteristics in MF radar observations, [Fraser and Khan, 1990].

Scattering or specular reflections from flat sheet structures could be expected to lead to very narrow aspect sensitivity measurements. However if such sheets have undulations in their surfaces, which could be caused by the passage of a gravity wave for example, or the presence of Kelvin-Helmholtz instabilities, then the apparent aspect sensitivity would widen and could lead to a much lower aspect ratio estimate than the sheet structure implies.

In general observations of aspect sensitivity widen with altitude, going from less than about 5°-10° (depending on the measuring technique) below 80 km to 5°-15° around 90 - 100 km, [Reid, 1990], although features such as PMSE are exceptions to this trend. For example [Lesicar et al., 1991] compiled climatologies of aspect sensitivity observations on

MF radars at three sites at low, middle and high latitudes. Using fading time measurements (discussed below) they report that the mean (apparently averaged over day time scales) aspect sensitivity increases by a few degrees going from 80 km to 100 km and varies from season to season by a degree or two. [Lesicar and Hocking, 1992] continued this study using the University of Adelaide MF Buckland Park radar, reporting that at this site scattering from the mesosphere is narrower in winter than in summer. They also used aspect sensitivity measurements to determine aspect ratios.

3.3.1 Measuring Scattering Scales and Aspect Sensitivity

Measures of the horizontal scale of the scattering structures can also be obtained via Full Correlation Analysis (FCA), ([Briggs, 1984] and section 6.2). FCA determines spatial scale factors such as the spatial analogue of $T_{\frac{1}{2}}$, $d_{\frac{1}{2}}$, a measure of the average scale of the diffraction pattern with advection effects removed. Also the spatial correlation ellipse is determined, usually parameterized in terms of the ratio of the major to minor axes, the length of the minor axis and the orientation of the major axis.

Frequency Domain Interferometry provides a measure of scattering depth, which estimates the spread in range of scattered signals as discussed in section 5.3.3. This measure is related to aspect sensitivity especially for layers confined to a particular altitude because the wider the angular distribution of scattering, the greater the scattering contribution away from zenith and thus the greater the apparent scattering depth.

The spatial correlation function is the Fourier transform of the polar diagram of the backscatter. [Briggs and Phillips, 1950] and [Ratcliffe, 1956], and early measures of the angular distribution or "angular spread" (the r.m.s. angular half width of the power distribution) used relationships of this form, although in general these require high levels of correlation across the observing spaced antennae. [Bramley, 1951] provided estimates of the angular spread of random backscatter using the distribution of measured phase differences between spaced antennae, such as

$$\theta_{sp} = \left(\frac{\lambda}{2\pi d}\right) \langle|\phi|\rangle, \tag{3.12}$$

(where θ_{sp} is the angular spread, λ is the radar wavelength and $\langle|\phi|\rangle$ the mean absolute phase difference between the antennae separated by distance d). [Lindner, 1975b], using the techniques of Bramley, reported observations of θ_{sp} made on the University of Adelaide MF radar in which typically θ_{sp} was less than 5° below 80 km, increasing to around 10° between 90-100 km altitude. If the mean absolute phase difference is less than about 0.75 radians, [Lindner, 1975a] notes that $\langle|\phi|\rangle$ should be replaced by $\sqrt{-\ln(\cos\langle|\phi|\rangle)}$.

Angular spread, θ_{sp}, describes the variation of power with zenith angle θ according to $e^{-\frac{1}{2}(\frac{\theta}{\theta_{sp}})^2}$, and aspect sensitivity, θ_s, was defined above by equation 3.11. The two measures can, therefore, be compared using the approximation $\theta_s \approx \sqrt{2}\theta_{sp}$.

It should be noted that the observed backscatter polar diagram and the observed spatial correlation function are actually due to the combined polar diagrams of the backscatter and the radar antenna polar diagram. [Briggs and Vincent, 1973] considered this while examining spatial correlation functions of scattering from thin layers and [Briggs, 1992] reported the useful simple approximation derived from their considerations,

$$\varepsilon_{0.5} \approx \frac{15.2}{\theta_{sb}}, \tag{3.13}$$

relating the spatial lag, $\varepsilon_{0.5}$ (measured in units of radar wavelength) at which the spatial correlation function falls to 0.5 to the combined backscatter aspect sensitivity and radar beam width θ_{sb} measured in degrees. (Note that this relationship has been previously incorrectly reported as being $\varepsilon_{0.5} \approx \frac{12.0}{\theta_{sb}}$, [Hocking et al., 1989]). If θ_o is the e^{-1} beam width of the radar antennae, then θ_{sb} is given by

$$\sin^{-2}\theta_{sb} = \sin^{-2}\theta_o + \sin^{-2}\theta_s. \tag{3.14}$$

The FCA parameter $d_{\frac{1}{2}}$ could be used as $\varepsilon_{0.5}$ in equation 3.13 to estimate θ_s, although on broad beam radars, as with the use of $T_{\frac{1}{2}}$ in eddy dissipation estimates, would only place a limit on θ_s because $d_{\frac{1}{2}}$ can be influenced by variations in horizontal velocity.

On a wide beam radar, another estimate of aspect sensitivity can be made by assuming that most of the width of the observed Doppler spectrum of the scattered signals is due to beam broadening, f_b, (figure 3.6), [Woodman and Chu, 1989, Hocking, 1989] and that f_{fluct} of equation 3.9 is negligible in comparison. If the horizontal velocity of the scatterers is known, say V_{hor}, then the beam broadening effect is responsible for a Doppler spectral width of

$$f_b \approx \frac{2|V_{hor}|\theta_{sb}}{\lambda}. \tag{3.15}$$

f_b is approximated by f_{ob}, the observed spectral width, and an estimate of θ_{sb} is found which can then be used, with knowledge of the radar's polar diagram, to estimate θ_s via equation 3.14. [Woodman and Chu, 1989] used an approach based on this method to obtain an aspect sensitivity function, that is the variation in power with zenith angle, rather than θ_s itself.

The beam broadening method can used if the spectral width is not directly available by using the fading time τ_{fad} which is the time for the autocorrelation function to fall to 0.5, (section 4.1.1). τ_{fad} unlike $T_{\frac{1}{2}}$ above, is not corrected for advection by wind. A half

power spectral width, $f_{\frac{1}{2}b}$ is approximated by $0.22/\tau_{fad}$ (assuming a Gaussian spectrum as in equation 3.10). $f_{\frac{1}{2}b}$ is used in equation 3.15 to find $\theta_{\frac{1}{2}b}$ which is then substituted in equation 3.14 (after division by $\sqrt{\ln 2}$ to convert from $\frac{1}{2}$ width to e^{-1} width) to approximate θ_s. This was the technique used by [Lesicar et al., 1991], whose observations were reported above. In [Lesicar and Hocking, 1992] this technique was compared with the spatial correlation method (equation 3.13). It was found that the results of both techniques followed similar trends although the beam broadening aspect sensitivity was generally a few degrees wider than that determined by the spatial correlation method.

The assumption that beam broadening is responsible for all of the spectral width and that fluctuations due to turbulence are insignificant could be modified by using the FCA parameter $T_{\frac{1}{2}}$ to approximate f_{fluct} as was done when estimating the eddy dissipation rate from $T_{\frac{1}{2}}$ in the previous section. τ_{fad} would be converted to f_{ob} and with f_{fluct} could be used in equation 3.9 to give f_b the beam broadening effect. Such a correction does not appear to have been reported in the literature.

On Doppler beam swinging radar, which normally can only point at zenith and at fixed angles away from zenith, aspect sensitivity is estimated by comparing the power received on the vertical and off-vertical beams, (for example [Tsuda et al., 1986] and [Hocking, 1987a]). [Tsuda et al., 1986] noted that as zenith angle increased, scattering appeared to change from specular like reflections to more isotropic random backscatter, indicating the coexistence of different scattering structures. A similar method is that of [Vincent and Belrose, 1978] who compared signals received on antennae with vertical beams of different widths to obtain angular distribution measurements.

Spatial interferometry which gives directional information about backscattered signals (sections 5.2 and 5.4) allows a more direct measurement of aspect sensitivity, for example [Adams et al., 1989]. A number of scattering targets are resolved within the radar volume and the power received from each target can be plotted directly with the zenith angle of that target to indicate aspect sensitivity. Corrections must be made for the gain of the radar as a function of zenith angle.

A related technique to spatial interferometry is the "postbeam" steering technique where the radar is artificially pointed in various directions during data analysis by introducing phase lags to data received on separated antennae (section 5.6). For aspect sensitivity measurements, the variation in power as the beam is pointed away from zenith is found, [Kudeki et al., 1990].

It is important to note that all of these techniques on wide beam radar will only place an upper limit on aspect sensitivity because as with measurements of turbulence intensity

discussed in the last section, effects such as horizontal variations in the wind field through the radar volume can greatly influence the observed polar diagram.

Very recently [Briggs, 1992] reported a new technique which uses the spatial correlation function in two dimensions. The method can under conditions of constant velocity, circular spatial correlations and small random changes, give aspect sensitivity to very fine resolution by an approach similar to aperture synthesis techniques in radioastronomy. An example given by Briggs shows with a wind velocity of 25 ms^{-1} under these constant conditions for 10 minutes, a 2 MHz radar could acheive an aspect sensitivity function of about $\frac{1}{4}^{\circ}$ resolution. Briggs also reports on a technique using aspect sensitivity measurements made on a spaced antennae radar to estimate the effective pointing angle of an off-vertical beam of a collocated Doppler beam swinging radar.

3.4 Signal Distributions

Statistical distributions of scattered signals are frequently used as a convenient method of parameterizing the short time scale fluctuations (or fading) that characterize middle atmosphere radar returns. This parameterization can provide useful indicators on the type of scattering process producing the fading.

Random or isotropic scatter frequently associated with turbulence can be modelled as a Rayleigh process, [Rayleigh, 1894]. The turbulence is assumed to consist of many similar scatterers each adding to a randomly varying backscattered signal (after removing the carrier wave) :

$$E_r = \sum A_r e^{i\phi_r} = \sum (X_r + iY_r), \tag{3.16}$$

where the phase ϕ_r is uniformly distributed over 2π and the in-phase and quadrature components (X_r, Y_r) each have similar distributions approaching a Gaussian distribution, [Ratcliffe, 1956]. The Rayleigh distribution is a subset of the Rice distribution, [Rice, 1944, Rice, 1945], in which a coherent signal (eg: specular reflector) is added to the random signals above and $\overline{X_r} = \overline{Y_r} = 0$. The probability distribution of A_r for random scatter can be modelled by a Rayleigh distribution,

$$P(A_r) = \frac{A_r}{\sigma_r} e^{\frac{-A_r^2}{2\sigma_r^2}} \tag{3.17}$$

where σ_r^2 is the variance of A_r.

If a coherent component of amplitude A_c is added to the randomly scattered signals, then the probability distribution can be modeled by a Rice distribution,

$$P_A = \frac{A_r}{\sigma^2} e^{\frac{-(A_r^2 + A_c^2)}{2\sigma^2}} I_o\left(\frac{A_r A_c}{\sigma^2}\right), \tag{3.18}$$

where I_o is the zeroth order modified Bessel function.

The ratio $\alpha = \frac{A_c}{\sigma}$ is the "Rice parameter" and is a measure of the comparative strength of the coherent component to the random component. The Rice parameter for a Rayleigh distribution is zero.

The Rice parameter can be determined by matching the population distribution of the scattered signals to the form given by equation 3.18. Alternatively it can estimated from the ratio of the mean signal amplitude $\overline{A}$ to the standard deviation of the standard deviation of the in-phase and quadrature channels, σ_{XY}, [Rastogi and Holt, 1981], [Hocking, 1987b]. The relationship between this ratio and the Rice parameter is illustrated in figure 3.8 from Hocking, a relationship involving the gamma and confluent hypergeometric functions. For a random signal, the ratio is approximately 2 (actually 1.913), and it increases as the coherent component becomes stronger.

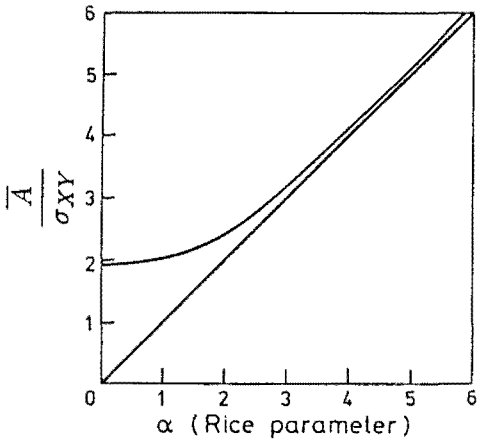

Figure 3.8: **Determining the Rice parameter** from $\frac{\overline{A}}{\sigma_{XY}}$. From [Hocking, 1987b].

The Rice distribution itself is a subset of the Nakagami m distribution, [Nakagami, 1960], which is defined by (for example [Kuo et al., 1987])

$$P(A) = \frac{2m^m A^{2m-1}}{\Gamma(m)\langle A^2\rangle^m} e^{-\frac{m}{\langle A^2\rangle}A^2}. \tag{3.19}$$

Γ is the gamma function and m is the Nakagami parameter,

$$m = \frac{\langle A^2\rangle}{\langle (A^2 - \langle A^2\rangle)^2\rangle}. \tag{3.20}$$

The Nakagami distribution is Rayleigh for $m = 1$, and Rician for $m > 1$.

3.4.1 Applying Signal Distributions

In principle, the longer the data set the more accurate the statistics determined above become as more fading cycles are observed, provided the characteristics of the random and any specular components do not vary during the recording time. The larger the number of independent samples (or fading cycles here) the more accurate the sample statistics become, provided the series is stationary.

Any gradual variation over time (or non-stationarity) of the component strengths distorts the distributions. MF radar returns frequently do display non-stationarity over time scales many times that of fading, typically in the form of bursts of enhanced power over several minutes. This non-stationarity of long data sets of MF radar returns needs to be considered in forming distribution functions.

[Hocking, 1987b] tested the effect of varying data lengths on the determination of Rice parameters. He generated Rice distributed data sets at various parameters and formed subsets of data of varying lengths. The subsets were then analysed to find resulting Rice parameters. These derived Rice parameters were found to be frequently in error, even when the simulations were extended to longer data lengths.

However when a distribution of the derived Rice parameters from a series of simulated data sets were grouped together, then these distributions of parameters correlated well with the original parameters. Even though individual distribution parameters from short data sets may be in error, averages of the parameters from short data lengths were found be accurate. Using a series of short data sets in this manner would filter out any non-stationarity and still reliably characterize the data. Hocking suggests that the optimum data length to use is one or two minutes provided the fading time is not too long. Approximately 20 times the fading time (typically 2-3 seconds) seems to be about the minimum length.

[Hocking, 1987b] tested this procedure on one minute data sets collected on the Buckland Park MF radar and another MF radar at Townsville. He compared the distributions of Rice parameters of suspected random and specular echoes (determined by beam width experiments, echo intensity and fading times) and found that data he associated with specular echoes were indeed biased towards higher Rice numbers.

Hocking found that scattering from low heights (less than 80km) appeared to have more non-Rician characteristics, such as the ratio $\frac{\overline{A}}{\sigma_{XY}}$ being significantly less than 2. Similarly [Sheen et al., 1985] found the Nakagami m parameter frequently was around 0.5 (for Rician distributions m is greater than 1), particularly when the Doppler spectrum of the signals showed large spikes suggesting specular reflections. [Sheen et al., 1985] suggests

this is due to scattering from focussed and de-focussed curved specularly reflecting layers or from multiple specularly reflecting layers.

[Kuo et al., 1987] examined the validity of using Rician and Nakagami type distributions. For such distributions the in-phase and quadrature components of the scattering should follow Gaussian statistics. They tested this by checking the third and fourth moments, the skewness and kurtosis[1], of the distributions of signals on the in-phase and quadrature channels, which for Gaussian distributions should be near zero and three respectively. They found a consistent relationship between the Nakagami m parameter and kurtosis; when m was less than one, the kurtosis increased significantly beyond three. (Such a value indicates that the distribution of the in-phase and quadrature signals has a sharper peak than a Gaussian distribution.) [Kuo et al., 1987] produced a scattering model to explain this behaviour in which the aspect sensitivity, range and the strength of the scattering was highly variable. They concluded that multiple specular reflecting layers within a radar volume could generate the statistics observed.

[1] If $\overline{x}$ is the mean or first moment of a series $\{x_1, \ldots, x_N\}$, and σ^2 is the variance or second moment, then the skewness, the third moment of the series, is defined by $\frac{1}{N}\sum(\frac{x-\overline{x}}{\sigma})^3$ and the kurtosis, the fourth moment, by $\frac{1}{N}\sum(\frac{x-\overline{x}}{\sigma})^4$, (for example [Brooks and Carruthers, 1953] or [Press et al., 1986]). Skewness measures the asymmetry of the distribution and kurtosis the flatness of the distribution with respect to a Gaussian distribution.

Chapter 4

Time Series Analysis

This chapter describes the two classes of time series analysis techniques used in this work, these being sample correlation functions and spectral analysis. There is considerable cross-over between these broad areas of time series analysis; indeed correlation functions and power spectra are fundamentally linked via the Wiener-Khintchine theorem.

Correlation analysis has a long history in the analysis of backscattered signals on radars of the sort used in this study, particularly in techniques such as full correlation analysis. Section 4.1 briefly backgrounds correlation functions and introduces the forms of these functions used in this project. Statistical uncertainties arising from sample correlation functions, in regard to both full correlation analysis and interferometry are also discussed.

The spectral analysis techniques used in this project are discussed in section 4.2. Spectral techniques have been less widely used and are less standardized in the analysis of backscattered signals observed on radars of the sort used in this study than are correlation analysis techniques, (although they are widely applied to Doppler beam swinging radars). This study attempts to extract greater detail about the behaviour and form of spectra than it does in regard to correlation functions. Therefore extended consideration will be given here to various aspects of spectral techniques, particularly as applied to the analysis of raw backscattered data.

4.1 Correlation Functions

Much data analysis in this work is based on examination of both the auto covariance (covariance of a time series with itself) and the cross covariance (covariance of two time series) of data shifted by a range of time offsets (or "lags"). The covariance estimates are normalized by the unshifted (or "zero time lag") covariance estimates to form correlation

functions.

Analysis of correlation functions can be used to provide measures of "signal to noise ratios" and temporal consistency or "fading time" as well as radial velocity. Correlation functions can also be used to measure phase parameters used in interferometry for determining direction of arrival and range. As discussed in chapter 5 directions of arrival can be found by measuring the phase differences between separated receivers and ranging can be inferred from the rate of change of phase with change in frequency.

Correlation functions are also used in the Full Correlation Analysis (FCA) procedure which determines horizontal winds (or "drifts"). FCA is discussed separately in section 6.2, although there is some cross-over between this section and that on FCA.

The complex correlation functions used in this work (both here and in FCA) are based on a general form (for example [Ratcliffe, 1956]) extended to include shifts in frequency.

$$\rho(\delta t, \delta\epsilon, \delta f) = \frac{\langle E(t,\epsilon,f)E^*(t+\delta t, \epsilon+\delta\epsilon, f+\delta f)\rangle}{\sqrt{\langle E(t,\epsilon,f)E^*(t,\epsilon,f)\rangle\langle E(t,\epsilon+\delta\epsilon,f+\delta f)E^*(t,\epsilon+\delta\epsilon,f+\delta f)\rangle}} \tag{4.1}$$

where $E(t,\epsilon,f)$ is the complex, zero mean [1], scattered signal received at time t, the vector receiver location ϵ (with eastward and northward components), and radar frequency f. $E(t+\delta t, \epsilon+\delta\epsilon, f+\delta f)$ is the signal received at lagged offsets in time, location, and frequency. $\langle\rangle$ denotes time averaging and * complex conjugate.

The averaging generally used here for, say, the l^{th} time lag, (that is $\delta t = l\tau$, τ being the time between samples in the series being analysed) followed the form

$$\langle E(t,\epsilon,f)E^*(t+l\tau,\epsilon+\delta\epsilon,f+\delta f)\rangle = \frac{1}{N-l}\sum_{i=1}^{N-l} z(t_i,\epsilon,f)z^*(t_i+l\tau,\epsilon+\delta\epsilon,f+\delta f), \tag{4.2}$$

(for series $\{z(t_1),\ldots,z(t_N)\}$.)

The amplitude of the complex correlation function describes the average conformity between the data series at a range of temporal, spatial and frequency offset lags. For example a slowly varying diffraction profile drifting past two receivers (separated by $\delta\epsilon$) would produce a cross correlation function with a peak at some value of lagged time that can be related to the time taken for the diffraction profile to drift past [Briggs et al., 1950].

Similarly, the argument of the complex correlation function describes the average phase conformity between two series as a function of the offset lags. The argument provides a direct measure of phase difference between the two series and how the phase of the series varies with time lags.

Typically the correlation functions found here are formed with fixed spatial ($\delta\epsilon$) and frequency (δf) lags, and range over a series of time (δt) lags. Generally only three receiver

[1] E is assumed to have zero mean for all of this chapter

locations and five radar frequencies were used resulting in three spatial and ten frequency non-zero lags available for cross correlation.

The correlation functions used are termed here the "auto correlation", the "cross receiver correlation" and the "frequency correlation" functions.

4.1.1 Auto Correlation

The auto correlation function describes the correlation of a data series to itself over a range of time lags. The auto correlation function is based on the form

$$\rho(\delta t) = \frac{\langle E(t)E^*(t+\delta t)\rangle}{\langle E(t)E^*(t)\rangle}, \tag{4.3}$$

(receiver location and radar frequency being held constant, $\delta\epsilon = \mathbf{0}$ and $\delta f = 0$).

High frequency random noise components in the data series appear uncorrelated at successive points in the series contributing to a much higher covariance estimate at zero time lag ($\delta t = 0$) than would otherwise be the case. When the correlation function is found for non-zero time lags, the function displays a spike at zero lag. A curve (usually parabolic was used here) is fitted to, typically, one second of time lags either side of, but not including, zero lag. The ratio of the interpolated value at zero lag to the spike less the interpolated value provides an estimate of the "signal to noise" ratio (SNR) of the series, [Goldstein, 1951], [Vincent and Röttger, 1980]. The correlation functions can be normalized again by the signal to noise ratio and the spike removed to form the auto correlation function of the signal only.

In practice the two normalizations are done in one step. The auto covariance values are found (top line of equation 4.3) and a parabola is fitted to either side of zero lag. The interpolated value of the auto covariance at zero lag is called the "signal" power. The signal power (or zero lag covariance of the series with no noise) is used instead of the measured value of zero lag covariance (bottom line of equation 4.3) for normalization to form the auto correlation function.

The amplitude part of the auto correlation function also provides the fading time (τ_{fad}) of the data series. The fading time is the time at which the auto correlation function drops to one half ($\rho(\tau_{fad}) = \frac{1}{2}$) [2].

The argument of the auto correlation function can be used to find the average rate of change in phase during sampling time. This average change in phase can taken to be the mean line of sight Doppler shift of the scattered signal (section 5.1). Consider a received time series of complex demodulated (transmitter component removed) signal of

[2] for fading time some workers use $\rho(\tau_{fad}) = \frac{1}{e}$

form $E(t) = A(t)e^{i\omega_D t}$ (where A is the amplitude and ω_D is the frequency of the Doppler component). The top line of the auto correlation function (the bottom line is real only so does not affect the discussion and is omitted here) is

$$\begin{aligned} \langle E(t)E^*(t+\delta t)\rangle &= \langle A(t)e^{i\omega_D t}A(t+\delta t)e^{-i\omega_D(t+\delta t)}\rangle, & (4.4)\\ &= \langle A(t)A(t+\delta t)e^{i\omega_D \delta t}\rangle. & (4.5) \end{aligned}$$

The argument of the auto correlation function at time lag δt, is the product of the mean Doppler frequency and the time lag, $\omega_D \delta t$. The derivative of the argument with respect to time is then the Doppler shift. Away from zero lag, secondary Doppler components and windowing effects add extra components to the correlation function. Therefore the auto correlation function is found to just one or two time lags, then a curve is fitted to the argument and the mean Doppler shift is the slope of the curve. The mean Doppler shift as found from the argument of the auto correlation function is equivalent to that found as the first moment (that is the mean) of the power spectrum, [Woodman and Guillen, 1974].

4.1.2 Cross Receiver Correlation

The cross receiver correlation function describes the correlation between two data series received at separated receivers (at ϵ and $\epsilon + \delta\epsilon$), over a range of time lags. The complex cross receiver correlation function is based on the form

$$\rho(\delta t, \delta\epsilon) = \frac{\langle E(t,\epsilon)E^*(t+\delta t, \epsilon+\delta\epsilon)\rangle}{\sqrt{\langle E(t,\epsilon)E^*(t,\epsilon)\rangle\langle E(t,\epsilon+\delta\epsilon)E^*(t,\epsilon+\delta\epsilon)\rangle}}, \quad (4.6)$$

(the radar frequency is kept constant, $\delta f = 0$).

The bottom line (the square root of the product of the zero lag auto covariance of the two receivers) is replaced here by the square root of the product of the average signal power received on both receivers, (the zero lag auto covariance with noise removed). Normalizing by the signals scales the cross correlation function to the auto correlation functions of the two series.

Noise that is correlated between receivers (such as radio interference picked up on both receivers) will produce a spike in the real and imaginary components of the cross correlation function at zero lag. This spike, which is usually weak if it exists at all, is removed by interpolation using a parabolic fit on correlation points out to two lags either side of zero lag.

As indicated above the amplitude of the cross receiver correlation function is used to find horizontal drift velocity of the received diffraction pattern in FCA.

The argument part of the complex cross receiver correlation function gives the average phase difference between the spaced receivers which can be used to determine directions of arrival of scattered signals (see section 5.2). Consider the received scattered signal on two receivers separated by distance $\delta\epsilon$, then $E(t,\epsilon) = A(t,\epsilon)e^{i\phi(t,\epsilon)}$ and $E(t,\epsilon+\delta\epsilon) = A(t,\epsilon+\delta\epsilon)e^{i\phi(t,\epsilon+\delta\epsilon)}$ (ϕ is the phase at each receiver). The top line of the cross receiver correlation function is

$$\begin{aligned} \langle E(t.\epsilon)E^*(t,\epsilon+\delta\epsilon)\rangle &= \langle A(t,\epsilon)e^{i\phi(t,\epsilon)}A(t,\epsilon+\delta\epsilon)e^{-i\phi(t.\epsilon+\delta\epsilon)}\rangle, & (4.7)\\ &= \langle A(t,\epsilon)A(t,\epsilon+\delta\epsilon)e^{i\phi(t,\delta\epsilon)}\rangle. & (4.8)\end{aligned}$$

The average instantaneous phase difference between the two receivers is then the argument of the cross correlation function at zero time lag, (for example [Pfister, 1971]).

4.1.3 Frequency Correlation

The complex frequency correlation describes the correlation between two series of different radar frequency (f and δf) received at one receiver, over a range of shifted offsets in time.

$$\rho(\delta t,\delta f) = \frac{\langle E(t,f)E^*(t+\delta t,f+\delta f)\rangle}{\sqrt{\langle E(t,f)E^*(t,f)\rangle\langle E(t,f+\delta f)E^*(t,f+\delta f)\rangle}} \quad (4.9)$$

(receiver location is kept constant, $\delta\epsilon = 0$).

This form of correlation function was first used by [Uscinski, 1965], although in Uscinski's form the time lag was not considered, $\delta t = 0$.

The function is normalized in practice similarly to the the cross receiver correlation function. That is the covariance is normalized by the square root of the product of the signal power (the zero lag auto covariance with noise removed) of the two series, rather than by the zero lag auto covariance directly.

Also, as with the cross receiver correlation functions, noise received on both frequencies can cause a spike at zero time lag. The radar only pulses one frequency at a time so that there is a slight time lag (typically 20 to 120 milliseconds - chapter 2) hidden in the frequency correlations. There still tends to be some discontinuity in the correlation functions at the (near) zero time lag corresponding to high frequency interference so these functions are similarly found to lags of plus and minus one second and a parabola fitted to interpolate through zero lag.

As discussed in the section on frequency domain interferometry, section 5.3.3, the amplitude of the complex frequency correlation function can give an indication of the scattering depth of a scattering layer and the phase gives the range of the layer.

Generally the radars were pulsed at five different frequencies which gives ten frequency lags (δf) at which the frequency correlation function can be found. The correlation function at these frequency lags (with $\delta t = 0$) could be plotted against the magnitude of δf, and examples of these plots appear in section 7.10. Typically, however the function was found only at the higher lags as these gave sufficient information for the purposes of this project.

4.1.4 Uncertainities in Correlation Functions

There have been a few studies of the uncertainties of parameters determined from correlation functions in FCA and interferometry analysis, and a notable summary of these is [Hocking et al., 1989]. The standard error of a sample correlation coefficient can be given by

$$\sigma_\rho = \frac{1-\varrho^2}{\sqrt{N-1}}, \tag{4.10}$$

for example [Brooks and Carruthers, 1953], (where ϱ is the population correlation coefficient and N is the number of independent points in the series). For data of the sort collected here, N (or $N-1$) can be approximated by the total length of the sampling period, T, over the fading time τ_{fad}, ($N \approx \frac{T}{\tau_{fad}}$), [Awe, 1964]. The length of the sample should be at least 50 independent points, $T \geq 50\tau_{fad}$, (which is considerably longer than the samples collected here where typically $T \sim 15\tau_{fad}$).

By carrying out numerical simulations [May, 1988] found expressions based on equation 4.10 for the uncertainties of some of the correlation function parameters used in full correlation analysis. An example is the expression for uncertainty in finding the time lag of the maxima of the cross correlation function,

$$\sigma_\tau = 0.5\tau_{fad}\sqrt{\frac{\tau_{fad}}{T}}\left[\frac{1-\rho_m^2}{\rho_m}\right], \tag{4.11}$$

where ρ_m is the amplitude of the cross correlation function at the maxima.

These expressions worked well for simulated data, however when they were applied to real data it was found that the errors appeared to be overestimated by about 50%. This test was done by comparing two independent FCA experiments operated together on the large University of Adelaide Buckland Park radar. Typically the wind estimates from the two experiments differed by about 10% for winds of the order of 100 ms^{-1}. [May, 1988] suggested this overestimate by the theoretical expressions was due to filtering of the data by the FCA acceptance criteria which only accepts those points that pass certain tests (section 6.2.2).

Along similar lines [Hocking et al., 1989] found an empirical expression for the uncertainty in measuring the phase difference between signals received on spaced antennae for spatial interferometry as found from the phase of the cross correlation function at zero lag. This uncertainty depends on the amplitude of the cross correlation function and the signal to noise ratio and in units of degrees is given by

$$\sigma_\phi^2 \approx \sqrt{\frac{\tau_{fad}}{T}}\left[50\left(1-\rho^2\right)\right]^2 + 65\frac{N}{S}, \tag{4.12}$$

where ρ is the amplitude of the sample cross correlation function (uncorrected for noise) at zero lag and $\frac{N}{S}$ is the noise to signal ratio. For values of τ_{fad}, T and ρ very similar to those observed in this project, [Hocking et al., 1989] found that typically the uncertainty in phase difference is of the order of $5-15°$.

In this project confidence in a measure could also be judged on the variance between multiple measurements of the same quantity. There were generally several measurements made of the same quantity, for example spatial interferometry was carried out at each of the five frequencies the radar was operated on; the variation between the determined angle of arrivals was used as an indicator of uncertainty. The uncertainties derived from the above expressions will be compared with these variations in section 7.13.

4.2 Spectral Analysis

4.2.1 Introduction

Spectral Analysis is the art of extracting information on the oscillatory behaviour of a sequence of data. The correlation analysis (or time domain analysis) of the previous section gave a measure of the mean variations with time of a data sequence. Spectral analysis (or frequency domain analysis[3]) provides more direct estimates of the frequency, amplitude and phase of variations in the data sequence. The results of time domain and frequency domain analysis essentially contain the same information although it is presented in the quite different guises of spectra and correlation functions. The results of these different methods can be directly related to each other, a property which is used in one spectral analysis technique as will be seen below.

Spectral analysis was used in two levels of data analysis in this project. The first level was at the raw data stage, in which the one minute sequences of raw data collected at each range bin were analysed. The spectra produced were examined for effects such as Doppler

[3]Frequency Domain analysis should not be confused with the Frequency Domain Interferometry of section 5.3.

shifts in the backscattered signal. The second level of spectral analysis was of the series of results from various analyses of the one minute samples. This level included, for example, spectral analysis of the series of average signal power from each sample, or of the FCA velocity results. The spectra at this level were examined for effects such as gravity wave activity.

The main spectral technique used in this project was based on Fourier analysis using the Fast Fourier Transform. The closely related Blackman Tukey method was used to produce spectra to compare against the direct Fourier analysis. Spectral estimates from a parametric analysis, the Maximum Entropy Method, were used as a comparison as well.

A number of textbooks discuss spectral analysis techniques in general, for example at an introductory level, [Chatfield, 1984] and [Otnes and Enochson, 1972]. [Bendat and Piersol, 1986] and [Kanasewich, 1975] illustrate the application of various spectral analysis techniques to experimental data. [Marple, 1987] provides a comprehensive and practical guide with algorithms (and computer code which is also on a floppy disk) to all of the techniques used here (although code that was used here was either homegrown or came from other sources), as does the review paper Marple's text grew from, [Kay and Marple, 1981]. [Press et al., 1986] also provide algorithms and computer code (also on floppy disk), and useful descriptions of Fourier transform and Maximum Entropy spectral analysis. Spectral techniques applied to middle atmosphere radars are discussed by [Rastogi, 1989], [Keeler and Passarelli, 1990] and [Rastogi, 1990], among others. Note that the notation in the literature on spectral analysis can vary as do scaling factors and advice on windowing and filtering.

4.2.2 Fourier Analysis

A time varying function $z(t)$, can be transformed into a function $\mathcal{Z}(\omega)$, of frequency (here using angular frequency $\omega = 2\pi f$). $\mathcal{Z}(\omega)$ is the "Fourier spectrum" of $z(t)$ and the "Fourier transform" operation shows how $z(t)$ can be decomposed into a continuous series of sinusoids whose amplitude and phase are described by $\mathcal{Z}(\omega)$. The Fourier transform and the reverse operation, the "inverse Fourier transform" are respectively,

$$\mathcal{Z}(\omega) = \int_{-\infty}^{\infty} z(t) e^{-i\omega t} dt, \tag{4.13}$$

$$z(t) = \frac{1}{2\pi} \int_{-\infty}^{\infty} \mathcal{Z}(\omega) e^{i\omega t} d\omega, \tag{4.14}$$

where $i = \sqrt{-1}$.

A similar relationship can be used to estimate the Fourier spectrum of a time sequence of discretely sampled data, for example the output of the phase coherent receivers used

in this project. (The in-phase and quadrature outputs of these receivers will treated here as the real and imaginary parts of complex valued data). If the sequence has form $\{z_j\} = \{z_1, z_2, \ldots z_N\}$, (sampled at constant time intervals of δt), the Fourier spectrum can be approximated by the Fourier components $\{Z_k\} = \{Z_0, Z_1, \ldots Z_{N-1}\}$ using the "discrete Fourier transform" and its inverse,

$$Z_k = \frac{1}{N}\sum_{j=1}^{N} z_j e^{-i\omega_k t_j}, \tag{4.15}$$

$$z_j = \sum_{k=0}^{N-1} Z_k e^{i\omega_k t_j}, \tag{4.16}$$

where the Fourier frequencies are $\omega_k = \frac{2\pi k}{N\delta t}$. The sequence $\{z_j\}$ is assumed statistically stationary, which means that statistical properties such as mean and variance would not vary if the samples were taken at a different time. (Note that various authors sometimes have different scale factors in these equations or sum over different ranges. but the general form of the equations is standard.)

The Fourier components describe how the time sequence can be constructed from a sequence of waves of form $e^{i\omega t}$, (where, by Euler's rule, $e^{i\omega t} = \cos\omega t + i\sin\omega t$). The Fourier components are generally complex since the constituent waves of various amplitudes, $|Z_k|$, also have various phase offsets, ϕ_k, with respect to each other ($Z = |Z|\epsilon^{i\phi}$). The second half of the sequence of frequency bins $\{\omega_0, \ldots, \omega_{N-1}\}$, (that is $\{\omega_{\frac{N}{2}}, \ldots, \omega_{N-1}\}$), can be considered to correspond to the negative frequencies $\{-\omega_{\frac{N}{2}-1}, \ldots, -\omega_1\}$. (So, for example, Z_{N-1} is the Fourier component at a frequency of negative $\frac{2\pi}{N\delta t}$.)

Rather than examining the Fourier components directly. the "Power Spectral Density" (PSD) function is usually found. The PSD gives the variance (or power) of the time series as a function of spectral frequency. There are a number of different definitions for PSD, most being in some way proportional to the spectral amplitude squared. Here the component of PSD, P_k, giving a measure of the variance over the frequency range $\omega_k \pm \frac{1}{2}\delta\omega (= \omega_k \pm \frac{\pi}{N\delta t})$, is defined as

$$P_k = \frac{1}{N\delta t} Z_k^* Z_k. \tag{4.17}$$

The zeroth Fourier component (Z_0 at $\omega = 0$) is just the mean of the data series and is usually removed before the analysis is performed. Ignoring the zero component, the lowest frequency, or equivalently the frequency resolution. of the Fourier series is the one that corresponds to the longest completely observable cycle over the total sampling time or $f = \frac{1}{N\delta t}$. This spacing between the spectral estimates can be decreased by attaching a sequence of zeros to the data effectively to increase N, a procedure called "zero padding".

The highest frequency that can be observed is defined by how often the sampling is carried out. At least two samples have to be taken during an oscillation before it can unambiguously be said an oscillation has occurred. However if a complete oscillation occurs before the two samples are taken, this oscillation cannot be distinguished from oscillations slower than the two sample period, an effect known as "aliasing". This "two sample" highest unambiguous frequency limit is the Nyquist frequency, $f_{\mathrm{Nq}} = \frac{1}{2\delta t}$.

Fourier analysis assumes that the data sequence endlessly repeats itself beyond the last point, and before the first, with a period equal to the length of the data sequence, $\{\ldots, z_N, z_1, \ldots, z_N, z_1, \ldots\}$. If there are oscillations in the series that have periods that are not harmonics of the length of the sequence (as is generally the case), then on Fourier analysis the power in these oscillations is leaked from the Fourier components corresponding to those oscillations into nearby components. This effect makes spectral features appear broader than they should and adds extra features or "sidelobes" to the spectrum particularly around the strongest spectral features. To reduce these effects, a tapering function is applied to the data sequence at both ends (before the addition of any zero padding). Many tapering functions have been devised, for example see [Harris, 1978], and the main one used in this project was the Hanning window which multiplies the jth data point in the series by

$$\frac{1}{2}\left[1 - \cos\left(\frac{2\pi j}{N-1}\right)\right]. \tag{4.18}$$

Examples of the effect of this window on test and real data will be given below.

The uncertainty associated with each estimate of the Fourier component in equation 4.15 is large. For example the Fourier components of a random series each have a variance which is equal to the square of the component, [Bloomfield, 1976]. The variance can be reduced by summing together spectral estimates from adjacent frequency bins which decreases the variance by the inverse of the number of bins summed together. Alternatively, the data set can be divided into subsets, each subset spectrally analysed and then the spectral estimates of each frequency averaged together to form the "modified periodogram". The subsets can be separate or can overlap each other, ([Welch, 1967]). The reduction in variance depends on the degree of overlap, if no overlap is used the variance is decreased by the inverse of the number of subsets. Both methods also result in a reduction in frequency resolution.

The Fourier components can be found directly using equation 4.15, although such a computation can be very time consuming if the sequence of data is very long or if, as was the case in this project, very many sequences have to be analysed. Fortunately techniques, collectively known as "Fast Fourier Transform" (FFT) techniques, have been developed

that eliminate many of the multiplication operations by factorizing the transforms. If, as is usually the case, there are many common factors, very substantial savings in computational effort can be made. These short cuts also enhance the accuracy of the computations because there are fewer operations and therefore fewer rounding errors. FFTs are discussed in [Brigham, 1974], and a Numerical Algorithms Group library routine based on Brigham's techniques was the principal Fourier transform routine used for this thesis.

Figure 4.1 gives an example of analysis of a synthesized data series. Numerous such data series were formed to test various aspects of spectral and correlation analysis. The synthesis procedure started by specifying Gaussian functions as a function of angular frequency ω,

$$\mathcal{S}_\omega = S\epsilon^{-\left(\frac{\sqrt{\ln 2}(\omega-\omega_0)}{\sigma}\right)^2} \tag{4.19}$$

where ω_0 and S are the frequency and amplitude respectively of the peak of the function, and σ is the half width at half power. The functions were evaluated for a sequence of frequency bins and these values were designated as being the amplitude of a synthetic spectrum. Phases were assigned to each frequency bin, either by a random number generator (uniformly distributed over $\pm\pi$) or by specifying preset phases. If more than one Gaussian spectrum was generated, they were coherently added and inverse Fourier transformed to produce a "time" series. (The above procedure was similar to that used by [Hocking, 1983a].) At this stage sinusoids of varying amplitude, period and phase could also be added to the synthetic time series. The range of the frequency bins generated, and thus the length of the time series, was much greater than those used in the various subsequent analyses to examine effects such as selective sampling and windowing. Identical series with different phase offsets could also be generated to test cross spectral routines.

The example in figure 4.1 was comprised of two Gaussian functions and three sinusoids to make a series of 2560 complex data points. The central 256 points were retained for testing spectral analysis procedures and are shown at the top of the figure. The synthetic spectrum before inverse Fourier transforming is also displayed. The superimposed dashed lines represent the sinusoids that were added after the inverse transforming. Two of the sinusoids were placed close together in the frequency domain, forming a doublet, to check the sidelobe behaviour and resolving power of the analyses. Also shown are the results of analysis of the series by the three main spectral techniques used in this project. [Kay and Marple, 1981] also generated Gaussian features in the frequency domain, transformed them to the time domain and added sinusoids in tests of various spectral analysis procedures and gives a similar figure.

The FFT power spectrum of the synthesized data was found with zero padding added to

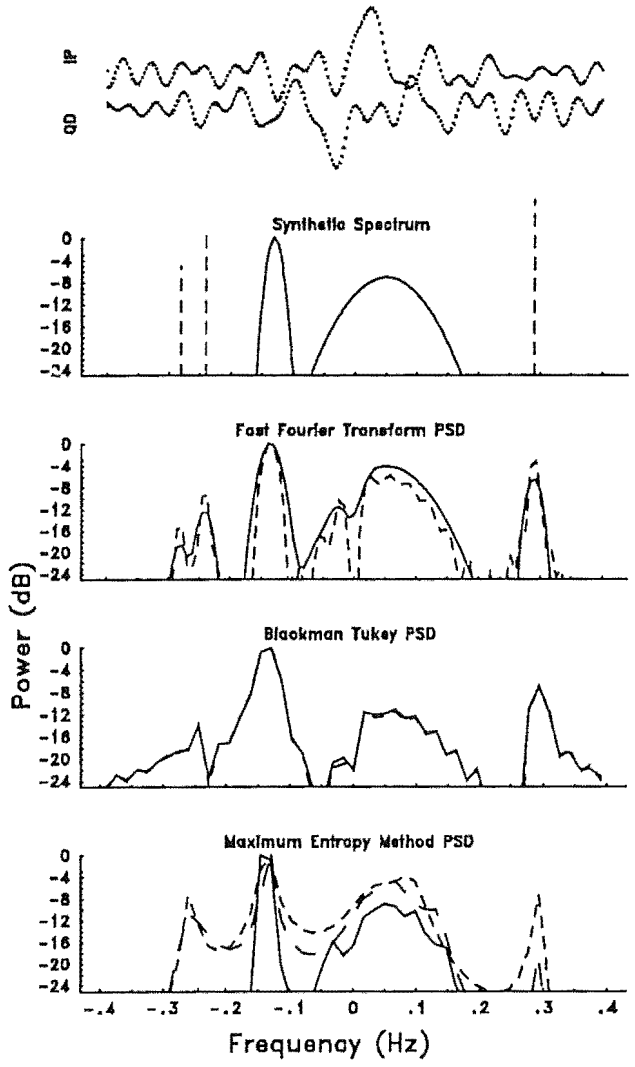

Figure 4.1: **Spectral analysis of a synthesized data set.** The complex data series is shown at the top of the figure. Below that is the spectrum it was synthesized from, two Gaussians, with sinusoids superimposed, indicated by the dashed lines. The spectral analysis results follow : **FFT PSD** with Hanning window (solid line) and without (dashed), **Blackman Tukey PSD** with a Hanning lag window (solid line) and without (short dashes) and **MEM PSD** at filter lengths of 10 (short dashes), 20 (long dashes) and 49 (solid line), the filter length with minimum FPE.

double the data length (to 512 points) and is displayed with and without a Hanning window applied (solid and dashed lines). The FFT power spectrum shows broader features than the original spectrum reflecting the effect of limiting the length of the sample. The spectrum without the Hanning window shows additional sidelobes due the cut-off of the sampling, although it does more accurately show the narrower features since without tapering the data set appears longer. (This also shows up in the more noticeable appearance of the removal of the mean at frequency zero.)

Fourier Analysis of Raw Data

Initially spectra were found for each of the one minute samples (256 points) at each range bin and at each radar frequency and receiver. Examples of these raw spectra can be seen in figure 4.2 which shows fifteen raw spectra collected on three receivers and at five radar frequencies and the average of these spectra. The sampling rate of the data is 4 Hz so the Nyquist frequency is 2 Hz. The spectra are shown out to spectral frequencies of ± 0.5 Hz, as are most of the raw data spectra in this thesis since the power at frequencies beyond this range was generally insignificant. As mentioned in section 2.1.7 the raw data was quarter-half-quarter filtered rather than coherently integrated to remove some of the highest frequency noise. The -3 dB low pass cutoff is approximately 0.73 Hz. at 0.5 Hz the attenuation is about -1.4 dB. A Hanning window was applied to the data, as was zero padding to double the data length which doubled the number of spectral estimates.

As can be seen there is considerable variability between the raw spectra. There has been some discussion about whether a one minute sample of MF radar data is sufficiently long, or has an adequate number of statistically independent points, to allow the formation of reliable spectra without excessive random components or spikes. [Hocking, 1983a]. The fading time (see section 4.1.1) is often considered to be the time between independent points of this type of data. The typical fading time observed in this study was of the order 1-6 seconds. therefore each one minute series contains between 10 and 60 "independent samples". Using the Buckland Park Doppler MF radar, Hocking concluded that a data series of at least 80-100 times the fading time was required otherwise the spectra formed would contain random or spurious spikes. However Hocking's work was with a Doppler beam swinging radar and so his study was primarily interested in obtaining spectra of Gaussian form originating from turbulent scatter. The zeroth, first and second order spectral moments are found from these spectra, which are equated to the mean signal, Doppler shift and Doppler spread respectively. Spikes in the spectra (either real or statistical) can have a considerable biasing affect on these mean parameters, so in Doppler

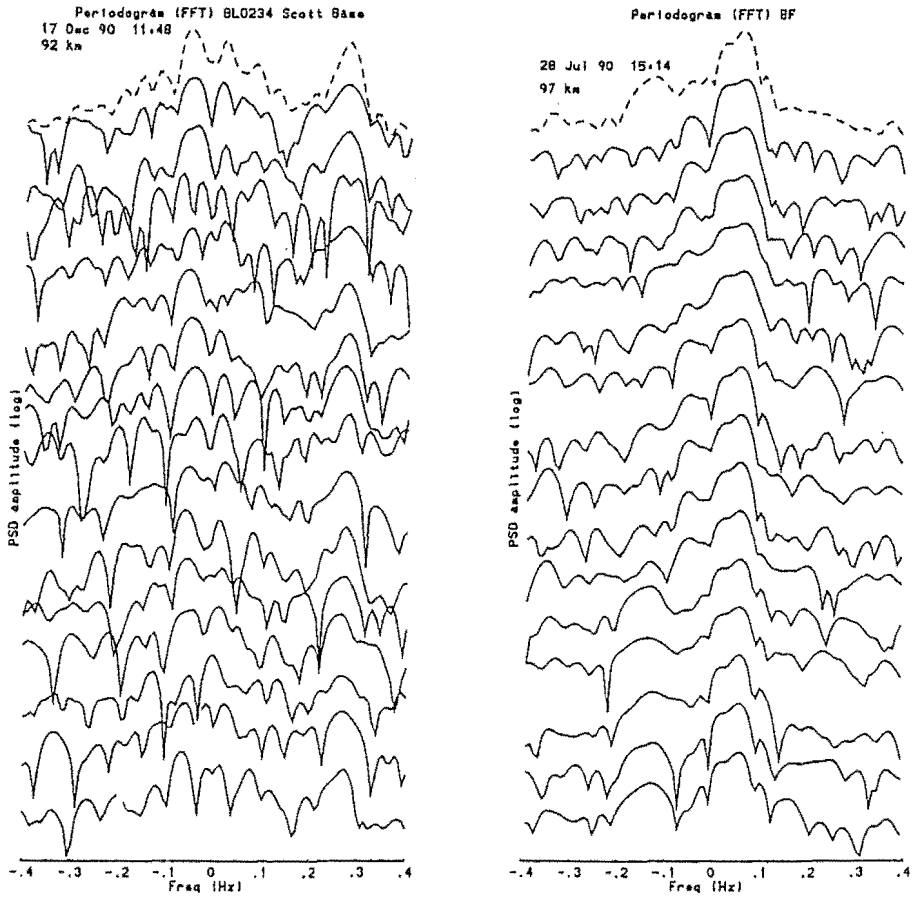

Figure 4.2: **Examples of raw data spectra** collected at (a) Scott Base and (b) Birdlings Flat. Both plots show the 15 raw FFT spectra collected from each of 5 radar frequencies and 3 receivers at range bins of 92 km and 97 km respectively. The average (or periodogram) spectrum is shown as the dashed line at the top of each plot.

beam swinging work efforts are made to minimize the amplitude and number of spikes.

This study was more interested in real spectral spikes as they seem to be associated with short lived strong scattering events (for example the Fresnel scatter of section 1.3.4). Also it was desired to use samples no longer than one minute, as changes in the scattering region can occur on time scales of a few minutes and there was concern that longer samples could suffer from non-stationarity.

The variance of the spectral estimates (and thus the random spikes) can be reduced using the averaging techniques mentioned above. However there was some reluctance to sum frequency bins together or sub-divide the data sets because it was felt that the series already had too few independent samples and it was desired not to decrease the spectral resolution. However if it is considered that on average the three receivers (being relatively close together compared with the swathe of atmosphere that passes overhead in the one minute sampling time), and the five radar frequencies (also being relatively close together in wavelength compared with the range of scales of scattering structures) all see the similar scattering features, then there are fifteen "subsets" that can be averaged conveniently. The raw spectra from each of these subsets (that is each receiver and radar frequency) do show inconsistencies which could be attributable to variance in the spectral estimates. The averaged spectra do display less variability, for example figure 4.2. However since the data series of these spectra are not strictly statistically independent, the reduction in variance is not as great as would be observed in a modified periodogram with the same number of independent sub-spectra.

All of the data series and spectra are complex but because each data series and spectrum are obtained either from separate receivers or from different frequency steps, each contains unique phase information and could not be coherently added. (The difference in phase between each receiver depends on the direction of arrival of the scattered signal and the change in phase at each frequency step depends on the range of the scattering targets). However the PSD can be added because if the power at each spectral frequency does originate from some scattering target, it should appear at the same frequency regardless on which receiver or at which radar frequency the data was recorded on. (The radar frequency is not varied sufficiently here to appreciably shift the Doppler frequency.)

When mean spectra from adjacent range bins and consecutive samples are compared (for example figure 4.3), it is found that many of the spectral features are similar, especially considering the natural variations in the scattering layers that can be expected to occur between range gates and samples. This consistency between over range bins and between successive samples is also apparent in the spectra that appear in section 7.4.

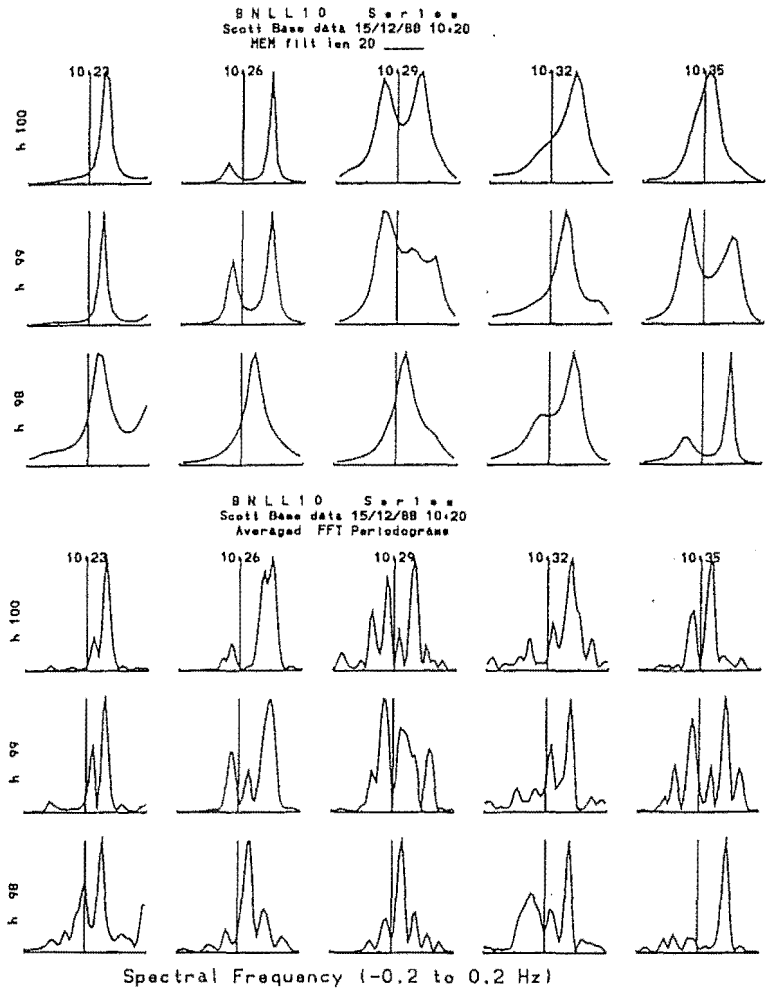

Figure 4.3: **Examples of averaged spectra** collected at Scott Base, (a) averaged MEM spectra, and (b) averaged FFT spectra or periodograms, both calculated from the same data sets. The data was collected on three adjacent range bins (displayed in the three rows) and at four successive sampling periods (four columns).

4.2.3 Other Spectral Analysis Techniques.

More evidence for reality of the main features of the spectra of the raw data series is their appearance in spectra calculated by different methods. Here the sample spectra were compared using two other spectral techniques, those of Blackman Tukey analysis and the Maximum Entropy Method.

Blackman Tukey Spectral Analysis

The Blackman Tukey technique of Fourier analysis, [Blackman and Tukey, 1958], is based on the Wiener-Khintchine theorem which relates the auto-covariance function to the power spectrum,

$$P_k = \sum_{l=0}^{m} R_l e^{-i\omega_k \delta t}, \tag{4.20}$$

where the spectral estimates P_k are at angular frequencies $\omega_k = \frac{\pi k}{m\delta t}$. The auto-covariance function here is

$$R_l = \frac{1}{N} \sum_{i=1}^{N-l} z_i^* z_{i+l}. \tag{4.21}$$

Note that this form of the covariance function differs slightly from the covariance and correlation forms given in section 4.1. $\frac{1}{N}$ is used instead of $\frac{1}{N-l}$ to scale the covariance since it results in a lower mean square error in covariance, [Jenkins and Watts, 1968], and the complex conjugate is taken for the unlagged term (z_i^*), rather than the lagged term (z_{i+l}) following the convention in Blackman Tukey analysis.

Blackman Tukey analysis assumes that the covariance terms beyond the maximum lag m, are zero, which can lead to sidelobes in the spectrum similar to those of direct Fourier analysis. The application of a window reduces these sidelobes. Here a Hanning (or cosine bell) lag window was applied to the covariance function to taper gradually the function before it was transformed by equation 4.20,

$$R_l' = R_l \frac{1}{2}\left(1 + \cos\frac{\pi l}{m}\right). \tag{4.22}$$

(note the similarity with the time domain Hanning window used in the Fourier analysis section, equation 4.18).

The variance of each of the spectral estimates depends on the maximum lag over the length of the data series, m/N. Generally the maximum lag should be restricted to approximately 10% - 20% of the length of the data series [Blackman and Tukey, 1958], although the maximum lag can be increased if a lag window is applied. The more lags that are used, the better the frequency resolution of the spectrum is. Similarly to FFT analysis,

further enhancement in frequency resolution can also be achieved by padding with zeros. The padding is done by defining the covariance (after the lag window is applied) at lags beyond those actually estimated by equation 4.21, to be zero. Increasing the maximum lag however increases the computational effort required, already considerably greater than that required for the FFT analysis so here generally only a 30% lag length was used, with no zero padding.

Figure 4.1, showing spectra of a synthesized series, includes a Blackman Tukey spectrum. The spectrum was found using lags out to half the length of the series, the solid line shows the spectrum with a Hanning lag window imposed and the dashed line without. The spectra are much coarser than the FFT PSD since the resolution is a quarter of that used in the FFT spectra. The sinusoid doublet appears as one feature and is nearly swamped by large sidelobes from the narrower of the two Gaussian peaks. Examples of Blackman Tukey analysis of raw receiver data appear in section 7.4.

With the wide spread use of the FFT and the development of newer techniques, the use of Blackman Tukey analysis has declined, however it is a relatively straight forward method and provides a useful check on the results of the other analyses.

Maximum Entropy Methods

The Maximum Entropy Method (MEM) attempts to create a model of the process that generated the data set, and uses this model to estimate the power spectrum of the data set. The method is often called "data adaptive" (or "parametric" or "modern") because the modelling process used adjusts itself so that a small variation in the estimated spectral power at one frequency causes minimal disturbance to estimates at other frequencies. The result can be high resolution spectra determined from short data series, provided caution is exercised in the selection of parameters.

The modelling technique used is autoregression, where unknown data points are approximated by performing multiple regression on the known data points. [Burg, 1978a, Burg, 1978b][4] initially developed the technique as a method of enhancing the spectral resolution of Blackman Tukey type analysis using extrapolation of the first few well known lags of the covariance function. MEM's guiding principle is that whilst the extrapolation is being performed as few assumptions as possible are made about the unknown lags (quite unlike standard Fourier techniques - including Blackman Tukey - where unknowns are equated to zero). This principle was stated by [Ables, 1978] as :

[4] Burg's original paper was presented in 1967, and appears in the classic collection of MEM papers, [Childers, 1978].

> The result of any transformation imposed on the experimental data shall incorporate and be consistent with all relevant data and be maximally non-committal with regard to unavailable data.

The spectra obtained using this principle are considered, in this type of analysis, to have "maximum entropy", or being the most random possible in terms of information content about the unknown data, yet are still consistent with the known data.

A series of coefficients, termed the "prediction error filter", is determined by autoregressive modelling, in accordance with the non-committal or maximum entropy principle. The filter coefficients can be used to estimate an extended covariance function or to extend the data series. When the frequency domain form of the filter is convolved with the to-be-determined power spectrum of the data, the filter acts to remove the predictable components of the data series and a white noise spectrum is produced. The white noise spectrum represents the maximally non-committed spectrum about the data series and has the same power at all frequencies. The prediction filter coefficients can be estimated, and since the white-noise spectrum is known, the original power spectrum of the data can be found. The extended covariance function or extrapolated data series need not actually be evaluated, the spectrum can be determined directly from the filter coefficients. Unlike Fourier transform techniques which provide spectral estimates at set frequencies, the filter coefficients of MEM can be used to obtain an estimate for any frequency within the Nyquist range. The technique therefore, is capable of directly producing higher resolution spectra than the $\delta f = \frac{1}{N\delta t}$ limit of Fourier techniques.

Details of how MEM carries out the autoregressive modelling and determines the filter coefficients is a specialized topic beyond the scope of this thesis. The collection of papers of [Childers, 1978] and also the texts by [Kanasewich, 1975] and [Marple, 1987] discuss the calculation of the coefficients and other aspects of MEM. The MEM procedure used in this thesis was based on a routine of [Hayashi, 1977].

The number of coefficients, known as the length or the number of "poles" of the prediction error filter (alternatively the number of lags of the known covariance function or order of the autoregressive model), is preset. The choice of filter length can have a considerable effect on the final spectrum. If the filter is too long, the spectrum tends to split and displays too many features. If the filter is too short, then the spectrum is too smooth and real components are not resolved. There are techniques that attempt to provide criteria for determining the ideal filter length and one that was tested here is Akaike's Final Prediction Error (FPE), [Ulrych and Bishop, 1978]. The FPE gives an estimate of the mean square error in the MEM predictions as a function of filter length.

The filter length with the minimum FPE is often considered the optimum length. However [Ulrych and Bishop, 1978] showed that if there is noise in the data, longer filter lengths than that indicated by the FPE (and other) criteria are more successful in extracting spectral components. As [Marple, 1987] states, subjective rather than scientific judgement is generally required when selecting the filter length. Often the filter length is arbitrarily preset to say 10% or 20% of the data length and checks made that the spectrum does not show much variation if the filter length is changed or even doubled.

Generally in this thesis, MEM spectra were found at one or two fixed filter lengths. An advantage of using the same length for all samples is that the spectra obtained will tend to have a similar tendency to split, provided that the characteristics of the data in each is not too dissimilar. Typically the filter lengths used in the raw data MEM spectra were ten and twenty or 4% and 8% of the data lengths (usually 256 samples), although some spectra were found at filter lengths of 50 (or 20%) or with the minimum FPE criteria. Figure 4.4 gives examples of the average variation in FPE with filter length and a histogram showing the relative number of spectra with minimum FPE against the filter length they were found at for data collected at Birdlings Flat and at Scott Base. The minimum FPE occurs typically at a filter length of about five and there is only a slow increase in FPE as the length increases beyond the minimum.

Examples of MEM spectra of raw data are shown in figure 4.3 with filter lengths of 20. (Note that unlike the Fourier and Blackman Tukey analysis, no preconditioning such as windowing or filtering was applied to the data so that as much information as possible is retained from which MEM makes its autoregressive predictions.) A consideration in finding MEM spectra of the raw data sets was the computation time, which like the Blackman Tukey analysis, is considerably greater than FFT computation, and increases with the order used.

There have been few studies of MEM analysis of middle atmosphere radar scattering. [Klostermeyer, 1986] discusses the application of MEM and the related Maximum Likelihood Method to spectral analysis of VHF Doppler beam swinging radar signals, and continues his MEM study in [Klostermeyer, 1989b]. He found that MEM gave more accurate results than periodogram analysis at low to moderate signal to noise ratios. Klostermeyer gives an alternative method of determining the optimum filter length and faster algorithms for estimating the zeroth, first and second order spectral moments of backscattered signals (used in beam swinging radars as estimates of the mean signal power, Doppler shift and Doppler spread). He suggested that these methods would be best applied to short pulse,

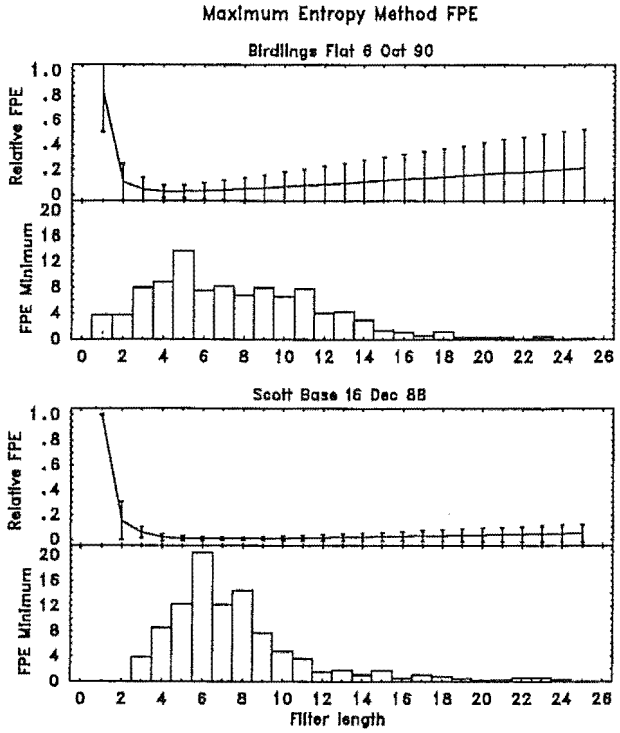

Figure 4.4: **Final Prediction Error filter lengths** for both Birdlings Flat and Scott Base data. The upper plots for each radar shows the average FPE (normalized to the maximum value) as a function of filter length. The error bars indicate standard deviation. The lower plots for each radar are histograms of the relative number of samples (expressed as a percentage) at each filter length for which the FPE was at a minimum. The Birdlings Flat data was from a five hour sampling period on 6 October 1990 and the Scott Base data was from a half hour sampling period at midday on 16 December 1988. These plots were compiled from approximately a thousand sample spectra evenly spread through both data sets.

narrow antenna beam radars because these radars obtain signals with narrow spectral features which are more suited to MEM analysis than broad band signals. (Narrow spectral features were frequently observed on the broad beam radars used in this study however.)

Figure 4.1 of spectra of a synthesized data series includes MEM spectrum at the filter length where FPE was at a minimum and at filter lengths of 10 and 20. The minimum FPE filter length for this series was 49. This length (and that from other synthesized series) was considerably longer than the most of the minimum FPE lengths observed on the Birdlings Flat and Arrival Heights radars, suggesting that the synthesized series were not particularly typical of the data in this study. The sinusoids do not, in this case, appear in the FPE minimum spectrum, although these lines were found to disconcertingly appear

and disappear in the FPE minimum spectrum if their amplitudes and frequencies were altered. The behaviour of spectra with filter lengths set at 10 and 20 was found to be somewhat more stable and these spectra do show the main features of the synthesized data with negligible sidelobes. Often, however, as in the example shown, the sinusoid doublet was not resolved into two features, although again this depended on the relative amplitudes and frequencies of various features in the spectrum and the filter length used. Generally the half power widths of the features at the frequencies of the sinusoids were much narrower than those in the FFT and Blackman Tukey spectra. Broad features were sometimes split (again depending on the relative amplitudes and frequencies of various features), particularly at longer filter lengths.

The impression gained from tests of MEM analysis on synthesized data was of instability; however MEM spectra of data collected on both radars were generally found to have less variance (provided filter lengths of 10 or 20 were used) from sample to sample or from range gate to range gate than spectra obtained from either FFT or Blackman Tukey techniques. This can be seen in figure 4.3 (and in similar figures in section 7.4). Generally at the filter lengths used, the MEM spectra of real data were much smoother than either the FFT or Blackman Tukey spectra.

4.2.4 Spectral Identification of Scattering Centres

Most of the spectra of backscattered signals observed in this project have a dominant peak, but also have significant power at other frequencies. In section 4.1.1 the mean periodicity of backscattered signals determined from the phase of the autocorrelation function was equated to the mean Doppler shift due to radial motion of the scattering targets in the radar's scattering volume (discussed further in section 5.1). This mean Doppler shift is equivalent to the mean frequency (or first spectral moment) of the PSD of the backscattered signals, [Woodman and Guillen, 1974]. Using spectral analysis makes it possible to identify many different periodicities in the backscattered signal and these can be equated to the different Doppler shifts of various scattering targets in the radar volume [Farley et al., 1981]. (This is termed "Doppler sorting" by [Meek and Manson, 1987].) A difficulty is that if there is more than one scattering target with the same Doppler frequency those targets cannot be resolved by Doppler sorting.

Another problem is sorting out which of the regions of enhanced power (or peaks) in the spectra are real and which are random statistical fluctuations. The averaging of the PSD of the signals observed at each radar frequency and each receiver did appear to reduce random spikes in the spectra. However the constituent spectra making up the

average PSDs cannot be considered entirely statistically independent and some random features can be expected to have survived the averaging.

Comparing Spectra

A scheme was devised to compare the spectra determined by FFT with those determined by the Blackman Tukey and MEM techniques. Each spectrum was examined to find the frequency of the spectral estimate with the greatest power and the frequencies of the various sub-maxima down to 10 dB below the maximum. The spectral estimates around the maximum and each of the sub-maxima was least squares fitted with parabolas or Gaussian functions[5] to resolve further the frequency and power of each "peak". A test was made to ensure that an adequate fit was obtained by checking that the fitted power was within 1 dB and the fitted frequency within two frequency bins of the maximum or sub-maxima the fit had been made around. The peaks of the averaged FFT spectra were then compared with peaks identified in the averaged Blackman Tukey or MEM spectra. If the frequency of the fitted peaks agreed to within 0.05 Hz and the normalized power agreed to within 3 dB then they were considered to be consistent and identified as corresponding to scattering centres. (The power and frequency values specified here were arrived at empirically by inspection of various spectra of many samples).

[5] Using the routines of [Press et al., 1986].

Chapter 5

Interferometry

Interferometry techniques compare waveforms and use any differences observed between the waves to make inferences about the history of the waveforms.

In this project, the interferometry techniques used concentrated on the use of phase as a measure of the difference between waveforms. Here the phase of a received signal on the radar refers to the phase difference between that signal and the phase of the signal the transmitted pulse was generated from.

The instantaneous phase of a signal backscattered from some target, depends on the length of the path traveled by the radar signal to the scattering target and back to the radar and on the radar wavelength. If p is the total path length (sometimes called the "phase path") and radar wavelength, λ, corresponds to wavenumber, $k = \frac{2\pi}{\lambda}$, then the instantaneous phase is

$$\phi = kp. \tag{5.1}$$

Making a measurement of absolute phase can be difficult due to uncertainties such as the additional contributions that many components of the radar can make to measured phase. Also, phase cannot usually be measured beyond 2π radians; a measurement of phase typically includes a large unknown number of 2π radian addenda. In general, absolute measurements of phase are fortunately unnecessary. Usually the variations of phase with time or comparisons of two separate phase measurements can supply all the information required and the unknown 2π radian component of the phase can be ignored. These variations can be basically described by

$$\delta\phi = \delta k p + k\delta p, \tag{5.2}$$

(where δ indicates variation).

The three different forms of interferometry used in this work are in fact variations on equation 5.2 applied to different situations. The first, *time domain interferometry*, is a standard technique, although it is normally described as measurement of Doppler shift and not directly as an interferometric measurement. The discussion of time domain interferometry is fairly brief here because it is a standard technique and methods of analysis of time varying quantities is discussed fairly extensively in chapter 4.

The second form of interferometry used in this project is *spatial domain interferometry* which describes the measurement of the angle of arrival of signals received by the radar. As was mentioned in section 1.4.2, the measurement of the angle of arrival of scattering is also an established technique on middle atmosphere radars.

The third form of interferometry discussed here is *frequency domain interferometry*. This technique has only recently developed and so the evolution of this form of interferometry as well as the principles behind it are outlined here.

The remaining sections in this chapter introduce some applications of interferometry techniques. Section 5.4 discusses how cross spectral techniques can be used to locate scattering centres and section 5.5 on "interferometric velocities" follows this up by showing how these cross spectral analysis results can be used to estimate the overall motion of the scattering region. Finally a different application of interferometry, that of postbeam steering, is introduced in section 5.6.

5.1 Time Domain Interferometry

Time domain interferometry examines the behaviour of the phase path over time. The wavelength of the radar is kept constant, ($\delta k = 0$),

$$\delta\phi = k\delta p. \tag{5.3}$$

and the variations in phase over time, t, of the received signals are found,

$$\frac{\delta\phi}{\delta t} = k\frac{\delta p}{\delta t}. \tag{5.4}$$

Any observed variations in phase with time are assumed to result from variations in the phase path. The rate of change of phase with time is, of course, the Doppler shift of the scattered signal. The path is the return path, so the rate of change in return path is actually twice the change in range of the scattering point, which per unit time is the apparent radial velocity, v_{rad}. (Apparent because the radial velocity does not necessarily correspond to the actual velocity of a target, only to the motion of a reflection point.)

The Doppler shift, ω_D, therefore is

$$\omega_D = \frac{\delta\phi}{\delta t}, \tag{5.5}$$

$$= 2kv_{rad}. \tag{5.6}$$

The average Doppler shift of a received signal over some sampling time is usually found, via either correlation or spectral analysis discussed in chapter 4.

5.2 Spatial Domain Interferometry

If the phase of scattered signals originating from a single nearby transmitter and received on two antennae after returning from a scattering target are compared, any phase difference between the antennae is due to the difference in the total path length traveled to the two antennae, δp_{ij},

$$\delta\phi_{ij} = k\delta p_{ij}, \tag{5.7}$$

($\delta k = 0$ again). As can be seen in figure 5.1, the difference in path length depends on the separation of the two antennae and their orientation with respect to the path of the scattered signals,

$$\delta p_{ij} = \xi_{ij}\cos(\beta_{ij} - \alpha)\sin\theta, \tag{5.8}$$

where α and θ are respectively the azimuth and zenith angles of the direction of arrival of the scattered signals, and ξ_{ij} and β_{ij} are the separation and orientation of of the two receiving antennae, (here ignoring any phase factors due to the components of the radar, for example different antenna feeder lengths). In this work, orientation angles such as α and β_{ij} are measured clockwise from north.

The phase difference between the received signals is then

$$\delta\phi_{ij} = k\xi_{ij}\cos(\beta_{ij} - \alpha)\sin\theta. \tag{5.9}$$

Two path differences with different orientations are required to uniquely specify the scattering direction. In general with the radars used here, three were available and the redundancy was used to improve the estimate of the scattering direction. Equation 5.9 was rearranged to the linear form

$$\phi_{ij} = \mathcal{E}\epsilon_{ij} + \mathcal{N}\eta_{ij}, \tag{5.10}$$

where

$$\epsilon_{ij} = k\xi_{ij}\cos\beta_{ij}, \tag{5.11}$$

$$\eta_{ij} = k\xi_{ij}\sin\beta_{ij}, \tag{5.12}$$

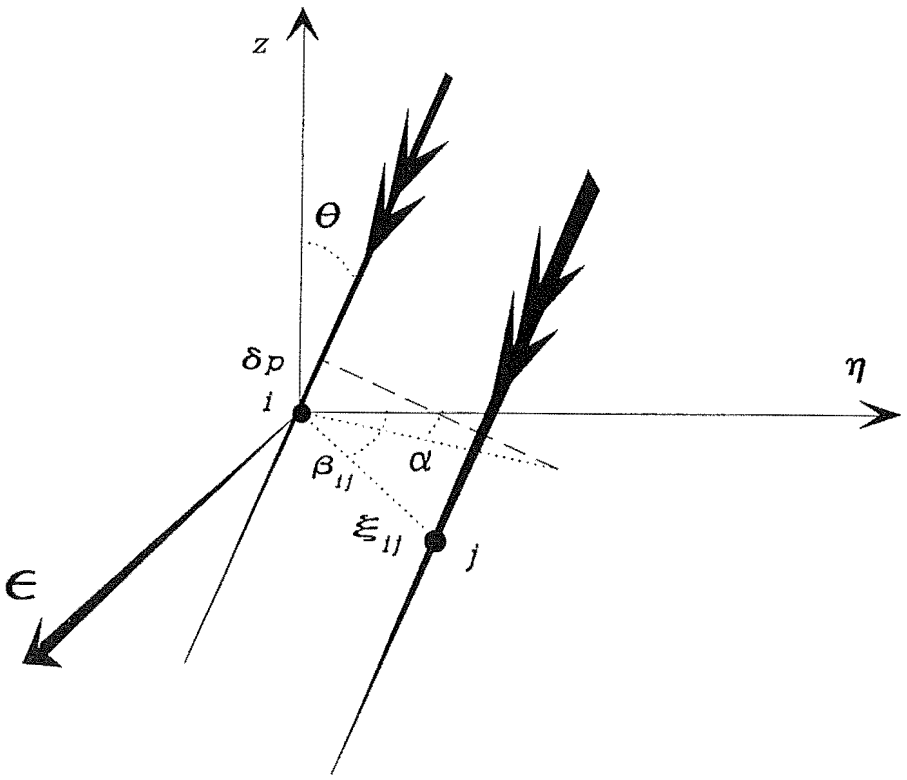

Figure 5.1: **Spatial interferometry path difference between two antennae**, i and j separated by ξ_{ij} along direction β_{ij}. The two heavy lines indicate the components of an approaching scattered signal (orientated at zenith angle θ and azimuth angle α) that are received at i and j. The difference in the path length travelled by the two components is δp.

and

$$\mathcal{E} = \cos\alpha \sin\theta, \tag{5.13}$$

$$\mathcal{N} = \sin\alpha \sin\theta. \tag{5.14}$$

ϵ_{ij} and η_{ij} are constant for each pair of antennae and with the measured phase difference for each pair, ϕ_{ij} (minus any equipment phase factors), three samples of equation 5.10 were available. A linear regression on was carried out to find $\mathcal{E}$ and $\mathcal{N}$ and thus determine α and θ.

Note that ϕ_{ij} cannot be measured beyond $\pm\pi$ radians; therefore there can be some ambiguity as to whether an extra 2π radians should be added to the measured phase

difference. For the Birdlings Flat radar this ambiguity begins to have an effect for zenith angles greater than about 15°, depending on the azimuthal orientation of the scattering. At Scott Base the receiving antennae are not so widely separated (minimum separation of 123 m compared with 250 m at Birdlings Flat) so zenith angles of beyond about 25° can lead to an extra π in the phase difference. (The layout of the receiving antenna for Birdlings Flat and Scott Base were given in sections 2.1 and 2.2 respectively.)

When there are extra π factors in the phase differences, the direction of scattering is misinterpreted as being closer to the zenith, and at a different azimuth than is actually the case. In general the greater the zenith angle beyond the ambiguity limit the closer to zenith the scattering appears to be.

The redundancy of having an extra antenna pair can be used to reduce some of this ambiguity. For example the sum of the phase differences along all three antenna pairs ideally should be zero, and extra πs can be added or subtracted from the largest phase differences to make this sum as close to zero as possible. Also the scattering direction can be found using just two pairs and compared to the regression result.

Fortunately the polar diagram of the radar antennae can act to limit the power of scattering at larger zenith angles. For example the half power half width of the Birdlings Flat radar is about 10° in the north-south vertical plane and about 15° in the east-west vertical plane; therefore scattering from larger zenith angles is to some extent restricted. The Scott Base antennae all consist of single elements and so have much wider polar diagrams with half power half widths of about 40°, although since the antennae are closer together there, ambiguities only occur at much larger zenith angles.

As has been mentioned previously, the polar diagram of the scattering appears to also be sometimes naturally limited. This occurs frequently for the scattering structures with the highest reflectivity, that is the specularly reflecting structures of section 1.3, that might otherwise be expected to dominate scattering from large zenith angle. Isotropic scattering is associated with structures such as turbulence which is more diffuse than specular reflecting structures and thus tends to originate from a much broader range of zenith angles and so, on average, appears to be fairly close to zenith. However individual scatterers identified using the Doppler sorting techniques of section 5.4 can appear at large zenith angles, and limits are set to the zenith angles that are considered reliable in section 5.5.1 (where spatial interferometry measurements are applied to finding the velocity of scattering). The limits applied in that section are 10° for the Birdlings Flat radar and 15° for the Scott Base radar.

5.3 Frequency Domain Interferometry

Frequency Domain Interferometry (FDI) is based on similar considerations to the other forms of interferometry discussed in this chapter. However rather than observing changes in the path length in equation 5.2, δp is assumed to be zero and the radar wavelength is changed, (the wavelength is changed over very short time periods so that variations in the path length with time can be ignored). The phase of backscattered signals changes in proportion to the path length

$$\delta\phi = \delta k p. \tag{5.15}$$

In terms of the transmitting frequency of the radar, ω_T, and the range, r,

$$\delta\phi = \frac{2\delta\omega_T r}{c}, \tag{5.16}$$

where c is the speed of light, (again ignoring phase factors due to the components of the radar). With an appropriate choice of δk, the range of a scattering target can be measured to greater precision using an analysis of this form than is normally available using timing techniques. As shall be seen, FDI can also be used to provide a measure of the distribution of ranges if there is a distribution of scattering targets. Before this FDI analysis is considered further, the development of techniques that shift the operating frequency of radars will be briefly discussed.

Some of the earliest ionospheric work was carried out using frequency shifting techniques. For example, [Appleton and Barnett, 1925] confirmed the existence of the ionosphere (then known as the Kennelly-Heaviside layer) using a frequency modulated continuous wave and examining the interference between the ionospherically reflected wave and the ground wave. Similar techniques were used in early studies of the D region of the ionosphere, for example [Titheridge, 1962].

On pulse radars, one form of frequency shifting that is fairly widely used (including many VHF atmosphere radars) is pulse compression. This technique also enhances the range resolution of a radar and section 5.3.1 backgrounds this technique. This study is mainly concerned with frequency stepping techniques and these are considered in the remainder of section 5.3. Section 5.3.2 reviews the development of frequency stepping experiments, first in ionospheric work, then in studies of the middle atmosphere on VHF radar, and the recently commenced work on MF radar. FDI analysis itself is discussed in section 5.3.3.

5.3.1 Pulse Compression

The range resolution of a simple pulse radar depends on, amongst other factors, the length of the pulse transmitted by the radar. The length of pulse is usually a compromise between power and resolution; shortening a pulse improves the resolution but at the cost of the reducing the overall power of the pulse.

One method by which the resolution can be enhanced without a reduction in power is to use "pulse compression" techniques. Unlike ordinary pulse radars which transmit pulses made up of a more or less pure sinusoidal carrier wave, pulse compression radars transmit pulses that contain some form of information pattern encoded onto them. On encountering scattering targets different portions of the coded pulses are scattered at slightly different times and on return to the radar the signals effectively have extra information convolved on to them about the relative scattering times of each portion of the pulses. When backscattered signals are received, the signals are decoded using the reverse of the encoding process, and the extra information in the signals due to the scattering process is revealed.

An example of pulse compression is the scheme temporarily installed on the Birdlings Flat MF radar by [Krenek, 1977] using "chirping" techniques. The frequency of the transmitter was continuously varied by up to 100 kHz following a predetermined pattern (generating the "chirp") while it was transmitting its pulse. Backscattered signals received by the radar were spectrally analysed and the Fourier spectrum of the encoding pattern was used to remove the chirp pattern from the signals, leaving behind a profile of the scattering process.

The system Krenek developed was capable of a resolution of about 0.75 km, and he used it to produce a number of profiles of D, E and F region scattering clearly resolving sharp ledges in scattering in several cases. The difficulty with pulse compression techniques is that they require a high level of complexity both in the pulse encoding process (typically an electronic chirp generator) and in the decoding process (usually some form of spectral analysis). The speed of the data collecting system has to match the enhanced resolution of the system, a limitation that Krenek's system encountered, and there are has to be either a fast recording system or fast on-line analysis system.

5.3.2 Frequency Stepping

Frequency stepping techniques also attempt to make high resolution observations of scattering structures using shifting of the radar frequency. However rather than altering the frequency during the transmission of each pulse, the frequency is altered between pulses.

Individual pulses are therefore not encoded; they are (approximately) pure bursts of carrier wave like standard pulse radars. However the frequency of the carrier wave in each pulse can vary from pulse to pulse. As shall be seen in section 5.3.3, as the radar frequency changes from pulse to pulse, the phase of the backscattered signals varies in direct proportion to the range and to the size of the step in frequency. Also scattering depth can be determined by observing the variation in coherence as the frequency is shifted; highly localized scatter (for example specular reflections) is highly correlated from pulse to pulse as frequency changes; volume or random scatter is not.

To measure the range then, scattered signals originating from separate pulses at different frequencies are compared, rather than isolating portions of pulses at different frequencies as is done with chirp techniques.

Various techniques have developed for analysing frequency stepping experiments. One of the two more recent techniques is in many ways similar to pulse compression and thus has been referred to as discontinuous chirping. Applications of this technique to frequency stepping observations have not, as yet, been reported. The other recent method is the technique followed in this project, that of frequency domain interferometry. On MF radar as implemented in this project, frequency domain interferometry allows the location of sharply defined scattering centres to be identified to within about two hundred metres (compared to about three or four kilometres using conventional timing techniques).

The Development of Frequency Stepping Techniques

The first reported experiments using frequency stepping techniques to investigate scattering processes were that of [Briggs, 1951]. Briggs developed a radar that could operate in the range 2-20 MHz and could sweep its frequency at the rate of 1 MHz a second. The radar was used to study reflection processes in the E and F regions of the ionosphere and could clearly identify different scattering processes such Bragg scatter and Fresnel reflections.

The radar measured variations in the amplitude of scattered signals as the frequency of the radar was changed with film recording techniques (commonly used in early ionospheric work). Fringes, apparently due to interference between multiple signal paths, were often observed and these could be related to the degree of roughness of the scattering layers using the rate of the frequency sweep. Briggs used this information to make estimates of the thickness of layers he observed down to a resolution of one kilometre.

Also on some occasions the angular distribution of the scatter was estimated. This was done by assuming that there was a thin, rough scattering surface, and that the apparent

thickness, or the variation in range, of the scatter was due to scatter over a cone of angles, the components of scatter at greater range coming from furtherer from zenith. The frequency shift apparatus was also used for some critical frequency studies of the E region.

After some time with no further reports of frequency stepping experiments, [Uscinski, 1965] developed techniques to analyse the observations of frequency stepping experiments. Uscinski formed a model based on a rough perfectly reflecting surface and showed how sweep frequency observations could be used to determine both the depth and horizontal scales of the irregular surface as well as a measure of the magnitude of the horizontal velocity of the surface. He found correlation functions that show correlation of the signals as a function of frequency step. Uscinski modelled the expected correlation function of the scatter as the frequency was changed for different irregularity scales, showing how the correlation between signals of different frequencies falls with increasing roughness of the reflecting surface. In his model the velocity of the layer is estimated by assuming that the surface shape is unchanging and that changes in the scattered signal over time (at a fixed frequency) are due to the motion of the irregular surface over the radar. The scales of the surface irregularities are estimated using the correlation with frequency step function and from the rate of change with time in the scattered signal and the scale sizes of the irregularities, the magnitude of velocity of the layer could, in principle, be estimated.

Uscinski's techniques do not appear to have been applied to any experiments, in part because some of the assumptions in the analysis are somewhat unrealistic and because the only experiments carried out since that time have been very recent and adequate analyses have developed along side these new experiments. However the concept of a correlation function of the scattering at different frequency steps, here called the "frequency correlation function", is one that proved useful in this project. An example of a frequency correlation function is given in figure 5.3 below. Similar functions are used in the related field of considering the fluctuations of satellite or radio star radio wave sources due the passage of their signals through the ionosphere, for example [Budden, 1965].

Another related field is that of ionosonde scanning of the ionosphere. Ionosondes are radars that transmit pulses at a wide range of frequencies, typically in a sweep from 1 to 20 MHz and record the range of (generally) just total reflection as a function of frequency, [Davies, 1990]. Some ionosonde sounders also use frequency stepping techniques to improve their range resolution over that available by simple timing. An example is the Dynasonde of [Wright and Pitteway, 1979] where pulses are generated at a base frequency and at an 8 kHz offset. The phase change on this offset is used to estimate range to a

resolution of a few hundred metres. In other ionosonde work [Wright and Fedor, 1969] carried out cross correlations of sporadic E layer echoes at different frequencies with at various time lags and found that often the echoes on one frequency lagged behind echoes at a nearby frequency (typically $\delta f \sim 10$ kHz) by a few seconds. They concluded this was a result of vertical motion of the layers because echoes at different frequencies have different penetration depths and they correlated vertical motions found in this way with changes in the virtual height of the layers.

The first reference to frequency stepping in middle atmosphere radar work was that of [Stitt and Bowhill, 1986] who suggested using "frequency hopping" to improve the range resolution of VHF radars. They proposed transmitting a series of pulses, starting at a base frequency (in their example, the 40.52 MHz frequency of their radar at the University of Illinois at Urbana in the United States) and increasing the frequency at each pulse (by 50 kHz for 16 pulses). They suggested a Fourier transform method of analysis, transforming the variation in signal (and phase) on each step to give a range profile. (This type of analysis can be termed "discontinuous chirping", [Röttger and Larsen, 1990].) They illustrated this using an ideal mirror reflector, thus giving uniform changes on each step, showing that the range could be resolved to about 200 metres (the standard range resolution for their radar is 3 km). They claimed that similar resolution would be possible given more realistic scatterers.

Using the same VHF radar [Kudeki and Stitt, 1987] reported the first application of frequency stepping techniques to middle atmosphere radar and introduced the term "Frequency Domain Interferometry" (FDI). They pulsed at two frequencies, 40.82 MHz and 40.92 MHz and used a more straight forward analysis based on simple cross correlation of the signal received at the two frequencies. As will be discussed further below, this analysis provides a range and a depth of range (or layer "thickness" as they referred to it). They achieved a resolution of about 200 metres, and observed several instances of layers of about this thickness in their observations of the mesospheric scattering. The radar they used, like most VHF radars, normally operates as a Doppler beam swinging radar and thus has a fairly narrow antenna polar diagram.

[Franke, 1990] considerably developed FDI analysis. He showed how a discrete pulse compression analysis could be applied, which was a development of the ideas in [Stitt and Bowhill, 1986], using multiple frequency steps to produce a profile of scattering position. He also further developed the analysis of [Kudeki and Stitt, 1987] showing that the layer thickness and range given by them can be biased by contributions due to the weighting function of the finite radar volume. The weighting function is determined by factors such

as the transmitter pulse length and shape, as well as the antenna polar diagrams; the response of the radar is generally strongest towards the centre of the radar volume. The maximum thickness measurable by the FDI method is limited by the extent of the radar volume. Also if the polar diagram is broad, an overly thick estimates for a thin scattering layer would result, because scattering further from zenith to a layer at a particular altitude has a greater range than scattering from zenith which would be interpreted as scattering from a thicker layer.

The following simplified example illustrates the effect of a broad angular distribution of scatter. Consider a thin layer at altitude h that is scattering with aspect sensitivity θ_s. The difference in range between the scattering from the vertical and scattering at this width is $h(\sec\theta_s - 1)$. The definition of the scattering depth used here can be approximated by half of this difference. For example a thin layer at 80 km altitude with an aspect sensitivity of 10° (about the half power half width of the Birdlings Flat radar) would appear to have a scattering depth due to aspect sensitivity alone of the order of 600 metres. Note however that if the layer has its scattering limited either by a narrow antenna beam width or by aspect sensitivity to 5° then it would appear to have a scattering depth of around 150 metres.

For this reason Franke considered that radars with broad antenna beams would be able to make only limited FDI measurements. However this argument presupposes that scattering from thin layers is spread over a significant portion of the antenna polar diagram. If scattering is highly localized or highly aspect sensitive then the horizontal spread of the scattering is naturally limited. Franke did note that below about 80 km scattering from the mesosphere is generally more aspect sensitive and considered that broad beam radars would be able to make useful measurements there. As shall be seen localized scattering can appear at times in all parts of the mesosphere, allowing useful FDI measurements to be made on broad beam radars.

Further FDI observations were made by [Kudeki and Stitt, 1990], this time on the the Jicamarca VHF radar and again of the mesosphere. This report also expands on the analysis of their earlier study including the points raised by [Franke, 1990]. [Palmer et al., 1990a] applied FDI measurements to the Japanese MU radar obtaining measurements from the troposphere and lower stratosphere and using a similar analysis.

[Stitt and Kudeki, 1991] reported the first combined spatial and frequency domain interferometry measurements. Using the VHF radar at Jicamarca, the techniques were used to make isolated observations of particular events. For example using the variations direction of arrival from the spatial interferometry and the variations in range from FDI,

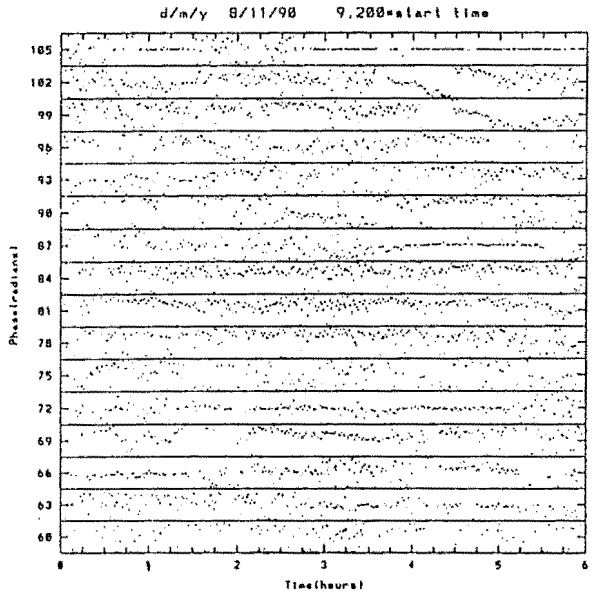

Figure 5.2: **Example of FDI on the Urbana MF radar.** Each panel represents a 3 km range gate and the dots show the range inside the gate as determined by FDI for a 64 second sample.

they were able to track distortions in thin layers due to the action of atmospheric gravity waves. Rather than using cross correlation functions between signals received on separate frequencies, cross spectral analysis techniques were used allowing determination of FDI range at different Doppler shifts.

Frequency Domain Interferometry on MF radar

As [Franke, 1990] pointed out, MF radars can be limited in their FDI observations by the broad beam width of their antennae smearing out range measurements. However highly localized or aspect sensitive scattering naturally limits the horizontal extent of scattering enabling FDI measurements of thin features. The first applications of FDI on MF radar were reported by [Stitt and Franke, 1991] at Urbana and by [Brown and Fraser, 1991] out of work associated with this thesis.

The Urbana MF radar began FDI operation in November 1990, and a sample of results taken then appears in figure 5.2. The radar operates at two frequencies 2.66 MHz and 2.71 MHz, (frequency difference of 50 kHz) and has an antenna beam of 15° – 18°.

Figure 5.2 shows the FDI range for a six hour sequence of 64 second samples (each dot) at 3 km range gates from 60 to 105 km. When the dots are scattered throughout the range gate, there is either no significant signal being received from that range gate, or the scatter there is highly disorganized. Frequently there seem to be stable rows of dots indicating stable layers in the scattering region. [Stitt and Franke, 1991] also measured coherence as frequency was stepped and relate this to layer thickness using the methods of [Kudeki and Stitt, 1987]. Associated measures such spatial interferometry, aspect sensitivity or velocity do not appear to have been available.

5.3.3 Frequency Domain Interferometry Estimation of Range and Depth

The frequency stepping observations made in this project were mainly analysed to determine an average range and depth of scattering for the data collected at a particular range gate. In general the approach here was to follow [Kudeki and Stitt, 1990] although elements of [Franke, 1990] were also used.

Let the instantaneous signal received on an antenna at two different frequencies be approximated by $E_1 = A_1 e^{ik_1 2r}$ and $E_2 = A_2 e^{ik_2 2r}$ where k_1 and k_2 are the wavenumbers of the two frequencies ($k = \frac{\omega}{c} = \frac{2\pi f}{c}$), and r is the range of the scattering centre, (here neglecting phase changes introduced by components of the radar). The time averaged product of the two signals is

$$\langle E_1 E_2 \rangle = \langle A_1 A_2 e^{i2\delta k r} \rangle. \tag{5.17}$$

where δk is the difference of the two wavenumbers. The cross correlation function (or the frequency correlation function of section 4.1.3) between the two signals can be given by

$$\rho(\delta k) = \frac{\langle A_1 A_2 e^{i2\delta k r} \rangle}{\langle A_1 e^{ik_1 2r} \rangle \langle A_2 e^{ik_2 2r} \rangle^*}. \tag{5.18}$$

Note that if there is a difference in gain between the E_1 and E_2 signals, the normalization leads to this canceling out.

If the scattering originates from a distribution of ranges, then the amplitude of the frequency correlation function will be less than one depending on the spread of the distribution. If the distribution of the scattering range is Gaussian, with mean $\overline{r}$ and standard deviation σ_r, the distribution can be described by

$$P(r) = e^{-\frac{(r-\overline{r})^2}{2\sigma_r^2}}. \tag{5.19}$$

[Kudeki and Stitt, 1987] describes σ_r in such a distribution as "layer thickness". Here σ_r shall be termed the FDI "scattering depth", since layer thickness assumes the variation

in range derives from scattering vertically distributed through a layer whereas here it is apparent that variation in range can also result from scatter spread horizontally as well as vertically.

The received signal of distributed scattering can be modelled by integrating over the distribution (for example [Uscinski, 1965] or [Doviak and Zrnic, 1984]). The distribution in equation 5.19 can be used as a weighting function. The frequency correlation function of such a distribution takes the form

$$\rho(\delta k) = \int e^{-\frac{(r-\overline{r})^2}{2\sigma_r^2}} e^{i\delta k \overline{r}} dr. \tag{5.20}$$

This integral can be solved using Fourier transform techniques to give

$$\rho(\delta k) = e^{-2(\delta k \sigma_r)^2} e^{i2\delta k \overline{r}}. \tag{5.21}$$

By this model the amplitude of the frequency correlation function then gives a measure of the scattering depth and the phase gives the mean range. This approach was the main method of FDI analysis used for examining the observations made in this project.

[Kudeki and Stitt, 1987] note if there a significant noise component to the signals equation 5.21 should be divided by $(1 + \frac{N}{S})$ where N and S are the noise and signal powers respectively. As discussed in section 4.1.3 in this work sufficient account of signal to noise ratios was made by interpolating the correlation functions through zero lag and the normalizing correlation function by the signal levels at both frequencies.

[Franke, 1990] extended Kudeki and Stitt's results to include factors such as the limited vertical extent of the radar volume, which thus limits the maximum scattering depth, and the beam width of the radar's antenna which can provide a lower limit to scattering depth as off vertical scatter increases the apparent depth. This was done by including weighting functions for these factors in an expression of the form of equation 5.21. The amplitude of the frequency correlation function Franke derived (adapting Franke's symbols to follow the notation used here), is given by

$$|\rho(\delta k)| = e^{-2(\delta k \sigma_{pr})^2} \frac{1}{\sqrt{1 + (\delta k \sigma_w^2)^2 / z_r^2}} \tag{5.22}$$

and the argument is given by

$$\angle\rho(\delta k) = -2(\delta k)^2 \left(z_r + \frac{4 z_l \sigma_{pr}^2}{\sigma_r^2} \right), \tag{5.23}$$

where σ_{pr} is the depth of the layer and radar volume together described by $\sigma_{pr}^{-2} = \sigma_p^{-2} + 4\sigma_r^{-2}$, ($\sigma_p = 0.35\frac{c\tau}{2}$, τ being the radar pulse length); σ_w is the depth of the radar volume

due to its width described by $\sigma_w = \sqrt{2} z_r \theta_b 0.3$; θ_b is the antenna beam width (half power full width), z_r is the range of the radar volume and z_l is the offset from this range of the range of the layer, $\overline{r} = z_r + z_l$. (Note that the definition of scattering depth Franke uses differs from that used here; Franke's depth was multiplied by $\sqrt{2}$ to obtain σ_r.)

The effects of directional scattering can be gauged by using aspect sensitivity in place of antenna beam width in this analysis (setting $\theta_b = 2\theta_s$ since aspect sensitivity is a half width measure). To consider the effect of the corrections of [Franke, 1990] compared to the analysis used here (equation 5.21), reasonably typical values of aspect sensitivity were included in this way and frequency correlation functions for layers of various depths were found.

Two examples of these correlation functions are given in figure 5.3. On the left are the frequency correlation amplitude and phase for a layer with a scattering depth of 200 metres with 5° aspect sensitivity. This layer is also offset from the centre of the range gate (set here to 80 km) by two kilometres to test the effect of scattering from near the edge of the radar volume (which is $4\frac{1}{2}$ km deep in this example). On the right is a layer with a scattering depth of one kilometre and aspect sensitivity of 10°, (approximately equivalent to the beam width of the Birdlings Flat radar thus the scattering would extend right across the radar volume there). A pulse length of 30 μs was used. The phases, and thus the FDI range $\overline{r}$, of the two correlation functions are indistinguishable from each other. The amplitudes do differ somewhat. At the 20 kHz step that was typically used in this project for determining scattering depth, the two approaches give estimates of scattering depth that differ from each other by about 40 metres and 20 metres for the left and right models respectively.

For deep scattering then, using a broad antenna beam with the analysis of equation 5.21 gives a similar result to using the analysis of [Franke, 1990]. For shallow scattering, if the spread of scattering is limited by localized scatter or by high aspect sensitivity then there are also similar results produced by the two approaches. However if there is shallow scatter, but wide aspect sensitivity the scattering depth found here would be too deep. Therefore if the scattering depth estimates found here are to be equated with layer thickness, the values found should be treated as an upper limit to the thickness of the layer enclosed by the radar volume.

It is possible to estimate aspect sensitivity using other measurements found in this project, and it would have been feasible to include these in an analysis such as [Franke, 1990]; however as noted in the discussion of these methods (section 3.3.1) these estimates also just place an upper limit on aspect sensitivity. As shall be seen the estimates of frequency

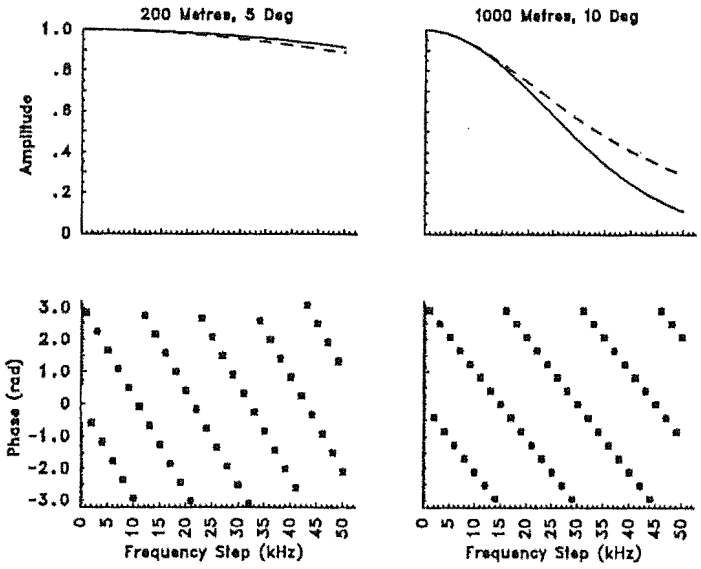

Figure 5.3: **Frequency correlation functions for two methods of analysis**, based on [Kudeki and Stitt, 1987] (solid line and crosses for amplitude and phase) and [Franke, 1990] (dashed line and pluses for amplitude and phase) for two scattering layers. The layers had scattering depth and aspect sensitivity of 200 m and 5°, and 1000 m and 10° for the functions on the left and right respectively.

correlation functions for the data observed in this project have considerable variability between the functions found on each of the three receivers and between similarly sized steps in frequency. This variability typically greatly exceeds the variation between the functions of figure 5.3. It was decided therefore to used the simpler analysis based on equation 5.21, [Kudeki and Stitt, 1987], as the main method of determining FDI scattering depth and range in this project.

5.4 Cross Spectral Analysis for Interferometry

The cross correlation function was found to be useful for comparing two data sequences in time domain analysis for interferometry and also for spaced antennae winds analysis. In spectral analysis, the Fourier components of the cross spectra ($Z_{12,k}$) are found using the components of the individual spectra, ($Z_{1,k}$ and $Z_{2,k}$).

$$Z_{12,k} = Z_{1,k}Z^*_{2,k} \tag{5.24}$$

$$= |Z_{1,k}|e^{i\phi_{1,k}}|Z_{2,k}|e^{-i\phi_{2,k}} \tag{5.25}$$

$$= |Z_{12,k}|e^{i(\phi_{1,k}-\phi_{2,k})} \tag{5.26}$$

As can be seen from equation 5.26, the phase of the cross spectrum is the difference in phase between the two series as a function of frequency. The cross spectral phase will be used here for interferometry analysis. It has also been shown that the cross spectrum can also be used for a form of spaced antennae winds analysis, [Briggs and Vincent, 1992].

Figure 5.4 gives an example of the cross spectrum of the synthesized data series of figure 4.1 with a second identical series added, except having different phase lags assigned to the various components. The two complex series and the cross spectral power and phase are shown. The phase was quite accurately determined in this case, as it generally was in all of the synthetic series tested.

Figure 5.5 gives an example of cross spectral analysis of signals observed on the Scott Base radar. The top panel shows the cross spectral power between signals received at separated antennae and the middle panel shows the cross spectral phase. Notice that around the spectral frequencies of the maxima of the power spectrum, the phase spectra displays greater consistency than at the spectral frequencies near the minima of the power spectrum. This figure just shows the spectra at one frequency (2.87 MHz); however in general the radars are pulsed at five frequencies and the mean cross spectra of these frequencies is found. As discussed in section 4.2.4 the peaks in the spectra found using FFT techniques are compared with peaks in Blackman Tukey or MEM spectra and those peaks which have similar magnitudes and spectral frequencies are identified as originating from distinct scattering centres. The phase spectrum at those peaks can be used to determine the direction of arrival of signals from those scattering centres using spatial interferometry techniques.

The cross spectrum of signals received at separated antennae has then "Doppler sorted" the phase differences due to the direction of arrival of the signals as a function of radial velocity. A minimum of three separated antennae, and two phase differences for each target are required to determine the direction of arrival; however as discussed in section 5.2, all

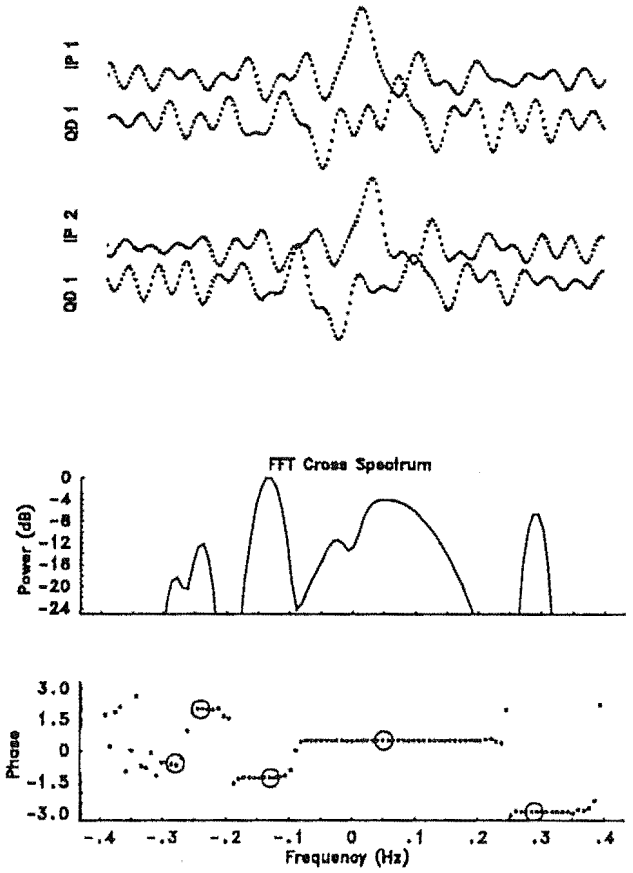

Figure 5.4: **Cross spectral analysis of two synthesized data sets.** The two data sets used were based on that of figure 4.1, with phase lags introduced between them. The two complex series are displayed in the upper part of the figure and the FFT cross spectrum is in the lower part. The dots in the phase plot are the cross spectrum of the two series and the circles at the peak frequency of the components indicate the phase lag introduced at those component frequencies.

three phase differences are used with a least squares regression fit. In section 5.5 it will be shown that given a spatial distribution of scattering centres, an estimate can be made of the average overall velocity of the scattering region, (for example [Meek and Manson, 1987]). Figure 5.6 displays a polar diagram showing the angle of arrival of signals from identified scattering centres for the same data as figure 5.5. In chapter 7 sequences of such diagrams found at different altitudes and times are shown.

The bottom panel of figure 5.5 shows the cross spectrum between data received on two different radar frequencies. In the section on frequency domain interferometry (section 5.3.3), it was shown how if the radar frequency is altered, the phase of signals returning

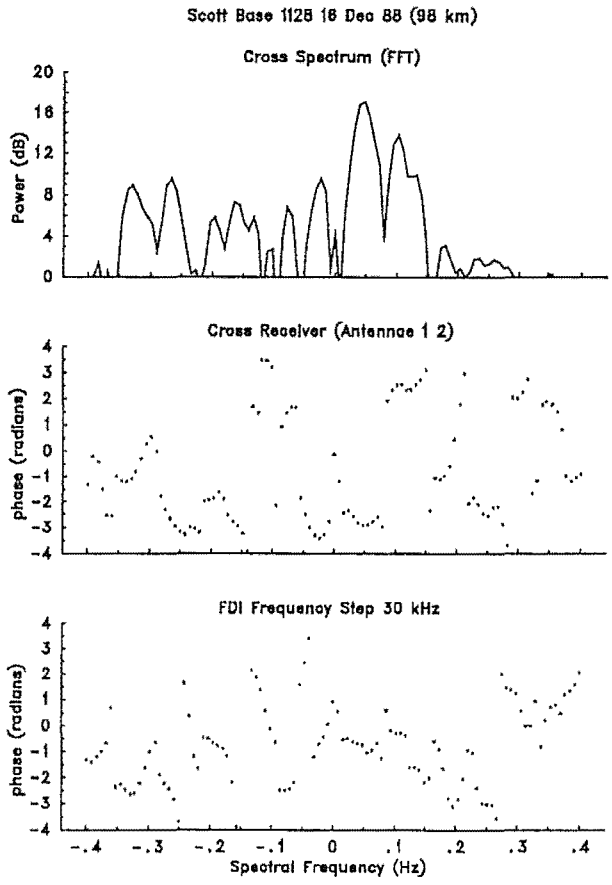

Figure 5.5: **Example of cross spectral analysis** of a one minute sample collected on the Scott Base radar. Cross spectral power and phase between signals received at two antennae (**1 & 2**) are shown and as is cross spectral phase between signals at two different frequencies (**step 30 kHz**). The spectra were found using FFT techniques.

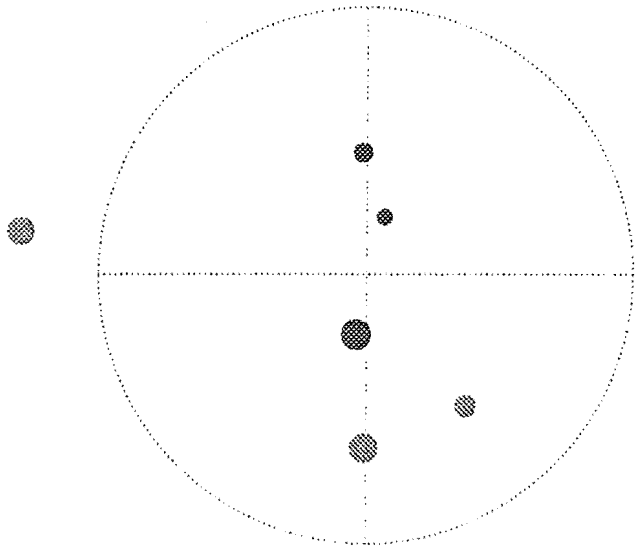

Figure 5.6: **Spatial Domain Interferometry from cross spectral analysis**, (data as for figure 5.5). The ⊕ symbol represents a sky map centred on zenith, extending out to 20° zenith angle with the vertical line indicating north-south and the horizontal line west-east. The grey/black dots indicate the location of scattering centres, the darker the dot the higher the scattered power, and the larger the dot, the broader the spectral width of the peak in the power spectrum.

from a scattering target shifts depending on the range or total path length the signal travelled. The cross spectrum of signals at different radar frequencies gives the Doppler sorted range as a function of radial velocity. The phase difference at the spectral peaks found above is assumed to correspond to the range of a scattering target moving with a Doppler shift of the peak frequency. There are three receivers and typically four radar frequency steps were used to find the range (the smaller steps gave smaller phase changes and were not retained) so each scattering target has up to twelve range estimates and the mean of these estimates was found.

5.5 Interferometric Velocities

Several studies have attempted to determine the velocities of scattering regions from interferometric measurements and spectral analysis. [Pfister, 1971] carried out cross receiver spectral analysis and established techniques for estimating the velocity of wave structures

in the E-region. [Farley et al., 1981] made radar interferometry measurements of the velocity of the equatorial electrojet with VHF radar. In mesospheric work, [Adams et al., 1986] first reported MF interferometric velocity measurements using their "Imaging Doppler Interferometer" (IDI) radar which consisted of evenly spaced rows of antennae aligned east-west and north-south in a cross-hatch arrangement. [Meek and Manson, 1987] first made MF interferometric observations of the mesosphere using a spaced antennae radar and compared their interferometric velocities with velocities found using FCA. [Franke et al., 1990] made similar comparisons experimenting with spectral averaging and obtained varying results.

The procedures used by these various authors have differed in details such as spectral averaging, regression weighting and data selection which has made for somewhat mixed results when comparisons are made between interferometric and FCA measurements. Generally the procedures followed start by locating Doppler sorted scattering centres using the cross spectral analysis, then using the Doppler velocity to infer the overall velocity. (Although some workers, such as [Pfister, 1971], used the slope of the cross spectral phase across a range of Doppler frequencies to determine velocity rather than tracking targets.)

5.5.1 Determining Interferometric Velocity

The identification and location by spatial interferometry of scattering centres as was carried out in this project was discussed above in section 5.4. A scattering centre i, whose line of sight direction from the radar has zenith and azimuth angles (θ_i, α_i), appears to have a radial velocity v_{rad_i} if it is moving with eastward, northward and vertical components (u_i, v_i, w_i), where

$$v_{\mathrm{rad}_i} = u_i \sin\theta_i \sin\alpha_i + v_i \sin\theta_i \cos\alpha_i + w_i \cos\theta_i \tag{5.27}$$

There are of course, too many degrees of freedom in equation 5.27 to determine (u_i, v_i, w_i) for each observed scattering centre. However if several scattering centres are observed, an "average" velocity (u, v, w) can be deduced provided the velocities of each the centres are not too dissimilar.

$$v_{rad_i} = u \sin\theta_i \sin\alpha_i + v \sin\theta_i \cos\alpha_i + w \cos\theta_i \tag{5.28}$$

Three estimates are required to uniquely solve equation 5.28. If more are available then a best fit regression analysis can be used to minimize the sum of the deviations between the observed Doppler velocities and the line of sight components of the average velocity

estimate, ([Adams et al., 1986]). This sum provides a measure of the goodness of the best fit that will be referred to below as the radial velocity RMS standard deviation, $\sigma_{v_{rad}}$,

$$\sigma^2_{v_{rad}} = \frac{1}{n}\sum_{i=1}^{n}\{v_{rad_i} - (u\sin\theta_i\sin\alpha_i + v\sin\theta_i\cos\alpha_i + w\cos\theta_i)\}^2 \qquad (5.29)$$

The regularly spaced antennae of [Adams et al., 1986] provided a straight line relationship between phase and antenna number, given an ideal scattering centre. The RMS deviation from the straight line was used as a weighting function when carrying out the regression analysis for velocity[1]. [Meek and Manson, 1987] used a different weighting function, based on the amplitude of the cross spectra at the Doppler frequency of the scattering centres. However they found the resulting velocities were insensitive to the amount of weighting used. Meek and Manson (like [Adams et al., 1986]) had redundant cross spectra due to an extra receiving antenna and applied a phase difference consistency criterion to test the spatial interferometry analysis of the scattering centre.

The spectral domain spatial interferometry of section 5.4 compared spectral peaks of periodograms and MEM spectra and declared consistent peaks to be scattering centres. However there were typically only two or three of these consistent peaks per sample. When the consistent peak scattering centres were run through the interferometric velocity analysis less than 10% of the samples produced a result. Therefore the periodogram spectra with generally between five and ten dominant peaks per sample were used producing a result for over 50% of the samples. The periodograms are means of usually fifteen spectra (five frequency steps and three receivers) which should reduce many of the spurious peaks, although some of the peaks that remain and are treated as scattering centres, undoubtedly are spurious.

If the vertical velocity is assumed to be zero ($w = 0$ in equation 5.28), then two scattering centres in each sample are sufficient to estimate velocity. The horizontal velocity with vertical velocity set to zero was found using the consistent peak spectra to compare against the full interferometric velocity found using periodograms. [Meek and Manson, 1987] also found interferometric velocity with vertical velocity set to zero, terming this the "two dimensional velocity", and the full interferometric velocity, "three dimensional velocity".

Given sufficient scattering centres spread uniformly throughout the radar volume, the variation of the wind field through the radar volume could be estimated. In this study however, it was found that in general there was insufficient confidence in the location of the scattering centres to determine the variation.

[1] Recently submitted work by the same group [Brosnahan and Adams, 1990] abandons this scheme on the grounds that it weights the antenna phases unevenly.

Acceptance Criteria

A series of acceptance criteria were invoked to remove scattering centres for which the spatial interferometry was deemed to be unreliable and velocity estimates that were considered to be non-physical.

In common with the other analysis procedures in this project, the signal to noise ratio of the sample had to be above a certain level.

- Signal to noise ratio of the sample has to be greater than 0.5 (-3 dB).

If the zenith angle of a scattering centre is too large, the phase difference of scattered signals as detected at the spaced antennae can be larger than π and an ambiguity in the measured phase difference can result leading to an erroneous calculated direction. For example a scattering centre with a zenith angle of 20° on the Birdlings Flat radar may appear to have a zenith angle of 10° in the opposite direction. Fortunately, the finite width antenna beams of the radars reduces the signal scattered from points with a large zenith angle so that scattering from zenith angles at, say, 20° is less likely to be identified as originating from scattering centres for the purposes of this experiment.

- The zenith angle has to be less than 10° at Birdlings Flat and 15° at Arrival Heights.

The uncertainty in the spatial interferometry position is of the order of one or two degrees and the zenith angle of scattering centres closer than this to directly vertical may be interpreted as having the wrong sign. Also the closer a scattering centre is to zenith, the larger is the relative uncertainty in inferring the horizontal velocity from the radial component. therefore

- the zenith angle is to be greater than 2°.

The horizontal velocity estimate is largely a function of the difference in Doppler velocity with angular separation of the line of sight of the scattering centres. If the scattering centres are clustered closely together, the small differences in Doppler shifts can result in large errors in velocity. Therefore a check was made that

- at least two pairs of points have angular separations of more than 5°.

The velocity vector was then determined using least squares regression on equation 5.28. The following checks were then made to remove extreme estimates.

- The rms standard deviation of the estimated velocity from observed radial velocity (square root of equation 5.29) has to be less than 20 ms^{-1},

- the horizontal velocity had a magnitude less than $300\,\mathrm{ms}^{-1}$ (the approximate speed of sound in the region) and
- the vertical velocity was less than $50\,\mathrm{ms}^{-1}$.

The above acceptance criteria were both relaxed and tightened in order to test various situations. For example, when the vertical velocity was forced to be zero, (finding just the two dimensional horizontal velocity), the criteria were relaxed in that only one pair of scattering centres had to have a separation of 5°.

5.6 Postbeam Steering

Postbeam steering (or sometimes **postset** beam steering) is an interferometric method whereby the signals received at each of the spaced antennae are added together. Combining the received signals in this way simulates the output of a single antenna that has a polar diagram equivalent to the combined polar diagrams of the individual antennae. The combined polar diagram is somewhat narrower than, and in general has a more complicated shape than the polar diagrams of the constituent antennae.

If an appropriate phase shift is added to each receiver output before adding to the others then the resultant beam can be "steered" in various directions. The polar diagrams of the constituent receiving antennae must greatly overlap to ensure the received signals that are added together originate from the same scattering centres. Also when steering, allowances should be made for the polar diagram of the transmitting antenna and the beam should not be steered to outside the transmitter polar diagram.

The method was introduced to atmospheric work by [Vincent and Röttger, 1980] on the German SOUSY VHF radar. [Röttger and Ierkic, 1985] made measurements such as determining wind velocity from the variation of Doppler shift as the beam was pointed in different directions. A further development of the method is "poststatistics steering", [Kudeki and Woodman, 1990] and [Palmer et al., 1990b]. Poststatistics steering involves synthesizing the new beam using the statistics (for example the spectra) of the constituent received signals rather than the raw signals from each beam themselves. This is somewhat more efficient in computational terms than postset beam steering.

In this project just the simpler postset beam steering method was used. Also the technique was used only for qualitative analysis to demonstrate its potential usefulness in building up a pictures of scattering processes. Images were formed of the variation of measured parameters, such as the signal power or the mean Doppler shift, as the beam was steered in different directions.

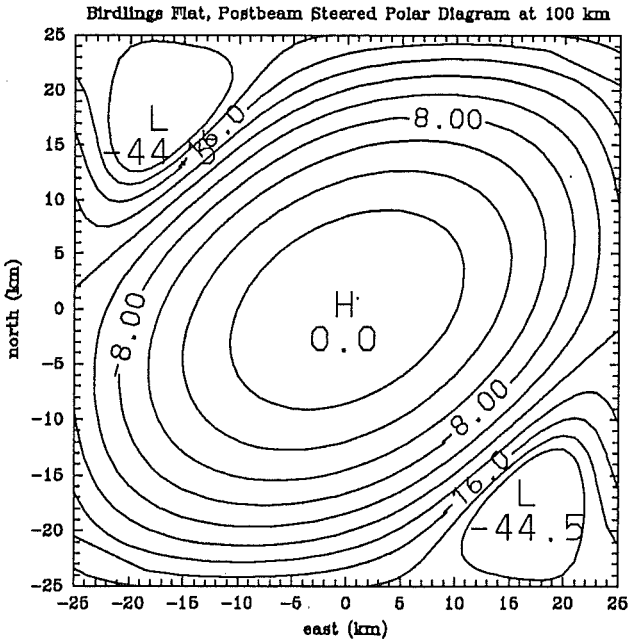

Figure 5.7: **Postbeam antenna diagram for the Birdlings Flat radar**, with the steered beam pointed to zenith. The polar diagram of the transmitter array is included.

A difficulty was that the polar diagram of the postset beam, although narrower than the constituent receiver beams, was still quite broad. For example the polar diagram of combined beam steered to zenith on the Birdlings Flat radar is shown in figure 5.7, calculated using the radiation pattern program discussed in section 2.1.2. The pattern is somewhat uneven, being elongated along north-east to south-west directions. With the inclusion of the polar diagram of the transmitter array, the half power full width of the diagram is very similar to that of the transmitter array at 16° along the dipoles (approximately east-west) and 18° across the dipoles.

With such a broad beam the images formed will have quite low resolution. If a rigorous analysis were to be attempted using a beam this broad, effects such as beam broadening, [Hocking, 1983b] (discussed in section 3.2), would need to be considered. For example if there is very strong scatter from some localized point, signals received when the beam was steered well away from that point may still be biased towards the characteristics of the strong scatter, an effect often apparent on beam steered radar, [Röttger, 1981].

Here the beam was steered to rectangular coordinates at different range bins, typically to points 5 km apart on a grid 50 km square which with the broad beam width means that the images formed are considerably over sampled. An example is figure 5.8. The lower

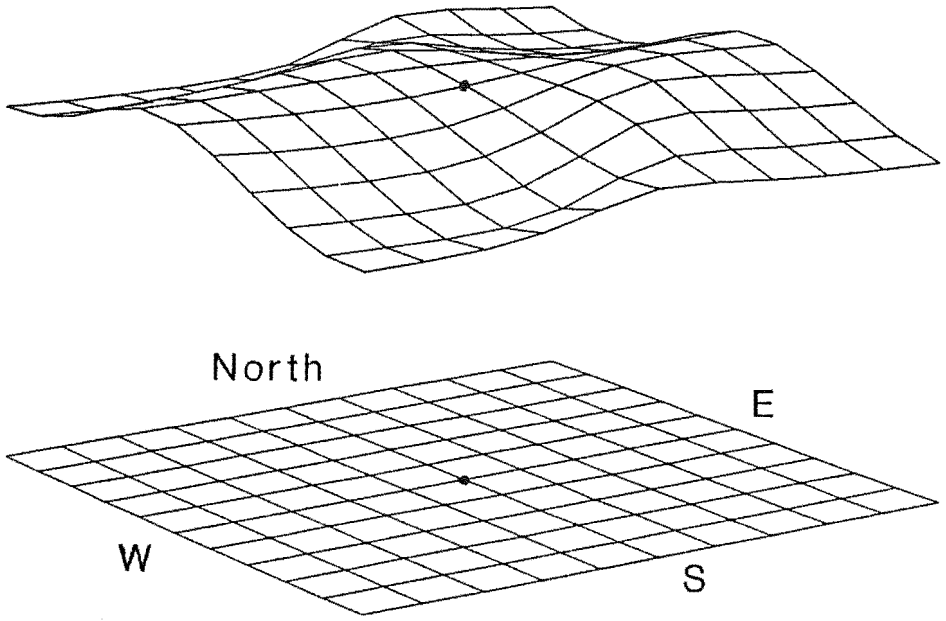

Figure 5.8: **Example of postbeam steering.** The direction of view used in the postbeam steering images presented here is indicated by the flat surface in the lower part of the figure, the central point of the grid being zenith. The upper surface gives an example of the variation in Doppler shift seen by the steered beam. Data collected on 6 October 1990, at a range of 89 km at 10:09. The depth of the surface is approximately 2 Hz, the lowest point being about -1 Hz and the highest point is about 1 Hz.

surface is flat with no variations across it to indicate the inclined viewing angle and the coordinates used in these images. The upper surface gives an example of the variation in the mean Doppler shift of signals as the beam is steered to different grid points.

Surface images such as these were used to display postbeam steering results to emphasize that variations across the viewing area are important, rather than the actual magnitudes of the parameters they display. The smoothness of the surface plots also emphasizes the coarseness of the images.

Frequency domain interferometry was also attempted in conjunction with postset steering. The change in phase as the frequency was stepped with the beam steered to some grid point was compared to the phase change with the beam steered to zenith. The difference of the phase changes gives the difference in range between each grid point and the zenith grid point. An example is given in figure 5.9. The results of more conventional interferometry

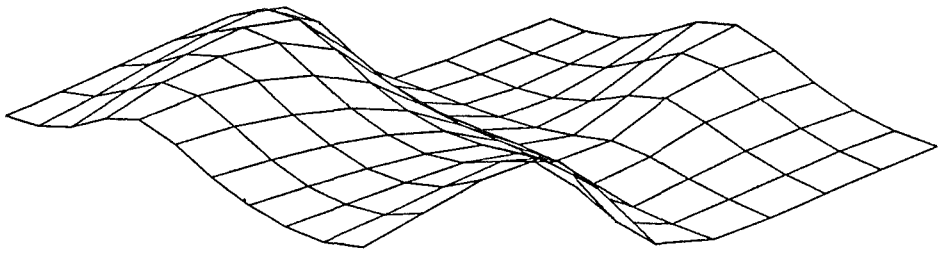

Figure 5.9: **Example of postbeam steering, variation in FDI range** as the beam is steered to a grid map. Data as for figure 5.8. The depth of the surface is approximately 200 metres.

for the same data will be compared with postbeam steering images in section 7.11.

It should be noted that at the corners of these images, where the zenith angle is 21°, the altitude is in principle approximately 7 km lower than at the central point. However because of the broadness of the steered beam the actual altitude of the data corresponding to the outer edges of the image is probably much closer to that of the central point. Figure 5.9 shows the variation in range not altitude, and so perhaps should be presented more as the surface of a sphere, however small variations in range can be seen more clearly when these results are shown as they are here.

The images of figures 5.8 and 5.9 are of the standard one minute samples used in this projects. Sequences of these images were formed for most of the five hour data sets collected on the Birdlings Flat radar and short sections of these will be presented in section 7.11. (Also in section 7.11 an image of the postbeam steered signal for this same data figures 5.8 and 5.9 appears).

Chapter 6

Spaced Antennae Drifts

6.1 Background

The Spaced Antennae Drifts (SAD) experiment is a procedure developed over many years for measuring wind and spatial and temporal scales of scattering structures. The basic premise is that radio waves scattered from structures in the atmosphere form fluctuating diffraction patterns on the ground which move around in a fashion that can be related back to the motion of the structures. As discussed in section 1.4.2, the diffraction pattern is sampled by receiving antennae that are separated, or "spaced", on the ground.

Much of the early work in the development of the technique was with observations of the ionosphere. The comparable nature of signals received on two separated (or "spaced") antennae, but with time delays between similar features of the separated signals, was first reported by [Pawsey, 1935]. The observations were taken to indicate a movement of some reflecting surface in the ionosphere. The surface also appeared to be changing in some manner as it moved along.

The next step was taken by [Mitra, 1949] who attempted to measure the velocity of the reflecting surface using three separated receiving stations. The rate of motion was estimated by finding the time delay between peaks of the signal observed on each station. The analysis used ignored the effect of random changes in the reflecting surface and the effect of a directional, or "anisotropic", bias in the structure of the surface features. The velocity found without allowing for these effects is termed the "apparent" velocity in drifts analysis. Both the random changes and anisotropic bias effects were subsequently found to be important.

An early summary of some of these measurements is [Briggs and Spencer, 1954] who include a report of a local spaced antennae drifts experiment. This experiment was run at

Lower Hutt, New Zealand, by the Department of Scientific and Industrial Research using a 2 MHz radar making E region drift measurements as early as September 1952.

A major development was the use of correlation functions, (section 4.1). As discussed in section 4.1.1, the auto correlation function can provide a measure of signal to noise ratios and scale the fading time of a varying signal. The cross correlation function can be used to find the correlation between separated receivers over a range of time lags. [Briggs et al., 1950] used correlation functions to develop "Full Correlation Analysis" (FCA) that allowed for the effect of the diffracting screen randomly changing. The drift velocity, and spatial and temporal scale were all estimated by the analysis. [Phillips and Spencer, 1955] showed how full correlation analysis can be extended to allow for anisotropic diffraction patterns. ([Briggs and Vincent, 1992] recently developed an analysis that uses spectra and cross spectra of signals received on spaced antennae rather than correlation functions, however only standard correlation function analysis will be considered here.)

An early application of FCA to partial reflection observations in the upper mesosphere and lower thermosphere was [Fraser, 1965]. FCA is now widely used on MF radars and is being increasingly used with VHF radars to measurement winds in the middle atmosphere. Many papers have been published on the FCA technique itself. some of these will be mentioned in section 6.2 where an outline of the procedure is given. The practicalities of applying FCA to middle atmosphere radars has been discussed by [Fraser, 1984a]. The technique and an analysis of its capabilities was also the subject of an extensive review by [Hocking et al., 1989]. This review also discussed uncertainties associated with the technique, some of which were considered here in the discussion on correlation functions in section 4.1.4 (particularly those points raised by [May, 1988]).

Various objections to the spaced antennae technique have been raised. For example if there are specular reflections from sharply defined layers that are distorted by, for example, a gravity wave, and if these distortions are sufficiently large to dominate the fluctuations in the diffraction pattern on the ground, then FCA traces the motion of the distortion rather than the background wind, (for example [Hines and Rao, 1968]). This objection does appear to have validity for total reflections in the E and F regions of the ionosphere; however lower down and into the middle atmosphere scattering processes are more complicated. Continuous sheets of specularly reflecting layers that could be distorted by waves are rare. The specularly reflecting layers that do occur are more intermittent in time and space. [Hocking et al., 1989] examined the effect of gravity wave distortion of specular reflector on FCA results. In their review they concluded there had been few reported cases

where specularly reflecting sheets in the middle atmosphere were sufficiently extensive to lead to domination of the diffraction pattern by such distortions. The intermittent nature of the reflecting structures, being blown along with the background wind, would lead to fluctuations being dominated by the wind rather than the waves (a conclusion also reached by [Hines, 1990c]).

There has also been some uncertainty as to how precisely the electron density (and thus the refractive index) fluctuations that give rise to the drifting diffraction pattern follow the motion of the neutral atmosphere. In the D region and lower E region, the collisional frequency between electrons and the neutral atmosphere is very high and below 100 km, there is little evidence that electrons could move independently of the wind, although the situation begins to change above this level. Between 100 - 110 km alignment of the diffraction pattern with the Earth's geomagnetic field has been observed, [Stubbs, 1977] (this effect is mentioned in section 7.5). In polar regions in particular geomagnetic effects can influence velocity measurements, [Reid, 1983], as discussed in section 1.2.2. It should be noted however that such effects would influence any radar observations, not just FCA measurements.

Comparison studies between the FCA method and other techniques provide the most convincing evidence for the validity of the results of FCA.

6.1.1 Comparison Studies

Comparison studies between FCA winds and the other radar techniques of Doppler beam swinging and spatial interferometry are discussed in sections 1.4.4 and 7.8.1 respectively.

Spatial interferometry tracks scattering centres using angle of arrival and Doppler information to determine velocity. Implementation of the technique varies somewhat in procedure from study to study; however in general good agreement between FCA and interferometry results is found, (for example [Meek and Manson, 1987]).

Doppler beam swinging involves measuring the Doppler shift of scattering received on antenna with very narrow polar diagrams pointed in various directions and inferring the wind field from these measurements. Comparison studies between Doppler beam swinging and FCA include [Vincent et al., 1987], who, in a quite extensive tropospheric study, were also able to compare both techniques with radiosonde (balloon) wind measurements. Very good agreement between the three methods was found by these workers.

In the D region, early studies showed that the technique was reliable. For example [Fraser and Kochanski, 1970] compared FCA measurements at the Birdlings Flat site with measurements made at other sites with methods such as meteor winds (the ionization trail

is tracked by radar) and chemical trail releases from rockets and found that very similar features were seen in the measurements from the various sites. Also at Birdlings Flat, [Fraser and Vincent, 1970] estimated the magnitude of the velocity of coherently reflecting layers using phase height techniques and were able to compare some of these measurements with velocity measurements made by FCA. The two methods showed good agreement.

More extensive simultaneous comparison studies in the mesosphere have also produced very similar results between FCA and other methods. For example [Vincent et al., 1977] compared FCA and tracking of inflatable spheres dropped from rockets and [Stubbs, 1973] compared FCA and meteor winds. Other comparison studies are discussed by [Hocking et al., 1989].

Another technique which can obtain wind measurements in certain regions of the middle and upper atmosphere is that of Fabry-Perot interferometry observation of airglow, (reviewed by, for example, [Hernandez, 1980]). This technique measures the shifting of spectral lines in airglow layers in various directions and relates the shifts in the different directions to Doppler shifting by wind. Some limited comparisons between wind measurements obtained by this method and FCA have been made. [Lloyd et al., 1990] operated an MF spaced antennae radar and a Fabry-Perot interferometer at a University of Saskatchewan site near Saskatoon, Canada. Comparisons between atomic oxygen (557.7 nm emission) airglow winds centred around 97 km and the radar winds produced very similar measurements, although only limited measurements were able to be directly compared.

6.2 Full Correlation Analysis

Full correlation analysis interprets auto and cross correlation functions of the signals received at spaced antennae to estimate the wind and spatial and temporal scales of scattered signals.

There have been several reviews of the actual procedure of FCA since the original work of [Briggs et al., 1950] and [Phillips and Spencer, 1955]. These include [Briggs, 1968], [Brown and Chapman, 1972], [Meek, 1980] and [Briggs, 1984]. These papers are based on the same ideas as the original works although they differ from each other to varying degrees in the way the procedure is carried out. The procedure followed here was that of [Briggs, 1984] because it was considered here that the geometric approach of this work was particularly straight forward.

6.2.1 The Full Correlation Analysis Procedure

The Full Correlation Analysis procedure starts with a time series of samples ($E(t)$), of a diffraction pattern as it drifts past a receiving antenna, first finding the auto correlation function,

$$\rho(\tau) = \frac{\langle E(t)E^*(t+\tau)\rangle}{\langle E(t)E^*(t)\rangle}, \tag{6.1}$$

at a range of time lags (τ). Here E is assumed to be a complex series with zero mean, E^* is the complex conjugate of E, and $\langle\rangle$ denotes averaging. The signal to noise ratio of the series is estimated from the auto correlation function and the noise portion found is removed as discussed in section 4.1.1. Generally the auto correlation function (with noise removed) is found at each antenna; then the auto correlation functions of all the antennae are averaged together. Ideally all the auto correlation functions are identical for a random pattern but in practice they tend to differ somewhat.

To determine the spatial scales and velocity of the diffraction pattern, the cross correlation functions of pairs of separated antennae are required. The complex cross correlation function for a pair of receiving antennae, i and j, separated by $\delta\epsilon_{ij}$ (which has eastern and northern components $(\varepsilon_{ij}, \eta_{ij})$) is given by

$$\rho(\varepsilon_{ij}, \eta_{ij}, \tau) = \frac{\langle E_i(t)E_j^*(t+\tau)\rangle}{\sqrt{\langle E_i(t)E_i^*(t)\rangle\langle E_j(t)E_j^*(t)\rangle}}, \tag{6.2}$$

where $E_i(t)$ and $E_j(t)$ are zero mean complex time series observed at antennae i and j respectively. Typical auto and cross correlation functions of series of observations of a diffraction pattern drifting past separated antennae take the form shown in figure 6.1.

In the remainder of this section and in FCA work generally, only the modulus of the auto and cross correlation functions are used. Hereafter in this section, ρ refers to $|\rho|$ in equations 6.1 and 6.2 unless otherwise stated.

The time lag for the cross correlation function in figure 6.1 to reach a maximum (τ'_{ij}), is taken to be the time delay due to the apparent velocity drift of the diffraction pattern past the pair of antennae. As can be seen from figure 6.2, the apparent velocity vector can be taken to be a projection of the implied velocity along the direction of the two antennae given the observed time delay ($\delta\epsilon_{ij}/\tau'_{ij}$). If two antenna pairs are available (that aren't collinear with the pair (i,j)), the apparent velocity can be found. We shall see below that if, as is usual, three pairs are available then a least squares regression procedure can be applied to determine the apparent velocity.

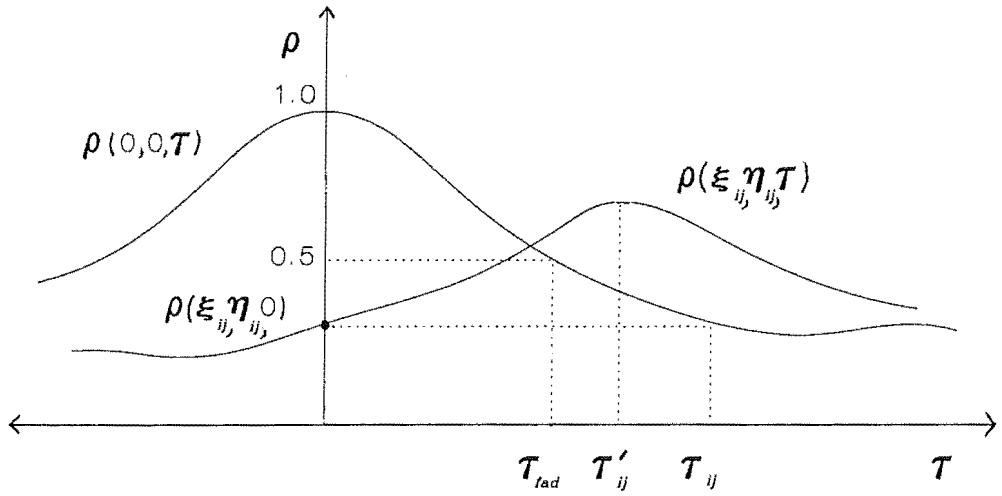

Figure 6.1: **Idealized auto and cross correlation functions**, $\rho(0,0,\tau)$ and $\rho(\varepsilon_{ij},\eta_{ij},\tau)$, of a diffraction pattern drifting past separated antennae i and j. Time parameters found from the auto and cross correlation functions, τ_{fad}, τ_{ij} and τ'_{ij}, are also indicated.

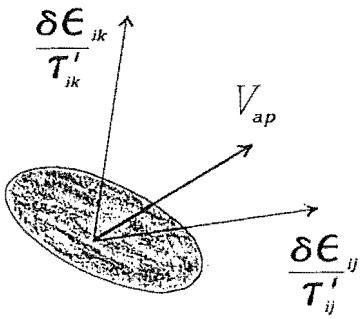

Figure 6.2: **Apparent velocity as projected from the time delays on antenna pairs** (i,j) separated by $\delta\epsilon_{ij}$ and (i,k) separated by $\delta\epsilon_{ik}$. Notice that the implied velocities $\delta\epsilon_{ij}/\tau'_{ij}$ and $\delta\epsilon_{ik}/\tau' ik$ are not components of the apparent velocity V_{ap}, along the antenna pairs but are projections of V_{ap} along the pairs. The shaded ellipse models a diffraction pattern drifting past.

The apparent velocity can be affected by changes in the diffraction pattern as it drifts along. Consider a randomly fluctuating pattern[1] that is drifting past two closely spaced receiving antennae aligned with the motion. The cross correlation function between the series observed at the antennae is found. Random fluctuations propagating past both

[1] [Briggs, 1984] uses the analogy of the surface of a boiling liquid.

antennae contribute to the cross correlation estimate at the time lag corresponding to the time of travel. The contribution depends on the degree of change the features undergo during the travel time. Those fluctuations that happen to propagate in the same direction as the motion contribute to a higher correlation coefficient at shorter time lags than would be the case if the pattern were not changing. Fluctuations travelling in the reverse direction are not so highly correlated at the longer time lags they take to drift past as they have more time to evolve to a different form. The net result of the random changes is to bias the peak cross correlation to shorter time lags leading to a higher apparent velocity than a non-changing pattern.

If the diffraction pattern is systematically elongated in some direction (other than along or perpendicular to the direction of travel) then the time difference between series received at aerials not aligned to the direction of travel can be increased or decreased, (see figure 6.3). This "anisotropic" nature of the drifting diffraction pattern leads to a bias of the apparent velocity vector towards a direction perpendicular to that of the elongation, [Phillips and Spencer, 1955].

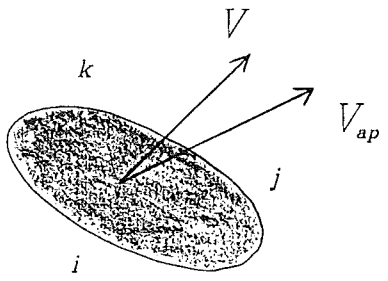

Figure 6.3: **An anisotropic diffraction pattern** represented here by elliptical shading, drifting at velocity V, over three antennae, (i, j, k). In this situation, an antenna at j records the presence of the pattern earlier than would be the case if the pattern were circular. Similarly k records the presence of the pattern later. The net effect in this case would be an apparent wind measurement such that indicated by V_{ap}.

FCA attempts to minimise the random changes and anisotropic effects by matching the temporal and spatial correlation functions of the diffraction pattern. The cross correlation function of an antenna pair at zero time lag is a measure of the spatial correlation function at the separation of the pair. If a large number of antenna pairs at a range of ε and η separations were available a comprehensive picture of the spatial correlation function could

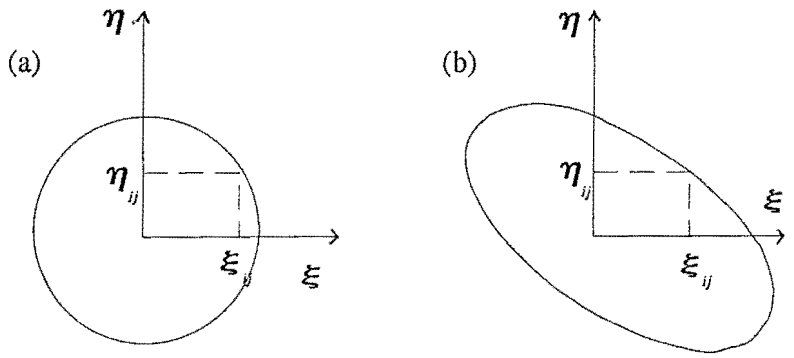

Figure 6.4: **Spatial correlation functions** showing cross correlation (at time lag $\tau = 0$), amplitude contours in the (ε, η) plane. (a) shows a circular diffraction pattern. (b) shows first order anisotropic pattern which can be parameterized as ellipses, $A\varepsilon^2 + B\eta^2 + 2H\varepsilon\eta = constant$. The marked point at $(\varepsilon_{ij}, \eta_{ij})$ on both figures can be matched to the marked point at $\rho(\varepsilon_{ij}, \eta_{ij}, 0)$ in figure 6.1.

be built up. For an isotropic diffraction pattern, the spatial correlation should also be isotropic, falling off evenly in all directions. A contour map in (ε, η) space of an isotropic spatial correlation function should display concentric circular contours, (one of which is modelled in figure 6.4a).

If the pattern is anisotropic, then to first order the elongated pattern can be modelled by stretching the spatial correlation in the direction of the anisometry. This stretching transforms the concentric circular contours into ellipses, (figure 6.4b). The ellipses take the form (generally following the notation of [Briggs, 1984]),

$$\rho(\varepsilon, \eta) = \rho(A\varepsilon^2 + B\eta^2 + 2H\varepsilon\eta). \tag{6.3}$$

Time evolution is modelled in FCA by the inclusion of a temporal axis orthogonal to the spatial correlation plane of figure 6.4. Three dimensional contour surfaces of temporal/spatial correlation amplitude are then formed in $(\varepsilon, \eta, \tau)$ space. The assumption is made that temporal correlation function has "the same functional form", [Briggs, 1984], as the spatial correlation function. This matching of forms models the correlation surfaces as ellipsoids. If there is no overall motion, this scheme just adds the term $K\tau^2$ to equation 6.3,

$$\rho(\varepsilon, \eta, \tau) = \rho(A\varepsilon^2 + B\eta^2 + K\tau^2 + 2H\varepsilon\eta). \tag{6.4}$$

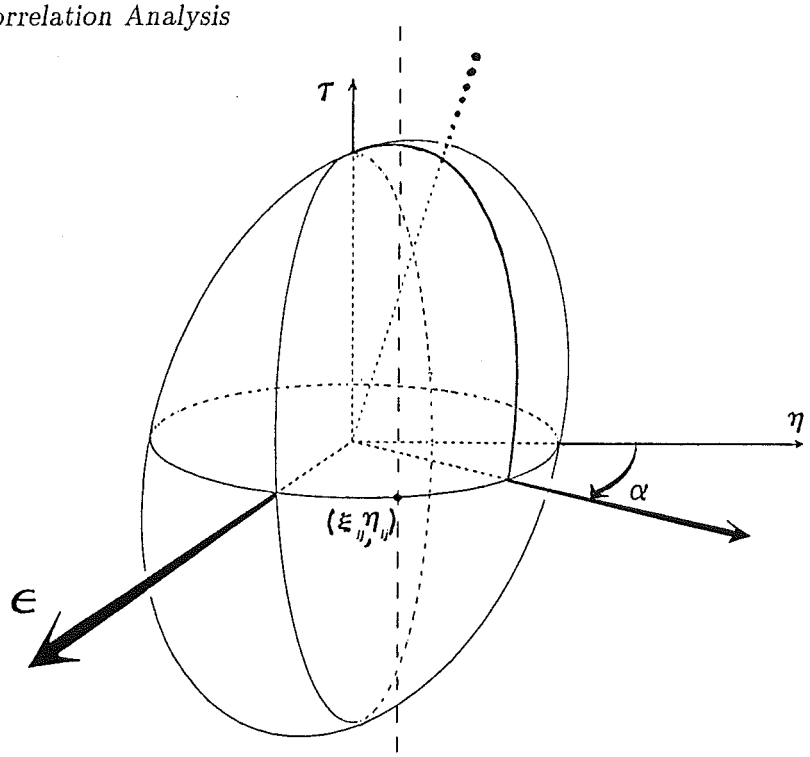

Figure 6.5: **Correlation ellipsoid** surface of constant correlation amplitude for a moving diffraction pattern. The velocity (directed at angle α from north) is the inverse of the slope of the tilted axis (dotted line up out of the page) of the surface with respect to the (ε, η) plane. The auto and cross correlation functions of figure 6.1 correspond to the τ axis and the vertical dashed line at $(\varepsilon_{ij}, \eta_{ij})$ respectively. The functional form of the correlation functions would only be displayed by the spacing of concentric ellipsoidal contour surfaces in this diagram.

It is important to note that the form of the correlation functions as a function of spatial and temporal lags is not set by the ellipsoidal surfaces, although the spatial and temporal components are expected to have the same form. The functional form itself is only displayed in the ellipsoid contour surfaces by the separation of those surfaces.

Motion of the diffraction pattern tilts the ellipsoids away from the temporal axis adding terms containing the product of temporal and spatial components,

$$\rho(\varepsilon, \eta, \tau) = \rho(A\varepsilon^2 + B\eta^2 + C\tau^2 + 2H\varepsilon\eta + 2F\varepsilon\tau + 2G\tau\eta). \tag{6.5}$$

The coefficient of the τ^2 term has changed because motion adds an extra variability (or fading) term to the time series seen at each antenna leading to a sharper fall off in the auto correlation function. The slope and direction at which the ellipsoids tilt away from the temporal axis indicates the velocity of the motion, see figure 6.5. (Random changes in the diffraction pattern may envisaged in this figure as a flattening of the ellipsoid in the τ dimension.)

Full correlation analysis attempts to parameterize the correlation ellipsoids and thus reveal the so-called "true" velocity of the originating diffraction pattern as well as the

spatial and temporal scales of the pattern. The parameters of the ellipsoids are determined from the auto and cross correlation functions (equations 6.1 and 6.2). The auto correlation function corresponds to a line section of the ellipsoids along the temporal axis. The cross correlation function corresponds to line sections parallel to the temporal axis but offset in the spatial plane by the separation of the antenna pair (the dashed line in figure 6.5 gives an example for an antenna pair separated by $\delta\epsilon_{ij}$). Generally only three antenna pairs are available, which with the auto correlation function gives only four line sections of the ellipsoid surfaces to work with.

The parameterization can be started by matching the spatial correlation points to the auto correlation function. The lags, τ_{ij}, are found at which the auto correlation function falls to the value of the each of the cross correlation functions at zero lag, $\rho(0,0,\tau_{ij}) = \rho(\varepsilon_{ij},\eta_{ij},0)$, (see figure 6.1). In terms of the correlation ellipsoids, (equation 6.5), τ_{ij} is the intersection point along the temporal axis of the ellipsoid surface that passed through $(\varepsilon_{ij},\eta_{ij})$,

$$\rho(C\tau_{ij}^2) = \rho(A\varepsilon_{ij}^2 + B\eta_{ij}^2 + 2H\eta_{ij}\eta_{ij}). \tag{6.6}$$

Rearranging for τ_{ij} we get

$$\tau_{ij}^2 = \frac{A}{C}\varepsilon_{ij}^2 + \frac{B}{C}\eta_{ij}^2 + \frac{2H}{C}\varepsilon_{ij}\eta_{ij}. \tag{6.7}$$

With three cross correlation functions, these three unknowns are determined uniquely.

The cross correlation function for an antenna pair separated by $(\varepsilon_{ij},\eta_{ij})$ is

$$\rho(\varepsilon_{ij},\eta_{ij},\tau) = \rho(A\varepsilon_{ij}^2 + B\eta_{ij}^2 + C\tau^2 + 2H\varepsilon_{ij}\eta_{ij} + 2F\varepsilon_{ij}\tau + 2G\eta_{ij}\tau). \tag{6.8}$$

At the time lag, τ'_{ij}, of the peak of the cross correlation function, the partial time derivative of equation 6.8 is zero, $\frac{\partial\rho}{\partial\tau} = 0$. Rearranging for τ'_{ij} leads to

$$\tau'_{ij} = -\frac{F}{C}\varepsilon_{ij} - \frac{G}{C}\eta_{ij}. \tag{6.9}$$

The unknowns in this equation, $\frac{F}{C}$ and $\frac{G}{C}$, describe the apparent velocity,

$$|V_{ap}| = \frac{1}{\sqrt{\left(\frac{F}{C}\right)^2 + \left(\frac{G}{C}\right)^2}}, \tag{6.10}$$

$$(V_{ap})_{\text{direction}} = \arctan\left(\frac{F}{G}\right). \tag{6.11}$$

Since there are two unknowns in this equation, $\frac{F}{C}$ and $\frac{G}{C}$, and three cross correlation functions, a least squares procedure can be applied to determine V_{ap}.

At this stage we can determine the true velocity by comparing the correlation ellipsoids of a stationary observer (figure 6.5 and equation 6.5) with the correlation ellipsoids an observer moving with the pattern would see. The ellipsoids of the moving observer would have no tilt and be of the form in equation 6.4. In the frame of the observer, (with the translations $\varepsilon' = \varepsilon - V_\varepsilon\tau$ and $\eta' = \eta - V_\eta\tau$),

$$\rho(\varepsilon', \eta', \tau) = \rho(A\varepsilon'^2 + B\eta'^2 + K\tau^2 + 2H\varepsilon'\eta'). \tag{6.12}$$

Transforming back to the stationary frame, we get an expression that can be matched to equation 6.5,

$$\rho(\varepsilon, \eta, \tau) = \rho\left(A[\varepsilon - V_\varepsilon\tau]^2 + B[\eta - V_\eta\tau]^2 + K\tau^2 + 2H[\varepsilon - V_\varepsilon\tau][\eta - V_\eta\tau]\right). \tag{6.13}$$

The $\eta\tau$ and $\varepsilon\tau$ terms in equations 6.5 and 6.13 can be equated,

$$AV_\varepsilon + HV_\eta = -F, \tag{6.14}$$

$$BV_\eta + HV_\varepsilon = -G. \tag{6.15}$$

We have all the coefficients (after dividing through by C) in these two equations and thus can solve them simultaneously for the the components of the true velocity, V_ε and V_η.

To find the spatial and temporal scales of the diffraction pattern we choose a particular correlation level, the ellipsoid surface at the one half level, $\rho = 0.5$. Along the temporal axis, the time the auto correlation function takes fall to one half is the "fading time", τ_{fad} (discussed in section 4.1.1)[2]. In terms of equation 6.5,

$$\rho(0, 0, \tau_{fad}) = \rho(C\tau_{fad}^2) = 0.5 \tag{6.16}$$

The spatial correlation ellipse at the one half level $\rho(A\varepsilon^2 + B\eta^2 + 2H\varepsilon\eta) = 0.5$. is called the "characteristic ellipse",

$$\frac{A}{C}\varepsilon^2 + \frac{B}{C}\eta^2 + 2\frac{H}{C}\varepsilon\eta = \tau_{fad}^2. \tag{6.17}$$

The characteristic ellipse is usually described in terms of the length of the minor axis, the axial ratio (major/minor), and the orientation of the major axis.

Another spatial parameter of the pattern that is found is the distance $d_{\frac{1}{2}}$, for the spatial correlation to fall to one half in the direction of travel of the pattern. In other words the distance from the origin to the characteristic ellipse in the direction of motion. Substituting ε with $\frac{d_{\frac{1}{2}}}{V}V_\varepsilon$ and η with $\frac{d_{\frac{1}{2}}}{V}V_\eta$ in equation 6.17, we get

$$\left[\frac{A}{C}V_\varepsilon^2 + \frac{B}{C}V_\eta^2 + 2\frac{H}{C}V_\varepsilon V_\eta\right]\frac{d_{\frac{1}{2}}^2}{V^2} = \tau_{fad}^2. \tag{6.18}$$

[2][Briggs, 1984] uses $\tau_{0.5}$ for fading time.

which can be rearranged to give $d_{\frac{1}{2}}$.

Full correlation analysis also attempts to quantify parameters of the diffraction pattern that would be seen by an observer moving with the pattern. Such an observer would see an ellipsoid as given by equation 6.12. The fading time observed moving with the pattern is called $T_{\frac{1}{2}}$,

$$\rho(0, 0, T_{\frac{1}{2}}) = \rho(KT_{\frac{1}{2}}) = 0.5\,. \tag{6.19}$$

$T_{\frac{1}{2}}$ can be related to the fading time observed by a stationary observer (equation 6.16),

$$T_{\frac{1}{2}}^2 = \tau_{fad}^2 \frac{C}{K}. \tag{6.20}$$

The coefficient $\frac{K}{C}$, can be determined from the known coefficients by equating the coefficients of τ^2 in equations 6.13 and 6.5,

$$C = AV_\varepsilon^2 + BV_\eta^2 + K + 2HV_\varepsilon V_\eta. \tag{6.21}$$

A so-called "random velocity parameter" $(V_c)_v$, is often found. This parameter is defined as the ratio of the spatial correlation parameter along the motion of the pattern, to the temporal scale observed moving with the pattern,

$$(V_c)_v = \frac{d_{\frac{1}{2}}}{T_{\frac{1}{2}}}\,. \tag{6.22}$$

$(V_c)_v$ is useful for describing random changes of the pattern, but although it has the dimensions of velocity, is not a direct measure of real physical motion. In practice $(V_c)_v^2$ is determined by equating it to $\frac{K}{C} d_{\frac{1}{2}}^2$ divided by the left hand side of equation 6.18. If the "random velocity" is close to zero, statistical fluctuations can lead to a negative $(V_c)_v^2$. In this case rather than making $(V_c)_v$ imaginary, the square root of the absolute value is found and is set negative to indicate a negative $(V_c)_v^2$ has occurred.

6.2.2 Acceptance Criteria

Various tests were applied to the data before and after full correlation analysis was carried out to test the quality of the data and to ensure the data conformed to the assumptions made in FCA. The criteria applied here broadly follow those of [Briggs, 1984]. The first checks were on the auto correlation functions :

Signal to Noise

The signal to noise ratio, as determined from the auto correlation function as discussed in section 4.1.1, had to exceed -6 dB, $[\frac{S}{N} > 0.5]$.

Oscillatory behaviour of the correlation functions

Oscillations in the correlation functions lead to errors in determining parameters from the functions. Therefore the functions were checked to ensure that oscillations greater than about -7 dB of the peak of the functions did not occur, [if $\rho_{1^{st}min}$ is the first minima and $\rho_{2^{nd}max}$ is the second maxima then $\rho_{2^{nd}max} - \rho_{1^{st}min} < 0.2$].

Fading time

The fading time had to be less than 10 seconds, [$\tau_{fad} < 10$ s].

The cross correlation functions were found next and the following checks were applied :

Amplitude of maxima of cross correlation

The amplitude of the cross correlation function had to have a maxima of at least 0.2, (that is the maxima had to within 7 dB of the mean signal of the two contributing antennae), [$\rho(\epsilon_{ij}, \eta_{ij}, \tau'_{ij}) \geq 0.2$].

Time lag of maxima of cross correlation

The time lag of the maxima of the cross correlation function had to be no greater than 6 seconds ($\sim 10\%$ of the length of the data set), [$|\tau'_{ij}| \leq 6$ s].

NTD

The Normalized Time Discrepancy, which is the sum of the time delays, τ'_{ij}, around the loop of antenna pairs (for example $\tau'_{12} + \tau'_{23} + \tau'_{31}$), normalized by the sum of the absolute time delays had to be less than 90%, [$\sum \tau'_{ij} / \sum |\tau'_{ij}| < 0.9$].

The FCA procedure was then carried out the results were checked for the for the following conditions :

True and apparent velocity directions

The directions of the true and apparent velocity vectors could not differ by more than 90°, [$|V_{ap_{dirn}} - V_{dirn}| \leq 90°$].

True and apparent velocity magnitudes

The magnitude of the true velocity had to be at least a third of that of the apparent velocity, [$\frac{|V_{ap}|}{|V|} \leq 3$].

True velocity magnitude

The magnitude of the true velocity had to be less than 300 ms^{-1}, the approximate speed of sound, [$|V| < 300\,\mathrm{ms}^{-1}$].

Random velocity parameter

The random velocity parameter $(V_c)_v$ can be zero or slightly negative because of statistical fluctuations; however it is checked to ensure it does not go more negative than -30 ms^{-1}, $[(V_c)_v \geq -30\ ms^{-1}]$.

Elongation of the correlation ellipse

The ratio of the major to minor axes of the correlation ellipse had to be less than five, [if d_{maj} and d_{min} are the lengths of the major and minor axes, $\frac{d_{maj}}{d_{min}} < 5$].

Size of the correlation ellipse

The minor axis of the correlation ellipse had to be at least 50 metres, [$d_{min} \geq 50$ m].

6.2.3 Full Correlation Analysis as used here

A computer program for determining FCA winds was written for this project by the author, based on the above algorithm. The similar algorithm of [Brown and Chapman, 1972] was included in the same program so that comparisons of the two methods could be made, although in general only the [Briggs, 1984] algorithm results will be quoted here.

Various options were made available in the program. The radar is repeatedly pulsed at several (typically five) different frequencies during a one minute sampling period. The minute samples at each frequency step can be analysed by FCA separately or the samples at the different steps can be averaged together, then FCA carried out.

integration	time series, ith element
coherent	$\ldots, \frac{1}{m}\sum_{j=1}^{m} E_i(f_j), \ldots$
incoherent	$\ldots, \frac{1}{m}\sum_{j=1}^{m} \lvert E_i(f_j)\rvert, \ldots$
averaged correlation function	$\frac{1}{m}\sum_{j=1}^{m} \lvert\rho_{E(f_j)}\rvert$

Table 6.1: **Methods of averaging correlation functions.** The top part of the table shows the time series for which the correlation functions are found after integration over m frequency steps f_j. The bottom part shows how the averaged correlation functions are found.

The method of averaging can be set to incoherent type averaging, whereby the modulus of the data point at each frequency is found and the mean of the points used for finding the correlation functions. Coherent averaging, whereby the complex sample at each frequency step is added, could not be used here as the phase changes with frequency depending on the range to the scattering centre (see section 5.3.3) in a way that cannot be easily

isolated[3]. Another averaging procedure involved determining the correlation functions at each frequency then finding the mean of correlation function amplitudes. This method was the method that generally used in this project. The different averaging methods are illustrated in table 6.1.

Other features in the program included the application of smoothing or window functions to the data. The form of the curve fitted to the correlation functions (used when finding signal to noise and parameters such as fading time), could be set to a polynomial (generally a quadratic) or to a Gaussian function.

[3]For testing purposes, some coherent integration was carried out on samples which had all the same frequency.

Chapter 7

Results

This chapter reports and discusses the results of the various analyses introduced in the preceeding chapters.

The Scott Base radar collected data on typically seven range bins generally two or three kilometres apart from about 90 to 105 km and the Birdlings Flat radar collected thirteen range bins, two kilometres apart typically from 79 to 103 km as was described previously. Both radars used three receivers and were generally cycled through five frequencies for the frequency shifting analysis. The observation period on both radars was one minute and series of these one minute samples were collected. The series typically spanned about half an hour at Scott Base, with sampling every third minute, and two to five hours at Birdlings Flat, with sampling every second minute. The dates, times and altitudes sampled of the main data series collected on the Scott Base and Birdlings Flat radars are listed in appendix B.

The analyses discussed here were applied to each of the one minute samples individually; raw data from each one minute sample were not concatenated to form longer samples. In general the results of the analyses of the one minute samples will presented as a series of results, since often variations in these results during the series are of more interest than the absolute values of the results themselves.

All of the analyses presented here were carried out using programs written entirely by the author, aside from some of the routines used in the spectral analysis programs as was mentioned previously. The analyses were in general carried out on all of the data sets, although only selected results will be displayed here with along with explanations. Results of similar analyses for much of the other data collected for this thesis are given in appendices C and D, and some of these will be referred to at various points.

The variations in gain as seen at each A/D channel, both between receivers and between

the in-phase and quadrature channels of each receiver were corrected for using the gain factors determined by the calibration methods of section 2.3.1. At various stages, phase factor corrections (section 2.3.2) were made as well.

7.1 Auto Correlation Functions

The auto correlation function for each sample at each range bin was found. This was determined from the auto covariance function of which an example is given in figure 7.1. The amplitude of the covariance functions typically have a discontinuity at zero lag and as was discussed in section 4.1.1 this is taken to originate from high frequency noise and interference, [Goldstein, 1951]. The signal power is estimated from the level of the auto covariance function would have at zero lag if no noise were present by carrying out a curve fit on the function at lags either side of zero lag. The signal is then, essentially the variance (standard deviation squared) of the sample with the uncorrelated noise component removed. The noise component is estimated from the magnitude of the discontinuity, this enabled determination of the signal to noise ratio. In general a quadratic regression routine was used for the curve fitting, although a Gaussian fit was also trialed and gave very similar results. The fits were typically carried out to lags of one second.

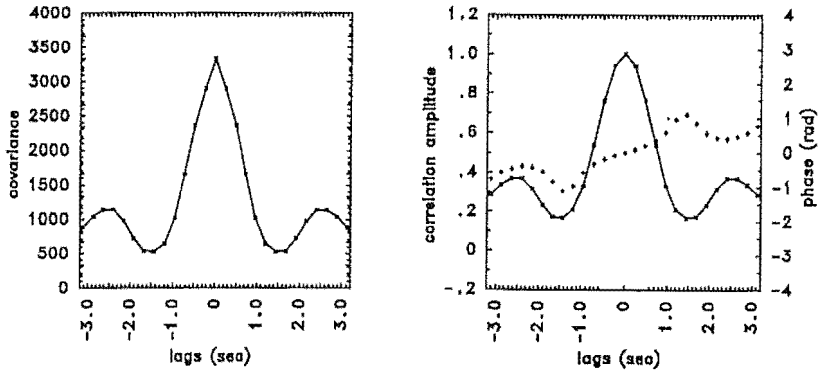

Figure 7.1: **Example of auto covariance and auto correlation functions.** The auto correlation function (on the right) is determined from the auto covariance function (on the left) by fitting a curve to the central portion and normalizing by the zero lag value implied by the fit which is the signal. The difference between the signal and the covariance at zero lag is the noise level. In this example, collected at Birdlings Flat at 16:00 on 23 July 1990 at 100 km altitude, the signal to noise ratio was determined to be 8.5 dB. The auto correlation phase is indicated by the plus symbols.

Auto correlation functions were formed by removing the noise discontinuity from the

auto covariance functions and normalizing with the signal level. An example of an auto correlation function is also given in figure 7.1.

7.1.1 Signal Power

Figure 7.2 displays the signal level for a data series collected at Birdlings Flat on 8 December 1990 of five hours and at thirteen height bins from 79 km to 103 km. The signal of each sample is the mean of the signals as found for each of the three receivers and each of the five frequencies used in each sample. The shade scale is here set to the A/D quantization step, that is 0 dB corresponds to a variance of one A/D unit, but can be considered to be arbitrary. On VHF and UHF radars, the signal to noise ratio is often displayed in preference to absolute signal because the noise level on these radars is largely comprised of relatively constant sky noise. However on MF radar much noise originates from highly variable interference and variations in the signal to noise ratio are not necessarily related to changes in the scattering region.

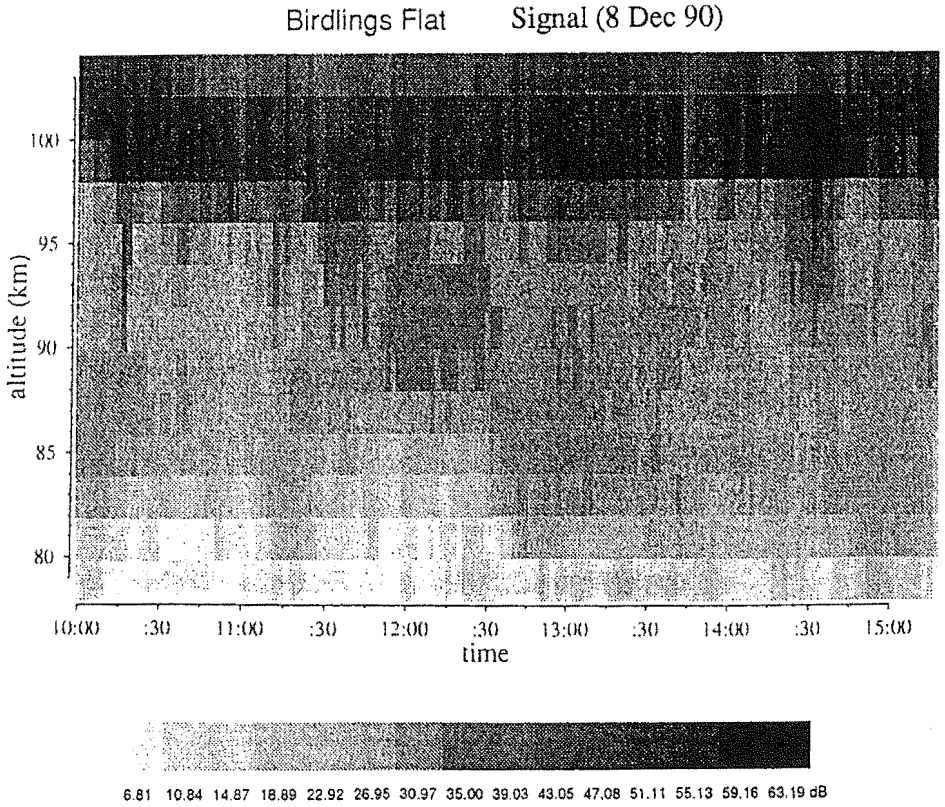

Figure 7.2: **Signal Power at Birdlings Flat on 8 December 1990**, the units are dB relative to the A/D quantization step.

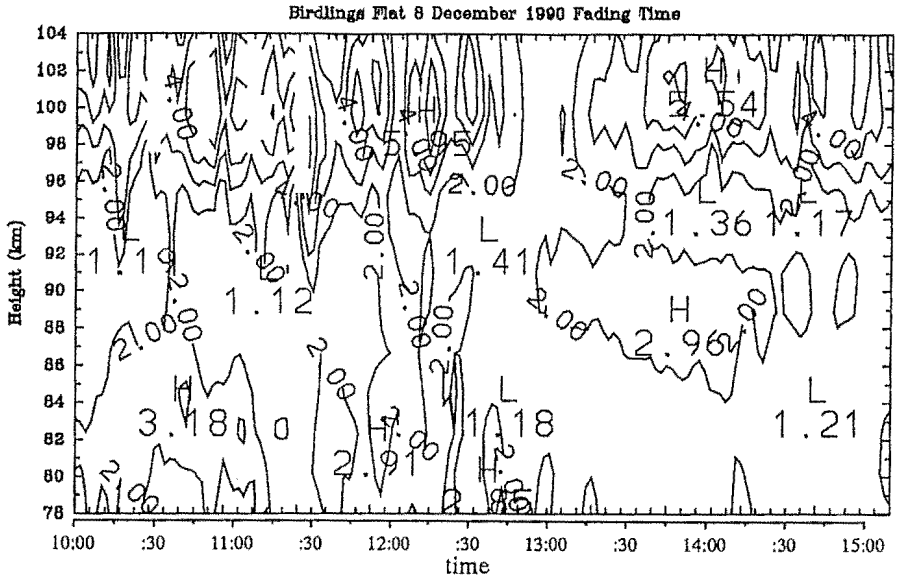

Figure 7.3: **Fading Time at Birdlings Flat on 8 December 1990**, the units are seconds (quarter-half-quarter filtered for clarity).

7.1.2 Fading Time

The fading time describes the characteristic time scale of scattering. It is the time for the auto correlation function (with noise component removed) to fall to 0.5, (section 4.1.1). Here the fading time measurements are used in full correlation analysis for winds as well as in estimating aspect sensitivity. An example of the fading time measured on the Birdlings Flat radar is given in figure 7.3. The fading time of each sample is the mean of that for the three receivers and five frequencies.

7.1.3 Mean Doppler Shifts

The slope of the phase of the auto correlation function at zero lag is a measure of the mean rate of change of phase of the signal, which in turn can be related to the mean Doppler shift imposed on the signal as a result of apparent motion along the line of sight in the scattering region (section 4.1.1). The phase of the auto correlation at zero lag is zero, so the slope of the phase near zero lag can be approximated by the phase at lag one divided by the single lag time to give the Doppler shift. In the example given in figure 7.1 the phase at one lag (0.24 sec) is 0.085 radians which implies a Doppler shift of -0.056 Hz and a radial velocity of 3.5 ms^{-1} away from the radar.

The average Doppler shift for all three receivers and five frequencies was found and converted to line of sight or radial velocity. An example of the mean radial velocities

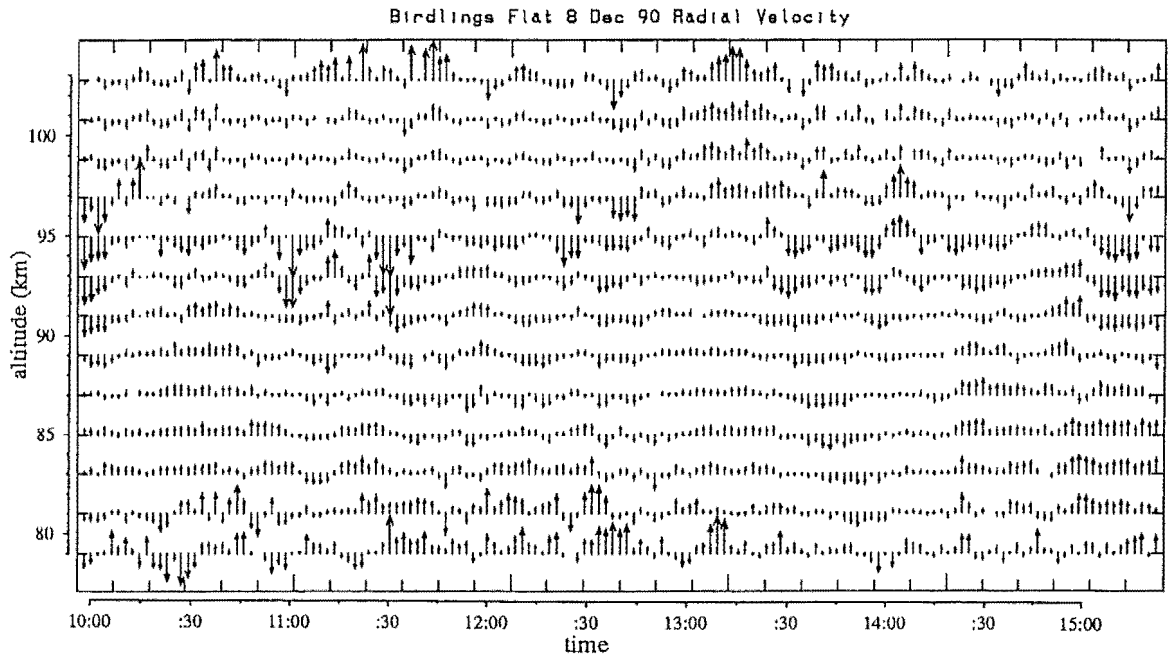

Figure 7.4: **Radial velocity at Birdlings Flat on 8 December 1990,** from the mean Doppler shifts determined using auto correlation phase. The largest vectors are 10 ms^{-1}.

found from auto correlation phase is given in figure 7.4. Although for convenience these velocities have been plotted as vertical vectors, generally the line of sight is not directly vertical and so the radial velocity is comprised of components of vertical and horizontal motion.

7.2 Cross Correlation Functions

The cross correlation functions between signals received on separated antennae were found, and a typical example is given in figure 7.5. The functions were determined from cross covariance functions normalized by the square root of the product of the signal power at each receiver thus correcting for high frequency noise, [Vincent and Röttger, 1980].

The amplitude of the cross correlation function is a maximum at a lag (at about +0.5 seconds in figure 7.5) that can be related to apparent motion in the scattering region. The cross correlation function amplitudes for each pair of receivers, along with the auto correlation function amplitudes were used in full correlation analysis.

The phase cross correlation function at zero lag gives the mean phase difference between the signals received on the separated antennae. The high frequency noise was removed from

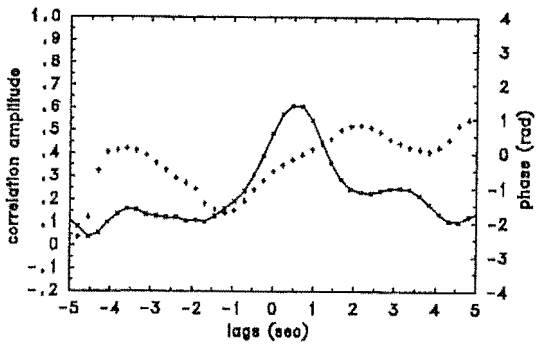

Figure 7.5: **Example of a cross correlation function.** The phase of the function is indicated by the plus symbols. Collected at Birdlings Flat at 16:00 on 23 July 1990 at 94 km on antennae F and C.

the correlation function amplitude, however a discontinuity is sometimes still evident in the phase. Here the phases at lags either side of zero lag were found and an interpolation across zero lag was carried out to give a "noise removed" phase estimate. The measured phase difference includes an equipment component due to factors such as the different lengths of the receiving antenna feeder cables and this component (estimated using calibration procedures of section 2.3.2) is removed before further analysis.

7.3 Frequency Correlation Functions

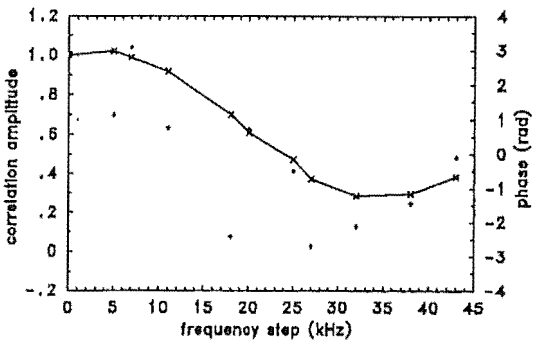

Figure 7.6: **Example of a frequency correlation function.** There are five frequencies used so the cross correlation function is found at 10 steps in frequency. The phase of the function is indicated by the plus symbols. Collected at Birdlings Flat at 16:00 on 23 July 1990 at 94 km.

Cross correlation functions were similarly found between signals at different frequencies in the frequency shifting part of the experiment. The zero lag amplitudes and phases (with noise removed by normalization and interpolation) for each pair of frequencies were found and grouped together as a function of increasing frequency step to give frequency correlation functions (section 4.1.3). Like the cross correlation functions used in FCA and spatial interferometry, the frequency correlation functions found here were corrected for the noise component as found from the auto correlation functions of each individual frequency. Figure 7.6 gives an example of a frequency correlation function. The variation in amplitude of the frequency correlation function with lag (or frequency step) gives a measure of the variance in range, or scattering depth, of a sample and the phase gives a measure the mean range of the sample. The phase must be corrected for equipment factors before being used to determine range and the adjustment factors were determined by the methods of section 2.3.2.

For example, in figure 7.6 the frequency correlation function at a lag of 20 kHz has an amplitude of 0.6 and phase of 0.72 radians. Using equation 5.21 in section 5.3.3, this amplitude implies a scattering depth of 1.2 km (assuming a Gaussian model to describe the distribution of the scattering, this would be the standard deviation of the distribution of ranges, [Kudeki and Stitt, 1987]). Phase can only be measured to the nearest 2π radians. This ambiguity is not a problem because the approximate range is determined by timing methods during the A/D sampling. The range of the A/D bin for this data is 94 km which implies that the phase should be between $12 \times 2\pi$ and $13 \times 2\pi$ radians (corresponding to 90 - 97.5 km) for a 20 kHz step. If $12 \times 2\pi$ is added to the above measured phase, the measurement is brought into this range. If a 2.54 radian equipment factor is also added, a corrected phase measurement of 78.66 radians is deduced which implies a range of 93.9 km.

The functions were determined for each receiver of the three receivers individually and were averaged together to carry out FDI of each sample. Figure 7.7 shows a sequence of the average frequency amplitude functions at a range of altitudes. The difference of the functions between the three receivers is indicated by the error bars and as can be seen the variation between the receivers was at times considerable. However frequency steps that are close together (in frequency difference) generally had similar mean amplitudes and the form of the functions is similar from sample to sample, so variations of the functions with time and height can be studied with more confidence than the individual profiles suggest.

Most of the FDI results presented here used frequency steps of between 15 and 30 kHz. A curve was fitted to the frequency correlation function amplitude versus lag at these steps and for all three receivers to obtain an "average" amplitude at a step of 20 kHz. Figure 7.8

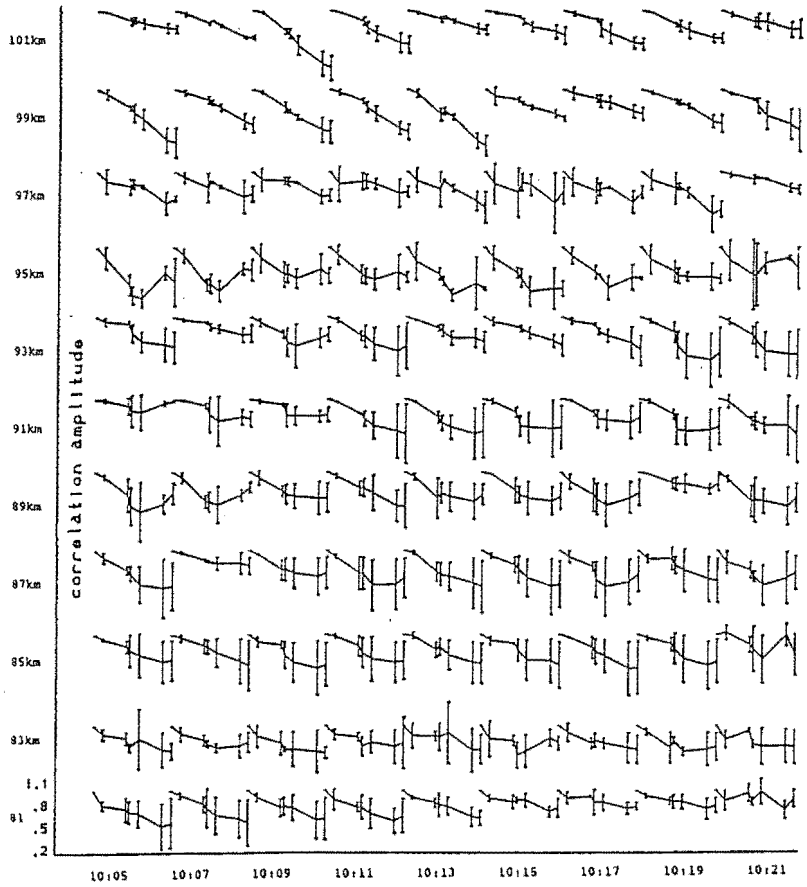

Figure 7.7: **Sequence of frequency correlation functions,** collected over heights from 81 to 101 km, 10:04 - 10:21, 6 October 1990. Each segment shows the average amplitude of the frequency correlation functions out to steps of 30 kHz, the error bars indicating the standard deviation of the function between receivers.

displays the average amplitude (smoothed for clarity) found in this way for the 6 October 1990 data. As for the example above, these amplitudes were used to obtain a measure of the scattering depth (shown below).

7.4 Doppler Spectra

Each of the data samples was spectrally analysed by at least two methods, FFT and MEM analysis, and much data were analysed using the Blackman-Tukey technique as well.

An example of these analyses is in figure 7.9, showing superimposed FFT and Blackman-Tukey spectra (dots and lines respectively). Each spectrum is actually an average of fifteen spectra, one for each of the five frequencies and each of the three receivers.

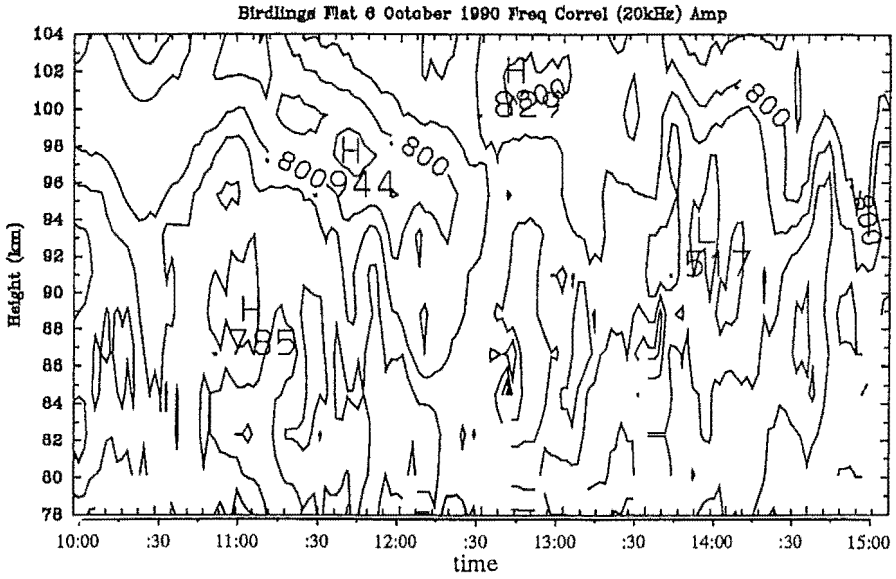

Figure 7.8: **Frequency correlation amplitude at a step of 20 kHz, on 6 October 1990,** 10 minute running mean.

The longer data sequences at Birdlings Flat made viewing spectra in this manner cumbersome, so a shade plot was developed to enable more compressed viewing. Figure 7.10 displays one of these plots. The thirteen panels correspond to each range bin and the spectra are stacked vertically in these panels. The spectral range shown in each panel is ± 0.5 Hz; each pixel, whose shading corresponds to the spectral power, covers a spectral bin of width 0.05 Hz. The spectra are arranged so that positive Doppler shifts in the scattered signals, corresponding to motion towards the radar, appear as spectral power towards the bottom of each panel. This sequence is of 160 samples over five hours and 20 minutes so 31200 spectra were computed to make up the figure. The FFT version of this plot appears in appendix D as figure D.2.

The spectra of figures 7.9 and 7.10, like most of the spectra found in this project, have many sharp features. There have been some suggestions, for example [Hocking, 1983a], that spectra collected on broad beam MF radar are somewhat unreliable, particularly as regards the sharp features that do appear in these spectra. It has been considered uncertain how many of the features in the spectra might be random fluctuations and how many can be traced to the discrete scattering centres with differing Doppler shifts. If individual spectra in figures 7.9 and 7.10 are compared to those that are adjacent in time or in range bin, it can be seen that many of the dominant features in the spectra are consistent with those in the adjacent spectra. Also if spectra found by one technique are compared to those found using a different technique, the spectra do appear to share many

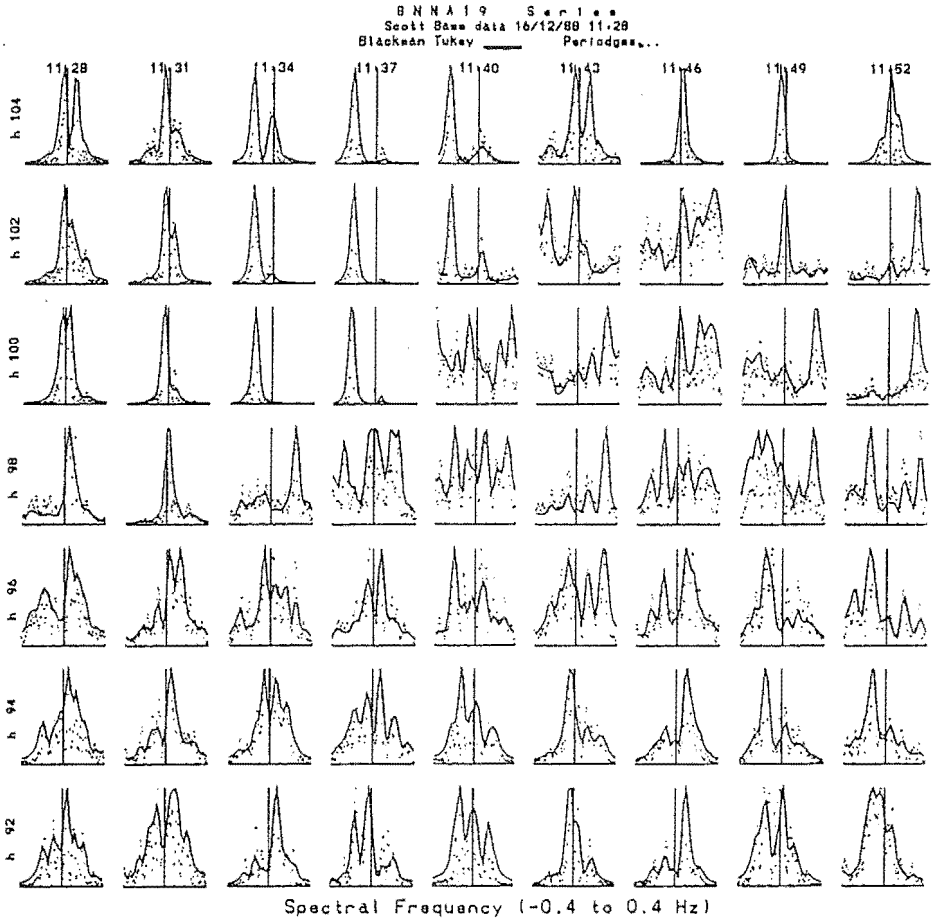

Figure 7.9: **Sample spectra at Scott Base** collected over 25 minutes on 16 December 1988 and analysed using Blackman-Tukey and FFT (periodograms) methods.

common features (for example the FFT and Blackman-Tukey spectra of figure 7.9 and the MEM and FFT spectra of figure 7.10 and figure D.2 in appendix D). There were on average about three or four consistent features identified in the spectra of each sample in both the Birdlings Flat and the Scott Base data sets. Also there were generally one or two more consistent peaks at lower altitudes (say below about 95 km) than higher altitudes.

The emphasis in this project's analysis of spectra, is examination of the prominent features in the spectra (rather than considering the overall spectral envelope as was done in [Hocking, 1983a]). These features do persist from method to method and from sample to sample so the spectra found here were considered reliable to the purposes of this work.

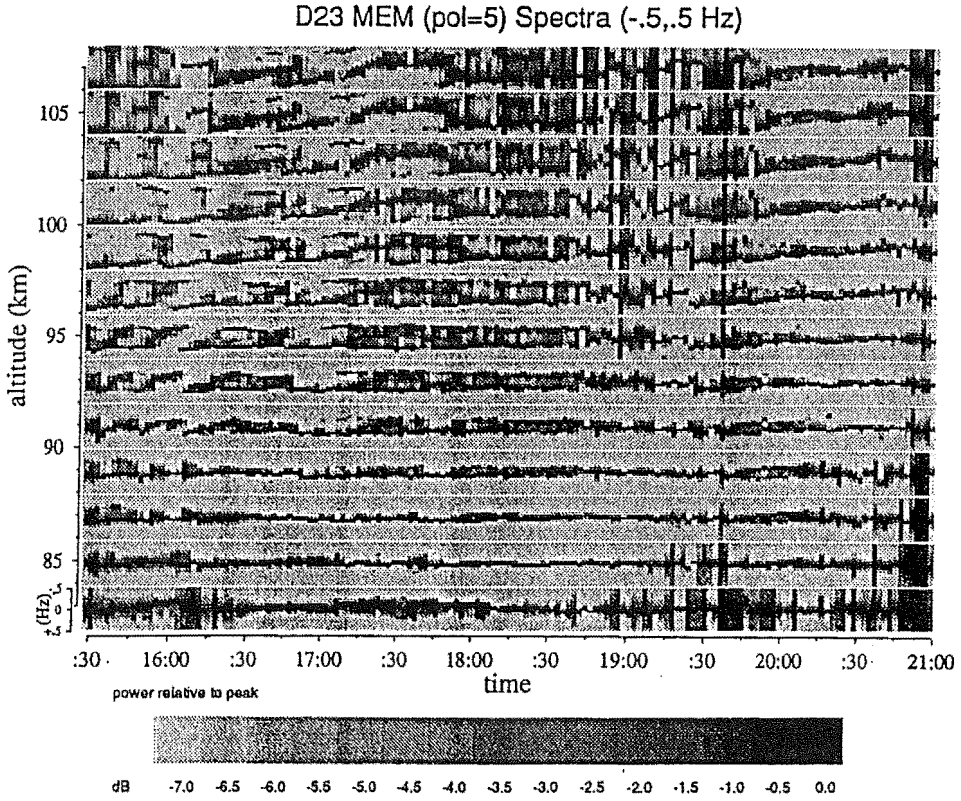

Figure 7.10: **Sample spectra at Birdlings Flat** collected on 18 August 1990 and analysed using MEM techniques (filter length set to 5).

7.5 Full Correlation Analysis

Full correlation analysis was carried out on all of the data collected for this work. All of the auto and cross correlation functions had the noise component removed before full correlation analysis was carried out. The FCA parameters found include all of the parameters discussed in section 6.2.1. All of the FCA results presented here were found using that the technique introduced in that section which is due to [Briggs, 1984]. Much data was also analysed by the related [Brown and Chapman, 1972] algorithm which differs somewhat from the Briggs algorithm in geometric approach and using somewhat less information in the correlation functions than the Briggs method. The two methods were found to give practically indistinguishable results. The same acceptance criteria were applied to results from both methods and the Briggs algorithm was found to produce a slightly higher ($\sim$<5%) acceptance rate, probably due to the extra information that the Briggs method uses.

Some correlation functions found from data collected for this project were fed into

the FCA programs (which follow the [Brown and Chapman, 1972] algorithm) of the drifts experiment [Fraser, 1989] that also runs on the Birdlings Flat and Scott Base radars. This was done as a test of the FCA programs written for this project. The results produced were very similar to the results found in this work's programs; any differences that did appear were traced to the slightly different curve fitting routines applied to the correlation functions and the different regression techniques used.

The routines were also tested on data generated by moving diffraction screen computer models (written by Dr. C. H. Cummack of the Department of Physics of the University of Canterbury) such as a simple distorted mirror model (based on routines used by [Cummack and Cooper, 1986]) and a randomly distributed reflecting points model. The FCA velocities produced were in good agreement with the parameters fed into the models.

Uncertainties in the FCA results are discussed in section 7.13.1 where it is found that typically the uncertainties in FCA velocity measurements are about 5 ms^{-1}.

Figure 7.11 gives an example of one of the summary diagrams of the analysis by the FCA programs written for this project. Included in this diagram are the apparent and true velocities, the correlation ellipses and the $T_{\frac{1}{2}}$ times. Also shown are results from data that failed the acceptance criteria tests (note that stricter tests were sometimes applied after this stage of analysis so that some of the results shown in these diagrams may not appear in later figures.) Such diagrams were found to be useful to readily ascertain the main features of the FCA results.

In general it is clearer to present one quantity at a time. For example figure 7.12 displays the FCA true velocity in vector form as found at Birdlings Flat on December 8, 1990. Here the 10 minute means are displayed; since a sample is taken every two minutes on this radar, each vector is the average of up to five samples. Note that in general, fewer than five samples made up each average because many samples do not pass the FCA acceptance tests. Mean profiles of the true wind for this data appear in figure 7.19 of section 7.6.2 where they are compared with the drifts experiment FCA results and profiles of the apparent wind appear in figure 7.27, section 7.8, where they are compared with velocities determined by the interferometry experiment. As will be seen, both of these comparisons display good agreement. The winds for this data are also consistent with the zonal winds of the [CIRA, 86] reference atmosphere shown in figure 1.2 of section 1.1.

The characteristic correlation ellipses (which to a first approximation can be taken to represent the average form of the drifting diffraction irregularities as seen by FCA) were frequently found to display a bias. There have been two main contributing factors identified to such bias on space antennae radars. [Kelleher, 1966] observed that the spatial

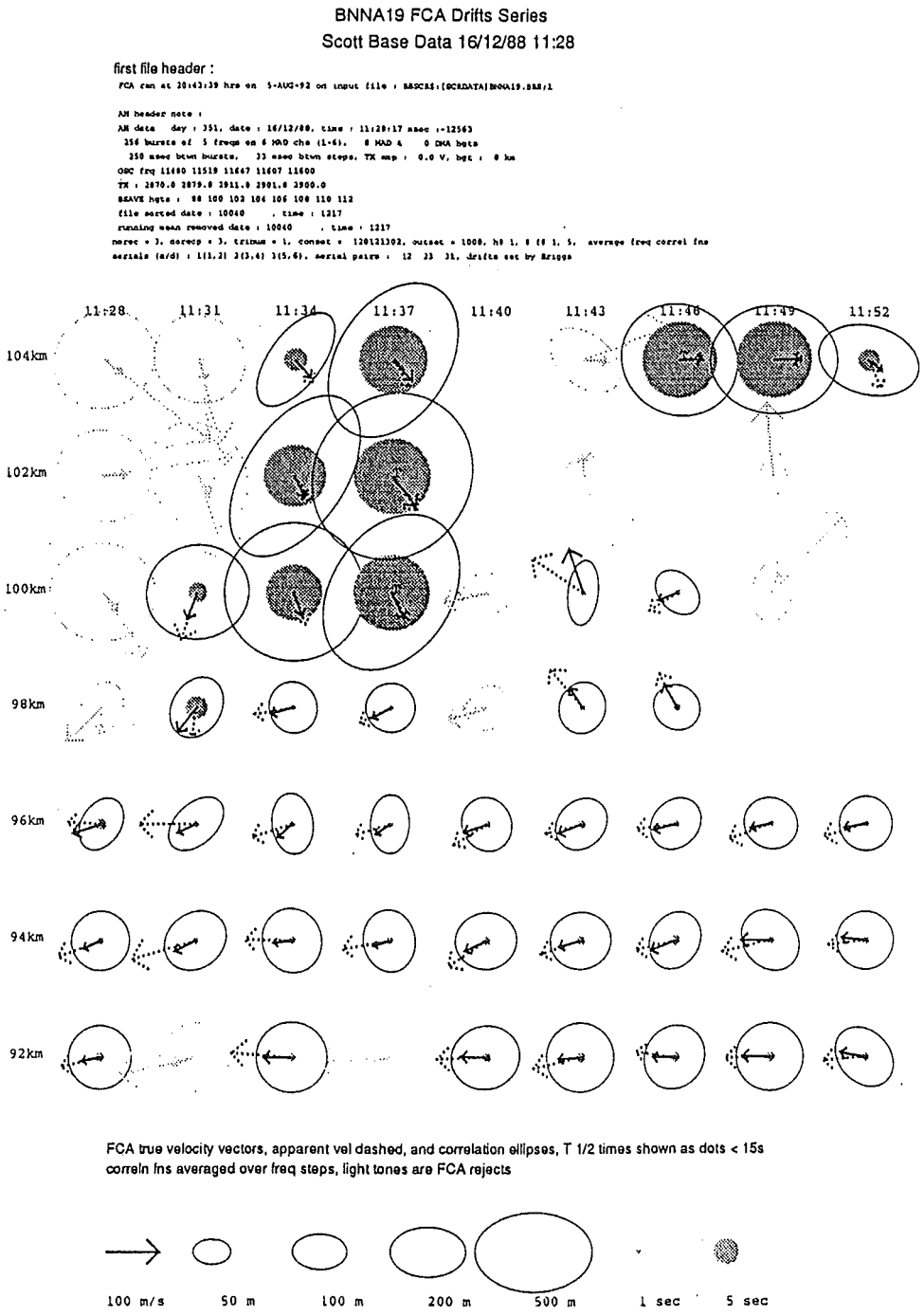

Figure 7.11: **FCA results summary diagram** for a data sequence collected over 25 minutes at Scott Base on December 16, 1988. The sequence consists of nine sample scans arranged in nine columns across the diagram, (the time of the sample is indicated at the top of each column), and each sample scan contains seven range bins of data at the altitudes indicated at the left of the diagram. The vectors represent the true and apparent velocities (bold and dotted arrows respectively), the ellipses are the correlation ellipses and the grey dots represent the $T_{\frac{1}{2}}$ times. The scales for these quantities are indicated at the bottom of the diagram, (note that the ellipse scale is non-linear) and north is vertical in the diagram. The very light arrows, dots and ellipses correspond to samples which did not pass the FCA acceptance tests. The points at which nothing is shown generally correspond to samples where the signal to noise ratio was too low.

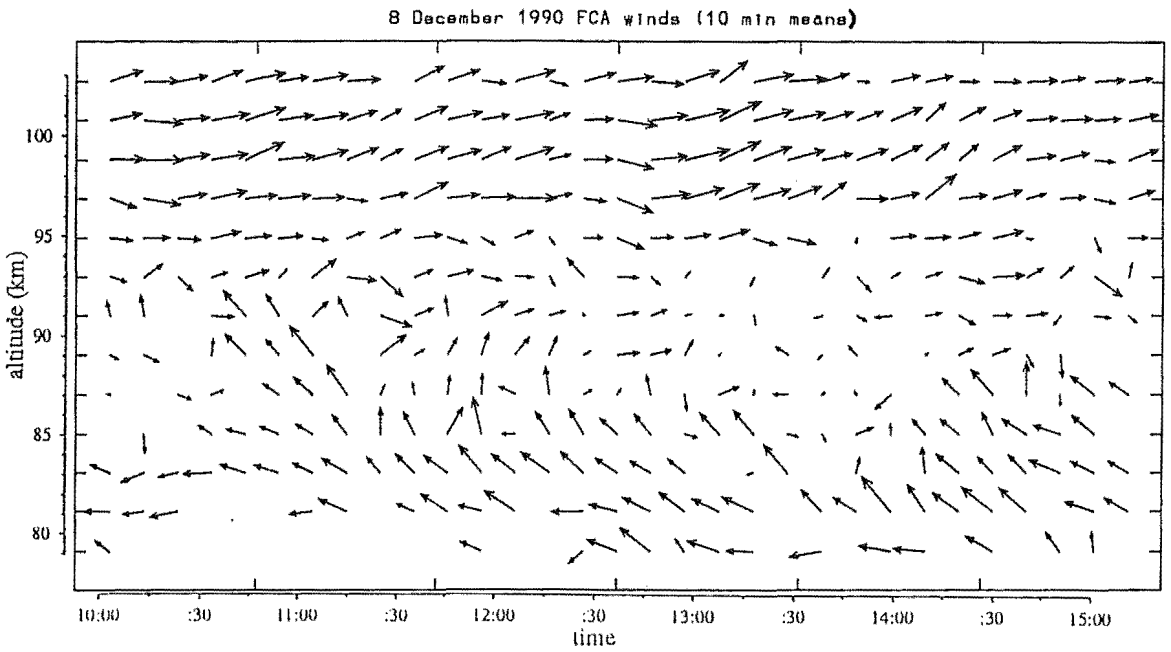

Figure 7.12: **FCA true velocity** (10 minute means) at Birdlings Flat 8 December 1990. North is vertical and the largest vectors correspond to 100 ms^{-1}.

correlation function falls off with increasing antennae separation at a more gradual rate than implied by the temporal correlation function (FCA assumes that the temporal and spatial correlation functions to have the same form). A result of this is that when the receiving antennae are laid out in the form of a right angled triangle, the spatial correlation functions are biased towards the longest side, [Golley and Rossiter, 1970]; such a bias is sometimes referred to as the "hypotenuse effect". Another biasing effect that can occur, particularly above 100 km, is the increasing elongation of the correlation ellipse with altitude and a tendency for correlation ellipses to be aligned with the geomagnetic field, reported by, for example, [Clemesha, 1963] and [Stubbs, 1977].

Figure 7.13 displays examples of axial ratio profiles with altitude and histograms of the orientation of the minor axis found in this project. There does not seem to be any trends in elongation with altitude in the Birdlings Flat data, although in the Scott Base data there is a steady increase with altitude. The Birdlings Flat data does however show significant bias to the orientation of the minor axis to approximately 30° east of north, implying a spatial correlation bias towards about 60° west of north. The longest side of the triangular arrangement of Birdlings Flat antennae is orientated towards 53° west of north. The orientation of the bias and the observation that it is similar above and below 98 km suggests that the hypotenuse effect is the main cause of the bias at Birdlings Flat.

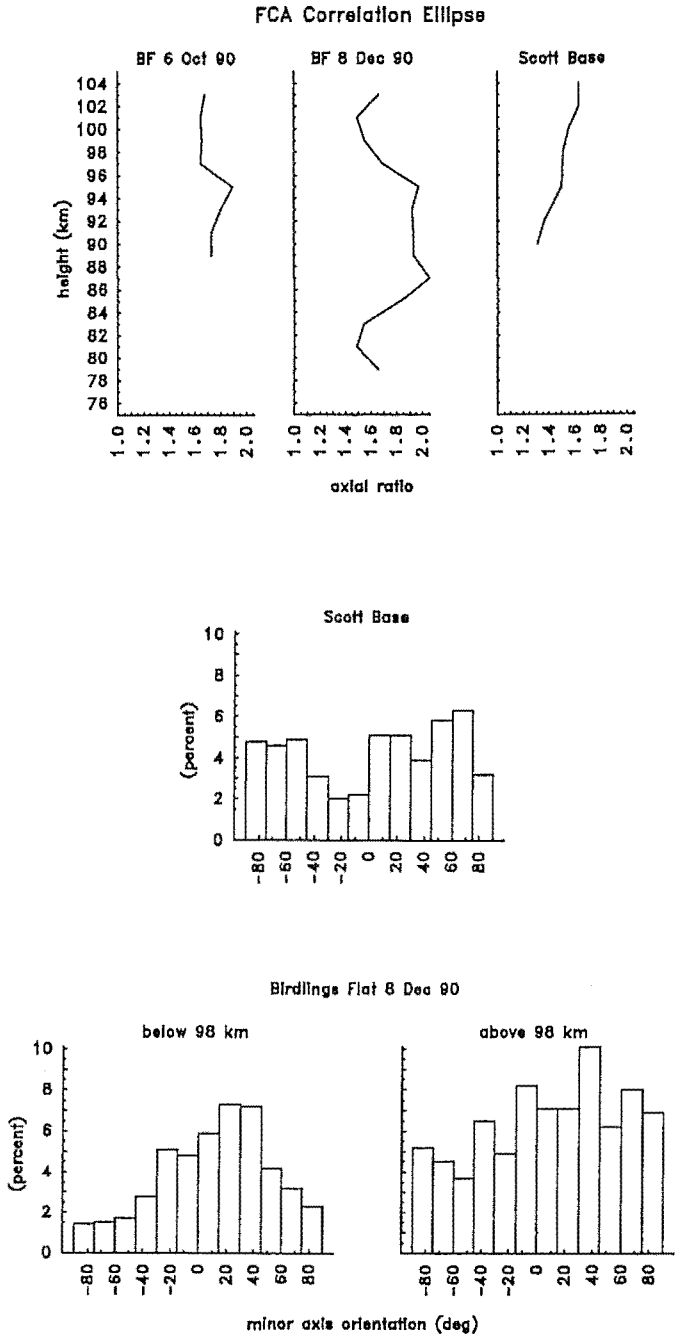

Figure 7.13: **Correlation ellipse axial ratio** (mean profiles) **and minor axis orientation** (histograms of relative occurrence, the bars have widths of 15°) at Birdlings Flat (5 hours on 6 October and 8 December 1990) and Scott Base (4 hours collected over 4 days, December 1988).

(Note that the plot of above 98 km is composed from considerably less data, and thus displays more variability, than the plot below 98 km.)

The histogram of orientations of the minor axis in the Scott Base data shows a dip around 20° west of north implying a spatial correlation bias in that direction and towards 20° east of south, (most of the Scott Base data is around 95 km or above so the variation of the orientation with altitude is not shown). The south magnetic pole is only approximately a thousand kilometres away in a north-west-north direction so the field at Scott Base is more or less vertical, although there is a small south-east-south component. The increase in elongation with altitude and the distribution of the orientations of the correlation ellipses imply that there is geomagnetic field effect in the Scott Base data.

7.5.1 FCA observations of tides

Another example of FCA winds is given in figure 7.14. The winds in this example follow an interesting pattern, starting out predominantly eastward, then towards midday turning to the north, then turning to the west. The rotation occurs at the highest range gates first, and propagates downwards.

The timing and orientation of this rotation is consistent with observations reported in [Manson et al., 1989] of fluctuations in the wind due to the semidiurnal tide. The semidiurnal tide is a solar driven inertial gravity wave with a 12 hour period and which propagates westward with the sun. The group velocity of the wave has an upward component, but the phase velocity has a downward component; therefore the velocity perturbations brought on by the wave appear as an anticlockwise rotation in the wind vector which propagates downwards (section 3.1). The observations in [Manson et al., 1989], some of which were made on the Birdlings Flat radar. [Smith, 1981], report a daily reversal of the zonal (eastward) wind component of the semidiurnal tide. This observation is repeated in drifts experiment observations made around the time of the figure 7.14 data which are presented in section 7.6.2.

The FCA time scale parameter $T_{\frac{1}{2}}$ for the same period is given in figure 7.15. There is a correlation between variations in $T_{\frac{1}{2}}$ and the behaviour of the wind velocity vector. $T_{\frac{1}{2}}$ is longest for a period shortly before the velocity vector rotates to north, decreasing further as the vector turns more westward and then increasing again later as the northward component increases. This behaviour is also consistent with drifts experiment observations of $T_{\frac{1}{2}}$, [Khan, 1988], although the drifts experiment uses incoherent receivers and so the measure does differ somewhat from that made here (discussed further in the next section). As mentioned in section 3.2, similar observations on the Scott Base radar of a decrease in

$T_{\frac{1}{2}}$, implying an increase in turbulence, have been associated with saturation of the tidal gravity wave, [Fraser and Khan, 1990].

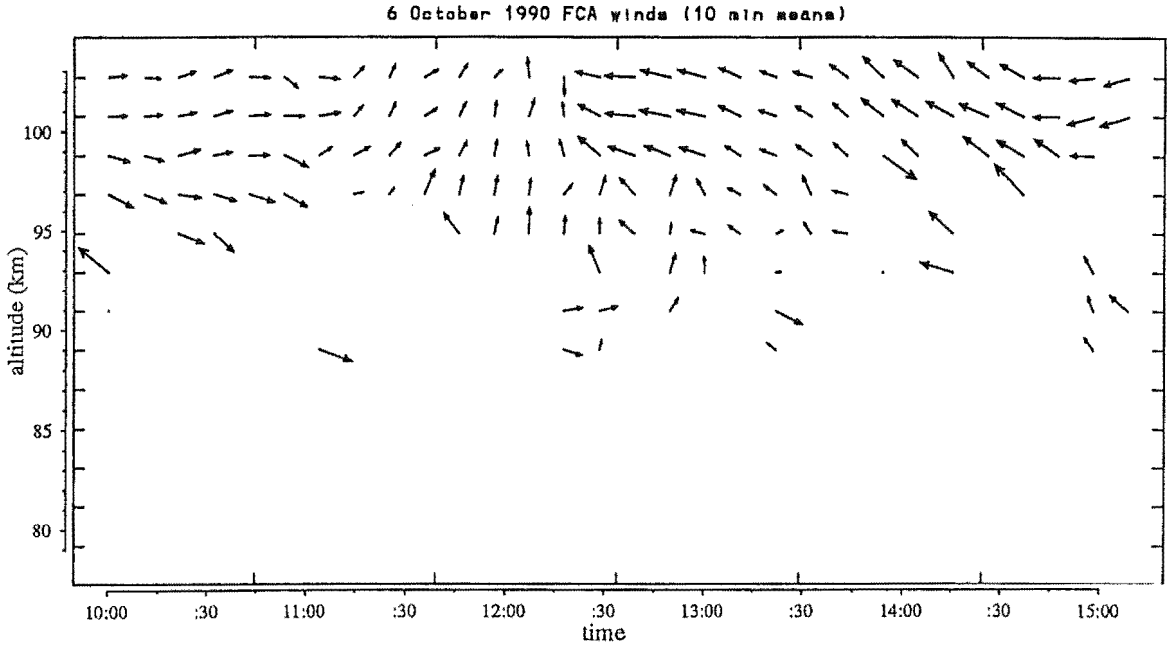

Figure 7.14: **FCA true velocity** (10 minute means) at Birdlings Flat 6 October 1990. North is vertical and the largest vectors correspond to 120 ms^{-1}. Apparent velocities for this data appear in figure 7.28, section 7.8.

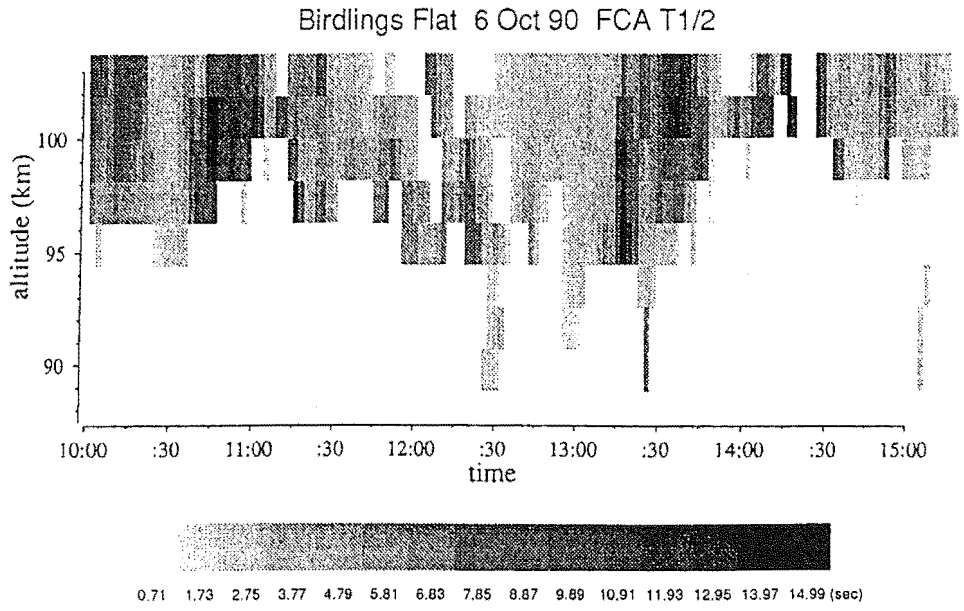

Figure 7.15: **FCA $T_{\frac{1}{2}}$ 6 October 1990** at Birdlings Flat, (smoothed by a quarter-half-quarter filter for clarity).

7.6 Comparisons with the Drifts Experiment

The drifts experiments at Birdlings Flat and Scott Base have been operating for a number of years and so a useful data base of observations at the two sites has been built up, [Fraser, 1965, Fraser, 1989]. Comparisons between the observations made in the current project and the drifts experiment are useful while considering how typical the observations made in this project are, and also so that the drifts data base might at some stage be examined in the light of conclusions from this project.

The drifts experiment uses incoherent receivers, while this project used phase coherent receivers, so comparisons are made of the different behaviour of the two types of receivers. Also the drifts experiment does its analysis using the FCA method and so comparisons of FCA results found in this project are made with the FCA results from the drifts experiment.

7.6.1 Coherent, Incoherent Comparison

The output of the incoherent receivers used by the drifts experiment is related to fluctuations in the signal strength of backscattered signals and interference between components of the backscattered signal with differing Doppler frequencies. In contrast, the output of phase coherent receivers of this project results from the superposition of the components of the backscattered signal. Interference between different signal components can be expected to add to the variability of observations made by incoherent receivers; therefore spectra of the output of the incoherent receivers should be broader than that of the coherent receivers and correlation functions should be narrower. [Bramley, 1951] showed that for a randomly phased signal the auto correlation function of an incoherent receiver is approximately the square of that for a coherent receiver. As the signals become less randomly phased, or as the scattering becomes more specular the correlation functions become more equal. In general then, in terms of FCA results, time and spatial scale parameters such as τ_{fad}, $T_{\frac{1}{2}}$ and $d_{\frac{1}{2}}$ can be expected to be somewhat smaller on an incoherent receiver.

The incoherent receivers used by the drifts experiment have logarithmic amplifiers in their final stage to increase the dynamic range of the receivers. This added non-linearity allows the receivers to have a high gain enabling them to detect scattering from lower altitudes than was possible with the phase receivers used in this project, and yet avoids saturation problems (leading to the output exceeding the full scale of the A/Ds) when observing the E region. However phase receivers can achieve better noise rejection for the signals they can detect and this was apparent in the higher success rates obtained during

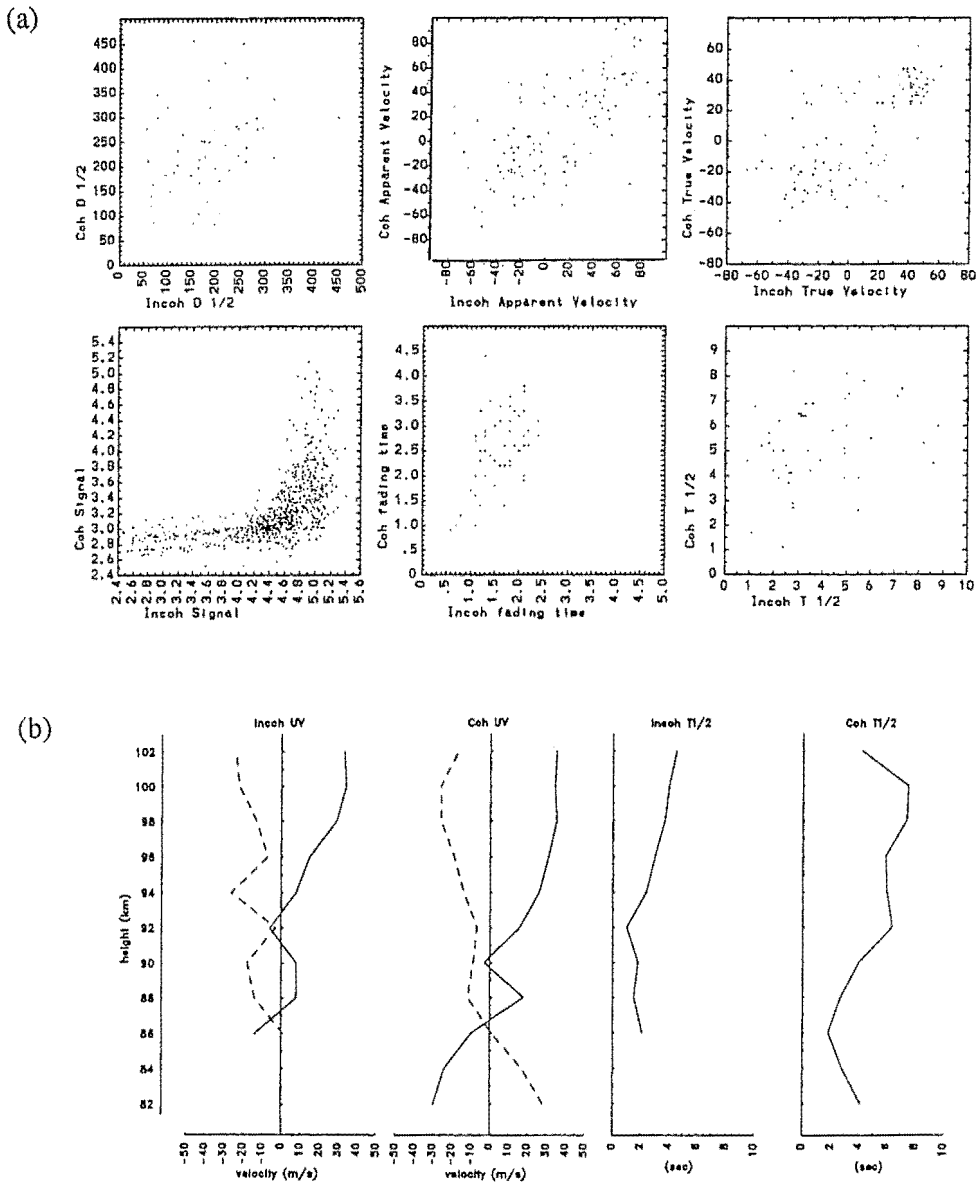

Figure 7.16: **Comparisons of FCA results between coherent and incoherent receivers,** of data collected simultaneously on both types of receivers. The data was collected over two hours on December 19, 1990 at 11 ranges between 80 and 100 km on the Birdlings Flat radar.
(a) scatter plot of parameters derived from instantaneous samples on both types of receiver. (There are many more points on the signal plot than the other plots, because the other plots only record samples for which FCA was successful for both types of receivers.)
(b) mean profiles with height of the FCA true velocity (solid line eastward, dashed line northward components), and $T_{\frac{1}{2}}$ for incoherent and coherent receivers.

full correlation analysis in this project.

Because the drifts and interferometry experiments use much of the same equipment, they could not be run simultaneously. However the data logging system at Birdlings Flat allows for up to nine channels of data to be recorded simultaneously. The interferometry experiment, with its three phase sensitive receivers, requires six of these channels leaving three channels free which were, on occasion, connected to the three incoherent receivers the drifts experiment uses. Running nine data channels instead of six leads to a 50% increase in the quantity of data to be recorded and so data from both types of receiver were recorded in this way for limited periods only.

The data from the incoherent and coherent receivers was separately analysed using the same FCA procedure. Figure 7.16(a) displays scatter diagrams of various FCA parameters found using the incoherent receivers against those found with phase coherent receivers. The logarithmic output of the incoherent receivers is apparent in the signal plot (bottom left). The expected broadening of the spectra of the incoherent receivers shows up in in the fading times plot and also in the FCA scale parameters $T_{\frac{1}{2}}$ and $d_{\frac{1}{2}}$ plots. The FCA apparent and true velocities are also plotted, (eastward and northward components plotted together) and show a considerable degree of scatter. The mean true velocity and $T_{\frac{1}{2}}$ profiles for both the incoherent and coherent receivers are displayed in figure 7.16(b) and these profiles do show similar trends with altitude. Notice that the incoherent receiver profiles appear to be offset a kilometre or two higher than those of the coherent receivers. This offset can be traced to the different impulse response of the coherent and incoherent receivers.

Since this work is interested perturbations such as gravity waves, it is useful to compare the behaviour of results from both types of receiver with time. Figure 7.17, displays plots of velocity vectors derived from incoherent and coherent receivers with height and time; the vectors in both plots do show similar variations with height and time.

In the limited data set available, there is broad overall agreement between the coherent and incoherent results, although the considerable scatter emphasizes that short period comparisons between the two modes of operation should be treated with caution.

7.6.2 FCA Results Comparisons

As mentioned above, the FCA algorithm used by the drifts experiment follows [Brown and Chapman, 1972]. The FCA parameters found by the drifts experiment include the main parameters defined in section 6.2.1. The experiment operates 24 hours a day, all year around, barring occasional break-downs or problems such as excessive radio interference.

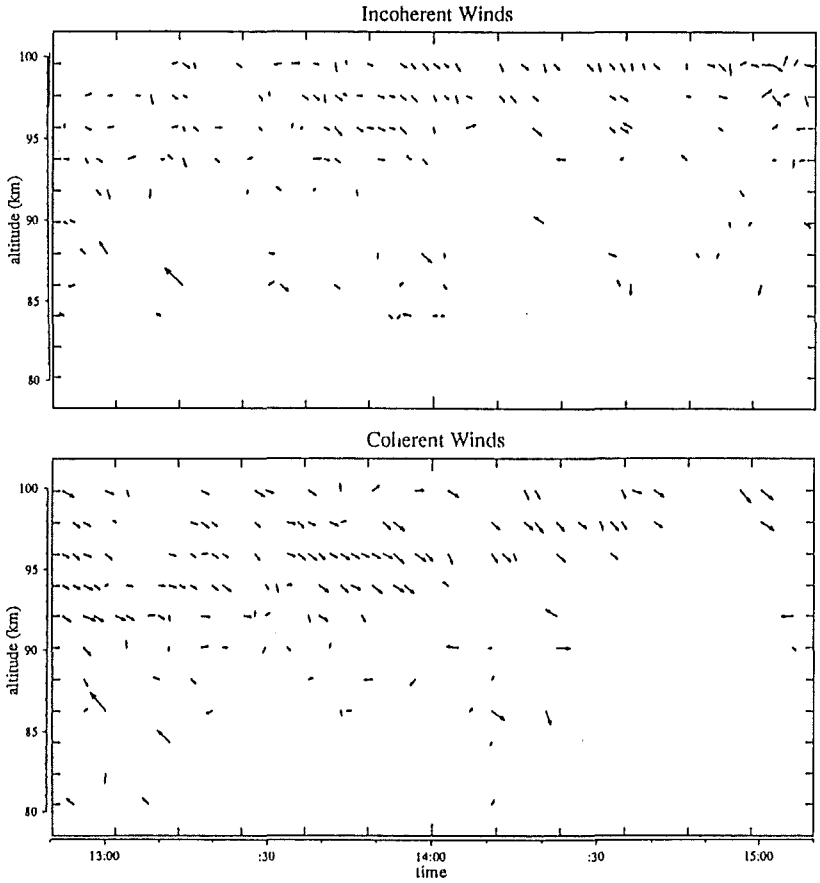

Figure 7.17: **Velocity vectors on incoherent** (upper panel) **and coherent receivers** (lower panel) for the same data as figure 7.16. North is upwards and the maximum vectors have a magnitude of about 150 ms^{-1}.

Like the interferometry experiment the sampling time is one minute. After the sampling is completed, the data is analysed on the data collection computer using FCA and the results are stored for further analysis.

After analysis the raw data is discarded and another sampling period starts. The time between successive samples depends on the time taken on analysis which depends on the quality of the data. During the analysis various tests were applied, such as the checks on the signal to noise ratio of the data and other acceptance criteria very similar to those discussed in section 6.2.2. If samples from a particular range bin fail these tests at any stage, those samples are discarded and analysis moves on to the next range bin samples. If all of the data at each range bin passes the tests, and the full analysis procedure is carried out on each sample, the analysis can take approximately ten minutes. However if all of the data has, for example, a very low signal to noise ratio, then it is discarded earlier in the analysis, a process that takes about three or four minutes.

Birdlings Flat

The Birdlings Flat radar collects drifts data on range bins corresponding to altitudes from 60 km to 105 km at one kilometre intervals. The average time between sampling runs is about seven minutes and the data on an average of three range bins passes all of the acceptance criteria tests, although there is considerable variability in both of these figures.

The data collection rate obtained by FCA of observations made for the interferometry experiment was somewhat higher than that of the drifts experiment using the same acceptance criteria. For example, at Birdlings Flat at altitudes between 90 km and 100 km, the drifts experiment has a success rate of about 10% - 15%, whereas the success rate with the interferometry data was about 25% - 30%. This higher success rate is mainly due to the use of phase sensitive receivers which can provide greater noise discrimination than the incoherent receivers of the drifts experiment. Note that because of the delayed impulse response of the incoherent receivers used in the drifts experiment (noted in the previous section), the quoted ranges for the drifts data shown here (figures 7.18 and 7.19), are approximately three and a half kilometres too high, [Dr. G. J. Fraser, pers.comm.].

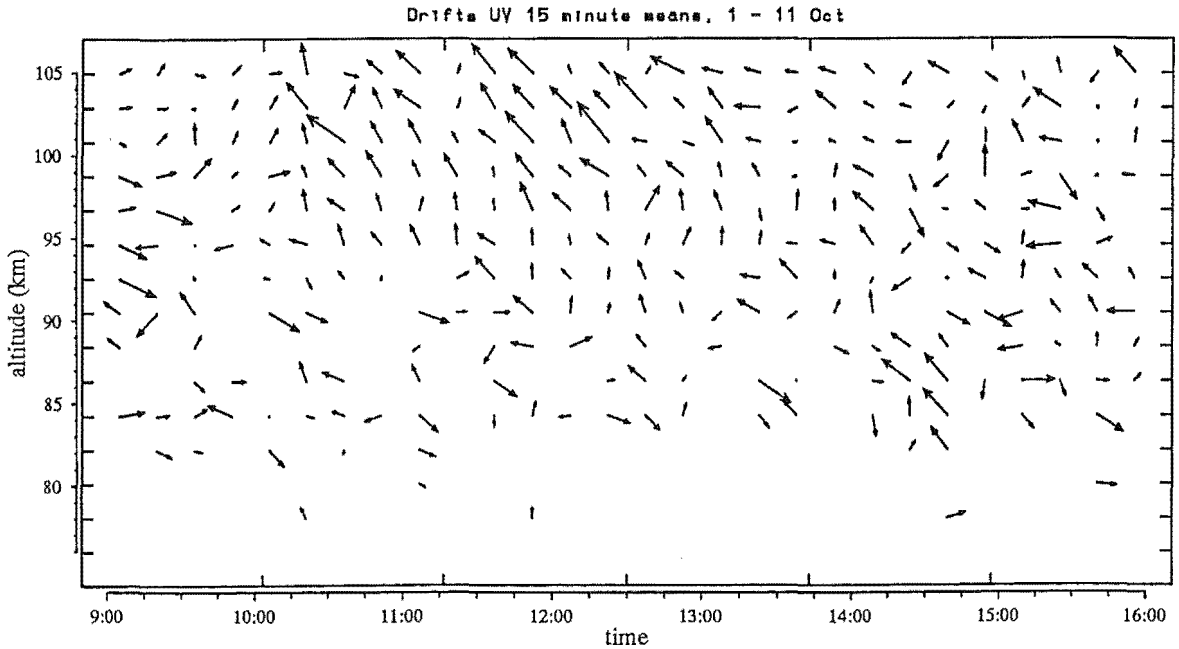

Figure 7.18: **Drifts mean velocity vectors around 6 October 1990,** 15 minute means over 5 days beforehand and 5 days afterwards. The maximum vectors correspond to a velocity of 100 ms^{-1}.

Figure 7.18 displays the 15 minute mean velocity vectors as as found by the drifts experiment wind averaged over five days before and after 6 October 1990, the day the DKS interferometry experiment was run. (Note that averaging several days together in

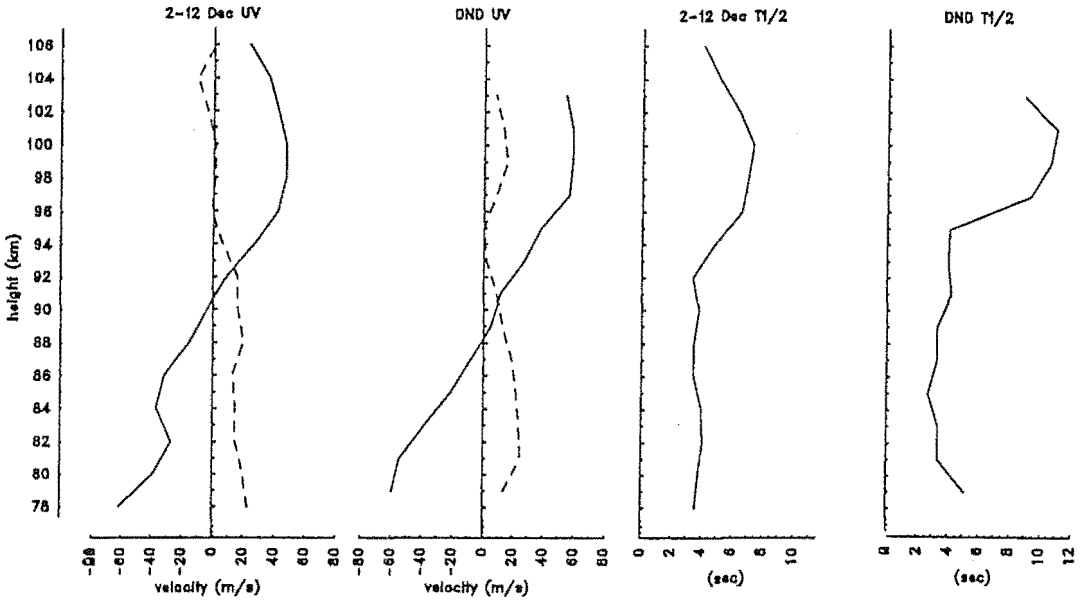

Figure 7.19: **Mean profiles of drifts and FCA** of interferometry data around and on 8 December 1990 for true velocity (solid line eastward, dashed line northward components), and $T_{\frac{1}{2}}$. The drifts data was collected from 2 Dec to 12 Dec between 9:00 and 16:00 and the interferometry data (labelled **DND**) was collected on 8 Dec between 10:00 and 15:00.

this manner emphasizes regular daily patterns, for example solar tides, and suppresses shorter period variations such as internal gravity waves, and longer period variations such as planetary wave activity.) The drifts winds plot covers an extra hour earlier and later than the time of day the interferometry experiment was run. FCA of observations collected by the interferometry experiment on 6 October 1990 at Birdlings Flat are shown in figure 7.14, (section 7.5.1). Both plots show a similar variation in velocity above 90 km, notably being rotation in the velocity vectors associated with the semidiurnal tide as discussed in section 7.5.1.

On days when the tidal variation is not as strong as the example in figure 7.18, the mean wind as a function of height can be compared. This is done in figure 7.19, showing the mean wind profile as found by the drifts experiment over ten days in early December 1990 between 9:00 and 16:00 hours local time, and 5 hours of interferometer FCA winds collected on December 8 1990 (labelled **DND**). Also shown are profiles of the FCA time scale parameter $T_{\frac{1}{2}}$. The mean flows, eastward above about 95 km and westward below about 85 km and the increase of $T_{\frac{1}{2}}$ with height (allowing for the aforementioned $3\frac{1}{2}$ km offset in range for the drifts profiles) are clear in both the drifts and interferometry FCA results.

Scott Base

The Scott Base drifts experiment collects drifts data on range bins corresponding to altitudes from 40 km to 99 km at two kilometre intervals. The operation of the Scott Base drifts experiment has proved to be somewhat more intermittent than that of the Birdlings Flat radar due to difficulties such as the extreme climate and remoteness of Antarctica. Members of the Department of Physics of the University of Canterbury are generally able to visit the site for several days each year; however the rest of the year the radar is maintained by staff of the DSIR Antarctic Division and when problems arise there can be extra delays as diagnostic procedures and advice are relayed from the University (for example see appendix A.1). When the radar is running smoothly, the data collection rate is very similar to that of the Birdlings Flat radar.

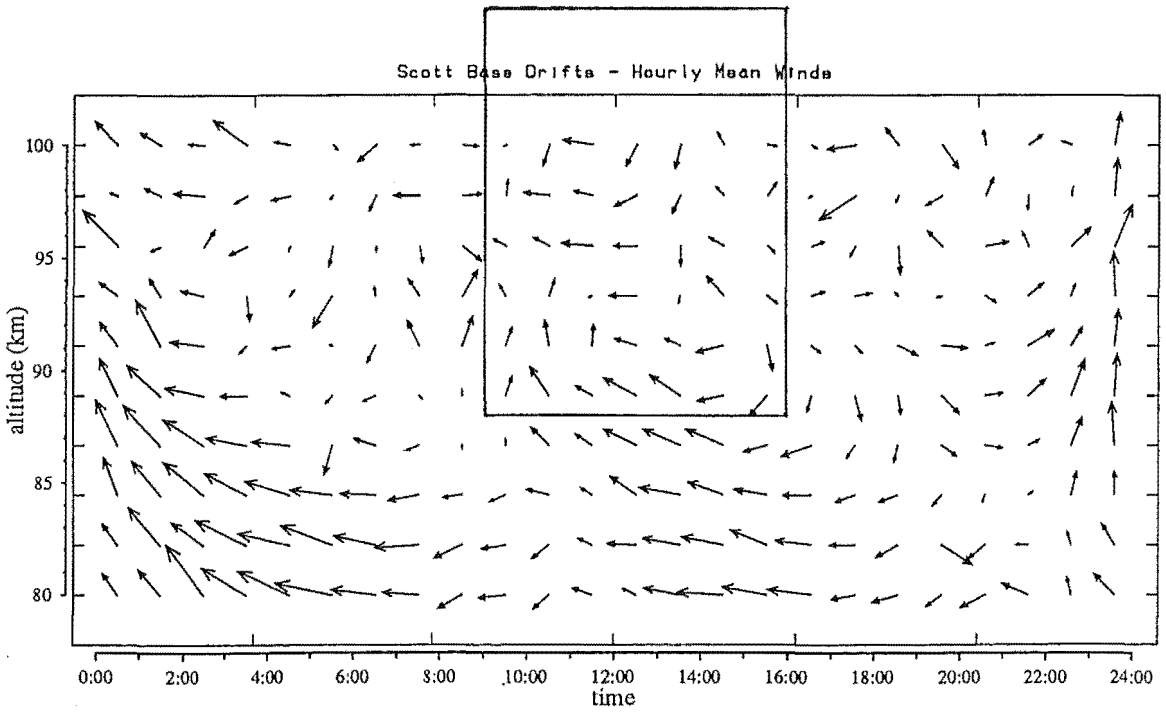

Figure 7.20: **Drifts mean velocity vectors at Scott Base, December 1988.** Averaged over the period 5 Dec to 25 Dec, the vectors represent the hourly means over two adjacent 1 km range bins. Northward is upwards and the magnitude of the greatest vectors is 50 ms^{-1}. The box indicates the period covered in figure 7.21.

The data sets collected by the interferometry experiment on the Scott Base radar were more intermittent than that collected at Birdlings Flat and could only cover periods of

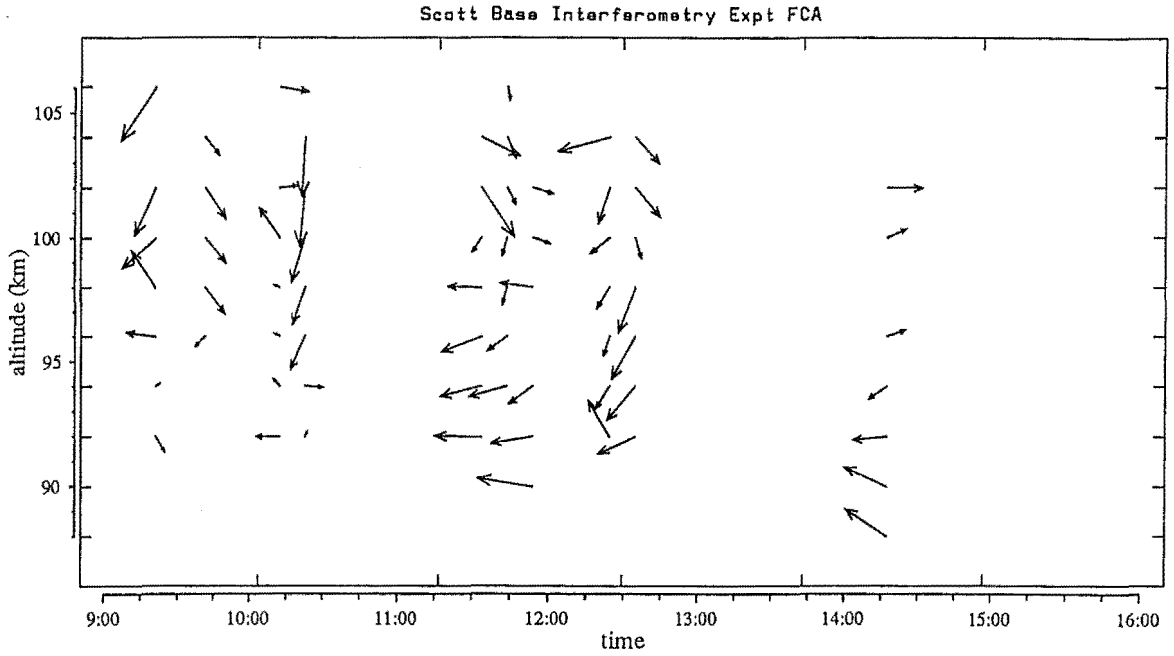

Figure 7.21: **Interferometry FCA velocity vectors at Scott Base.** The data was collected from 14 Dec to 17 Dec 88 during several half hour runs at various times of the day. Here each column of vectors represents the average FCA velocities during each of these runs plotted at the time of day the data was collected.

about half an hour so tidal variations in each data set could not be observed. However means of the half hour data sets collected at various times over the four day period during which the interferometry experiment operated can be compared with the mean drifts winds. Figure 7.20 shows the hourly mean wind vectors as averaged on about ten days spread over twenty days from December 5 1988 to December 25 1988. (Because of all of development work going into the interferometry experiment, as well as the maintenance work on the drifts system itself, the drifts experiment only operated approximately every other day during this period.) The averaged FCA winds for the interferometry data sets are shown in figure 7.21. Apart from isolated runs, most of the interferometry data was collected around mid-morning to mid-day, so only a limited period corresponding to these times is shown. Also the receivers used in the interferometry experiment were not as sensitive as the drifts receivers and so the altitude range of the interferometry experiment is somewhat higher than the drifts experiment. The height and time range of figure 7.21 is indicated by the box in figure 7.20.

At around 90 km the flow patterns for both experiments are similar, being mainly westward, also the southward flow at higher altitudes after mid-day appears in both results. However many of the other velocity vectors disagree, although there is expected to be

some variability from day to day because of the strong two and four day variations due to planetary waves that have been reported in the Antarctic (for example [Lawrence, 1990] and [Andrews et al., 1987]).

The mean wind and $T_{\frac{1}{2}}$ profiles for two hours around mid-day as observed by both experiments is shown in figure 7.22. The mean winds on the drifts experiment are somewhat lower in magnitude in the limited region of cross over shown in this figure. As was observed at Birdlings Flat, $T_{\frac{1}{2}}$ is somewhat lower for the drifts experiment as would be expected for incoherent receivers. (Note that the offset in the range calibration applied to data collected on the Birdlings Flat incoherent receivers is not required for data collected on the incoherent receivers at Scott Base.)

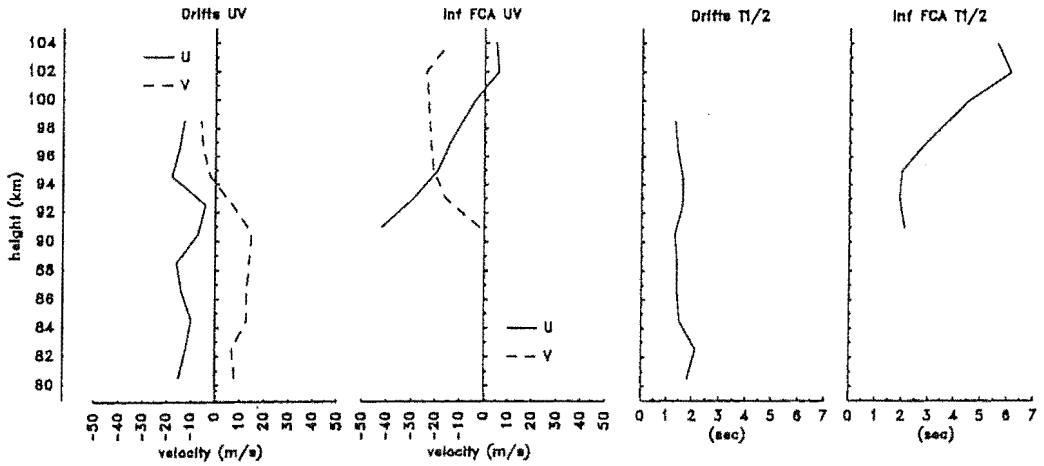

Figure 7.22: **Mean midday profiles of drifts and FCA results at Scott Base.** The profiles represent the means from 11:00 to 13:00 for the drifts results from 5 Dec to 25 Dec, and the FCA of interferometry data for the same times collected on 14 Dec to 17 Dec 88 for FCA true velocity (solid line eastward **U**, dashed line northward **V** components), and $T_{\frac{1}{2}}$.

7.7 Spatial Interferometry

Spatial interferometry was carried out using phase differences between signals received on spaced antennae derived from cross correlation functions and cross spectra, (sections 5.2 and 5.4). Calibration corrections (estimated by the methods of section 2.3.2) were made to these phase differences before spatial interferometry was carried out.

7.7.1 Spatial Interferometry from Correlation functions

As mentioned above, the mean phase difference can be determined from the phase of the cross correlation function at zero lag. With three spaced antennae, three of these phase difference estimates were available to determine a mean direction of arrival for each sample. Figure 7.23 displays an example of the determined direction of arrivals in the form of a scatter plot for each range bin, showing the position of the implied scattering centre. In this example the locations of the centres are biased towards the east-west axes for the height bins between 85 and 95 km; in the other height bins the distributions are more evenly scattered around zenith (particularly at 99 and 101 km). The time evolution of the directions of arrival for some of this data appears in figure 7.56, section 7.12.

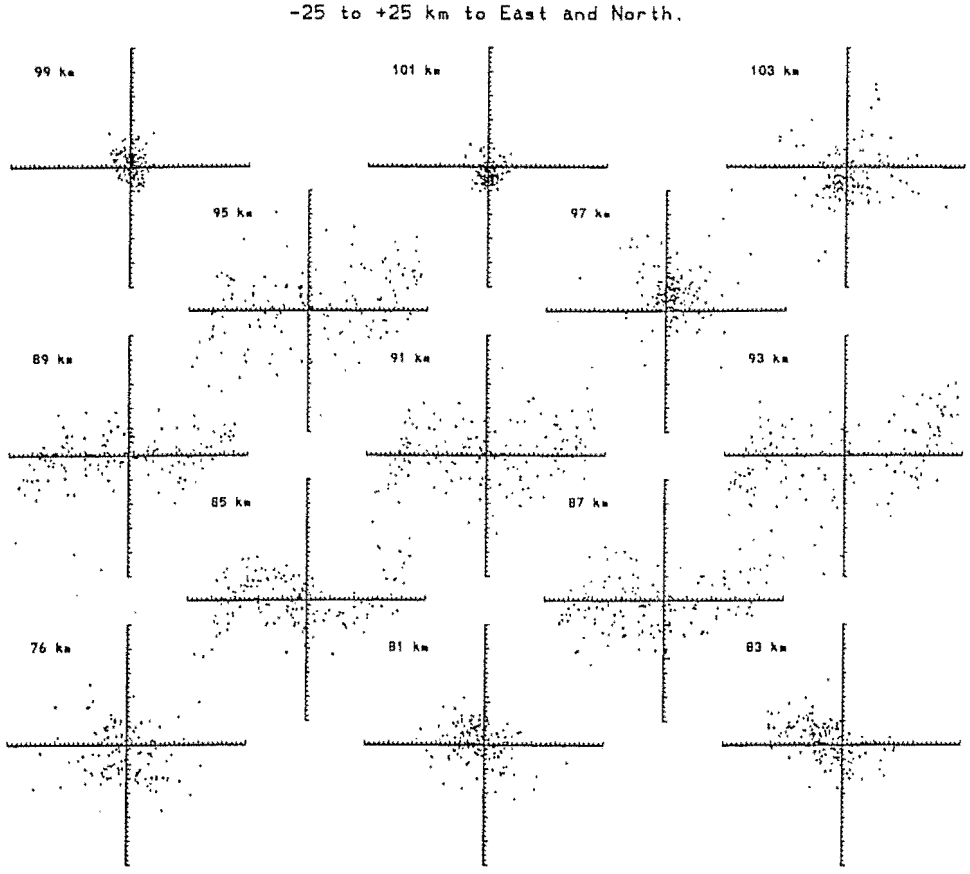

Figure 7.23: **Mean scattering centre location, 8 December 1990** at Birdlings Flat for each sample at each range bin over the 5 hour data set. Locations were found using spatial interferometry of cross correlation phases.

The phase difference between each pair of receivers was found for each of the five frequencies of the experiment and the mean of these for each receiver pair was used to

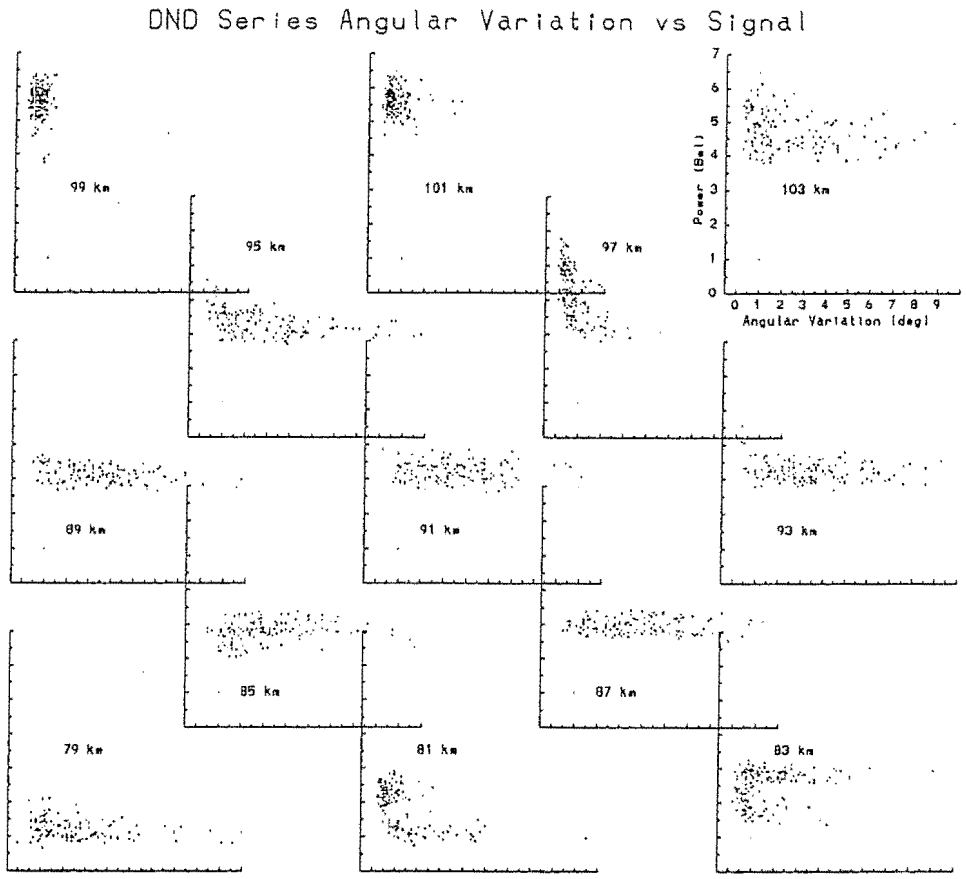

Figure 7.24: **Variation in mean angle of arrival vs Signal, 8 December 1990** at Birdlings Flat. The points represent the mean for each sample. (The scale is indicated on the top right hand plot.)

determine the direction of arrival. The variation of the phase differences at each frequency was used to give some measure of the variation in the mean angle of arrival. Figure 7.24 shows this angular variation plotted against signal at each height bin for the 8 December 1990 Birdlings Flat data set. This gives a simple picture of the angular distribution of the mean scattering direction; further analyses of the angular distribution of scattering power will be given in a later section on aspect sensitivity.

7.7.2 Vertical Velocities

The mean cross correlation directions were assumed to give the directions of the radial velocities determined from the mean Doppler shifts in section 7.1.3. As mentioned in that section, these velocities are comprised of components of both the vertical and horizontal wind. If the horizontal wind is known, it can be used with the radial velocity and the mean scattering direction to give the vertical wind. Here vertical winds were found in this manner using the FCA true velocity as an estimate of the horizontal wind, (if the

FCA velocities contain a vertical component, for example due to a tilted scattering layer, it is generally much smaller than the horizontal and can be ignored to a first approximation).

An example of the vertical velocities found in this way is given in figure 7.25 for the October 6 1990 Birdlings Flat data. (Vertical winds for the December 8 1990 data appear in figure D.7, appendix D.) The vertical velocities in this figure show a trend from upwards before near midday to downwards after midday. The FCA winds were given in figure 7.14. The change in vertical velocity direction appears to be correlated with the rotation of the horizontal winds apparently associated with the semidiurnal tide. If the observed variation in vertical velocity is associated with the semidiurnal tide, which is a westward propagating 12 hour inertial gravity wave, following the somewhat simplistic model of figure 3.1 in section 3.1, it would be expected that the vertical velocity would be downward for the eastward and upward for the westward phases of the wave. However the response of the atmosphere to a tidal wave depends on latitude and on which mode of oscillation of the tide dominants. Observations of tides (for example [Forbes, 1990]), and gravity waves in general (for example [Reid and Vincent, 1987b]), do show considerable variability in behaviour, and the observations made here are consistent with these reports.

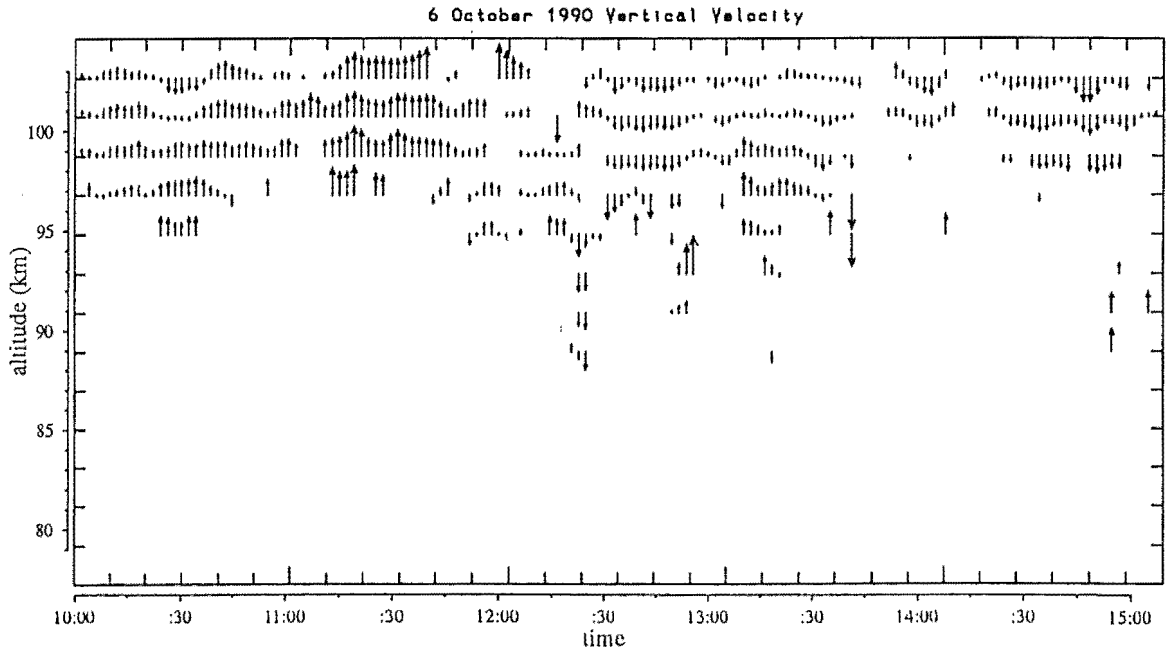

Figure 7.25: **Vertical velocities, 6 October 1990** at Birdlings Flat (maximum vectors correspond to 4 ms^{-1}, quarter-half-quarter filtered).

It is possible that there is some error in the vertical velocity measurements for this data set. Typically the vertical wind in the mesosphere is of the order of 1 ms^{-1} or less, (for example [Balsley and Riddle, 1984]), much lower than the horizontal wind. There only

needs to be a small error in determining the direction of arrival of scattering for the horizontal wind to be misinterpreted as an apparent vertical wind that completely swamps the real vertical wind. As will be discussed in section 7.13.2, except for the most localized scattering, typical uncertainties in individual direction of arrival measurements are about 2° or more, which with a horizontal wind of 50 ms^{-1} would give an error of 2 ms^{-1} in the vertical wind. Alternatively the observed vertical wind may be better explained by a systematic error in the phase calibration for this data set than by random uncertainties in direction of arrival. A 0.2 radian error in the mean phase differences used for phase calibration between, say, antennae F and D, could lead to an error of about 1° in the estimates of zenith angle. If, as a result, the directions of arrival pointed 1° too far to the east and actual vertical winds were zero, the eastward winds observed here could produce an apparent upward velocity, and similarly the observed westward winds would produce a downward velocity, close to the velocities shown in figure 7.25.

7.7.3 Spatial Interferometry from Spectral Analysis

Spatial interferometry on the results of cross spectral analysis gave directions of arrival for typically three to five or more scattering centres identified in each sample by Doppler sorting. The spectra presented in a previous section had dominant features that were presumed to originate from discrete scattering centres. The cross spectra of signals received at spaced antennae give phase difference as a function of Doppler frequency and so the direction of arrival of signals with different Doppler shifts can be determined using spatial interferometry. Figure 7.26 gives an example of spatial interferometry results determined from cross spectra of a sequence of data collected on the Scott Base radar. Each sample was analysed using FFT and MEM techniques, and the spectra of both techniques were compared using the criterion test of section 4.2.4 to find consistent features. The cross spectral phase of the consistent features was used to determine the locations of the centres given in figure 7.26.

An interactive viewing program was written to through scan the data sets as the spatial interferometry analysis techniques were being developed. The program displayed the locations of successive scattering centres on an screen giving an evolving picture of the centres that could be sped up, slowed down or jumped from height bin to height bin. The program was found to be very useful as a diagnostic and demonstration tool.

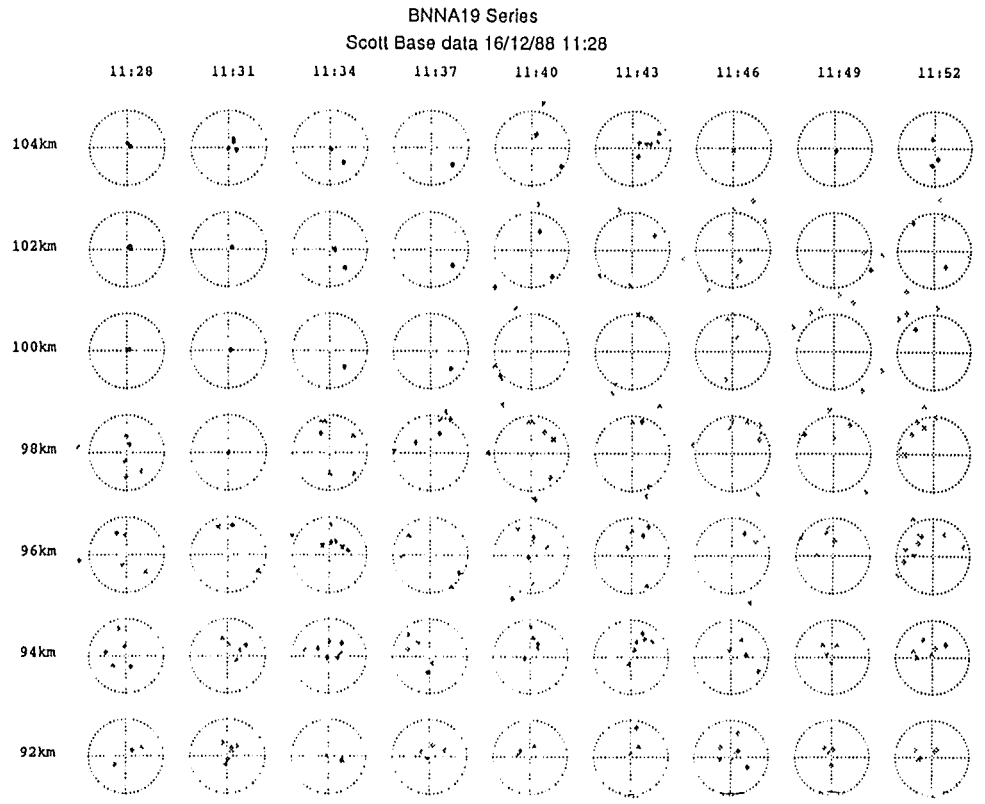

Figure 7.26: **Spatial interferometry of scattering centres** identified from spectral analysis of a sequence of data collected at Scott Base on 16 December 1988. The circles indicate a zenith angle of 20° and north, east, south and west by the quadrant lines (north being up). The shaded dots mark the position of the scattering centres, the shading indicating the power of each feature and the size indicating the spectral width.

7.8 Interferometric Velocity Results

Interferometric velocity estimates were made for all of the data sets collected on the Birdlings Flat and Arrival Heights radars. Both three dimensional and two dimensional interferometric velocities were found, using both periodogram and MEM spectra. Examples of interferometric velocity results from the Birdlings Flat radar are displayed in figures 7.27 and 7.28. Also displayed are corresponding FCA apparent velocity results. The variability between different variations of the interferometric velocities, which can be taken as a measure of the uncertainty in the interferometric velocities, is typically about 10 ms^{-1}. Ten minute means of the interferometric and FCA apparent velocity vectors for the 6 October 1990 data set are shown in figure 7.28. Figure 7.29 compares the eastward and northward FCA apparent and interferometric velocity components for data obtained on the Scott Base radar.

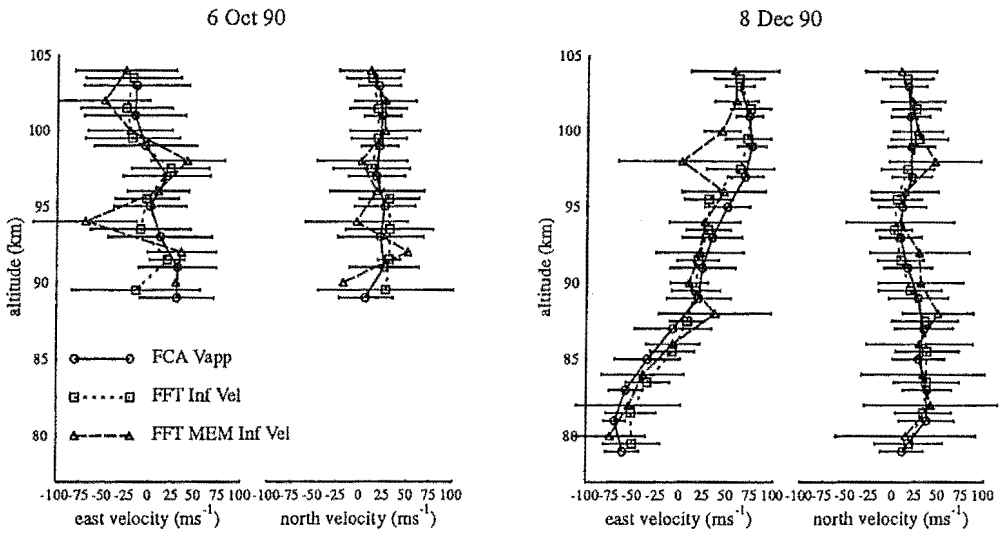

Figure 7.27: **Examples of mean FCA and interferometric velocity profiles** at Birdlings Flat. The 6 Oct 1990 interferometric velocities are three dimensional, the 8 Dec 1990 interferometric velocities are two dimensional and the FCA velocities for both days are the apparent winds. The FFT and MEM spectra were compared against each other to find consistent peaks for the 'FFT MEM Inf Vel' profiles. The error bars indicate standard deviation of the velocity at each range bin. Only points for which both FCA and interferometric velocities were available are included and points beyond two standard deviations from the mean were removed.

7.8.1 Comparing results

The FCA and interferometric mean velocity profiles of figure 7.27 agree within the standard deviations at each range bin and follow similar trends with altitude. Averaging over shorter time spans shows more mixed agreement, as can be seen in figure 7.28. Comparisons of instantaneous velocity components show considerable scatter, for example figure 7.29, although general agreement between the two methods is displayed.

Previous comparison studies of velocities found via two methods, (for example from FCA and interferometry, [Franke et al., 1990]), have either compared mean velocity profiles (as in figure 7.27) or have produced scatter plots of the velocities plotted against each other (such as figure 7.29). Here it was decided to devise a comparison test which classified the samples into two groups : those samples whose velocities determined by the two methods agree and those samples whose velocities disagree. Then other characteristics (for example signal power or fading time) of the samples having velocities that agree could be compared with the same characteristics of the samples whose velocities disagree. Also various methods of finding velocity could be compared against each other to find which

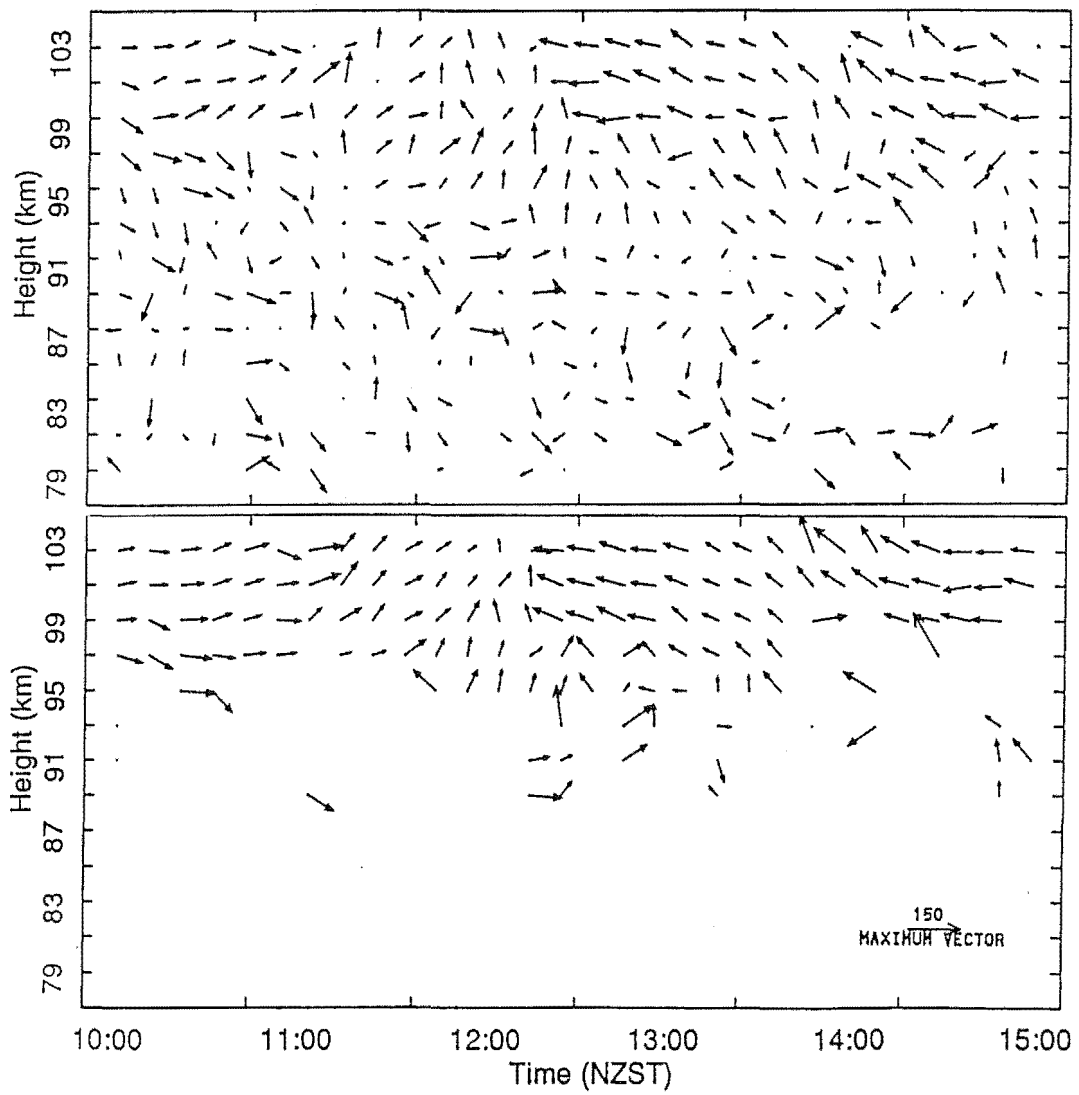

Figure 7.28: **Ten minute means of FCA and interferometric velocity vectors** for 6 October 1990 at Birdlings Flat. The interferometric velocities (upper panel) are the three dimensional velocities from periodogram spectra and the FCA velocities (lower panel) are the apparent winds. FCA true winds for this data are given in figure 7.14, section 7.5.1.

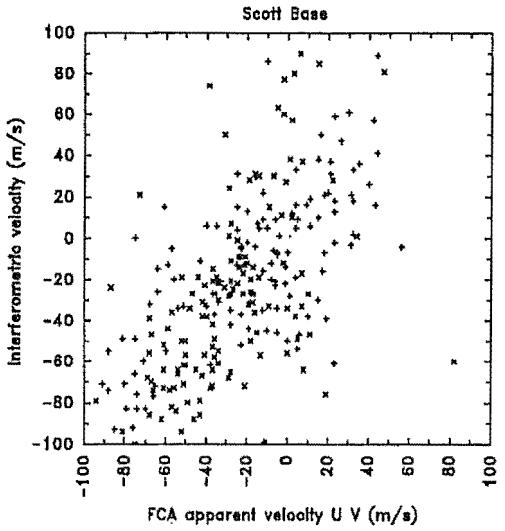

Figure 7.29: **FCA apparent and interferometric velocity components on the Scott Base** radar (approximately two hours of data, 15 - 17 Dec 1988). The pluses indicate the eastward components and the crosses the northward components. The interferometric velocities are two dimensional velocities.

two methods had the greatest number of agreeing samples (expressed here as a percentage rate of agreement).

A somewhat loose criterion was established, in which "agreement" was declared between two velocity vectors of a sample if

- the magnitudes of the vectors concurred to within 30% (of the larger) and the directions concurred to within 30°, or
- the eastward and northward components (u, v) concurred to within $10\,\mathrm{ms}^{-1}$.

The second criterion was designed to include velocities of low magnitude, since both the interferometry and FCA techniques have larger relative uncertainties at low velocities than at higher velocities. In practice it was found that more than 90% of the velocity vectors declared to be in agreement passed the 30% in magnitude, 30° in direction criterion.

In order to ascertain at what level it could be said that significant agreement existed between two sets of velocity vectors, several series of random velocity vectors were generated and compared using the above criterion. The random vectors were confined to a range of values that typically are observed in real data, and formed into data sets of lengths that was typical of the length of data sets collected for this study.

The results of the comparisons are displayed in table 7.1. As can be seen, the agreement rates between totally random series seems to be around 5%. When the magnitudes are

similar but the directions random (±180°), or the magnitudes random but the directions similar, the agreement rate for these series was of the order of 10-15%.

distribution type	mean (std.dev.)	imposed limits	agreement rate (std.dev.)
uniform in u & v		$\pm 150\,\mathrm{ms}^{-1}$	5.7 (0.7) %
Gaussian in u & v	$0(50)\,\mathrm{ms}^{-1}$	$\pm 150\,\mathrm{ms}^{-1}$	4.9 (1.2) %
Gaussian Amplitude uniform in direction	$100(50)\,\mathrm{ms}^{-1}$	$10-200\,\mathrm{ms}^{-1}$ $\pm 180°$	5.4 (0.8) %
Gaussian Amplitude uniform in direction	$100(50)\,\mathrm{ms}^{-1}$	$10-200\,\mathrm{ms}^{-1}$ $\pm 60°$	13.9 (0.9) %
Gaussian Amplitude uniform in direction	$100(20)\,\mathrm{ms}^{-1}$	$10-200\,\mathrm{ms}^{-1}$ $\pm 180°$	11.6 (2.8) %
Gaussian Amplitude uniform in direction	$100(20)\,\mathrm{ms}^{-1}$	$10-200\,\mathrm{ms}^{-1}$ $\pm 60°$	28.8 (0.9) %

Table 7.1: **Agreement rates between randomly generated velocity series.** The generated series consisted of 500 velocity vectors, the typical number of vectors compared in the observed data sets. Five series of each of the quoted distribution types was generated, enabling ten comparisons to be made. The agreement rate column displays the mean and standard deviation of the agreement rates of the ten comparisons. Uniform distribution indicates that the values were uniformly distributed between the quoted minimum and maximum limits. The Gaussian distributed data had the quoted means and standard deviations, with limits on the minimum and maximum imposed as well.

7.8.2 Interferometric Velocity Comparison with FCA

The percentage rates of agreement between three dimensional interferometric and FCA velocities are given in table 7.2. This table shows the percentage of samples for which both interferometric and FCA velocities could be determined (column labeled "coincident velocities"), and the agreement rate between both interferometric and FCA apparent velocity and interferometric and FCA true velocity.

The data sets labeled DKS and DND show significantly more agreement between interferometric and FCA velocities than the other Birdlings Flat data sets. In section 2.3.2 it was noted that for these two data sets there was found a somewhat clearer cross receiver phase calibration than the other data sets suggesting that the spatial interferometry results for some of the other data sets may be incorrect[1]. For example, it was found that by

[1]This clearer phase calibration may have resulted from the addition of a set of isolation buffers that

adjusting the phase calibrations of the D23 data set agreement rates of up to 16% (compared with 10%) between interferometric and FCA apparent velocities could be achieved even though the phase calibrations used did not correspond to probable calibration values as determined in section 2.3.2. Therefore the results presented in the remainder of this section will concentrate on those from the DKS and DND data sets.

Data set Date, time	length of data set	coincident velocities	agreement with FCA		ratio of apparent:true
			apparent	true	
D20					
28 July 90	2 hr 8 min	18%	11%	6%	1 : 0.5
D23					
18 Aug 90	5 hr 20 min	24%	10%	8%	1 : 0.8
DJY					
16 Sep 90	2 hr 40 min	7%	10%	6%	1 : 0.6
DKS					
6 Oct 90	5 hr	15%	49%	38%	1 : 0.77
DND					
8 Dec 90	5 hr 10 min	36%	37%	24%	1 : 0.64

Table 7.2: **Agreement between Interferometric and FCA winds** for data collected on several days at Birdlings Flat. The coincident velocities column shows the percentage of samples for which both interferometric and FCA velocities could be found. The following two columns show the percentage of the coincident samples for which interferometric velocities agreed with FCA apparent and FCA true velocities. The ratio in the last column indicates the ratio of the apparent to the true velocity agreement rates with interferometric velocities.

It is interesting to note that both the DKS and DND data sets display greater agreement between interferometric velocities and FCA apparent velocities than between interferometric velocities and FCA true velocities. As discussed in chapter 6, FCA in determining the true velocity, makes some corrections[2] for time evolution and anisotropy of the drifting diffraction pattern, whereas the apparent velocity is determined from timing only, [Briggs, 1984].

Comparisons were made of the rate agreement between interferometric velocities and

was installed on the October 6, 1990, the day the DKS data set was collected.

[2]The size of the correction FCA makes to the apparent velocity to find the true velocity depends on the degree of random evolution and anisotropy, and can lead to quite a significant difference between the apparent and true velocity vectors of a sample. For example, when the FCA apparent and true velocities of the DKS and DND data sets are compared with each other using the same comparison test, 47% of the samples in the DKS set for which FCA estimates were available agreed and 39% of the samples in the DND set agreed.

Condition tested	data set	coincident velocities	agreement with FCA		ratio of apparent:true
			apparent	true	
consistent peak spectra	DKS	4%	51%	44%	1 : 0.9 (±.1)
	DND	7%	38%	24%	1 : 0.6 (±.1)
1^{st} radar freq. (unsmoothed)	DKS	15%	40%	33%	1 : 0.83
	DND	34%	31%	23%	1 : 0.75
evenly sampled spectra	DKS	22%	24%	15%	1 : 0.60
	DND	47%	25%	14%	1 : 0.58
two dimensional velocity	DKS	18%	46%	43%	1 : 0.93
	DND	43%	33%	26%	1 : 0.78

Table 7.3: **Agreement between Interferometric and FCA winds at various conditions.** Comparing interferometric velocities and FCA velocities using consistent peak spectra, using periodogram spectra of just the first radar frequency ("unsmoothed"), using evenly sampled spectra (rather than using the peaks of the periodograms for interferometric analysis) and using two dimensional interferometric velocity. The uncertainty in the ratio of agreeing apparent and true velocities is 0.05 or less, excepting the case of the consistent peak condition when much fewer samples were available for comparison.

the two FCA velocities for various conditions of the spectral and interferometric analysis as well as with diffraction pattern parameters of FCA. A summary of some of the spectral and interferometric conditions tested appears in table 7.3.

Many of the periodogram peaks used to determine the interferometric velocities were probably spurious. However when using consistent peak spectra (section 4.2.4), much fewer samples had sufficient peaks from which to calculate interferometric velocities. The interferometric velocity results that could be found with the consistent peak spectra are compared with FCA velocities in table 7.3. Although there are much fewer samples available for comparison (just 73 velocity estimates in the DKS data set), it can be said that the agreement rates do not differ greatly from the results found using the periodogram spectra. (The "coincident velocities" column in the table indicates the proportion of samples in the data set for which both FCA and interferometric velocities could be found.)

Also in table 7.3 there appear comparisons of interferometric and FCA velocities with different smoothing and sampling conditions. [Franke et al., 1990] concluded that the agreement between interferometric and FCA velocities depends on the degree of smoothing performed on the spectra. They claim that smoothing the spectra leads to an over emphasis on strong scattering centres and a bias towards apparent velocities. When they

used sample (or "unsmoothed") spectra, they found greater agreement with true velocities. Here "unsmoothed" spectra were formed by averaging together spectra from just the first radar frequency and each of the three receivers instead of the normal five frequencies and three receivers. There was some decline in the agreement rates with both apparent and true velocities using these spectra, although the ratio of apparent to true velocity agreement does show a some shifting in the bias towards true velocity.

To test the effect of using just strong peaks in the spectrum for interferometry, spectra were sampled evenly in the spectral frequency domain ignoring the power of the spectrum (provided it was above a certain noise level). The "evenly sampled" results in table 7.3 used spectra evenly sampled in the region ± 0.25 Hz. As might be expected the agreement rates were significantly reduced, however an even greater bias in these results is shown towards apparent velocity.

When finding just the "two dimensional" velocity (with vertical velocity set to zero), the bias of the interferometric velocities towards apparent velocity is reduced somewhat. [Meek and Manson, 1987] suggested that the two dimensional velocity would follow the apparent velocity if there is a wave-like diffraction pattern although they found that this occurred only rarely in their observations.

The radial velocity RMS standard deviation ($\sigma_{v_{\text{rad}}}$) of the interferometry observations from the fitted velocity was given by equation 5.29 in section 5.5.1. A high radial velocity RMS deviation implies that the locations and Doppler shifts of the scattering centres are not consistent with a constant motion. Figure 7.30 displays the observed probability histogram of the rate of agreement and disagreement between interferometric and FCA apparent velocities as a function of the radial velocity RMS deviation. Those samples that disagree show some tendency to higher deviations in the fit than those that agree. These higher deviations may indicate greater variations in velocity across the radar volume and/or errors in the spatial interferometry of those samples. Note that the error bars given in this figure and the similar figures in the remainder of this section are simply based on Poisson type standard deviations (the square root of the count) and not derived from the uncertainties in measuring the quantities displayed. They are only given as an indication of the number of samples used to determine each statistic.

Figures 7.31 and 7.32 display the agreement/disagreement rates versus the FCA parameters, $T_{\frac{1}{2}}$ and the spatial correlation ellipse major/minor axes ratio. $T_{\frac{1}{2}}$ provides an estimate of the time scale of random changes in the diffraction pattern as it moves along. The axial ratio parameter provides a measure of the anisotropy of the the pattern.

There is a strong bias in the samples with disagreeing velocities towards shorter time

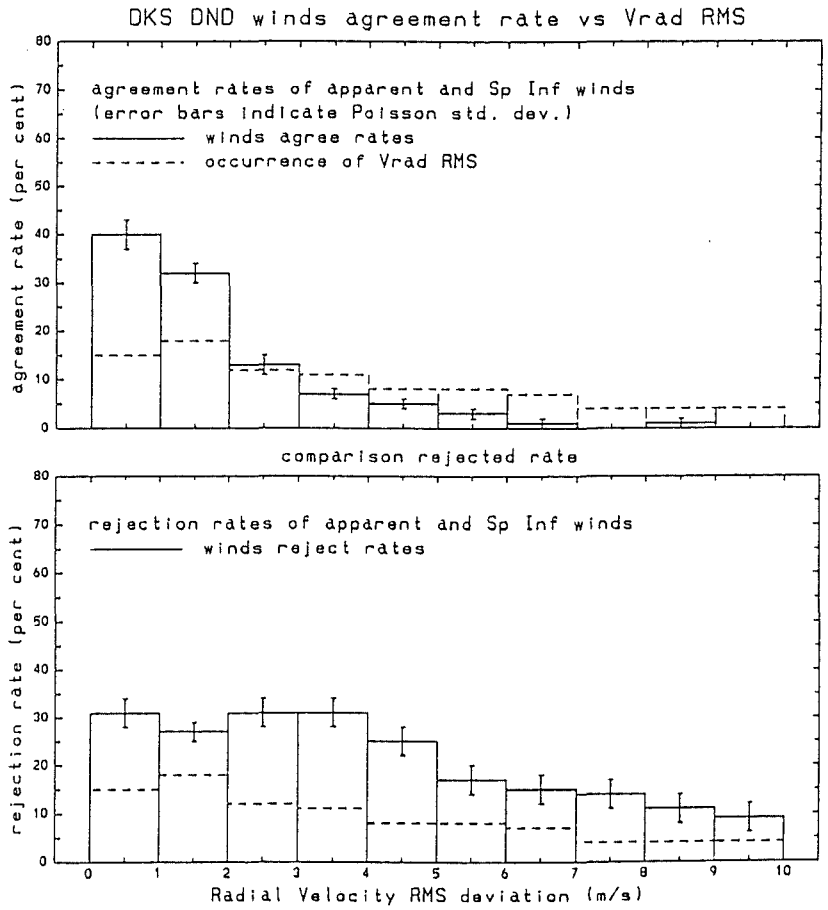

Figure 7.30: **The rate of interferometric and FCA velocity agreement/disagreement with $\sigma_{v_{rad}}$,** (from equation 5.29 in section 5.5.1). The error bars are only an indication of the number of samples used in determining each count rate. Compiled using all the data of table 7.2, for which both interferometric and FCA velocity estimates were available.

scales than those that agree. When the time scale is of the order three seconds or less, there is somewhat more agreement between apparent and interferometric velocities than between true and interferometric velocities (not shown here). Apart from these short time scales, the relative rates of agreement between apparent or true velocities with interferometric velocity does not significantly vary with $\sigma_{v_{rad}}$, $T_{\frac{1}{2}}$ and axial ratio. (The apparent velocity was used in figures 7.30, 7.31 and 7.32.) The axial ratio results show some tendency to higher values among those samples whose velocities disagree.

As the angular spread of the scattering centres increases, the mean magnitude of the velocities obtained by both FCA and interferometric techniques declines as can be seen in figure 7.33. The angular distribution is given by aspect sensitivity (discussed further in

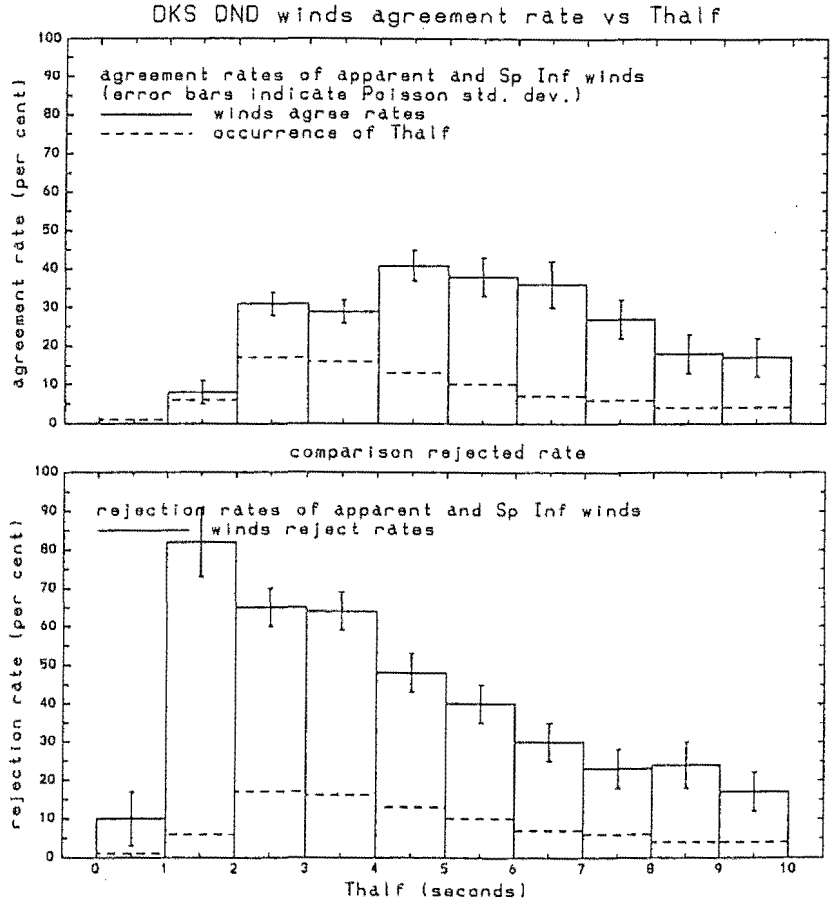

Figure 7.31: **The rate of interferometric and FCA velocity agreement/disagreement with $T_{\frac{1}{2}}$,** (as for figure 7.30).

the next section), a measure found to be closely related to the spread of scattering centres as determined by spatial interferometry.

7.8.3 Discussion

Those data sets for which the clearest phase calibrations for spatial interferometry could be made had significant agreement between interferometric and FCA velocities. The agreement with FCA velocities was found to be greater when the scattering region seemed to be changing the least as it moved as indicated by the radial velocity RMS deviation parameter $\sigma_{v_{\text{rad}}}$ and by the FCA time scale parameter $T_{\frac{1}{2}}$. Also there was found to be a somewhat lower agreement rate when the diffraction pattern became elongated. The interferometric velocities for those data sets were found to be closer to the FCA apparent velocities than true velocities, particularly when the time scale of the diffraction pattern was low.

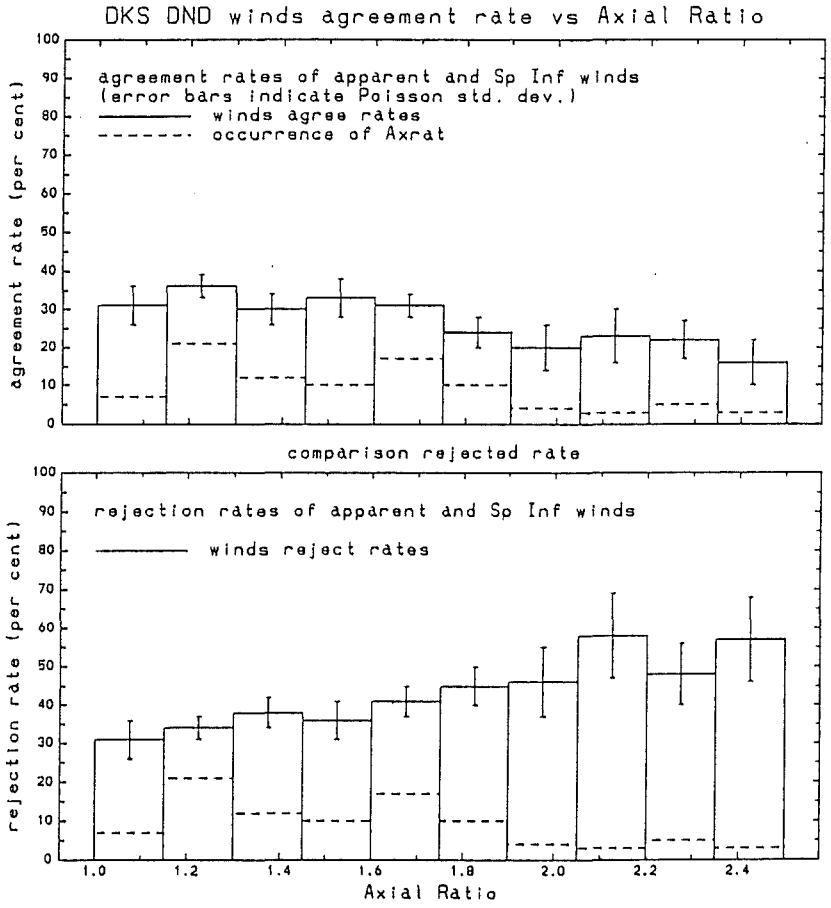

Figure 7.32: **Rate of interferometric and FCA velocity agreement / disagreement with axial ratio**, (as for figures 7.30 & 7.31).

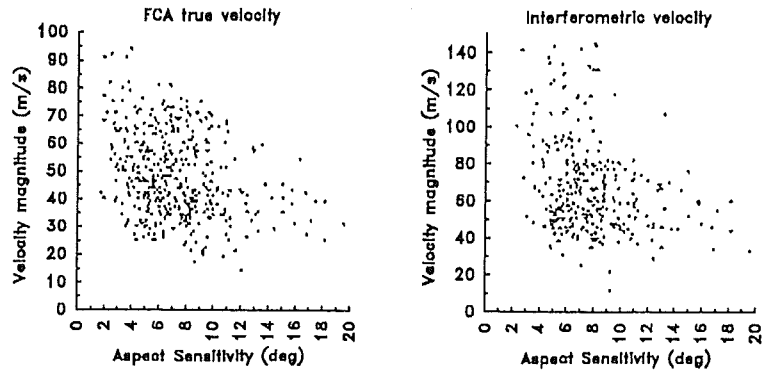

Figure 7.33: **FCA and interferometric velocities vs angular distribution** of scattering (aspect sensitivity as measured by the beam broadening effect using the fading time and $T_{\frac{1}{2}}$), October 6 1990, Birdlings Flat.

[Meek and Manson, 1987] also found closer agreement between their interferometric velocities and apparent velocities than true velocities. Similarly [Franke et al., 1990] found closer agreement between interferometric and FCA apparent velocities when their cross receiver spectra were smoothed (by averaging adjacent spectra together). However when their "sample" (not averaged) spectra were used, they found their interferometric velocities gave closer agreement with FCA true velocities. They argue that when the spectra are smoothed, the cross spectral phases of the strongest peaks tend to dominant the phase spectra leading to an over-emphasis in the spatial interferometry stage of the strongest scattering centres. Scattering centres around zenith tend to appear the "brightest" because of the radar's antenna diagram which leads to a predominance of near zenith centres when finding interferometric velocity. Smaller zenith angles for a given Doppler frequency imply a larger horizontal velocity and since FCA apparent velocities are nearly always larger than true velocities, the resulting interferometric velocities tend towards apparent rather than true velocities. Using unsmoothed spectra might sample over a larger area of the radar volume rather than just near the zenith since they have randomly distributed spurious peaks.

Here it was found that reducing the spectral smoothing did lead to somewhat more agreement between interferometric and true velocities compared with apparent velocities although at the expense of reducing the number of samples for which interferometric velocities could be found. However when velocities were determined from phase values evenly spread throughout the Doppler spectra, rather than just at the peaks, the velocities had an even greater bias towards apparent velocities.

[Franke et al., 1990] suggest phase consistency checks made by [Adams et al., 1986] and [Meek and Manson, 1987] in spatial interferometry also lead to velocity estimates that are too large. Both groups used the additional information supplied by their extra antenna pairs to verify scattering centres identified by spatial interferometry. [Adams et al., 1986] used the phase deviations as a weighting function in fitting velocity and [Meek and Manson, 1987] applied phase consistency constraints when selecting scattering centres. [Franke et al., 1990] claim that these phase consistency checks, like spectral smoothing, lead to an over-emphasis on strong, near zenith scattering centres. They argue that the best phase consistency test may be no test since any checks would lead to biased velocity results. As in the [Franke et al., 1990] study, no such phase consistency checks could be made here since there were no redundant antenna pairs.

As the the angular spread of scattering increases the interferometric, and FCA velocities, tends to decrease; also there is a decline in in the proportion of samples for which an

estimate of the velocity can be made. This would appear to be because when the scattering is too widely distributed both methods fail if the velocity is high; FCA fails because the fading time becomes very small and thus the spectra become broad resulting in extra uncertainties in the interferometric analysis. A consequence of this is that samples with scattering centres with a wider angular spread had less bias towards apparent velocities, as compared with true velocities, than those with a narrower spread.

7.9 Scattering Measurements

This section summarizes observations of scattering processes as made using aspect sensitivity, turbulent scale and signal distribution measurements.

7.9.1 Aspect Sensitivity

Aspect sensitivity provides a measure of the angular distribution of scattering and the results of five methods of measuring aspect sensitivity which were introduced in section 3.3.1 are discussed here. Recall that the aspect sensitivity measure θ_s is the half width at e^{-1} power of the backscatter polar diagram. The methods of measuring θ_s are

beam broadening using fading time. The fading time is used to estimate the magnitude of broadening of the Doppler spectrum due to the combined width of the antenna polar diagram and the polar diagram of scattering, [Hocking, 1989]. An estimate of horizontal velocity is needed for this calculation, and here the magnitude of the FCA true velocity was used.

beam broadening using fading time and $T_{\frac{1}{2}}$. The standard beam broadening method assumes that all of the width of the Doppler spectrum as estimated by the fading time is due to beam broadening and that fluctuations due to turbulence are insignificant. Here the FCA parameter $T_{\frac{1}{2}}$ was used to estimate and remove the spectral broadening due to turbulence from the overall spectral width. (section 3.2.1). The magnitude of the FCA true velocity was also used in this method.

the spatial correlation function. The distance over which the spatial correlation ε function falls to $\frac{1}{2}$ can be used to approximate the combined polar diagram of the scattering and antenna $\theta_{sb} \approx 15.2/\varepsilon_{0.5}$, [Briggs and Vincent, 1973] and [Briggs, 1992]. Here the FCA parameter $d_{\frac{1}{2}}$ was used for $\varepsilon_{0.5}$.

rms deviations of phase difference. The magnitude of the rms deviations from the mean phase difference between signals received on spaced antennae provide a measure

of angular spread, [Bramley, 1951, Lindner, 1975a], which can be related to aspect sensitivity.

spatial interferometry. Spatial interferometry was used to determine the azimuth and zenith angles of Doppler sorted scattering centres (section 5.4). The direction of strongest scatter was identified and the variation in power with the angular separation of the scattering centres from this strongest scatter direction was used to estimate aspect sensitivity.

Allowances were made in all of these methods for the contribution of the width of the polar diagrams of the radar antennae to the observed aspect sensitivity, although it is difficult to include all spectral broadening effects when using broad beam antennae as were used here. As a result, the estimates of aspect sensitivity made here can only be taken as an indication of the upper limit of the actual aspect sensitivity of the scattering structures.

Results of the different methods are compared against the fading time method in figure 7.34 for five hours of data collected on the Birdlings Flat radar on 6 December 1990. Also mean height profiles of aspect sensitivity found by the five methods for data on four days on the Scott Base radar and on the Birdlings Flat radar are given in figures 7.37 and 7.38 along with turbulent eddy dissipation estimates in section 7.9.2. The mean profiles of the fading time, fading time $T_{\frac{1}{2}}$ and spatial correlation methods of finding aspect sensitivity (and the eddy dissipation profiles) are found from the same data points in each set; the rms phase difference and spatial interferometry profiles include some extra data points for which FCA was not successful and so for which the other methods could not make aspect sensitivity estimates.

The profiles of aspect sensitivity follow similar trends with altitude within each data set. There are however significant differences in magnitude and variability between the different methods which are particularly apparent in figure 7.34. Of the two beam broadening methods, the fading time with $T_{\frac{1}{2}}$ removed method gives a somewhat lower and less variable aspect sensitivity suggesting the turbulent fluctuations component in fading time may well be significant.

In general the spatial correlation method using $d_{\frac{1}{2}}$ gives a result very similar to the fading time with $T_{\frac{1}{2}}$ removed method, although occasionally the method does give a much wider estimate. The similarity in results from the two methods might be expected since $d_{\frac{1}{2}}$ is a diffraction scale parameter, like $T_{\frac{1}{2}}$, determined in FCA with the effects of advection of scattering structures through the radar volume by the background wind removed. [Lesicar and Hocking, 1992] also found aspect sensitivity using both the beam broadening method (from the fading time, without corrections by $T_{\frac{1}{2}}$) and the spatial correlation

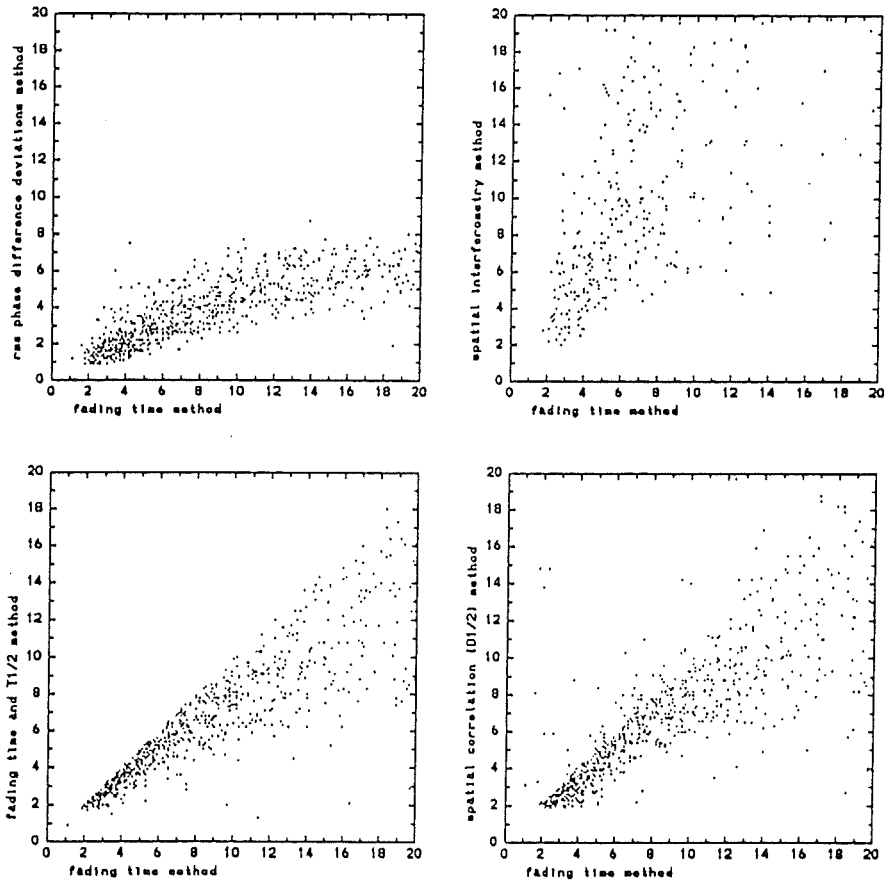

Figure 7.34: **Comparisons between different methods of finding aspect sensitivity.** The fading time method is compared with the fading time with $T_{\frac{1}{2}}$ removed, spatial correlation, rms phase difference and spatial interferometry methods. The points represent the aspect sensitivity found for all height bins and samples of the DND collected over five hours on December 6, 1990. The units of aspect sensitivity are degrees.

method. Similarly to this study, they observed that the spatial correlation method gives a somewhat narrower aspect sensitivity than the beam broadening approach.

The rms phase difference method gives the lowest and least variable aspect sensitivity. However the values obtained by this method should be treated with caution because the phase differences between signals received by spaced antennae are limited by the separation of the antennae. For example, a totally random series having a mean rms phase deviation of $\frac{\pi}{2}$ would, with the spacing of the antennae at Birdlings Flat, give an aspect sensitivity of about 10° and at Scott Base would give an aspect sensitivity of about 18°. Therefore, particularly on the Birdlings Flat radar, this method is of limited value unless the aspect sensitivity is low.

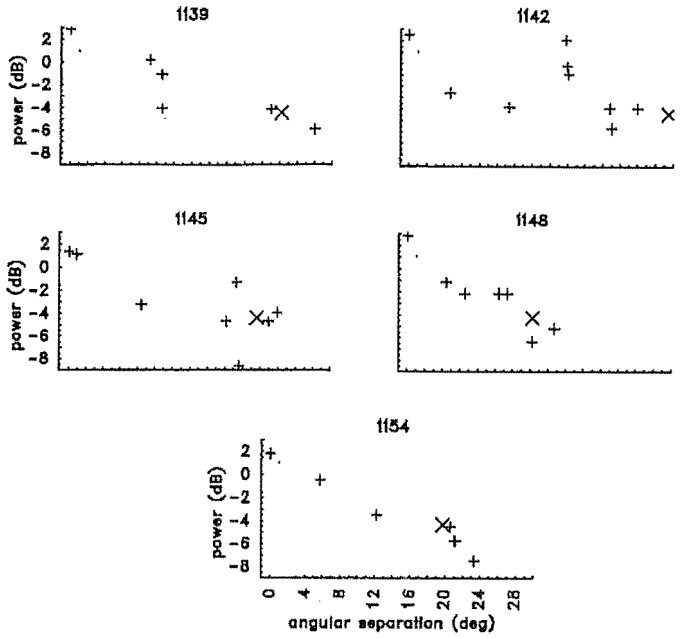

Figure 7.35: **Variation of scattered power against angular separation** of the scattering centres from the point of strongest scatter for a sequence of five samples collected on the Scott Base radar at an altitude of 100 km, 11:39-11:54, 17 Dec 1988. The pluses mark the identified scattering centres and the crosses mark the fitted e^{-1} (~-4.3 dB) power.

Of the five methods, spatial interferometry would appear to give the most direct measurement by revealing the variation in power with angular distribution. Figure 7.35 gives examples of the variation in power of scattering centres plotted against the angular separation of the centres from the direction of strongest scatter. The aspect sensitivity of the scatter is determined from the e^{-1} width (marked with crosses) taking into account the beam width of the radar's antennae.

A curve is fitted to the variation in power to find the e^{-1} width and frequently this fitting proved to be somewhat variable. There are also uncertainties in relating spectral amplitude to scattering power. Here the amplitude of the peak of spectral features identified as per section 4.2.4 was used as scattering power, whereas a better measure may have been found by integrating over the width of each feature. Spatial interferometry contributes further uncertainties particularly at large zenith angles where there can be 2π ambiguities in the measurement of the phase difference between the separated antennae. The spatial interferometry aspect sensitivity estimates are therefore the most variable of the methods as can be seen in figures 7.34, 7.37 and 7.38.

The fading time (with correction by $T_{\frac{1}{2}}$) beam broadening method is the main technique for estimating aspect sensitivity that will be used in the remainder of this project since it was considered to give the most reliable measures. The mean aspect sensitivity determined by this method for the Scott Base data was 11° (with a standard deviation 6°). The Birdlings Flat data appeared to have a somewhat narrower mean aspect sensitivity, for example 7° (standard deviation 2°) for the October 6 data and 9° (standard deviation 5°) for the December 8 data, although this may be a result of differences in the antenna polar diagrams between the two radars. Also the Scott Base data was mainly collected from altitudes above 90 km where aspect sensitivity tends to maximize. These values are typical of those found in other studies (for example the review of [Reid, 1990]) and indicate that there is a significant specular or "quasi-specular" component to much of the scattering observed in this project.

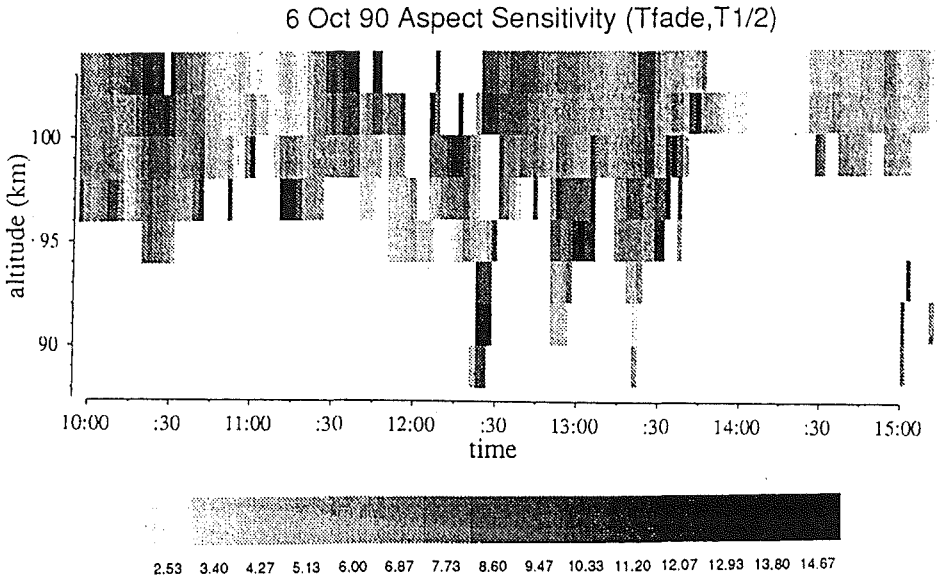

Figure 7.36: **Aspect sensitivity for 6 October 1990** found using the fading time, $T_{\frac{1}{2}}$ beam broadening method. (Quarter-half-quarter filter and points beyond two standard deviations from the mean removed.)

Figure 7.36 is a plot of the aspect sensitivity for the Birdlings Flat 6 October 1990 data set. The method used was the fading time and $T_{\frac{1}{2}}$ method and a result was only able to be found for about 25% of the samples. As might be expected the trends followed in this data are similar to the trends of figure 7.15, section 7.5.1.

7.9.2 Turbulent Eddy Dissipation

The turbulence parameter, the eddy dissipation rate, introduced in section 3.2, was estimated for much of the data collected in this project. Eddy dissipation was estimated by approximating the spread of the Doppler spectrum due to turbulent fluctuations to the spread of the Doppler spectrum implied by the FCA parameter $T_{\frac{1}{2}}$, ($f_{\frac{1}{2}} = 0.22/T_{\frac{1}{2}}$), using the method of [Hocking, 1983b] as discussed in section 3.2.1. Following Hocking, a fairly arbitrary value of 200 m was used for the scale of turbulence, which is approximately the outer scale for inertial turbulence in the mesosphere. The frequency of fluctuations is raised to the third power in this analysis so using a different turbulence scale, such as $d_{\frac{1}{2}}$, makes little discernible difference to the profiles using the scales on the figures shown here.

Profiles of these estimates, along with profiles of aspect sensitivity, are presented in figures 7.37 and 7.38, for Scott Base and Birdlings Flat respectively. As for the aspect sensitivity estimates, broad beam radars of the type used in this study can only provide an indication of the upper limit of eddy dissipation.

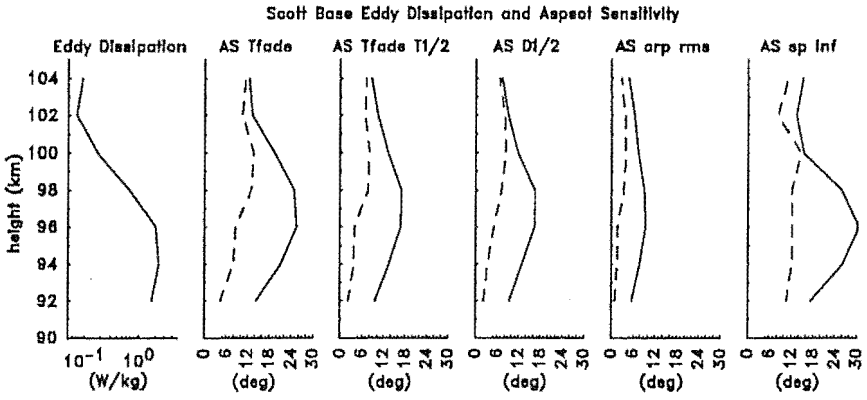

Figure 7.37: **Eddy dissipation and aspect sensitivity profiles at Scott Base.** The aspect sensitivity profiles were found using the fading time (**AS Tfade**), fading time with $T_{\frac{1}{2}}$ removed (**AS Tfade T1/2**), spatial correlation function (**AS D1/2**), rms phase differences (**AS crp rms**) and spatial interferometry (**AS sp inf**) methods discussed in sections 3.3.1 and 7.9.1. The profiles are means (solid line) and standard deviations (dashed line) of data collected over half periods around midday on December 14-17 1988.

The values of eddy dissipation found here are similar to those reported in summaries of various experiments such as [Hocking, 1987c] who reported a mean eddy dissipation rate of 10^{-1} W/kg with a range of $10^{-3} - 1$ W/kg. The fall off in the eddy dissipation in the two later Birdlings Flat profiles and the Scott Base profile give the appearance of being due to

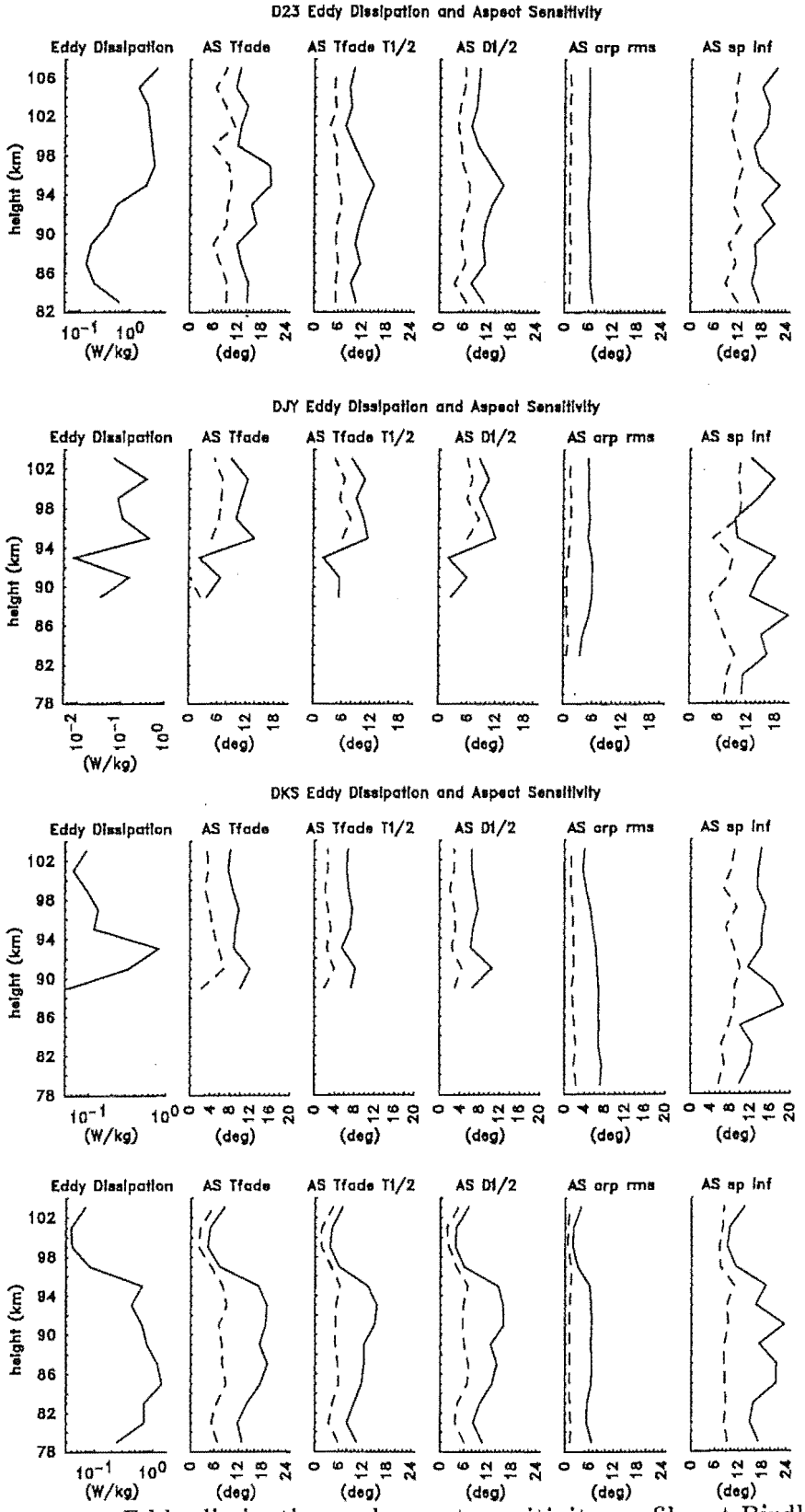

Figure 7.38: Eddy dissipation and aspect sensitivity profiles at Birdlings Flat, (as for figure 7.37). Data collected over 3-5 hours, about midday to late afternoon, on 18 Aug (D23), 16 Sept (DJY), 6 Oct (DKS) and 8 Dec 1990.

the presence of the turbopause (above which turbulence is greatly damped), but are more likely to be due to strong E-region reflections. E-region reflections give coherent echoes and are due to a high electron density, thus a near zero refractive index, and are not so directly related to turbulent fluctuations (unlike scattering from lower in the mesosphere).

7.9.3 Signal Distributions

As was discussed in section 3.4, signal distributions can provide indicators on the nature of scattering processes. The data collected in this project was analysed using both the Rice and Nakagami distributions. The Rice analysis followed [Hocking, 1987b] in which the ratio of the mean signal amplitude over the standard deviation of the in-phase and quadrature channels, $\frac{\overline{A}}{\sigma_{XY}}$, is found and related to the Rice parameter along the lines of figure 3.8 of section 3.4. The Nakagami m parameter was found using equation 3.20 also of section 3.4, [Kuo et al., 1987]. The parameters were determined for each of the one minute samples at each receiver and frequency and the mean of these (typically fifteen depending on SNR) values was found.

The results here will be either distributions of the parameters or running means because as [Hocking, 1987b] noted individual estimates from short data samples display considerable variability, whereas averages or distributions display more consistent characteristics.

With the Rician model, when the Rice parameter is zero (and $\frac{\overline{A}}{\sigma_{XY}}$ is 1.913) the scattering is entirely random, or Rayleigh, and as the Rice parameter (and $\frac{\overline{A}}{\sigma_{XY}}$) increases, a single specular component is increasingly dominating the scattering. However much of this project's data was found to have $\frac{\overline{A}}{\sigma_{XY}}$ of significantly less than 1.913 . For example the smoothed $\frac{\overline{A}}{\sigma_{XY}}$ for the October 6 Birdlings Flat data, plotted in figure 7.39, is less than 1.913 below 90 km for the whole data set; suggesting that much of the scattering in this data is more complex than the random scatter with a single specular component model of Rician statistics. The Rice parameters for this data appear in figure D.5, appendix D; those samples for which $\frac{\overline{A}}{\sigma_{XY}}$ is less than 1.913 were assigned a Rice parameter of zero. The semidiurnal tide was prominent in this data set (section 7.5.1) and during the downward propagation of the phase change of the wind due to this tide, the Rician model does seem to be valid and indicates there was a strong specular component to the scattering.

Nakagami m parameter is 1.0 for a Rayleigh distribution and greater than (or equal to) 1.0 for a Rician distribution. The Nakagami m results correlate very well with the Rice parameter estimates, the samples for which $\frac{\overline{A}}{\sigma_{XY}}$ is 1.9 coinciding with a Nakagami m parameter of 1.0.

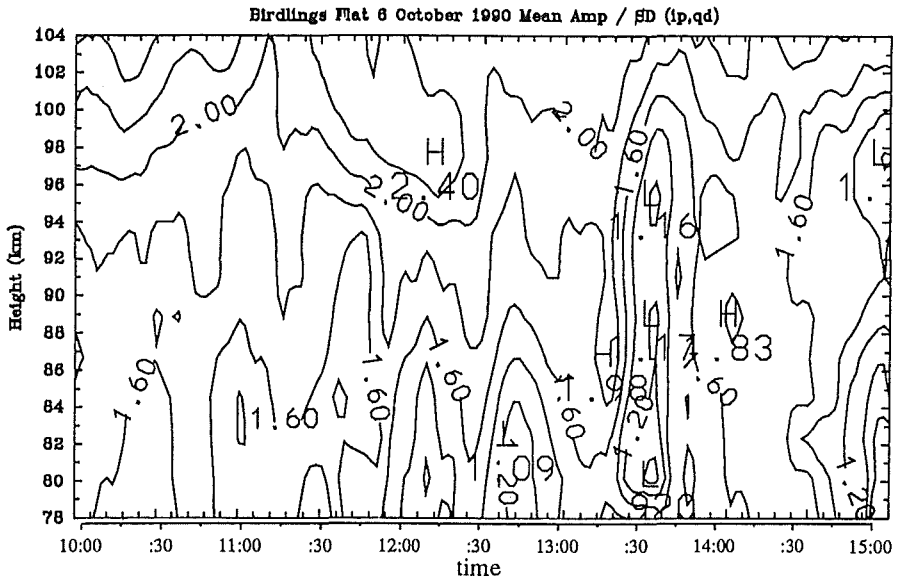

Figure 7.39: **Mean over standard deviation, $\frac{\overline{A}}{\sigma_{XY}}$**, 6 Oct 90, Birdlings Flat. 15 minute running mean; the contour interval is 0.2.

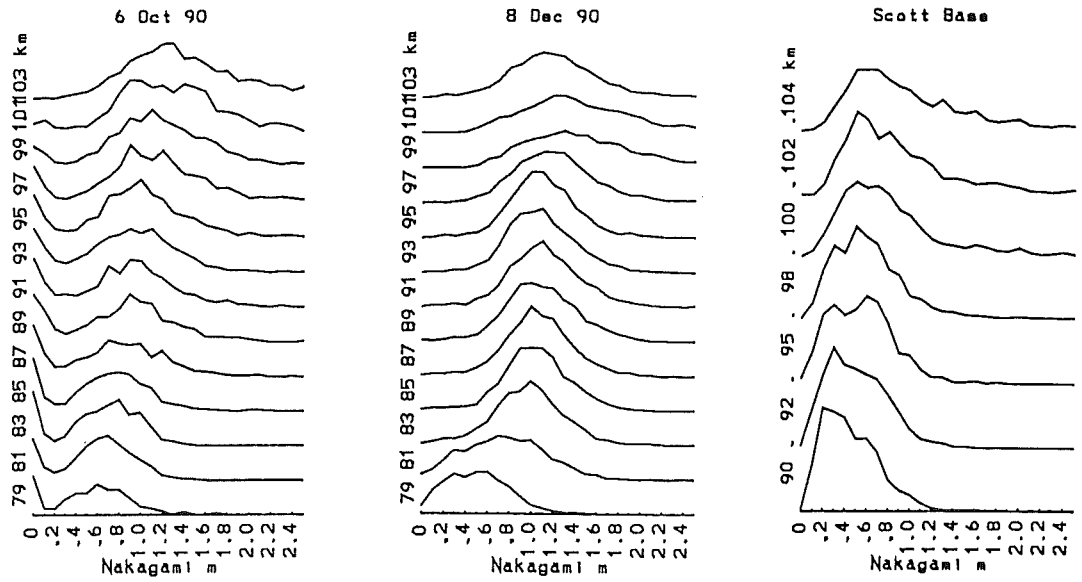

Figure 7.40: **Distributions of the Nakagami m parameter** at Birdlings Flat (6 Oct and 8 Dec 90) and Scott Base.

Distributions of the Nakagami m parameter for the samples collected at each range gate for the 6 October and 8 December 1990 data at Birdlings Flat and for all of the interferometry data at Scott Base (approximately four hours spread over four days) appear in figure 7.40. The parameter increases with altitude at both sites; however it is significantly

lower in the Scott Base data, being predominantly below 1.0 at all altitudes, than in the Birdlings Flat data, where it is around 1.0 above 90 km. 85% of the Scott Base data has a Nakagami m parameter of less than 1.0, whereas for the Birdlings Flat data two thirds of the October 6 and one third of the December 8 data has a Nakagami m parameter of less than 1.0 .

[Kuo et al., 1987] noted that the signals on the in-phase and quadrature channels of the receivers should follow Gaussian distributions. They tested this by plotting Nakagami m values against the kurtosis of the in-phase and quadrature signals and a plot of this for data observed here appears in figure 7.41. For Gaussian distributions, the kurtosis should be near three and should show no variation with Nakagami m. As can be seen the kurtosis is significantly above three when the Nakagami m drops below one. A high value of kurtosis indicates that the distribution of the signals on the in-phase and quadrature channels have a sharper peak around their means than a Gaussian distribution would have. Very similar relationships were noted in [Kuo et al., 1987] and they concluded that these were a result of multiple reflections such as might arise from multiple scattering layers in the radar volume.

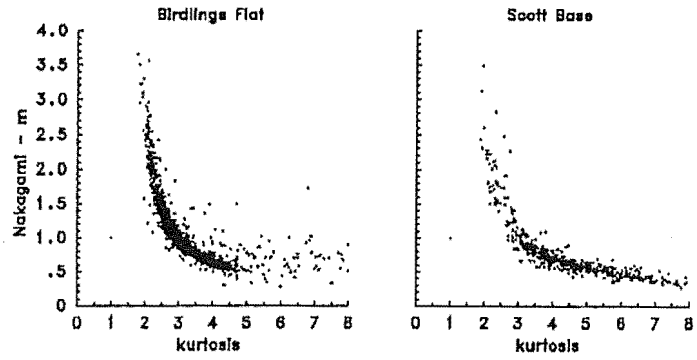

Figure 7.41: **Relationship between Nakagami m and kurtosis** of the in-phase and quadrature channels for five hours of Birdlings Flat data (6 Oct 90) and four hours of Scott Base data.

7.10 Frequency Domain Interferometry

Frequency domain interferometry was carried out using results of cross correlation function and cross spectral analysis of signals received at different frequency steps (as mentioned in section 7.3 above, several steps around 20 kHz were generally used). An estimate of range was determined using the phase of each of the steps for each receiver (corrected

for equipment factors determined by the methods of section 2.3.2), and the mean and standard deviation of these estimates were found. Depending on the signal to noise ratio, typically about ten estimates of range were available for averaging at each height bin of each sample.

Figure 7.42 gives the range determined from the phases of the frequency correlation functions, with error bars showing the scattering depth (note that for clarity the scattering depth is equivalent to the full length of the error bars, even though scattering depth as defined here is the standard deviation of the distribution of scattering ranges). Much of the time the scattering depth is several hundred metres or more, indicating that the scattering originates from centres located more or less throughout each radar volume. Notice that the ranges are fairly smooth from sample to sample, they are not distributed over the ranges indicated by the scattering depths as might be expected.

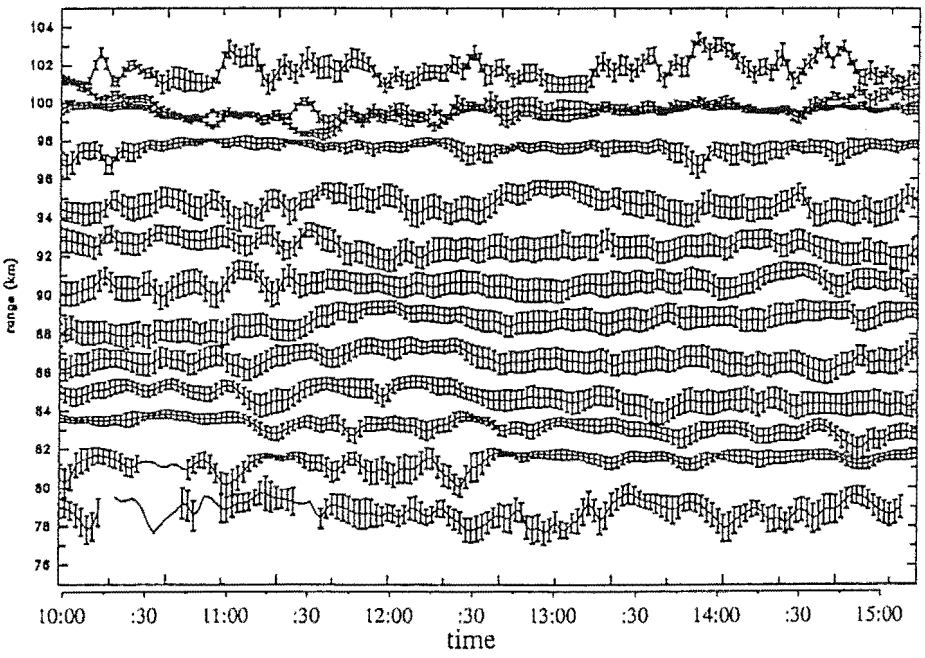

Figure 7.42: **FDI range and scattering depth, 8 December 1990,** Birdlings Flat. The scattering depth is indicated by the error bars. Note that for clarity, the depth is the full length of the errors and that those samples with no error bars are samples for which the scattering depth could not be estimated rather than indicating negligible estimates.

The FDI results seen here display features in common with those seen in the FDI results of [Stitt and Franke, 1991], (the only other MF FDI experiments that have been reported), as shown in figure 5.2 in section 5.3.2. The phase changes in that figure and

the ranges seen here sometimes remain fairly consistent for periods of an hour or more. In fact the averaging over several steps and three antennae done here seem to have resulted in FDI ranges that display even less variability than those of [Stitt and Franke, 1991] who used only one frequency step received on just one antenna. By using spaced antennae, relationships between FDI results and characteristics such as the FCA wind or spatial interferometry results can be examined.

The scattering depths indicated in figure 7.42 display pronounced narrowing at various altitudes and times. The narrowing around 100 km altitude appears to be due to reflections from the bottom of the E-region. The E-region reflections dominate the data of range bins at both 99 and 101 km leading to their FDI ranges coinciding for much of the data set.

There is also some narrowing below 85 km. This narrowing appears to be loosely correlated with regions where the wind (figure 7.12, section 7.5) is fairly steady, just displaying minor fluctuations. For example the narrowing at 84 km for approximately the first hour of figure 7.42, and at about 82 km around 12:45 and towards the end of the data set, occurs during a constant westward wind with relatively minor fluctuations. A similar effect can be seen in the 18 August Birdlings Flat data in figures D.3 and D.4 in appendix D.

On 6 October 1990, FDI observations reveal narrowing of the scattering depth apparently associated with the inertial gravity wave (the semidiurnal tide) seen in that day's wind vector observations (section 7.5.1). Figure 7.43 displays the FDI results for this data. The range estimates for each sample have been multiplied by the cosine of the zenith angle as found by spatial interferometry analysis of the cross correlation functions between receivers. This gives the mean altitude of the scattering, rather than the range. The narrowing of the scattering depth occurs about the time of the rotation to north of the wind vector (figure 7.14, section 7.5.1), and like the velocity rotation propagates downwards. The narrowing is followed by a disturbed period, then the scattering seems to settle down again. Turbulence, as approximated by $T_{\frac{1}{2}}$, follows similar behaviour (see figure 7.15, section 7.5.1).

On two occasions during this disturbed period, three range bins, nominally two kilometres apart, appear to originate from the same altitude; at about 12:00 at 100 km, the 99, 101 and 103 km range bins meet and at about 12:30 at 95 km, the 93, 95 and 97 km range bins meet. There also is some overlapping at various times at lower altitudes. Overlapping to this extent is not apparent in the FDI range estimates; it is revealed when the ranges are converted to altitude using the zenith angles of arrival. During the overlapping, the scattered signals in the higher range bins must therefore be originating from directions

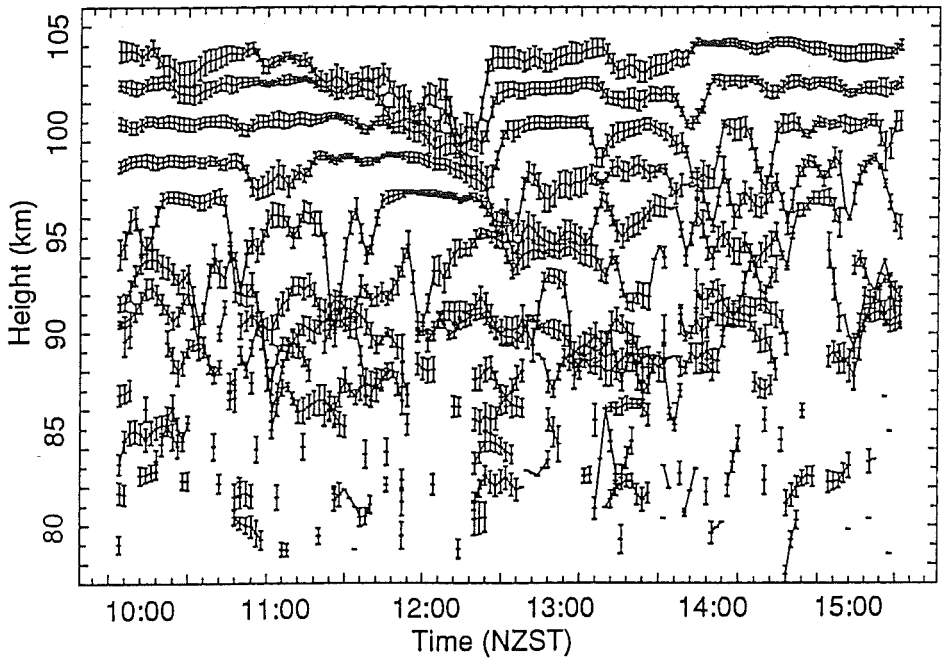

Figure 7.43: **FDI altitude and scattering depth, 6 October 1990,** Birdlings Flat. The altitude is determined from the FDI range and the spatial interferometry zenith angle. The scattering depth is the full length of the error bars.

further away from zenith than those in the lower bins, which implies preferential layering in the scattering. (Even more overlapping appears in figure D.1 in appendix D of data collected at Birdlings Flat on 28 July 1990. Here on two occasions four range bins, bins at 101 - 107 km and 83 - 89 km, overlap.)

Examples of altitude and scattering depth found on the Scott Base radar appear in figure 7.44. In the upper range bins of the two data sets shown the presence of the E region leads to shallow scattering depths. There is a region of shallower scattering than the regions above and below at around 98 km in the 17 December data. The FCA wind for this data (figure C.1 in appendix C) has a fairly steady westward component at this level with a weaker southward component just below. In this example the localized scatter may be occurring as a result of wind shear, although like the Birdlings Flat data there does seem to be a constant wind at the level of the narrowing itself.

As mentioned above, the FDI range for each sample is an average of up to ten estimates from different frequency steps and receivers. The mean and standard deviation of these are found and the standard deviation can be also provide some measure of the spread in scattering range of each sample. Figure 7.45 compares the mean profiles with height of the standard deviation in each FDI range estimate and the mean profile of the scattering

depth for the 6 October data set at Birdlings Flat and for two hours of data at Scott Base. Although of different magnitude, both measures follow similar trends with altitude on each radar.

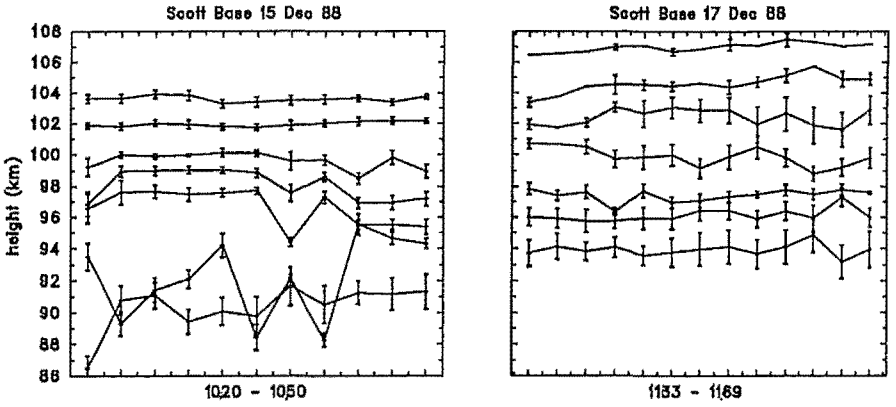

Figure 7.44: **FDI altitude and scattering depth, Scott Base.** Data collected 10:20 - 10:50 on 15 December, and 11:33 - 12:09 on 17 December, 1988. The altitude is determined from the FDI range and the spatial interferometry zenith angle. The scattering depth is the full length of the error bars. The range bins are 2-3 km higher in the 17 December data.

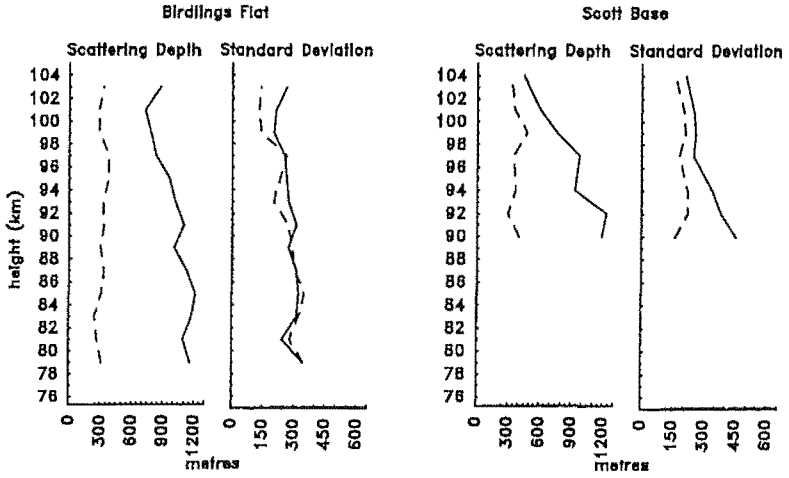

Figure 7.45: **Profiles of the FDI scattering depth and standard deviation of range**, for 6 October 1990 at Birdlings Flat and four data sets totaling two hours on the Scott Base radar. The mean profiles are the solid lines, the dashed lines are standard deviations of the means.

7.10.1 Distributions of FDI range

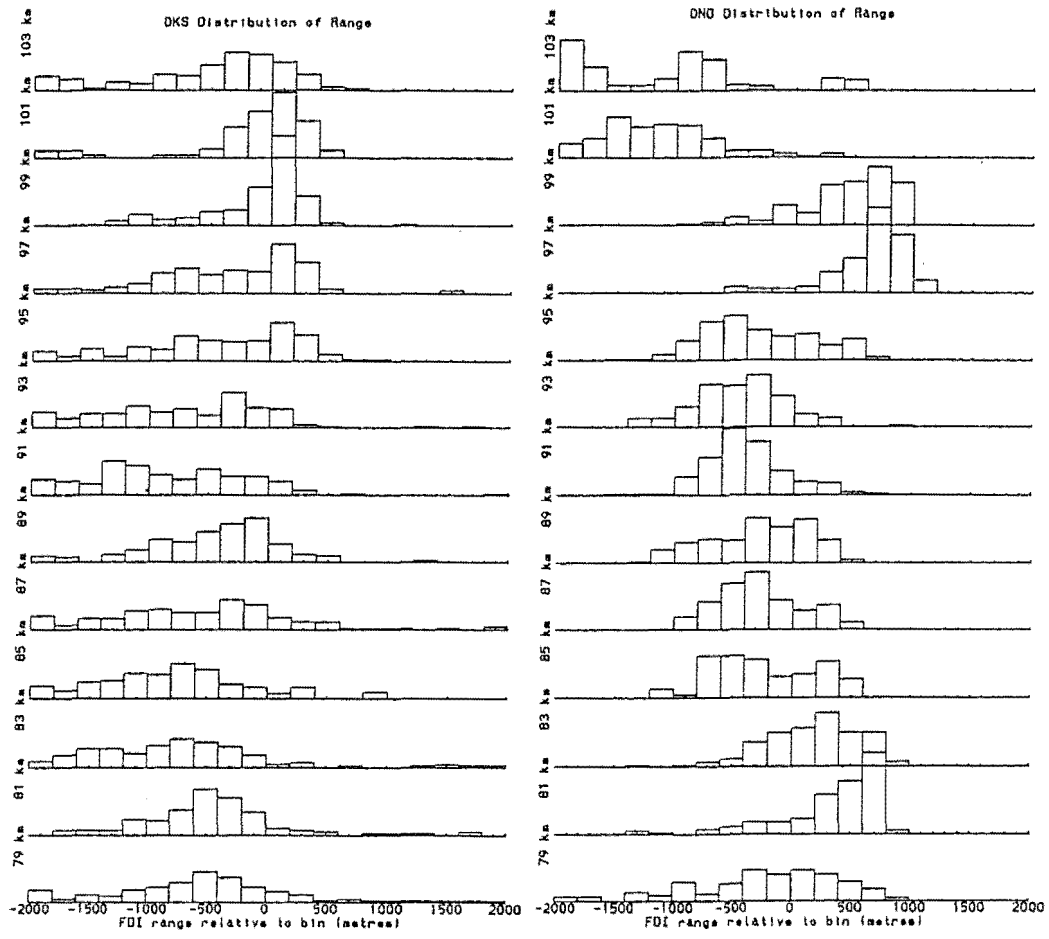

Figure 7.46: **Distributions of FDI range at Birdlings Flat**, for 6 October (DKS) and 8 December (DND) 1990. Ranges found using the phase of the frequency correlation functions. The distribution of the variation in range from the range of the A/D gate is shown. The width of the bars is 200 metres.

In section 2.3.2 calibration for FDI range measurements was discussed using the distribution of phase changes at each range bin. It was noted then that the spread in ranges at each range bin as implied by these phase distributions (for example figure 2.19 of that section) are considerably narrower than might be expected since a 30 μs ($\sim$ 4.5 km) transmitter pulse is used.

Figure 7.46 gives the distributions of the variation in range found at each range gate for the 6 October (DKS) and 8 December (DND) 1990 data sets at Birdlings Flat and figure 7.47 gives the distributions for two data sets at Scott Base. The widths of many of

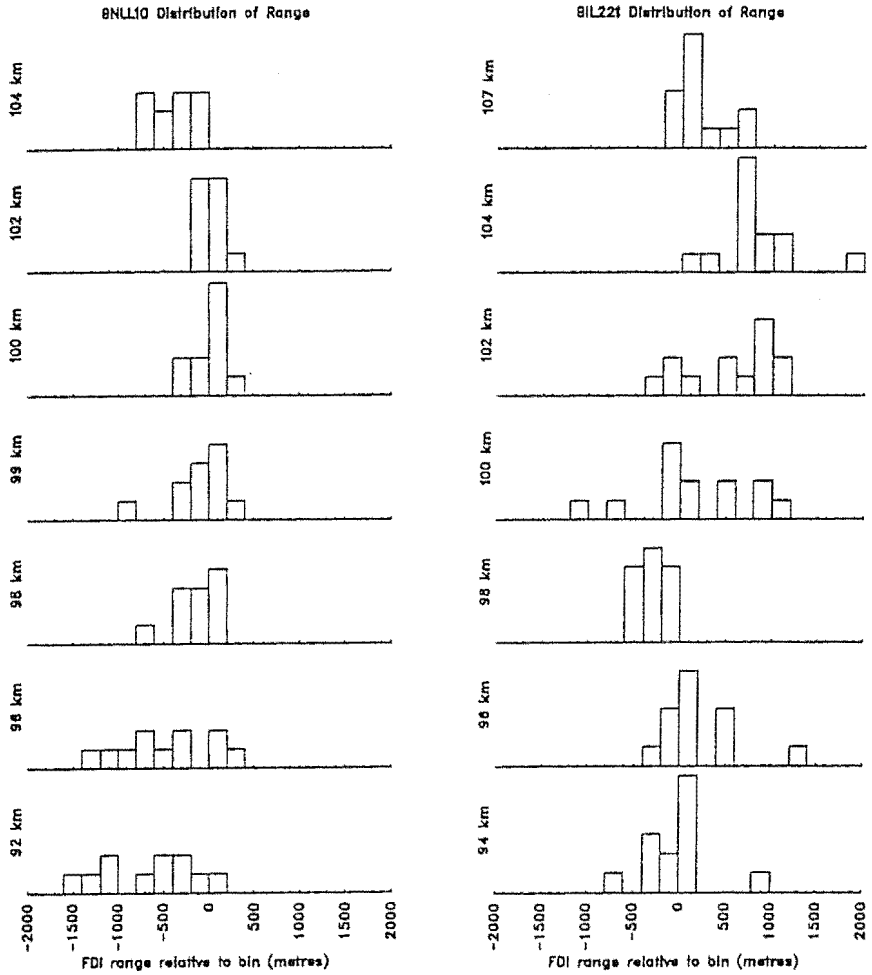

Figure 7.47: **Distributions of FDI range at Scott Base** for data collected at 10:20-10:50 on 15 Dec (BNLL10) and 11:33-12:09 17 Dec 1988 (BIL221), the same data sets in figure 7.44. The width of the bars is 200 metres.

these distributions, particularly the 8 December Birdlings Flat and the Scott Base data, are approximately a kilometre or less; again substantially narrower might be expected given the $4\frac{1}{2}$ km depth of the radar volume. Somewhat broader distributions appear in the 6 October data set.

The scattering depth of the 8 December as shown in figure 7.42 does not display many narrow features, aside from the E region reflections at 100 km. The narrow distributions in this data in figure 7.46 can be explained in terms of scattering that is spread evenly throughout the radar volume sampled at each range gate. In such a situation the only biasing should be the weighting function of the radar volume which is centred on a range

corresponding to the range of the A/D gate. If dominant reflections from thin or isolated scattering centres were occurring, these centres would be expected to have varying ranges from sample to sample spread over a range more consistent with the width of the transmitter pulse. Such a spread appears in the higher distributions of the 8 December data. The 6 October data which does have features with narrow scattering depths at various ranges, shows much broader distributions as the features vary in range from sample to sample.

The distributions of the ranges in the Scott Base data are more uneven than the Birdlings Flat data because the number of samples is much less. Also some of the narrowness of the Scott Base distributions can be explained by localized scattering from preferred heights over the short time scales of these data sets. (Over longer time spans, such the Birdlings Flat data, localized scattering leads to broad distributions as the scattering moves up and down.) For example the two highest range gates in both data sets are dominated by E region specular reflections at a particular altitude, (see figure 7.44 which displays the height, range multiplied by cosine of the zenith angle, for these two data sets). However at the range gates where the scattering depth is broad and the range fluctuates (particularly below 98 km in the 15 December (BNLL10) data) the distributions are still narrower than implied by the depth of the radar volume.

7.10.2 FDI and Aspect sensitivity

Aspect sensitivity measurements for the 6 October 1990 data were presented in figure 7.36. As discussed in section 5.3.3 there is expected to be a correlation between aspect sensitivity and scattering depth since a large angular distribution in scattering should also appear as deep scattering. The trends followed by aspect sensitivity in figure 7.36 and scattering depth in figure 7.43 are indeed similar.

The relationship between aspect sensitivity and scattering depth is more clearly seen in figure 7.48 which compares the two measurements for the October 6 data and for eleven sets of Scott Base data. The aspect sensitivity for this figure was found by the fading time, $T_{\frac{1}{2}}$ beam broadening method; as noted above, only an upper limit to aspect sensitivity can be placed on measurements on broad beam radar. The apparent depth of a thin layer at an altitude of 90 km, approximated by $\frac{1}{2}h(\sec\theta_s - 1)$, is given by the dashed lines. Generally the scattering depth is greater than that modelled by the thin layer, also implying distributed scattering.

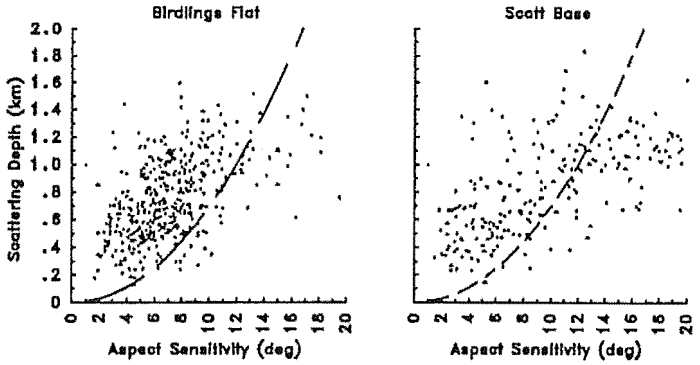

Figure 7.48: **Aspect sensitivity and scattering depth.** Five hours of data collected at Birdlings Flat on 6 October 1990, and four hours of data from Scott Base. The dashed lines model the variation in depth seen for a thin layer at 90 km.

7.10.3 Comparing FDI and Doppler radial velocities

The behaviour of the FDI range with time can be compared with the radial velocities determined from the mean Doppler shifts of the scattered signals. The phase of the cross correlation function between signals received at different frequencies was used. The rate of change was estimated from the difference between the cross correlation at lag plus one second and lag minus one second. This difference between the cross correlation phase at lags two seconds apart is fairly small. For example a radial velocity of 5 ms^{-1} measured with a frequency shift of 30 kHz would give a phase difference of 0.013 radians. This difference is smaller than the uncertainty that was attached to the FDI range measurements, although because the variation with time is being measured here, somewhat more confidence can be attached to this measurement.

Figure 7.49 compares the radial velocities determined from FDI and those determined from Doppler shifts for an hour and half of data collected on the Birdlings Flat radar. There is clearly very good agreement between the two estimates of radial velocity.

7.10.4 FDI from Cross Spectral Analysis

Most of the FDI results presented here were found using the frequency correlation function. Cross spectral analysis can also be used to obtain FDI information.

Spatial interferometry results using cross spectral analysis between data received on spaced antennae were presented above. Peaks in the Doppler spectrum were identified as scattering centres and the phase of the cross spectrum was used to locate the centres. The cross spectra between signals at different frequency steps were also found and the phases at the Doppler frequencies of the identified scattering centres were used in FDI analysis.

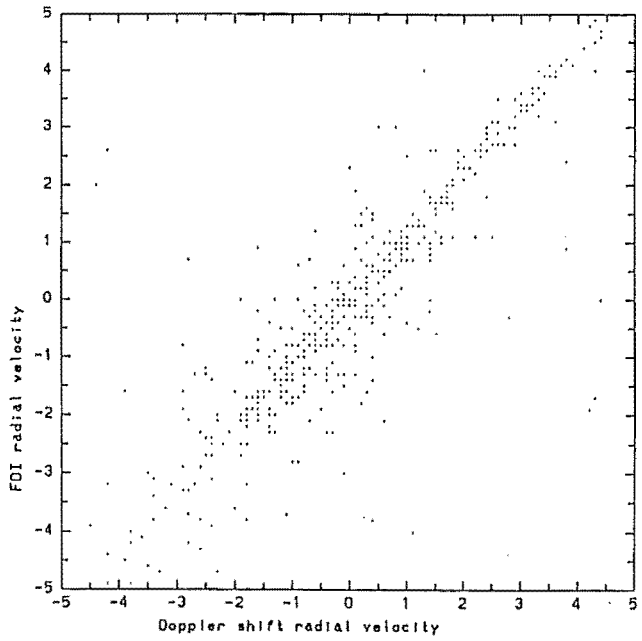

Figure 7.49: **FDI and Doppler shift radial velocities compared** for $1\frac{1}{2}$ hours of data collected on the Birdlings Flat radar on 6 October 1990 (the units are ms^{-1}).

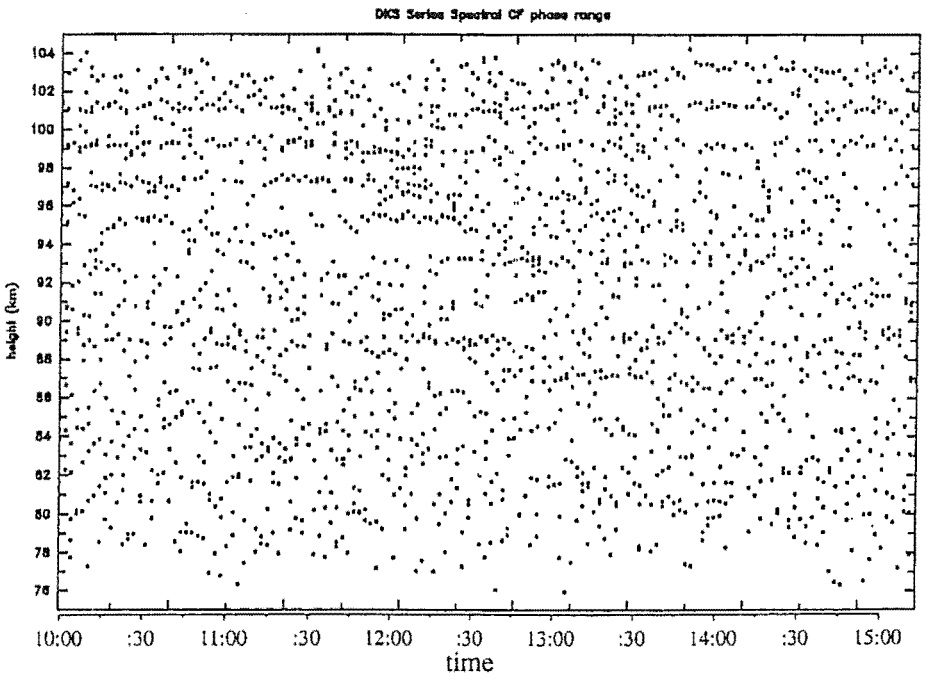

Figure 7.50: **FDI range from cross spectral analysis, 6 Oct 90** at Birdlings Flat. The points indicate scattering centres identified by spectral analysis, the ranges being determined by cross spectral phase.

Figure 7.50 gives the FDI ranges of the scattering centres identified in the October 6 data. At each range bin of each sample there can be anywhere from one to ten scattering centres, usually fairly evenly distributed throughout the radar volume so the resulting picture is somewhat confused. However at times, particularly at the times of the narrowing of the scattering depth in figure 7.43, the centres do become more clustered.

7.11 Postbeam steering

Postbeam steering (introduced in section 5.6) was carried out on various data sets collected on this project. The results of postbeam steering presented here take the form of surface plots displaying the variations observed in different parameters as the beam was steered. The steered beam was still very broad at about 17° (half power full width) and the images found are very coarse so qualitative rather than quantitative conclusions will drawn from this analysis.

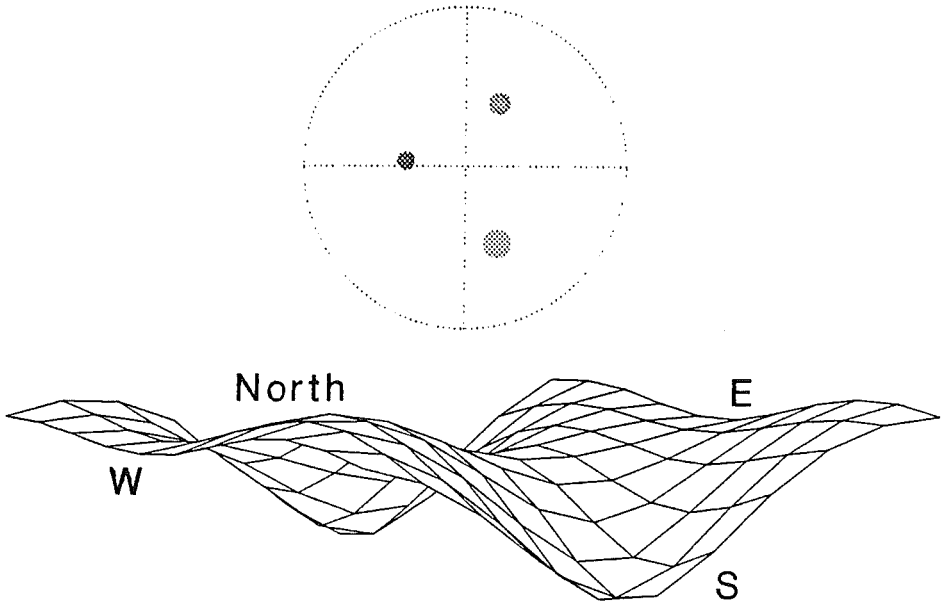

Figure 7.51: **Example of postbeam steering, variation in signal** received as the beam is steered. Data collected on the Birdlings Flat radar on 6 October 1990 at 10:09 and a range of 89 km as for figures 5.8 and 5.9 in section 5.6. The grid points are 5 km apart and the variation in power across the surface is approximately 10 dB.

Figure 7.51 gives an example of the postbeam images found here. The figure displays the variation in the power in the received signals as the beam was steered to points on a grid. Spatial interferometry using the phase of cross spectra between the separated receivers for the same sample identified and located a number of scattering centres as

indicated in the sky map in the figure. The locations of the centres do correspond fairly well with the regions of increased signal in the postbeam steering image. In general this was found to be the case, although frequently towards the corners of the images there seemed some distortion probably due to aliasing of the central regions (in figure 7.51 this would explain the increased power in the south-east and north-west corners as signal from the central regions is misinterpreted as originating in these corners).

Sequences of postbeam steering images were of more interest than isolated snapshots. For demonstration purposes some of the complete data set sequences, comprising of 150 images or more, were recorded on video tape. The images were then played back at 500 times faster than real time so that each one minute image appeared for $\frac{1}{4}$ second. Viewed in this manner, there were many interesting features to the sequences that are not so apparent in still images. The surfaces frequently appeared to behave as though there were ripples travelling through them, although given the lack of resolution it cannot be said whether or not these were due to waves or were isolated scattering centres travelling through the radar volume.

A sequence of images is shown in figure 7.52. The variation in received signal, Doppler shifts and FDI range as seen by the beam over five consecutive samples are shown. The spatial interferometry results for the same sequence is shown in figure 7.53. The scattering centres are clustered around zenith for all the samples and the postbeam signal images similarly not do show much variation from sample to sample. The corners of the signal images are raised somewhat higher than expected, which indicates wrapping of the signal as the beam is pointed away from zenith.

The Doppler shift images show more variation from sample to sample. The horizontal wind at this time is north to north-west (figure 7.14) in which case along the line of sight (that is the steered beam) scattering towards the south and south-east would be expected to have a positive Doppler shift and scattering towards the north and north-west would have a negative Doppler shift. This behaviour is indeed displayed in the Doppler images.

This sequence is at the time and altitude of very narrow FDI range variation (or layer thickness) in figure 7.43. This lack of variation in range is apparent in the last four postbeam steered images of FDI variations, although the first image shows a considerable variation in range that is not displayed in figure 7.43

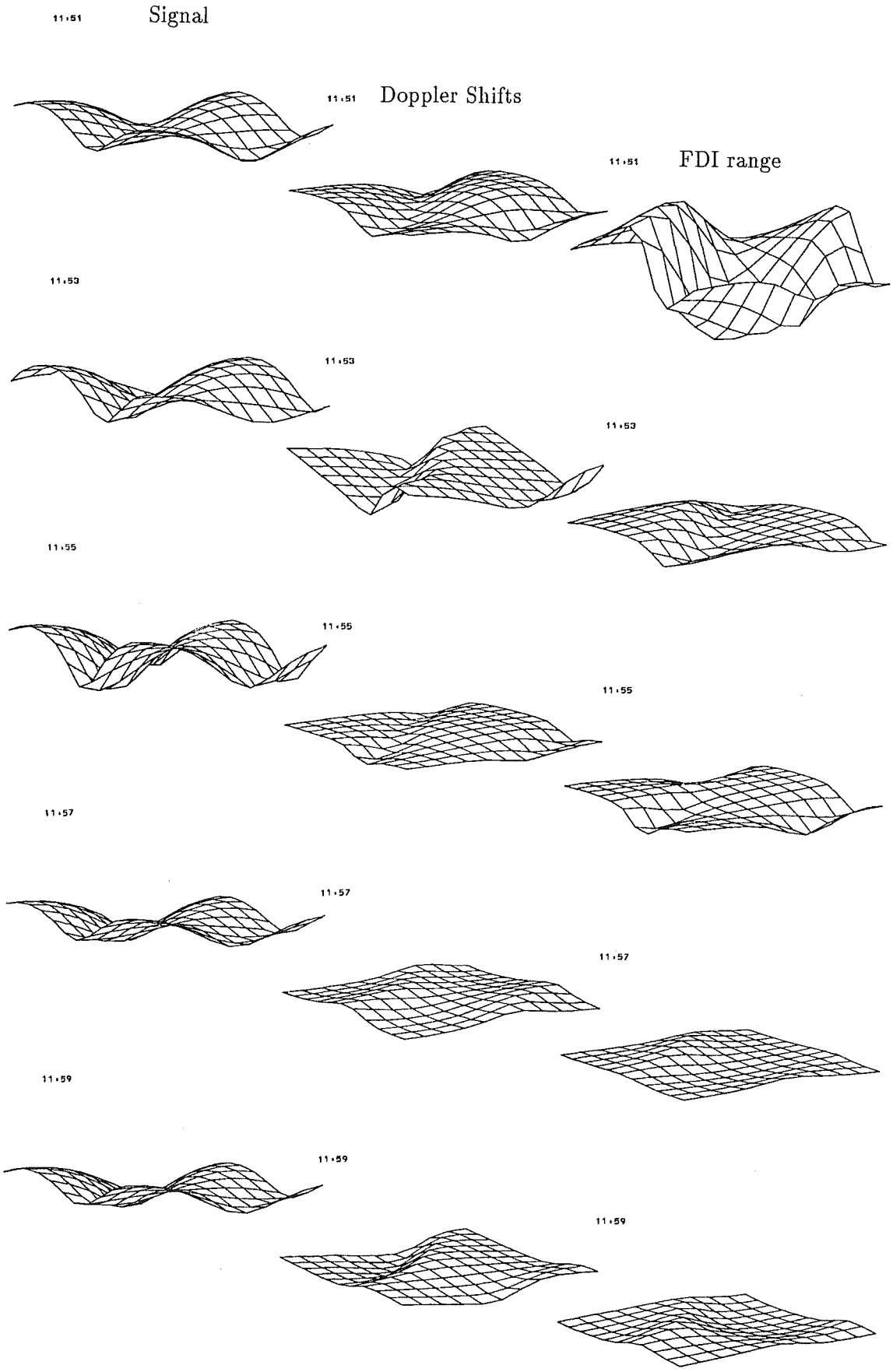

Figure 7.52: **Sequence of postbeam steering images**, 6 October 1990, at 95 km, 11:51 - 11:59, Signal, Doppler shift and FDI range.

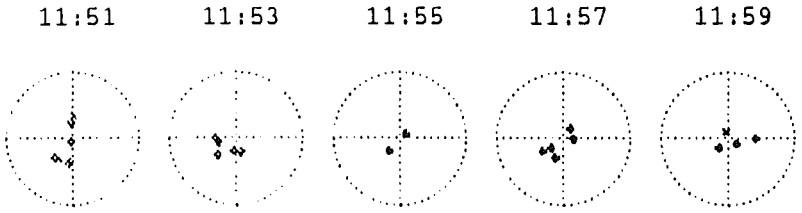

Figure 7.53: **Spatial interferometry results for the postbeam sequence** of figure 7.52.

7.12 Gravity Wave Activity

The clearest gravity waves observed in this project were tides, particularly the semidiurnal tide in the 6 October 1990 Birdlings Flat data which, as discussed above, revealed itself in the downward propagation of an anti-clockwise rotation of the wind vector and an associated narrowing of the scattering depth. Aside from tides, such observations of distinct monochromatic gravity waves are relatively rare on middle atmosphere radar. In general there tends to be a broad spectrum of activity.

Spectral analysis of wind fluctuations at other sites have reported a characteristic $f^{-\frac{5}{3}}$ relationship between the power of the fluctuations and the spectral frequency (for example figure 3.4 in section 3.1 from [Carter and Balsley, 1982]). Similar analyses on results from this project also appeared to follow this relationship, for example figures 7.54 and 7.55 ($f^{-\frac{5}{3}}$ is indicated by the dashed lines). In these figures the power spectra of FCA zonal and meridional winds are averaged over the indicated height ranges (the October 6 1990 data only had sufficient points to obtain reliable spectra above 95 km).

Other oscillatory behaviour was frequently observed in this project. An example is figure 7.56 which displays four minute mean profiles of the eastward and northward components of the mean direction of arrival of scattering over a two hour period on 8 December 1990 at Birdlings Flat. Many of these profiles contain oscillations with apparent vertical wave lengths of 10 - 15 km. However these oscillations are not necessarily direct observations of monochromatic gravity waves, they may be a result of random variations in the location of scattering structures with altitude or the result of eddies produced by the wind shear on this day (see figures 7.12 and 7.19).

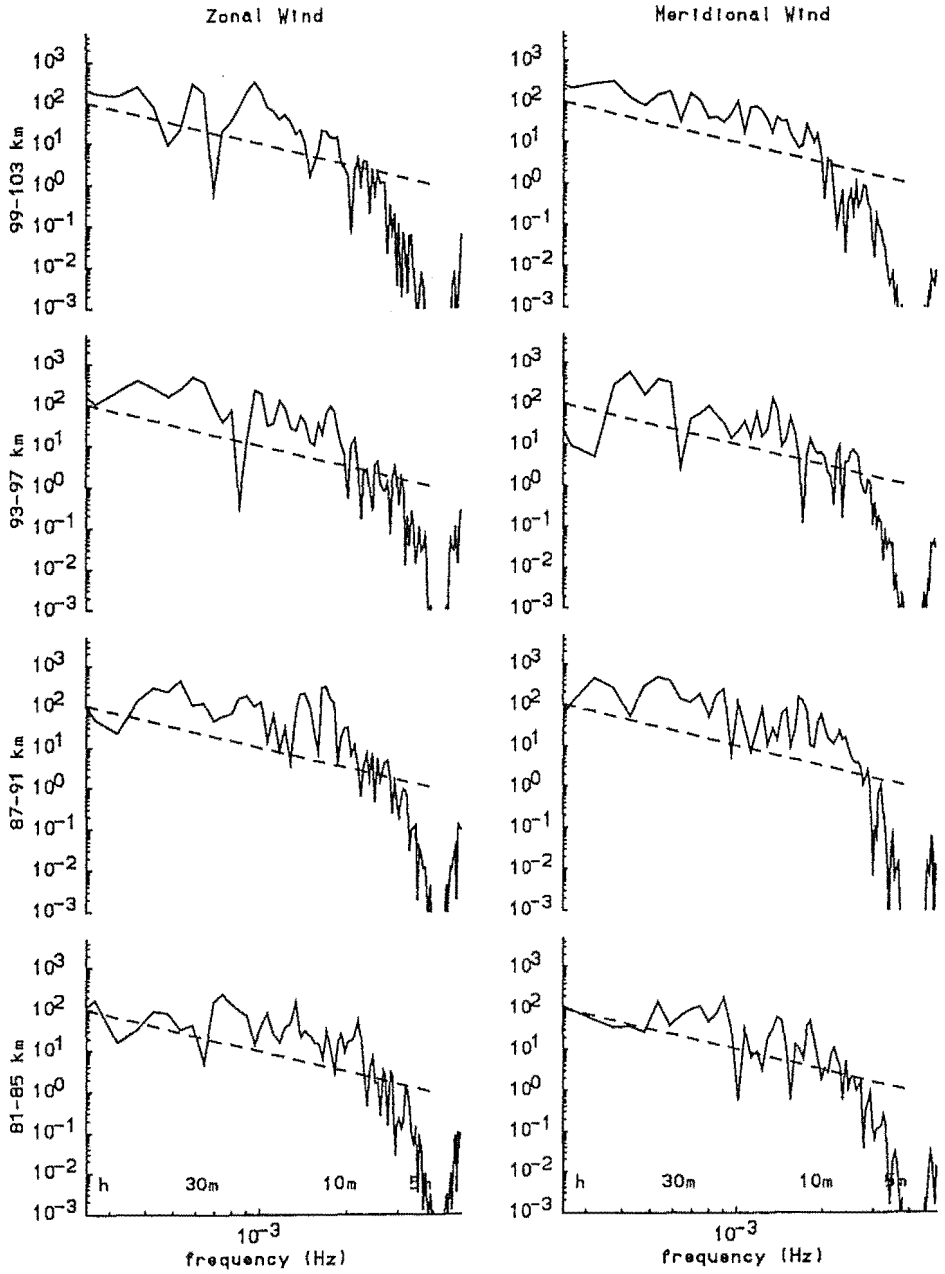

Figure 7.54: **Power spectra of 8 December 1990 FCA winds** averaged over the indicated height bands. The units of spectral power are $m^2s^{-2}Hz^{-1}$ and the frequency scale is logarithmic with 1 hour, 30, 10 and 5 minute periods indicated. The dashed line indicates $f^{-\frac{5}{3}}$ with an arbitrary offset.

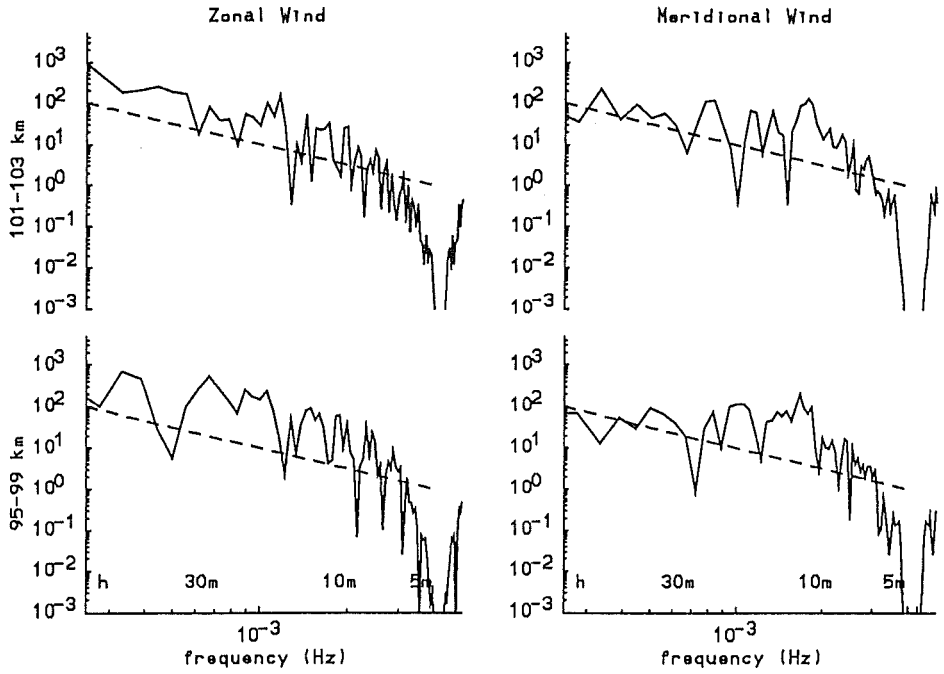

Figure 7.55: **Power spectra of 6 Oct 90 FCA winds** (as for figure 7.54).

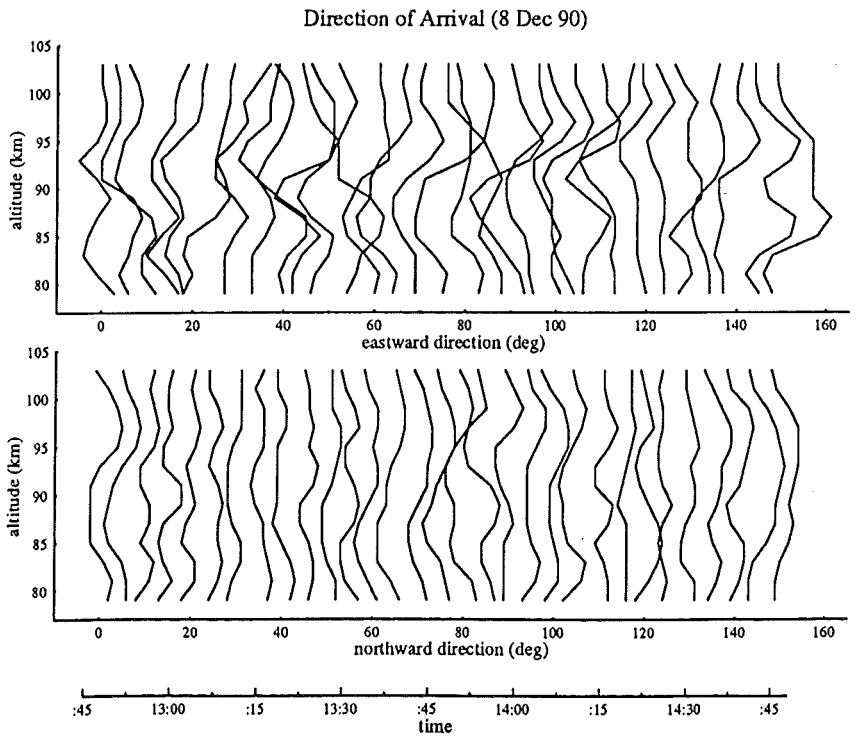

Figure 7.56: **Profiles of angle of arrival, 8 Dec 90** for two hours at Birdlings Flat. Each profile is the mean of two samples (thus four minute means) smoothed using a quarter-half-quarter filter and are offset from each other by five degrees.

There does appear to be some distinct gravity wave activity on this day however, and these can most clearly be seen in the radial velocity plot of figure 7.4 (section 7.1.3). There are various oscillations in the radial velocity that may or may not be directly associated with gravity waves. Some of these oscillations propagate vertically however, for example at around 13:30 the downward phase of the radial velocity propagates downward from about 95 km to 80 km over approximately 20 minutes, behaviour that is particularly indicative of gravity waves.

7.12.1 Momentum Flux Measurements

In section 3.1 on gravity waves, the parameters $\overline{u'w'}$ and $\overline{v'w'}$, the upward fluxes of zonal and meridional momentum, were introduced. These quantities provide measures of horizontal and vertical velocity perturbations in the atmosphere which can be linked to gravity wave activity. The quantities are often measured on Doppler beam swinging radars by measuring the difference in radial velocity perturbations between radar beams pointed in two opposite directions, [Vincent and Reid, 1983]. The perturbations are usually averaged over time bands of up to an hour, up to several hours and up to the inertial period to obtain momentum fluxes that can be related to gravity waves with periods in these time bands.

In this project, horizontal and vertical velocity estimates are available at two minute intervals (that is when the data passes the acceptance tests). The general procedure followed here was to find the mean horizontal and vertical velocities, $(\overline{u}, \overline{v}, \overline{w})$, over some time band and form sets of the products of the horizontal and vertical differences from these means, ($u'w'$, $v'w'$ where, for example, $u' = u - \overline{u}$), and average these sets over the time band to form the momentum fluxes $(\overline{u'w'}, \overline{v'w'})$. Two different averaging techniques were applied. One involved binning the data into discrete subsets, each of these subsets being of the length of the chosen time band. The other involved forming running means of length equal to the chosen time band and running these right through the data set. At each stage data points lying beyond two standard deviations from the mean were removed since these points can have a disproportionate affect on the results, (a standard procedure in momentum flux analysis, for example [Murphy, 1990]).

Figure 7.57 displays an example of $\overline{u'w'}$ (upper panel) and $\overline{v'w'}$ (lower panel) momentum fluxes found in this manner at Birdlings Flat for the 8 December 1990 data set. The averaging periods are indicated above the plots, the five left most sets being determined from one hour bins, the second from right set being from a five hour bin (10:00-15:00) and the far right set from a one hour running mean run through the five hours of data.

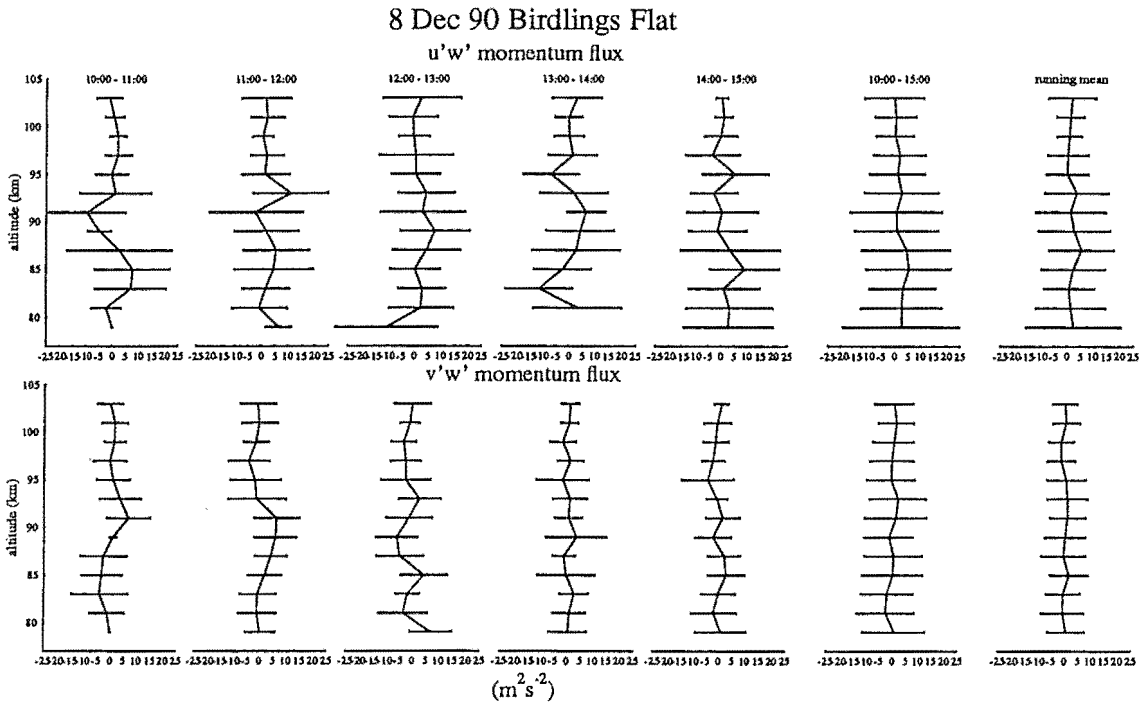

Figure 7.57: **Momentum flux measurements** at Birdlings Flat on 8 December 1990, as found using three averaging periods. In the upper panel are profiles of the upward flux of zonal momentum $\overline{u'w'}$ and in the lower panel are profiles of the upward flux of meridional momentum $\overline{v'w'}$. The periods over which the fluxes were found are indicated above the $\overline{u'w'}$ profiles, the running mean being a one hour running mean over the five hour data set. The error bars indicate standard deviations.

The momentum flux profiles obtained in this project were found to vary somewhat depending on the averaging periods used and the placing of those averaging periods. This variability is indicated by the error bars which show the standard deviations over the averaging periods. Similar variability has been seen in other more comprehensive studies of momentum flux. For example both [Fritts and Vincent, 1987] and [Murphy, 1990] observed fluxes ranging from 1 or 2 m^2s^{-2} up to around 20 - 50 m^2s^{-2}. As noted in section 3.1, [Fukao et al., 1988b] also found that, particularly with shorter averaging periods, considerable variability in momentum flux estimates can occur. These workers suggest that the averaging technique used can have a considerable influence on the estimates obtained.

Similarly to [Fukao et al., 1988b], it was found here that if slightly different averaging schemes were used the one hour profiles varied significantly from those shown here. However, in general the one hour profiles for this data set displayed more activity than the five hour and running mean profiles irrespective of the averaging scheme used. The zonal

momentum flux, $\overline{u'w'}$, displays more variability than the meridional flux, an observation also made by [Murphy, 1990]. The variability in the one hour profiles after midday is somewhat greater than those before midday which could be indicative of the oscillatory behaviour mentioned for this data in the last section (figure 7.56).

The momentum fluxes for the 6 October 1990 data appear in figure D.6 of appendix D. The enhancement of particularly $\overline{u'w'}$ over the five hour averaging period compared with the one hour periods would appear to be a result of the semidiurnal tide that appears in this data set (figure 7.14 in section 7.5). As discussed in section 7.7.2 when considering the vertical winds for this data set, the observations are consistent with other reported observations of tides and with tidal theory. However because of the uncertainties in accurately calibrating for spatial interferometry, it is possible there is a small but significant systematic error in the vertical velocity measurements. Therefore the momentum flux estimates for this data should be treated with some caution.

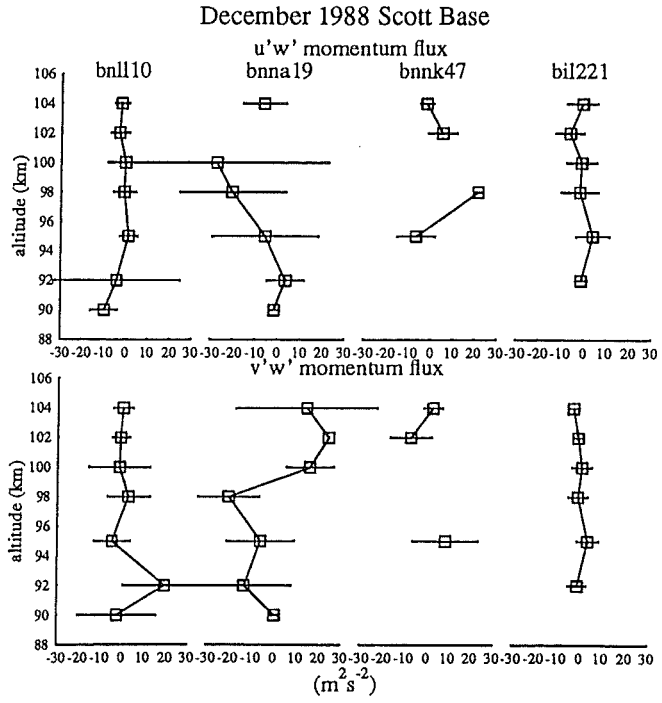

Figure 7.58: **Momentum flux measurements at Scott Base.** The data sets are **bnll10** 10:20-10:50 15 Dec 88, **bnna19** 11:28-11:52 16 Dec 88, **bnnk47** 10:14-10:38 and **bil221** 11:33-12:09 17 Dec 88. Averaging was carried out over the length of each set and the error bars indicate standard deviations.

[Fritts and Yuan, 1989] suggested that momentum flux is greater in polar regions than

at lower latitudes. Figure 7.58 gives examples of momentum flux determined for the some of the data collected in this project at Scott Base. The data sets collected on the Scott Base radar are mainly only about half an hour long, therefore the only averaging done for this data was over the entire length of each data set. Even using all the available data points in each set, some estimates were comprised of only three or four points which resulted in large variability in some of the estimates, (particularly in the bnna19 data). Aside from these points, the magnitudes of the fluxes (and the standard deviations indicated by the error bars) are fairly similar to those obtained at Birdlings Flat, although there is insufficient data available here to be able to draw any firm conclusions on comparisons between the two sites.

7.13 Uncertainties

There are many elements that can make varying contributions to the uncertainty in a particular measurement made by this experiment. Because the magnitudes of all of these contributions can be difficult to estimate, the general philosophy followed here (as is often done in research of this nature) has been to gauge the confidence in a measurement by examining the consistency between multiple or successive measures of the same quantity. Multiple measures were available for many observations in this project, because these observations were made independently either at different frequencies or at different antennae.

There has been some research done on estimating uncertainties arising from correlation functions. [Hocking et al., 1989] reviewed this work, summarizing expressions for parameters used in full correlation analysis and giving an expression for the uncertainty in phase differences determined from cross correlation functions. These uncertainties are now compared with the consistency approach used in this work.

7.13.1 FCA uncertainties

Full correlation analysis uses measures of the time evolution of a drifting diffraction pattern determined from auto and cross correlation functions. Estimates of the uncertainty in using some of these measures were given by [May, 1988]. One of these, the uncertainty in determining the time lag of the maxima of the cross correlation function was given by equation 4.12 in section 4.1.4. This expression related the uncertainty to the amplitude of the maxima and the fading time.

The left hand plot of figure 7.59 displays the observed relationship between relative variations in velocity and the amplitude of the maxima of the cross correlation function

of signals received at antennae **F** and **D** (which lie approximately along an east - west line) at Birdlings Flat. The variations in velocity are the standard deviation of apparent eastward velocity (which is determined directly from the maxima of the cross correlation function) as found independently at the five frequencies the radar was operated at. As can be seen there is considerable variability in the individual estimates of velocity variation, although as the maxima increase this variability does reduce somewhat.

The right hand graph of figure 7.59 shows mean profiles of the variation in FCA true velocity (solid line) and uncertainty in velocity found using the analysis of [May, 1988]. Similar trends are followed by both measures; however unlike May's study who, in a similar comparison between his analysis and variations between independent FCA experiments, found that the analysis uncertainties were overestimated by $\sim 50\%$, the analysis uncertainties here underestimate the variability by $\sim 50\%$. Since the variations in the simultaneous FCA velocities are greater than the uncertainties implied by analysis of the correlation functions, the variations should be taken to indicate the uncertainty in the FCA as used here. A reasonably typical magnitude of this uncertainty in wind measurements seems to be about 5 ms^{-1}.

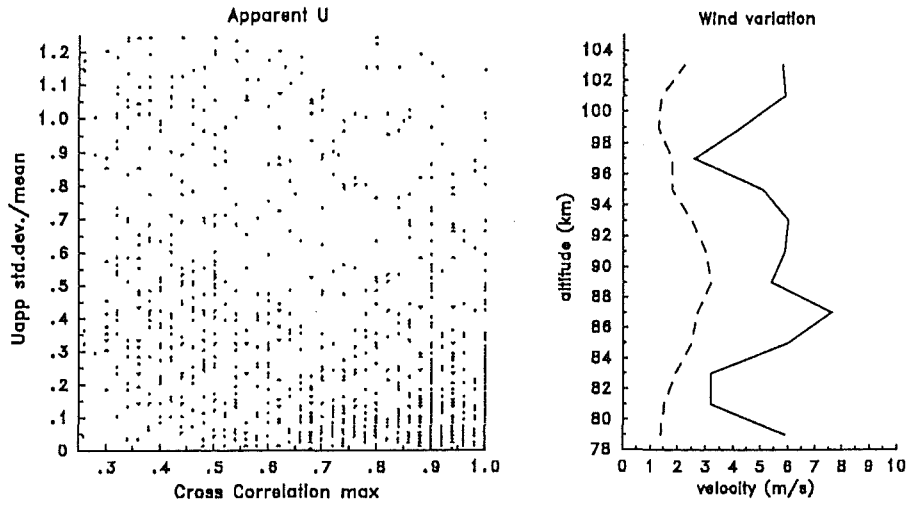

Figure 7.59: **Correlation function uncertainty in FCA winds.** The plot on the left is a scatter diagram of the uncertainty in determining the maxima of the cross correlation function of signals received on an east - west pair of antennae and the standard deviation normalized by the mean of the eastward component of FCA apparent velocity as found at five different radar frequencies. On the right are mean profiles of the standard deviation of the magnitude of the FCA true winds at found simultaneously at different frequencies (solid line) and the estimated uncertainty in wind using the uncertainty analysis of [May, 1988] (dashed line). Data collected over five hours on the Birdlings Flat radar on 8 December 1990.

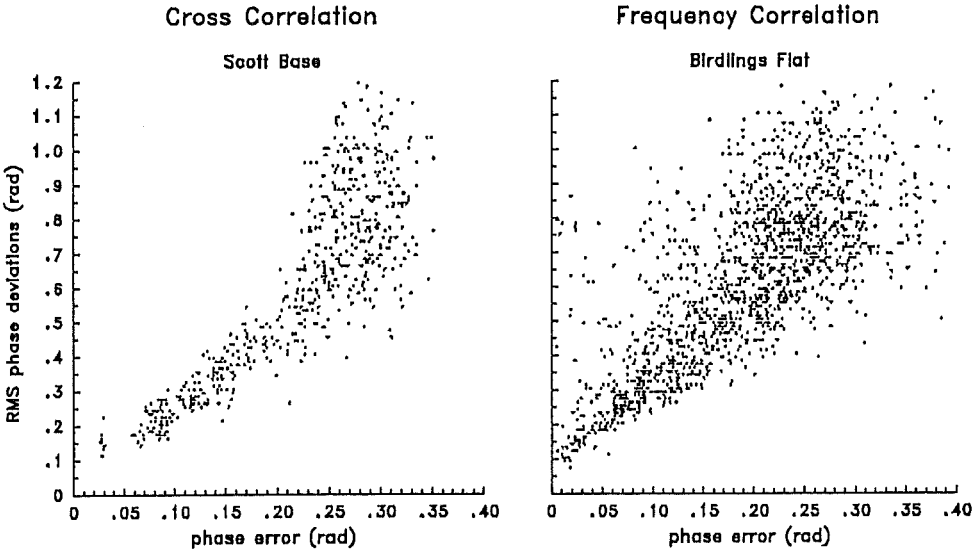

Figure 7.60: **Correlation functions, phase uncertainties**, [Hocking et al., 1989] uncertainty (labeled **phase error**) versus the RMS deviations of phase difference from the mean value for cross correlation and frequency correlation functions. The cross correlation data was collected over four hours at Scott Base (14-17 Dec 88) and the frequency correlation data was collected over five hours at Birdlings Flat on 6 Oct 90.

7.13.2 Uncertainties in phase

Along similar lines to [May, 1988], [Hocking et al., 1989] found an empirical measure of the uncertainty in phase as found from the zero lag of the cross correlation function. (This expression was given as equation 4.12 in section 4.1.4.) The variability in phase can also be estimated by finding the RMS deviation of instantaneous phase from the mean phase. For example when considering the phase difference between signals received on different antennae, the mean phase difference for each one minute sampling period is found using cross correlation functions. The RMS deviation of the phase differences at each pulse in the sampling period from the mean phase difference can also be found.

Figure 7.60 compares the RMS deviation in phase with the uncertainty given by [Hocking et al., 1989] for cross correlation functions and for frequency correlations functions as found for four hours of data at Scott Base and for five hours of data at Birdlings Flat. There is a clear relationship between the two measures, however the magnitude of the RMS deviations are considerably greater than the uncertainty estimates. The RMS deviations are a measure of the width of the phase difference distribution during each sampling period whereas the analysis of [Hocking et al., 1989] is effectively a measure of the uncertainty in determining the maxima of this distribution.

Figure 7.61 displays mean profiles of uncertainties in spatial and frequency domain interferometry. The dashed lines were determined using the uncertainty analysis of [Hocking et al., 1989] and the solid lines were determined from the standard deviation of simultaneous spatial and frequency domain measures. Very good agreement is displayed in the range plot; however the variation in mean direction of arrival is generally much larger than implied by the uncertainty analysis. The variation in direction of arrival was usually determined from five measurements (at each of the five frequencies), whereas the variation in range was determined from typically twelve measurements (four frequency steps at three receivers) so the standard deviation in range would be expected to display less variability than the direction of arrival measurement.

The standard deviation in mean direction of arrival is very similar to the aspect sensitivity profiles for the same data (bottom panel of figure 7.38, section 7.9.2). It appears that if scattering is highly aspect sensitive individual measurements of direction of arrival may have an uncertainty that can be approximated by the uncertainty analysis; however when scattering is more widely spread extra variability becomes apparent.

In summary then, typical uncertainties in direction of arrival measurements appear to be approximately 2°-4°, although if the scattering is highly aspect sensitive the uncertainty is less than 1°. These uncertainties result in an uncertainty in interferometric velocities of 10-15 ms^{-1} (assuming a typical wind of around 50 ms^{-1}) which is similar to the variability (around 10 ms^{-1}) in these velocities noted in section 7.8. Typical uncertainties in frequency domain interferometry range are about 300 metres.

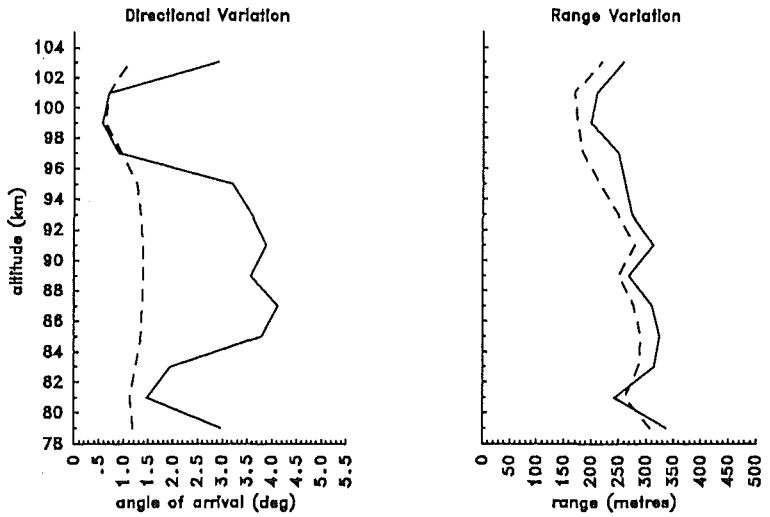

Figure 7.61: **Spatial and frequency domain interferometry uncertainties.** Mean profiles of standard deviation of simultaneous estimates (solid lines) & [Hocking et al., 1989] uncertainty analysis (dashed lines). Five hours data on 12 Dec & 6 Oct 90 at Birdlings Flat respectively.

Chapter 8

Conclusion

This project developed three forms of interferometry, temporal, spatial and frequency domain interferometry on MF spaced antennae radars and operated these techniques together with the standard mode of operation of these radars, that of spaced antennae drifts using full correlation analysis. The experiments carried out for this project appear to have been the first to have combined these three forms of interferometry and the first to operate them together with full correlation analysis.

Carrying out the interferometry required converting the radars from their normal incoherent reception to phase coherent operation. This was reasonably straight forward on the Birdlings Flat radar as some phase measurements had previously been made on this radar. The main modifications that had to be made involved the installation of a phase locking system to properly synchronize the various components of the radar and a frequency stepping system for the frequency domain interferometry experiments.

The Scott Base radar had not been operated in phase coherent mode before and so required extra modifications, the most important, and the most problematic, of which was an external feed to supply the carrier signal from oscillators at the Arrival Heights receiving site to the transmitter at Scott Base. The interferometry experiments were demonstrated to operate very satisfactorily on the radar, and a useful, although somewhat truncated, series of observations was made on the radar.

Gain and phase calibration techniques were devised for this project based on examination of the distribution of signal amplitudes and phases over a period of time and a range of different altitudes. The assumption for the gain calibration was that over a sufficiently long time frame and over a range of altitudes, the overall signal seen by each channel (antenna, receiver channel or radar frequency) should be identical. For the phase calibrations it was assumed that over time scattering should be distributed through the radar volume

giving an even distribution of directions and ranges.

The directional distribution of signals (used in calibrating for spatial interferometry) need not be spread over the entire horizontal extent of the radar volume so long as the only directional bias consistently displayed over all range gates is towards the zenith. The overall agreement (for the later Birdlings Flat data sets and the Scott Base data) between spatial interferometry results and FCA results indicates that phase calibration for spatial interferometry was reasonably accurate. However it should be noted that estimates of more highly derived quantities, such as vertical velocities and momentum fluxes, should be treated with some caution because of the accumulation of uncertainties from both spatial interferometry and FCA during the calculation of these quantities.

The phase calibration for frequency domain interferometry, which does not appear to have been attempted before this study, was based on the similar assumption that significant scatter occurs at a distribution of altitudes rather than at exactly one altitude for the whole data set. The range of the radar volume for each sample was known using the usual timing methods. The distribution of FDI ranges of a series of samples spread evenly within the radar volumes was assumed to be biased only by the weighting function of the radar volumes, which here primarily results from the shape and length of the transmitter pulse. The calibration technique then equated the mean FDI ranges to the range of the centre of the radar volumes. In practice samples from range gates at altitudes near the E region did have extra biasing due to specular reflections, however these samples were found to not significantly affect the calibration determined using samples from all range gates.

Both the gain and the phase calibrations were found to be self-consistent in various subsets of the full data sets the calibrations were carried out over.

Full correlation analysis was carried out on all of the data collected for this project following the procedure of [Briggs, 1984]. The results of this analysis were compared with observations made by the partial reflection spaced antennae drifts experiments that normally operate on these radars, [Fraser, 1989]. It was found that in general the FCA observations made in this project were consistent with those of the drifts experiments indicating that the data collected for this project are not atypical of conditions that generally occur at the sites. The incoherent mode of operation of the drifts experiment was also compared with the coherent operation of this project. Scale parameters (such as $d_{\frac{1}{2}}$ and $T_{\frac{1}{2}}$) were found to be greater using coherent receivers than incoherent receivers as was expected from the different detection modes of the two types of receivers. The phase coherent receivers achieved greater signal to noise ratios, higher data rates and less

variability in the FCA results than the incoherent receivers.

The analysis for the three forms of interferometry, temporal, spatial and frequency domain interferometry, generally commenced with time series (temporal domain) analysis. This involved finding either correlation functions, giving mean quantities (such as the mean phase difference between signals on different channels), or power spectra, giving Doppler sorted quantities (such as the phase differences as a function of Doppler frequency), of the scattered signals received during each one minute sampling period. If the different channels are spaced antennae, then the phase differences can be used in spatial domain interferometry to find the direction of arrival of scattered signals. If the different channels are different radar frequencies, then frequency domain interferometry can be carried out, giving information about the range of the scattered signals.

Power spectra of the scattered signals generally contained a number of distinct features rather than a broad spectral envelope. This suggests that there were a number of localized reflecting points rather than a diffuse distribution of targets; however spectra of short series of data of the sort collected in this project can contain spurious spikes so some caution was exercised in interpreting these features. To assist in this interpretation, the spectral analysis was carried out using conventional Fourier techniques (FFT and Blackman-Tukey) and maximum entropy methods. Spectra obtained using the different techniques were compared, and common features in the spectra were identified as being the most likely to correspond real scattering centres (being labelled here "consistent peaks"). Spatial and frequency domain interferometry techniques were applied to the features using cross spectral analysis, and the direction of arrival and ranges of the features were found. They were found to be fairly evenly distributed in range and direction.

The directional and Doppler information allowed estimates to be made of the overall motion of the scattering region. If at least three scattering centres can be identified, a full three dimensional velocity vector can be determined: if only two centres are available then the horizontal velocity can be estimated if it is assumed that the vertical velocity is negligible. These "interferometric" velocity estimates were compared with velocities determined using FCA. Provided a clear phase calibration could be made, there was found to be general agreement between the interferometric and FCA velocities as has been found in other studies (for example [Meek and Manson, 1987] and [Franke et al., 1990]). Various aspects of calculating interferometric velocities were tested as was the behaviour of various scattering characteristics as a function of the degree of agreement between interferometric and FCA velocities.

When interferometric velocities were calculated from spectra for which consistent peaks

had not been determined the rates of agreement between interferometric and FCA velocities were very similar to those determined using just consistent peaks. This implies that reasonable interferometry can be carried out without being too selective about the spectra that are used, although when raw spectra are used (without any averaging) or when spectra are sampled randomly (say at regular intervals, ignoring both consistent and spurious peaks) the agreement rate between the two methods falls. It was also found that the agreement rate does not vary greatly if it is assumed that the vertical velocity is negligible. By using spectra without testing for consistent peaks and by assuming the vertical velocity is negligible, interferometric velocities can be estimated for many more samples than would otherwise be the case.

In terms of the scattering conditions it was found that the more stable the scattering region (measured by, for example, the FCA parameter $T_{\frac{1}{2}}$) the greater the agreement between interferometric and FCA velocities. When the scattering region changes as it moves along, the interferometric velocities show more agreement with the FCA apparent velocities than the FCA true velocities. This appears to be because like the FCA apparent velocity, the interferometric velocities do not include allowances for evolution in the scattering region as the region is advected by the background wind. If the region is evolving rapidly as it moves along, then Doppler sorting can fail to resolve widely separated scattering centres that have similar Doppler shifts leading to a misleading spatial interferometry measurement and thus an incorrect velocity.

Another form of spatial interferometry investigated was postbeam steering, [Röttger and Ierkic, 1985], in which an antenna beam is synthesized from signals received on spaced antennae and "steered" in different directions to study the spatial distribution of various scattering characteristics. The postbeam antenna formed here had a wide polar diagram leading to postbeam images of low resolution so the results were examined qualitatively rather than quantitatively.

Much of the data collected for this project included samples taken at a number of radar frequencies allowing Frequency Domain Interferometry to be carried out. FDI provides a useful method of improving the range resolution of a radar, without requiring the sophistication of pulse compression techniques. The FDI technique used here (similar to that of [Kudeki and Stitt, 1987]) gives the mean range and standard deviation (or "scattering depth") of ranges of distributed scattering targets. The technique cannot individually resolve multiple targets within a radar volume, unless they can be separately identified using Doppler sorting (however such resolution may be possible with the development of "discontinuous chirping" techniques, for example [Franke, 1990]). The mean range and

depth of scattering was measured here to a resolution of about 300 metres although higher resolution was possible when the scattering depth was narrow.

Distributions of the range determined by FDI were in the main narrower (typically about one kilometre half height full width) than might be expected given the $4\frac{1}{2}$ km width of the transmitter pulse. The average scattering depth was about one kilometre (equivalent to two kilometres full width) which is more indicative of the depth of the radar volume. At altitudes where the scattering depth was narrow the distributions of FDI range over time periods of hours were broadened because of fluctuations in the range of the scatter. The lack of variation in range for those samples with large scattering depths suggests that the windowing function provided by the radar volume is primarily responsible for the observed ranges when the scattering is deep. This in turn suggests that scattering was occurring throughout the radar volume for these samples.

Narrow scattering depths seemed to be associated with either a steady flow or with long period fluctuations in a steady flow, one particularly clear example being associated with the onset of a phase change in the semidiurnal tide (discussed further below). Scattering depth was observed to be closely related to the angular distribution of scattering as measured by aspect sensitivity. Narrow scattering depths correlated well with narrow angular distribution, indicating localized reflections.

The scattering and turbulence scale parameters, aspect sensitivity and eddy dissipation, were derived. When determining these parameters on radars with broad antenna beams as were used here, it can be difficult to include all of the effects of the different variations in motion (or spectral beam broadening effects), so the estimates of these parameters made here should be taken as upper limits to the true values. The values that were obtained here are reasonably typical of values obtained elsewhere. For example the turbulent eddy dissipation rate, determined using the $T_{\frac{1}{2}}$ technique of [Hocking, 1983b], was estimated to be around $10^{-1} - 1$ W/kg which compares well with values summarized in [Hocking, 1987c].

Several methods of determining the aspect sensitivity of scattering were compared. These methods fall into two categories, those based on either temporal or spatial scattering scales or those based on interferometry.

The two interferometry methods involved measuring the RMS deviations of the phase difference between signals received on spaced antennae, [Bramley, 1951], and fitting a function to the variation in power with angular separation of the Doppler sorted scattering centres along the lines of [Adams et al., 1989]. The RMS phase deviations method only gave aspect sensitivity estimates consistent with the other methods when aspect sensitivity

was around 5° or less because the antenna spacing was too wide for this method when the aspect sensitivity was broader. The method using the variation of power of the scattering centres potentially provides much information on the angular distribution of scattering. However the combination of uncertainties encountered in determining both the power and angular position of each scattering centre resulted in variable estimates that generally were considerably wider than the other estimates of aspect sensitivity.

The main scattering scale method of finding aspect sensitivity used was based on beam broadening. In this method the time scales of signal fluctuations are related to the velocity at which the scattering region travels through the radar volume of known width, giving the aspect sensitivity of the scattering, [Hocking, 1989]. Another scattering scale method that was used is based on the spatial correlation function, [Briggs and Vincent, 1973] and [Briggs, 1992].

The standard beam broadening method assumes that turbulent fluctuations in the scattering region are insignificant compared to the beam broadening effect as estimated using the fading time. Here the turbulent fluctuations were estimated using the FCA parameter $T_{\frac{1}{2}}$ and removed. It was found that the aspect sensitivity with this $T_{\frac{1}{2}}$ adjustment was typically about 2° lower and had less variability than the standard beam broadening estimates, indicating that turbulent fluctuations are significant when determining aspect sensitivity. This adjusted beam broadening technique gave very similar results to the spatial correlation method using $d_{\frac{1}{2}}$ as an estimate of the spatial correlation function.

Typical values of aspect sensitivity were around 10° which are consistent with observations reported elsewhere (for example [Reid, 1990]). There was generally a widening of aspect sensitivity by 2°-5° with altitude going from 80 to 90-95 km, then often a narrowing around 100 km as E region specular reflections dominated the scattering. The aspect sensitivity estimates made during this project on the Scott Base radar were typically two or three degrees wider than those made on the Birdlings Flat radar; however this may be due differences the radars' antennae and the higher average altitude of the Scott Base data.

The statistical distributions of the scattered signals were examined using the Rice and Nakagami m parameters. These distributions model scattering as a single specular reflector-like signal superimposed on random (or Rayleigh) scatter. It was found that 85% of the Scott Base data, and around half the Birdlings Flat data were not consistent with the standard Nakagami and Rician models, suggesting that multiple reflections are occurring in the radar volume for much of this data, [Kuo et al., 1987].

The non-Rician behaviour of the statistical distributions, the identification of discrete

scattering centres by temporal domain interferometry and their distributed locations as revealed by spatial and frequency domain interferometry, as well as the degree of aspect sensitivity displayed by the scattering, would seem to indicate that a distributed anisotropic scatterer model along the lines of Fresnel scattering would best explain many of observations made in this project.

The occasions when the scattering depth is very narrow, such as the events associated with the semidiurnal tide as well as the E region reflections, are relatively clear examples of specular reflection as can be described by the more standard Fresnel reflection model. There were also occasions when scattering was very broad in both scattering depth and aspect sensitivity. This scatter could be described by random scatter models; however it may be the result of multiple Fresnel reflections or scattering.

The most prominent atmospheric oscillations observed in this project were of the semidiurnal solar tide. In one particularly clear example, the onset of a downward propagation of a phase change in the wind induced by the tide was accompanied with a downward propagation of localized scatter made particularly apparent by FDI observations. An association between stability and the phase change of the semidiurnal tide had been reported previously (for example [Fraser and Khan, 1990]). Such reports, however, have concentrated on the increase in scattered signal strength and turbulence assumed to be associated with breaking of the tidal gravity wave rather than the occurrence of highly localized scatter seen here.

Interferometry techniques have been shown to be useful tools in radar studies of the middle atmosphere. In particular, frequency domain interferometry clearly identified localized scatter; temporal and spatial domain interferometry enabled comparison studies to be made with standard techniques such as FCA; and all three interferometry techniques together provided useful information on the nature and distribution of scattering.

Appendix A

Antarctic Reports

This appendix includes two reports regarding the experiments and associated activities carried out for the Antarctic component of this project. The first is a logistic report to the organisation that provides operational support for the New Zealand Antarctic Research Programme, the Antarctic Division of the Department of Scientific and Industrial Research. The second is a science report to the body that oversees the New Zealand Antarctic Research Programme, the Ross Dependency Research Committee. The format of these reports follows that recommended by the Antarctic Division of the Department of Scientific and Industrial Research.

A.1 Logistic Report

D.S.I.R. Antarctic Division

Event K055

Antarctic Middle/Upper Atmosphere

HF Radar Programme

1988/1989 Season

William O.J. Brown

Department of Physics

University of Canterbury

Christchurch

Aims

This season's programme involved the annual maintenance and calibration testing of the HF radar at Scott Base and Arrival Heights. The radar normally operates in programmes that collect wind and electron density profiles of the middle and upper atmosphere (approximately 40 to 100 km height range). These experiments are the Partial Reflection Winds and the D-region Polarimeter experiments, both of which run all the year round under automatic computer control.

The major part of this seasons programme was a short term experiment that involved modifying the radar to operate in phase coherent, frequency shifted mode. This involved substantial alterations to the receiver and data collection equipment as well as the installation of a high speed data link between the Arrival Heights receiving equipment and the Scott Base transmitter.

The original intention was to spend one to two weeks on maintenance of the on-going winds and polarimeter programmes and the installation of the coherent frequency shift experiment. Then two to three weeks on running the new experiment, and the final few days reconfiguring the radar to the original programmes.

Planning

The department operates a similar, more extensive HF radar at Birdlings Flat near Christchurch. The maintenance procedures used at Arrival Heights are well established at our Birdlings Flat field station. The phase coherent, frequency shift experiment has been under development at Birdlings Flat for approximately two years. The same receiving equipment used at Birdlings Flat was used for the Arrival Heights programme. Some of the control equipment had to be partially remodelled for Arrival Heights. This equipment was tested as far as possible at Birdlings Flat. The major element of the experiment that could not be tested was the high speed data link between Arrival Heights and Scott Base. This link consists of a fibre optic cable and the optical transmitting and receiving equipment attached. All of the optical link equipment is owned and maintained by the Antarctic Division of DSIR.

Our technician responsible for the setting up the electronic side of the experiment, Stephen Beuzenberg (of the University of Canterbury Physics Department) and I had discussions with the manager of the Scott Base Geophysical laboratory, Cass Roper. These discussions were held both prior to and during the Tekopo training course. These discussions yielded valuable planning information for the programme. Heavy reliance had to be made on the specifications of the fibre optic link provided by the manager. Unfortunately in the event this link did not meet these specifications.

Cargo

Cargo consisted of several boxes of electronic equipment amounting to approximately 200 kg. Also there was a small butane gas type soldering iron that was transported down by stores as inflammable cargo. There were no difficulties experienced in the shipment of our cargo.

Personnel

Andre von Biel, Scientist. Arrived 26 Oct 1988, departed 28 Oct. Primarily there for maintenance checks on the polarimeter experiment. Advised on calibration procedures for and assisted on the setting up of the coherent frequency shift experiment. Andre has had numerous trips to the Antarctic.

Stephen Beuzenberg, Technician. Arrived 18 Oct 1988, departed 26 Oct. Made the electronic modifications to the radar for the coherent frequency shift experiment and attempted to setup the necessary fibre optic link between Arrival Heights and Scott Base.

Also carried out electronic checks on the winds and polarimeter experiments. On return to Christchurch, Stephen continued to work on the fibre optic link problem. After much effort by him and other members of the Physics Department, modifications were able to be made in the form of extra components being made up, mailed down and included in the experiment by Bill Brown. This was Stephen's second trip to the Antarctic.

Geoff Graham, Technician. Arrived 26 Oct 1988, departed 28 Oct. Primarily there for familiarisation of the technical aspects of the radar on his first trip to the Antarctic. Also provided assistance in setting up the coherent frequency shift experiment and assisted in maintenance checks of the winds and polarimeter programmes.

Bill Brown, Scientist. Arrived 18 Oct 1988, departed 20 Dec. Principal investigator for the coherent frequency shift experiment. Setup and operated this experiment. Also carried out maintenance and updated the winds programme and assisted with maintenance on the polarimeter programme. This was Bill's second trip to the Antarctic.

Relations with Base Staff

Various members of the base staff were very helpful to this event. Tim Exley (winter-over technician) was the most closely associated with the event. Tim is responsible for maintaining the winds and polarimeter experiment for the rest of the season. This consists of regular checks of the experiments and changing the data disks as necessary. Also Tim is responsible for any repairs that may need to be carried out to keep the experiments going. Tim was very helpful in the setting up of the coherent frequency shift experiment and assisting with checks and repairs of the winds experiment.

Management of the Base provided were most helpful with transport and telecoms staff were also most helpful with the frequent communications back to New Zealand. We had useful discussions with the telecom technicians on various technicial aspects of the programme. To some extent this was reciprocated by information on how to obtain and interpret ionospheric communication forcasts provided via the electronic mail system on the McMurdo communications computer.

Transport

The principal transport used was four-wheel drive vehicles. As components of the experiment are at both Scott Base and Arrival Heights (approximately 8km distance by road), regular (daily) travel was required. Use of the vehicles was frequently shared between this and other events. Even given this coordination, there were one or two occasions when travel was not possible due to a lack of suitable vehicles. Frequently, Tim Exley or one of

the other base staff drove personnel up to Arrival Heights returned to Scott Base to carry on their work and then had to drive back up to pick people up again. This diversion of staff time was appreciated.

Unfortunately the road frequently had heavy snow cover and was occasionally impassable by four-wheel drive. Previously the road has been occasionally cleared by an American grader, but this spring this was not so regular and combined with an apparent abundance of snow, travel was made more difficult. Concern was expressed at the additional wear and tear this added to the vehicles. The Ford pickup F10 with its power and large, wide tyres was found to be the most effective vehicle in these conditions. At one stage the Americans provided their personnel at Arrival Heights with a ASV tracked vehicle. Scott Base management suggested the same and this may be necessary in winter. The manager arranged for one of the Scott Base bulldozers to clear the road on a few occasions.

Event Diary

14 Oct.

Planned departure date from Christchurch. Weather and aircraft problems delayed departure.

18 Oct.

Bill Brown and Stephen Beuzenberg arrived Scott Base. Laid wire cable from end of fibre optic cable in Scott Base Geophysical lab to transmitter hut.

19 Oct-26 Oct.

Worked on winds experiment maintenance and updating and setup coherent frequency shift experiment. Discovered that an aerial used in the drifts experiment had been damaged during the winter, apparently by wind blown rubbish. This would have caused some data loss. Also quickly found that the fibre optic link did not work up to the specifications we had been told it work work to. This was a serious blow to the experiment. We needed the link to be able to operate at 3MHz. We found that the link would barely operate as we had been told at 500kHz. In principle such a fibre should manage at least 10MHz. It was decided that Stephen Beuzenberg should return to Christchurch to try and come up with a way around this problem. Meanwhile Bill Brown would remain and continue the

maintenance and updating of the winds experiment and setup as much of the rest of the coherent frequency shift experiment as he could.

26 Oct.

Stephen Beuzenberg returned to Christchurch and Andre von Biel and Geoff Graham flew down to Scott Base. Their arrival had been delayed by weather and aircraft delays.

26 Oct-28 Oct.

Andre von Biel and Geoff Graham carried out their programmes. Andre von Biel did maintenance and calibration on the polarimeter experiment and Geoff Graham was familiarised with both the polarimeter and winds experiment and assisted with the maintenance of both. Both Andre and Geoff provided assistance and advice for the coherent frequency shift experiment.

28 Oct.

Andre von Biel and Geoff Graham returned to Christchurch. Their stay was shorter than intended because of their delayed arrival and other commitments back in New Zealand.

29 Oct-18 Nov.

Carried out maintenance and updating on the winds experiment. This included repairs (assisted by Tim Exley) to an aerial apparently damaged by wind blown rubbish. Instructed Tim on the operation and maintenance of the winds and polarimeter experiments.

It was determined that the fibre optic transmitters and receivers were the main problem in the link problem and that the optic cable itself is alright. Experimented unsuccessfully with modifications to the link and the radar equipment in various attempts to get the operation going. Also setup as much as possible the coherent frequency shift experiment. Found that in places the fibre optic cable has been damaged by being blown around in the wind. Tried to get electroic mail back to the University of Canterbury computers via the McMurdo communications computer and showed the Scott Base technicians how to use the communications programs to link to McMurdo and how to manage their electronic mail . Was in regular telephone contact with Stephen Beuzenberg and others back in New Zealand for suggestions and advice on the fibre link problem. Tim Exley was of great assistance during this time.

19 Nov.

Stephen Beuzenberg sent down modifications to adapt the experiment to work within the limited capabilities of the link.

20 Nov-9 Dec.

Found that the adaptions still did not allow the link to work properly. After much experimentation and alterations got to a position whereby the link worked although not to a good enough standard. The power supply, more particularly the instablity of the electrical earth in the lab appeared to be the major remaining problem. During this time showed various VIP groups around the Arrival Heights lab. Also during this time work was delayed several times by bad weather and the road being blocked by snow drifts. Laid out the remaining parts of a new wire cable between Arrival Heights and Scott Base. The previous cable had been getting increasingly unreliable causing interference for communications and the winds and polarimeter experiments to fail. At the time of the failure, American tracked vehicles were travelling along the cable path and these may have contributed to the problems. Assisted Bob Thomson for event K015 with radio noise level measurements.

10 Dec.

Gell cells were sent down from Christchurch. It appears there have been a couple of days of delay in stores at Scott Base. These cells in combination with the equipment send down on 19 Nov allowed the frequency shift experiment to get properly under way.

11 Dec-17 Dec.

Data collection for the coherent frequency shift experiment. This involved mainly operating the control computer at Arrival Heights as well as some data analysis on the PC computers in the Geophysical lab at Scott Base.

18 Dec-19 Dec.

The coherent frequency shift experiment was dismantled and final checks on the winds and polarimeter experiments were made.

20 Dec.

Bill Brown returned to Christchurch. The return was delayed one day by weather conditons.

Weather

Weather conditions caused the usual delays. All transfers of the events personnel between Antarctica and New Zealand were delayed by some extent. Also the weather caused some problems in travelling between Arrival Heights and Scott Base. Previous seasons experence had caused us to alter some of our procedures so that extra work could be done at Scott Base if delays occurred as indeed happened. Some of our repairs to aerials and cables require good weather conditions and this season there were some delays to these repairs due to the weather.

Radio Communications

Communications between Scott Base and Arrival Heights relied on telephone (via the McMurdo exchange) and VHF radio. While the experiments were being setup and calibration checks were being made, extensive use was made of the VHF radios as much of the time the adjustments had to be made away from the telephones. The only channel that seems to work between the two locations was channel 4. Part of the time, the Arrival Heights telephone was not working due to a fault in the McMurdo exchange.

Facilities

The main facility used apart from that equipment at Arrival Heights and Scott Base that is part of the radar, was the fibre optic link between Scott Base and Arrival Heights. This was crucial to the coherent frequency shift experiment. In the event this was not up to the specifications detailed back in NZ. Adaptions eventually allowed the link to be used but this caused some degradation in the experiment.

Extensive use was made of various items of electronic test equipment belonging to the Geophysical lab. Also the PC computers in the lab were used. These computers were not properly operational. Initially only one PC was working because of problems in disk controller and communications boards of the other. The keyboard of the PC that wasn't working was used in the command centre and wasn't available for some time after the lab PC was repaired. Sporadic problems occurred with many of the various computers on Base. The major problem appears to be related to static electricity. There are practial

solutions to this problem. One is education, those using computers should be aware that they can reduce the risk of expensive damage by good earthing and avoiding some seating and clothing combinations. Earthing bands and mats should be made available and their use encourged. Another solution would be to lay down conductive mats in areas of sensitive equipment, carpet is not very practial in the dry environment.

Some use was made of the AT computer belonging to Tim Exley, for which we are very grateful. This class of computer has a high density disk drive which was necessary for an application we tested. We had made arrangements to use this computer back in New Zealand. The use of this machine allowed us to do some preliminary data analysis at Scott Base to test if our equipment was behaving. We consider the lab to be short of computer equipment for communications, experimental, and general use. The computers there had fairly heavy use by various members of the base for science and word processing. A computer with a high density disk drive (eg:AT type) would be particularly convenient for occasional use with our programmes.

Huts

The hut at Arrival Heights is a very good facility. Several nights were spent there by Bill Brown.

Waste Disposal

All rubbish at Arrival Heights was taken back to Scott Base. There some are problems at Arrival Heights with liquid and human waste disposal. The American hut at Arrival Heights has a good solution for the latter in the form of an electric toilet.

Extra Comments

Communications to New Zealand

Any scientific facility must have good communications to other institutions particularly where experiments are being operated in absentea. Communications back to New Zealand were a problem at times. The approaching solar sun-spot maximum frequently made the HF radio link to NZ unusable. This problem is likely to get no better in the next few years.

Attempts were made to get computer communications via the McMurdo communications computer back to New Zealand. Extensive use is made of this electronic mail facility of computers by our department and many other institutes for correspondence around

the world. The McMurdo communications computer regularly connects to this network and attempts were made to use this facility. Members of two other events were also very interested in using the same facility if we could get it working. Efforts to do this were hampered by a lack of a formal arrangement with the Americans to use the facility.

Electronic links generally are becoming more and more useful for the monitoring of experiments and the transfer of data. Some arrangement to use the American or other satellite links, or at least the development of a HF data link to New Zealand should be investigated.

The Fibre Optic Cable

The fibre optic cable was a critical link in this season's programme. It is envisaged that further use might be made of this valuable facility in some future programme. We are concerned however at the deterioration that is in evidence along portions of this cable. It appears that wind is causing the cable to rub on rocks and also causing the cable to move and stretch. Also there have been instances where vehicles have run over the cable. Repair of the cable would be difficult and replacement could be delayed and expensive. It is important for continued confidence in the use of the link, that steps be taken to adequately protect and maintain the existing cable.

Rubbish

At some time during the last winter, it appears that rubbish, probably from the nearby McMurdo dump got caught around one of the aerials of the winds programme and caused part of the aerial to break away. The possibility of this occuring was raised in a previous report to the Ross Dependency Research Committee (event K059 1986-87). Such damage leads to a degradation in data quality. At various times items of rubbish were removed from around aerial masts and cables on the ground (including the fibre optic cable). The further damage that this rubbish could cause, even with the new barrier fence that has been recently erected around the McMurdo dump, is a cause for some concern.

S.S.S.I.

Event K015 carried out a review of Sites of Special Scientific Interest including the Arrival Heights site. Bill Brown assisted Bob Thomson with radio noise level measurements as part of this review. These measurements were spot comparisions of the background noise at HF frequencies at Scott Base and Arrival Heights. There is some concern that electrially quiet nature of the Arrival Heights site has been degraded in recent years. Frequently

there are high levels of broadcast interference apparently from sources in McMurdo or on the Transmitter Hill site. During a period over Christmas and on other occasions, this interference has apparently reached a level such that the radar has gone several days collecting no data. This sort of radio interference and other sources of radio noise degrade the quality and quantity of data collected by the radar programmes. Further study into the level and sources of radio noise is required to determine whether some restoration of the electrically quiet nature of the site can be achieved.

There is also some concern that unauthorized or unaccompanied personnel are entering the site area. Although the winds and polarimeter experiments are not directly affected by their presence (unlike some other experiments on site), they may have sources of radio noise or may accidently damage one of the many cables associated with the radar.

Conclusion

The support received by this event was very helpful and appreciated. The problems that did occur were resolved by the full cooperation of the Antarctic Division of DSIR. This assistance allowed the events programme to come to a successful conclusion and preliminary analysis of data collected has lead to some interesting scientific results.

A.2 Science Report

Ross Dependency Research Committee

Event K055

Antarctic Middle/Upper Atmosphere

HF Radar Programme

1988/1989 Season

William O.J. Brown

Department of Physics

University of Canterbury

Christchurch

Abstract

Antarctic Middle/Upper Atmosphere HF Radar Programme

Event K055, 1988/1989 Season

The University of Canterbury Physics Department operates a HF Middle and Upper Atmospheric radar at Scott Base and Arrival Heights. This radar normally operates two experiments, the Partial Reflection Winds and the D-region Polarimeter experiments for determining the wind and electron density profiles of the mesosphere and lower thermosphere (approximately 40 to 100 km altitude). These two experiments operate all the year around under automatic computer control. Part of this season's programme was the annual maintenance, repair and calibration of these two projects.

The major part of this season's activities was the extension, on a short term basis, of the winds programme to operate in phase coherent, frequency shifted mode. The aim of this experiment was an intensive study into the nature and structure of the reflecting features of the Upper Atmosphere used in the winds programme. The project has been under development at a separate HF radar site in New Zealand. Adapting the technique to the Ross Island radar involved substantial alterations to winds receiver and data collection

equipment and the installation of a high speed data link between the Arrival Heights receiving site and the Scott Base transmitting site to achieve phase coherency.

After various technical problems had been overcome, the radar was operated successfully in the new mode. Preliminary analysis of the data collected suggests that the upper atmosphere at the time of observations was of a less sharply defined but more of a more stable nature than has been observed in the New Zealand upper atmosphere.

Proposed Programme

The Physics Department of the University of Canterbury has operated a HF incoherent radar on Ross Island for several years for studying the Antarctic middle and upper atmosphere (specifically the mesosphere and lower thermosphere). The programme has until now consisted of two experiments, the D-region polarimeter experiment (for determining electron density profiles with height) and the partial reflection drifts experiment (for determining wind and turbulence parameters). These two projects operate automatically under computer control, requiring only occasional technician intervention. This seasons programme included annual maintenance and calibration tests of these experiments.

The major portion of this season's activities however was the setting up of a new experiment: the coherent, frequency shift experiment. This experiment has been under development for two years at the Physics Department field station at Birdlings Flat near Christchurch. The aim of the experiment is determine to further the structure of the upper atmosphere. The winds experiment to some extent determines the degree of turbulence in the region and this new experiment aims to extend those studies. Shifting the radar frequency over small steps allows more precise determination of the range of reflecting structures in the upper atmosphere. Phase coherency allows further determination of motions using Doppler shifts and directional information.

This experiment was based on the drifts experiment equipment, although it required a major reconfiguration of that equipment. The original intention was to make the necessary modifications over one-two weeks, operate the experiment for two-three weeks and then reconfigure the equipment to the winds experiment.

Science Endeavours and Achievements

The maintenance operations on the on-going experiments (winds and polarimeter) involved routine testing and calibration of the many components of both experiments.

The following modifications of the winds experiment had to be made to setup the coherent frequency shift experiment

- amplitude receivers used by the winds programme replaced by phase sensitive receivers
- the data collection system expanded from three A/D convertors to six to collect the extra information available from phase receivers
- the radar transmitter modified to accept an external frequency source
- the controlling frequency source, receivers and transmitter had to be locked together to achieve phase coherency
- the control and data processing computer had to be reprogrammed to carry out the new experiment.

The new experiment was also constrained by the requirement to be readily convertable back to the original configuration to allow normal operation of the winds and polarimeter experiment between runs of the new experiment.

Locking together the frequency source, receivers and transmitter was the most difficult operation. The receiving equipment is at Arrival Heights and the transmitter is at Scott Base four kilometres distant. A high frequency link between the two sites had to be made. It was decided that the existing fibre optic cable provided by the Antarctic Division of DSIR would be suitable. Advice was taken both prior to and during the Tekapo training camp from the Geophysical lab manager on how to use this link. We designed the experiment around the specifications given to us at that time, allowing considerable margin for variations. In the event it was discovered on our arrival at Scott Base, that the link did not meet the specifications as stated by the manager.

Stephen Beuzenberg and Bill Brown arrived at Scott Base on 18 Oct, 1988. It was quickly discovered that we could not use the fibre optic link as originally planned. Considerable efforts were made to modify the optical receiving equipment of the fibre optic link which appeared to be the main limitation of the link. Some maintenance of the winds experiment was also carried out. Stephen Beuzenberg returned to New Zealand on 26 Oct. Over the following few weeks, he and other members of the Physics Department worked on a solution to the link problem which basically involved redesigning part of the frequency shift experiment to allow it to work under the reduced specifications of the fibre optic link.

On 26 Oct Andre von Biel and Geoff Graham arrived at Scott Base. Andre ran calibration and maintenance checks on the polarimeter experiment assisted by Geoff. Geoff was primiliary there on a familiarisation tour of the winds and polarimeter experiments.

Both were able offer advice and assistance on the fibre link problem. They returned to New Zealand on 28 Oct.

Bill Brown remained until 20 Dec. The first several weeks were spent attempting to get the link going, doing repairs and maintenance to the winds experiment and setting up as much of the frequency shift experiment as could be setup without the link. The components that allowed adaption of the experiment to the link's capabilities arrived and were working adequately by 10 Dec. The next week was spent running the experiment. This was done at a more intensive level than had been planned since data collection had to be done over a shorter time frame than the two to three weeks originally planned. Bill Brown return to New Zealand on 20 Dec after reconfiguring the radar to operate solely in winds and polarimeter modes.

During this time we were greatly assisted by the winter-over technician responsable for operating the experiments over the winter, Tim Exley.

Preliminary Conclusions

The delay and shortening in the data collection phase of the frequency shift experiment did result in some change in emphasis in the programme. One of the features that it had been planned to study was a low altitude feature that has in previous seasons been occurring in mid-spring. The delay resulted in this feature begin missed, but the delay did allow study of a new feature that is gaining prominence, the Polar Mesosphere Summer Echo. Analysis carried out so far has revealed some trends. The echos received by the radar were of a weaker strength although of a greater stability than was expected. The analysis is also revealing pronounced Doppler shifting of echos although it has not yet been established whether this is due to any vertical motion. Time series analysis is showing very broad spectral features suggesting a more diffuse nature to the radio reflecting surfaces in the upper atmosphere than had been expected. Interpretation and further analysis is continuing.

Publications

There has been a series of publications relating to both the winds and polarimeter programmes. The original winds experiment publication was

1984 Summer circulation in the Antarctic middle atmosphere.
G.J. Fraser, *J.Atmos.Terr.Phys.*, **46**, 143.

Some of the more recent and upcoming publications associated with the Arrival Heights winds

experiment include

1988 Seasonal and Height Dependence of Turbulence in the Middle Atmosphere.
Usman Khan. *M.Sc. thesis*, Physics Department, University of Canterbury.

1989 Monthly mean winds in the mesosphere at 44S and 78S.
G.J. Fraser. *Pure Appl. Geophys.* **130**, No. 2/3 (in press).

1989 Inter-annual variability of tides in the mesosphere and the lower thermosphere.
G.J. Fraser, R.A. Vincent, A.H. Manson, C.E. Meek and R.R. Clark.
J.Atmos.Terr.Phys., **51** (in press).

1989 High latitude tides.
S. Avery et al. *J.Atmos.Terr.Phys.*, **51** (in press).

1989 Long-term variations in mid-latitude southern hemisphere mesospheric winds.
G.J. Fraser. *Adv.Space Res.*, **9** (in press).

1989 Semi-diurnal variations in the time scale of turbulence-like irregularities near the Antarctic summer mesopause.
G.J.Fraser and U.Khan. *Proc.4th MST radar conference, Kyoto*, MAP (in press).

The most recent publication associated with the polarimeter programme is

1989 An Investigation of the Antarctic D-region.
H.A. von Biel *Planetary and Space Science* (in press).

The frequency shift experiment is part of research being undertaken for a PhD. thesis. We are currently considering the publication of certain aspects of the research carried out in this experiment in an appropriate atmospheric journal at some stage and are looking forward to doing so.

Future Research

The winds and polarimeter programmes are on-going projects which we plan to continue on with into the next season. The coherent frequency shift experiment was intended to be a one off. Further analysis and consideration may lead to inclusion of certain aspects of the experiment in future programmes, particularly the phase coherent elements which lead to a greater data quality as a result of increased separation of noise and signal components of echos.

Acknowledgements

The Antarctic Division of DSIR has been very cooperative and helpful towards this events programme, as have the base and technicial staff of the Scott Base 1988/89 summer season.

Appendix B

The Data Files

This appendix outlines the structure of the sorted data files used in this project. There are also tables showing the data file names, dates, times and altitudes sampled of the main data sets collected in this project, both at Scott Base and at Birdlings Flat.

The data files are composed of DEC[1] blocks of 512 bytes or 256 two byte words. Each file contains the data collected during the one minute sampling period used in this project. Note that these files are in binary format.

The sorted files are not the raw data files collected at Birdlings Flat or Scott Base. Those files, which were basically series of A-scans, had a somewhat variable structure depending on the media used (floppy disk or magnetic tape) and on the time available before more data had to be collected (if there was plenty of time just selected range gates were saved, otherwise consecutive range gates were saved). Data arranged in such a series of A-scans is inconvenient (and inefficient) to analyse because normally it is of more interest to examine data at a particular range rather than data at several ranges, and so each A-scan would have to be read and the data at the range of interest extracted. Instead the data is sorted by translating the data into blocks of series of particular ranges, (section 2.1.7). This translation was done on the University computer rather than on the field station computers because it would been a time consuming task for those computers. During the translation process the DC level of the receivers (section 2.1.4) was removed and the time that each of the A-scans was recorded was checked because there were occasional glitches in the radar control system which lead to unintentional pauses in the data.

The sorted files have the following structure. The first block, the "header" block, contains information such as when the data was collected and what channels and frequencies were used. This is laid out according to table B.1.

[1] Digital Equipment Corporation

The data itself is arranged in blocks, each block containing samples from one frequency and one receiver channel at a particular range. Generally there were five frequencies and three receivers, each with two A/D channels (in-phase and quadrature) so that there were a total of thirty blocks for each range gate. There were typically thirteen range gates retained of the Birdlings Flat data (fifteen were recorded; however two of these were DC levels removed during the data translation) and seven in the Scott Base data (eight were recorded of which one was a DC level, although many of the data files retain this level so consist of all eight range gates). The six receiver channels are nested together for each frequency. To obtain the in-phase and quadrature channels of the third receiver (A/D channels five and six) at the second frequency and the fourth range gate, block numbers 102 and 103 would have to be read ($102 = 1$ header block $+ (4^{th} - 1)$ range number $\times 30 + (2^{nd} - 1)$ frequency $\times 6 + 5^{th}$ A/D channel). The first word of each block contains a code (frequency number $\times 1000+$ range number $\times 10+$ channel number) and 255 samples (the 256^{th} sample is discarded) for that channel.

location	description
1 - 10	title string (ASCII)
11	year $\times$ 100 + month (9010 = Oct 90)
12	day of month
13	hour of day
14	minute of hour
15	second of minute
16	tick counter time
17	number of raw samples (256)
18	number multiple A/D channels (6)
19	first multiple A/D channel number (1)
20	ticks between samples (240)
21	ticks between frequency steps (20)
22	transmitter ground pulse range (7 km)
23	transmitter ground pulse amplitude (5 V)
25	number of DMA A/D range gates (0)
26	data code
28	sampling run number
30	number of frequency steps (5)
31 - (30 + 5)	oscillator frequencies (9600 kHz)
(31 + 5)	number range gates saved (13)
(32 + 5) – (31 + 5 + 13)	range gate numbers
200	translation date
201	translation time
202	number samples retained (255)

Table B.1: **Contents of the header block** of the sorted data files. Note that the format is binary, each location being a two byte word so there are 256 words in each block. The numbers in brackets are typical values for the Birdlings Flat data. Other numbers in the header block are mainly radar control codes or computer memory location codes.

date (1988)	time	file title	size	altitude (km)
14 Dec	11:40	bnkm06	257	90,92,94,97,100,102,104
"	11:43	bnkm11	"	"
"	11:46	bnkm17	"	"
"	11:49	bnkm21	"	"
"	11:52	bnkm25	"	"
"	11:55	bnkm29	"	"
14 Dec	23:02	bnlj08	257	88,92,94,97,100,102,104
"	23:05	bnlj12	"	"
"	23:08	bnlj18	"	"
"	23:11	bnlj22	"	"
"	23:14	bnlj30	"	"
15 Dec	10:20	bnll10	257	92,96,98,99,100,102,104
"	10:23	bnll14	"	"
"	10:26	bnll20	"	"
"	10:29	bnll24	"	"
"	10:32	bnll28	"	"
"	10:35	bnll33	"	"
"	10:38	bnll44	"	"
"	10:41	bnll50	"	"
"	10:44	bnll58	"	"
"	10:47	bnlm03	"	"
"	10:50	bnll05	"	"
15 Dec	12:23	bnlm58	257	92,96,98,99,100,102,104
"	12:26	bnln02	"	"
"	12:29	bnln08	"	"
"	12:32	bnln30	"	"
"	12:35	bnln34	"	"
"	12:38	bnlm53	"	"
16 Dec	9:40	bnmk28	257	90,92,96,98,100,102,104
"	9:43	bnmk32	"	"
"	9:46	bnmk38	"	"
"	9:49	bnmk43	"	"
"	9:52	bnmk47	"	"
"	9:55	bnmk17	"	"
16 Dec	11:28	bnna19	257	92,94,96,98,100,102,104
"	11:31	bnna23	"	"
"	11:34	bnna29	"	"
"	11:37	bnna32	"	"
"	11:40	bnna36	"	"
"	11:43	bnna42	"	"
"	11:46	bnna47	"	"
"	11:49	bnna51	"	"
"	11:52	bnna56	"	"

date (1988)	time	file title	size	altitude (km)
16 Dec	12:27	bnmn14	257	92,94,96,98,100,102,104
"	12:30	bnmn20	"	"
"	12:33	bnmn24	"	"
16 Dec	12:42	bnmn07	257	92,94,96,98,100,102,104
"	12:45	bnmn03	"	"
"	12:48	bnmn00	"	"
16 Dec	14:08	bnmx05	257	89,90,92,94,95,100,102
"	14:11	bnmx09	"	"
"	14:14	bnmx25	"	"
"	14:17	bnmx30	"	"
"	14:20	bnmx34	"	"
17 Dec	9:21	bnnj56	257	92,94,96,98,100,102,106
"	9:27	bnnj59	"	"
"	9:30	bil224	769	82 - 106
"	9:33	bil225	"	"
"	9:36	bil226	"	"
"	9:39	bil227	"	"
"	9:42	bil228	"	"
"	9:45	bnnj53	257	92,94,96,98,100,102,106
17 Dec	10:14	bnnk47	257	92,94,96,98,100,102,106
"	10:17	bnnk50	"	"
"	10:20	bnnk56	"	"
"	10:23	bnnl00	"	"
"	10:26	bnnl08	"	"
"	10:29	bnnl18	"	"
"	10:32	bnnl22	"	"
"	10:35	bil223	769	82 - 106
"	10:38	bnnk44	257	92,94,96,98,100,102,106
17 Dec	11:33	bil221	769	82 - 106
"	11:36	bil222	"	"
"	11:39	bil229	"	"
"	11:42	bil230	"	"
"	11:45	bil233	"	"
"	11:48	bil234	"	"
"	11:51	bil235	"	"
"	11:54	bilb15	"	"
"	11:57	bilb16	"	"
"	12:00	bilb17	"	"
"	12:03	bnnm22	257	94,96,98,100,102,104,107
"	12:06	bnnm18	"	"
"	12:09	bnnm15	"	"

Table B.2: **The Scott Base data sets**, dates, times and altitudes observed by the interferometry experiment. The data sets were usually named after the first file (for example the last set, Dec 17 11:33-12:09, was titled `BIL221`) and the sorted files in the sets have the extension `.BBS` (for example the last file is `BNNM15.BBS`).

date	time	num. samples	num. range bins	altitudes (km)
D204				
23 Jul 90	16:02 - 16:44	20	13	84 - 109
D209				
28 Jul 90	13:18 - 15:24	64	13	83 - 107
D23				
18 Aug 90	15:29 - 20:47	160	13	83 - 107
DJY				
16 Sep 90	12:18 - 17:16	150	13	78 - 102
DKS clear semiduirnal tide				
6 Oct 90	10:05 - 15:03	150	13	79 - 103
DND highest FCA acceptance rate				
8 Dec 90	10:04 - 15:15	155	13	79 - 103
DNO coherent & incoherent receivers, no freq. stepping				
19 Dec 90	12:51 - 15:09	70	11	80 - 100
EAP coherent & incoherent receivers, partial solar eclipse				
16 Jan 91	10:22 - 14:40	130	11	80 - 100
ECO severe interference				
8 Mar 91	3:08 - 5:28	70	13	80 - 103

Table B.3: **The Birdlings Flat data sets**, dates, times and altitudes observed by the interferometry experiment. The file titles are indicated by the bold faced letters, for example the 6 October 1990 data consists of 150 sorted files, `DKS000.BBS` - `DKS149.BBS`. The 23 & 28 July 1990 data files are numbered from 1 rather than 0.

Appendix C

Additional Results, Scott Base

This appendix displays further selected results to those presented in chapter 7 for data collected by the interferometry experiment on the MF radar at Scott Base / Arrival Heights on Ross Island in the Antarctic.

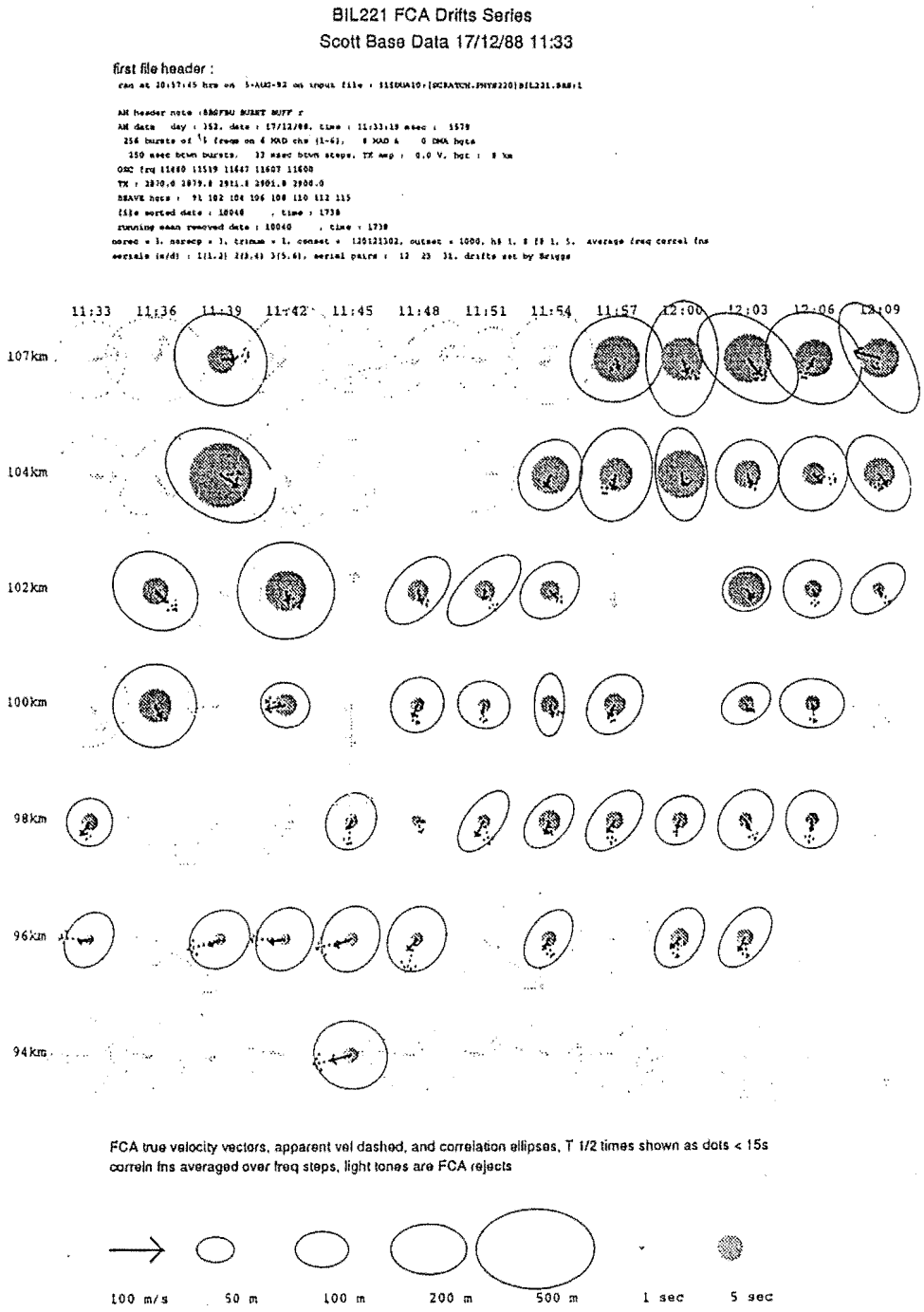

Figure C.1: **FCA results summary BIL221** data set, collected at Scott Base on December 17, 1988. (As for figure 7.11, section 7.5.)

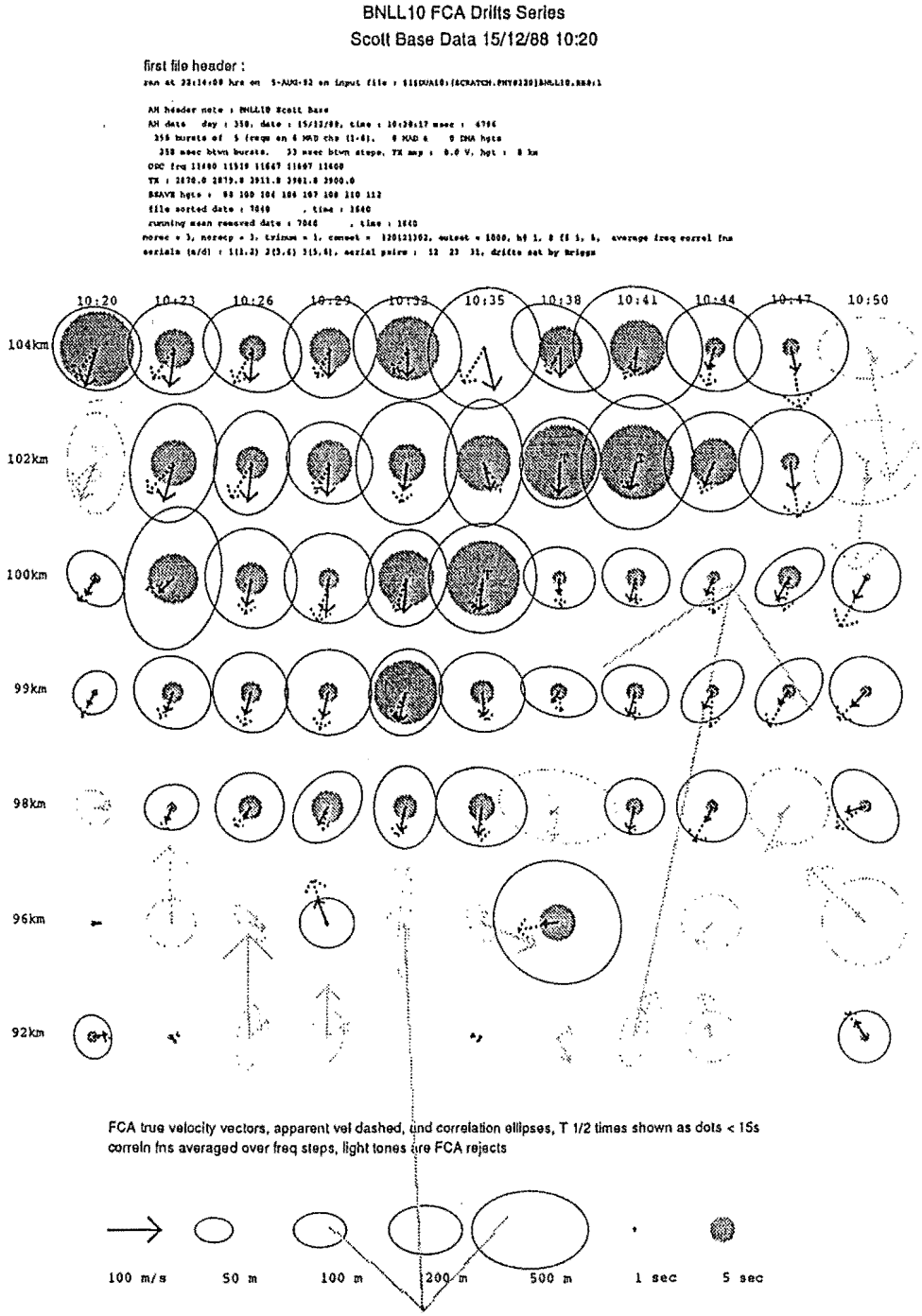

Figure C.2: **FCA results summary BNLL10** data set, collected at Scott Base on December 15, 1988.

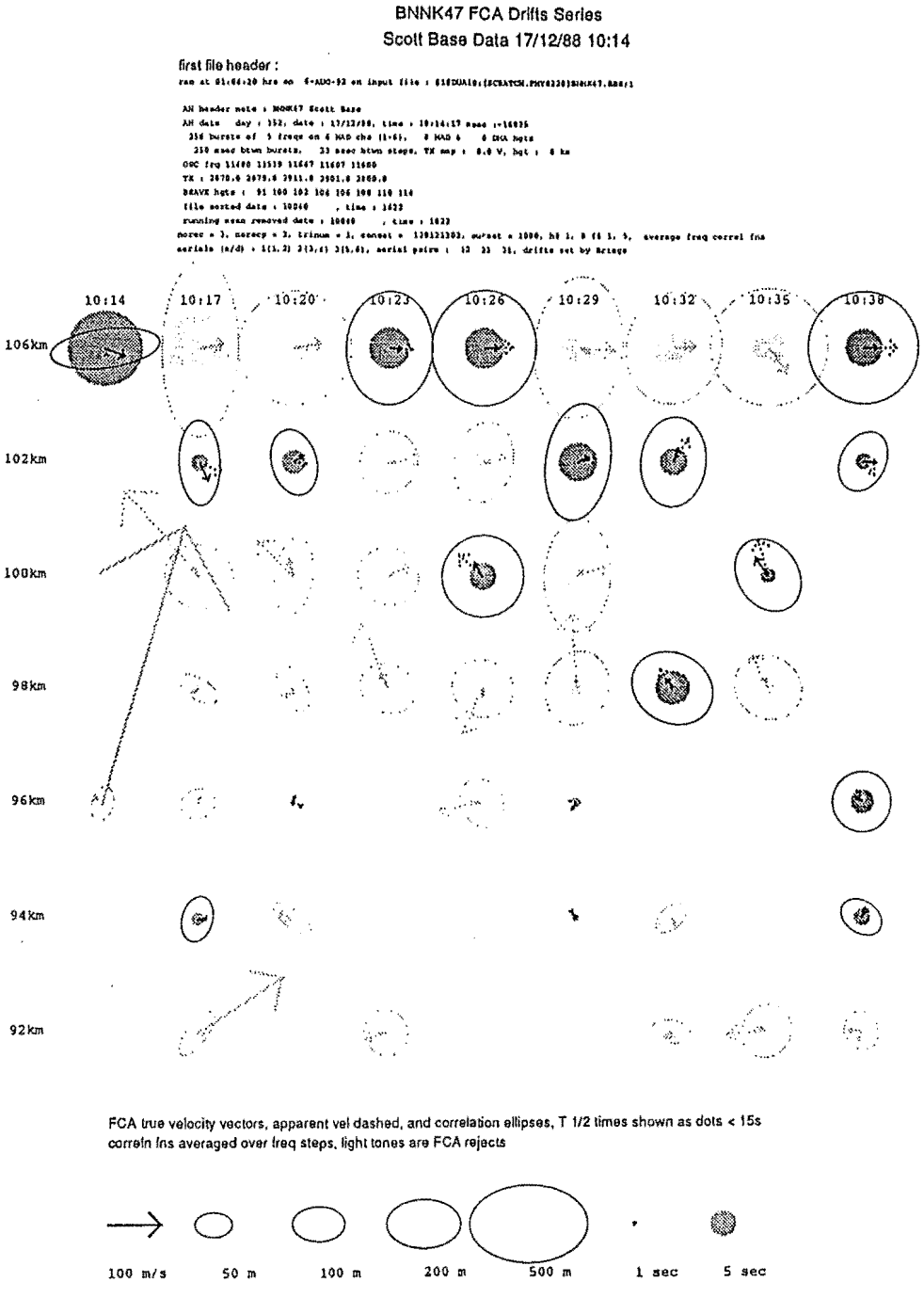

Figure C.3: **FCA results summary BNNK47** data set, collected at Scott Base on December 17, 1988.

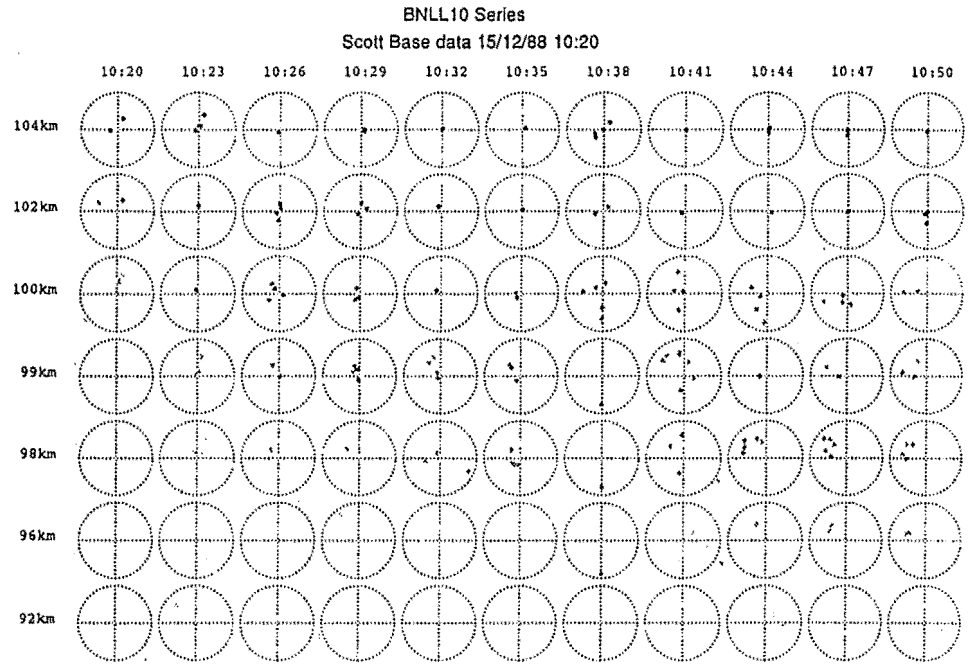

Figure C.4: **Spatial interferometry of scattering centres**, BNLL10 data, collected at Scott Base on 15 December 1988. (As for figure 7.26, section 7.7.3.)

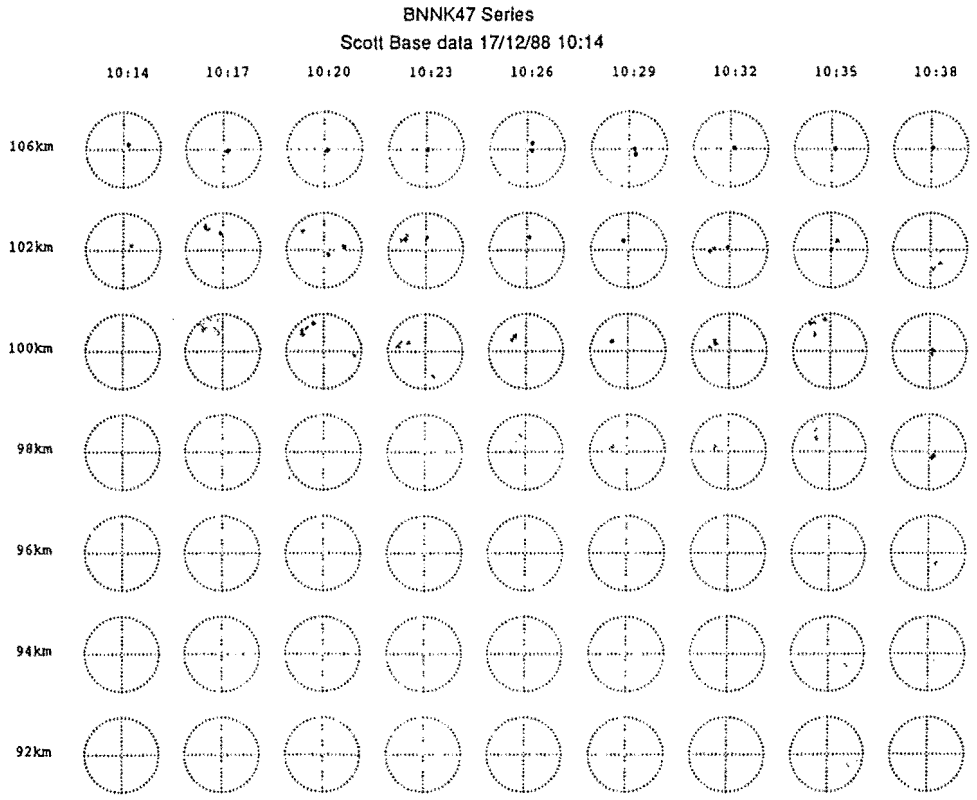

Figure C.5: **Spatial interferometry of scattering centres**, BNNK47 data, collected at Scott Base on 17 December 1988.

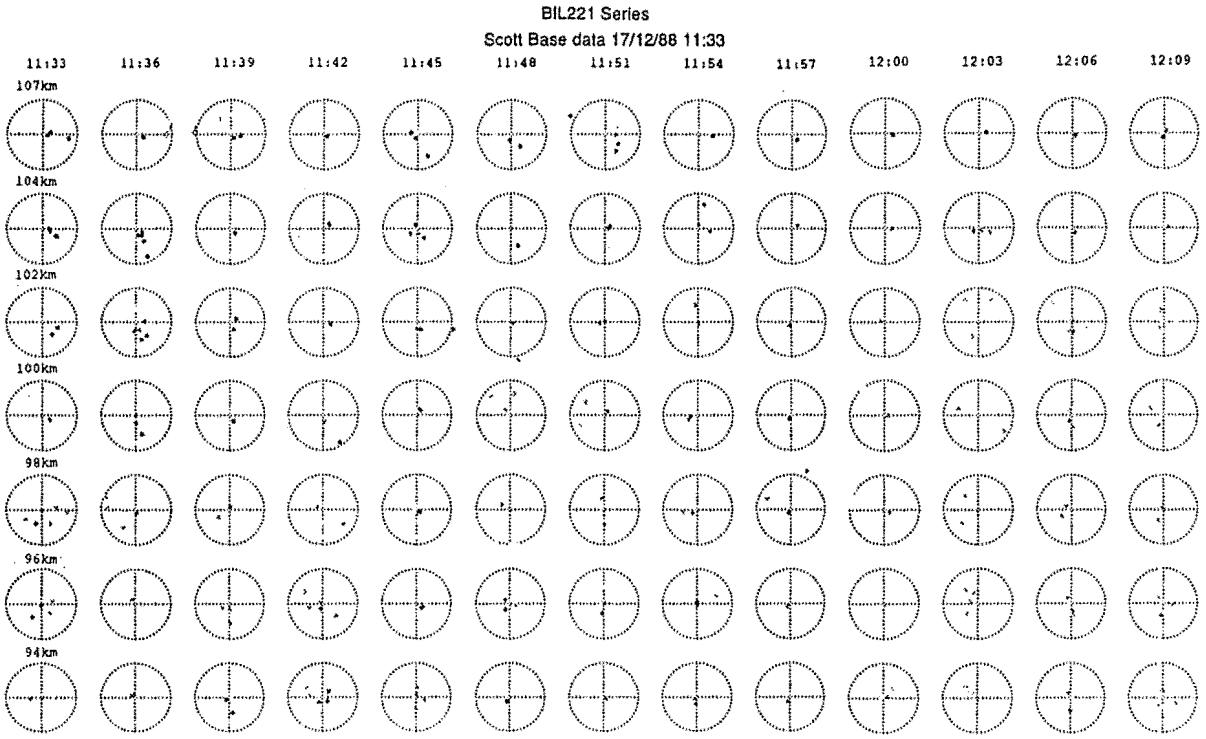

Figure C.6: **Spatial interferometry of scattering centres**, BIL221 data, collected at Scott Base on 17 December 1988.

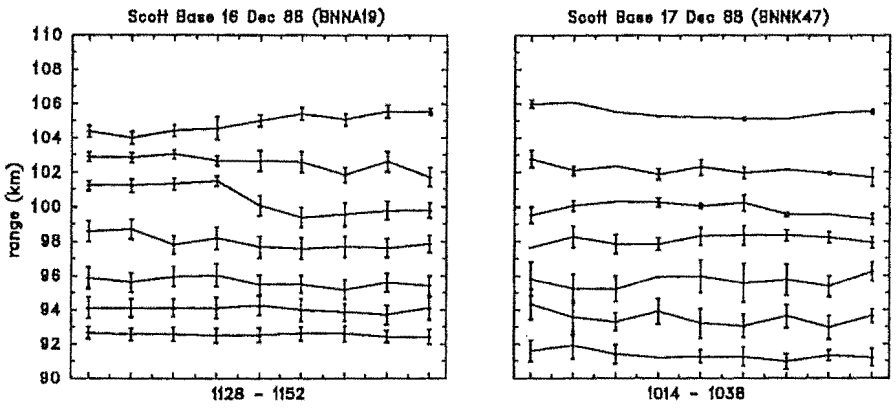

Figure C.7: **FDI range and scattering depth, BNNA19 and BNNK47** data sets (11:28-11:52 on 16 Dec, and 10:14-10:38 on 17 Dec, 1988). The scattering depth is the full length of the error bars.

Appendix D

Additional Results, Birdlings Flat

This appendix displays further selected results to those presented in chapter 7 for data collected by the interferometry experiment on the MF radar at Birdlings Flat near Christchurch.

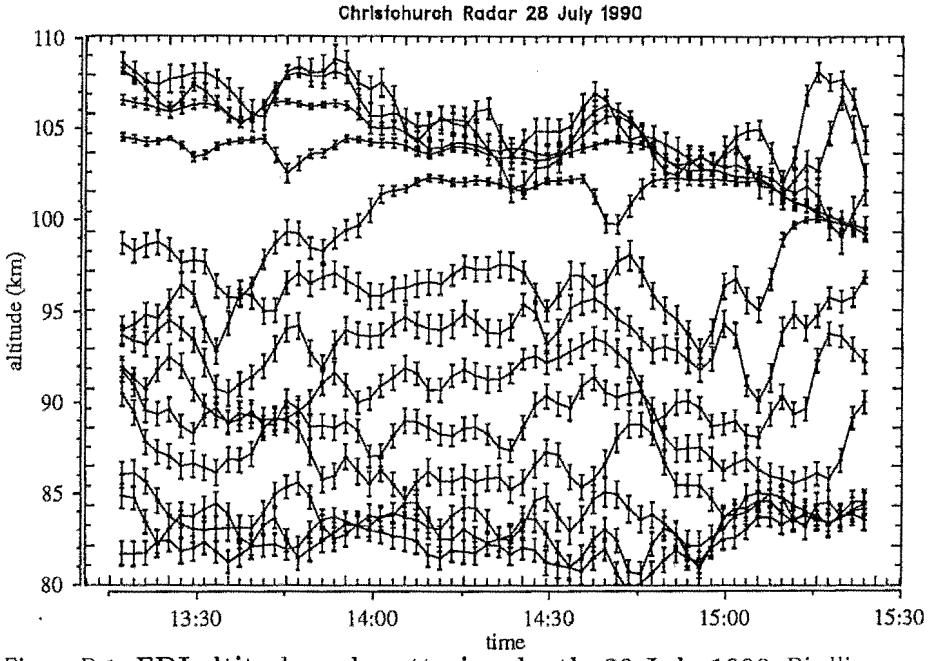

Figure D.1: **FDI altitude and scattering depth, 28 July 1990**, Birdlings Flat. The altitude is determined from the FDI range and the spatial interferometry zenith angle. The scattering depth is the full length of the error bars.

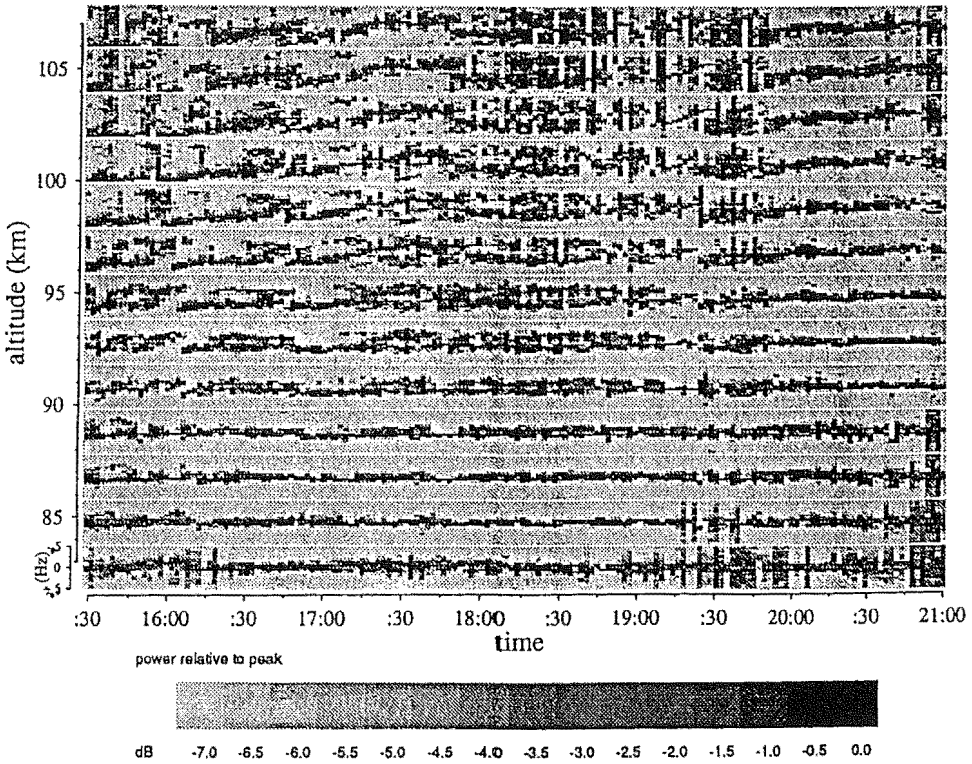

Figure D.2: **Sample FFT spectra on 18 August 1990.** As for figure 7.10, section 7.4.

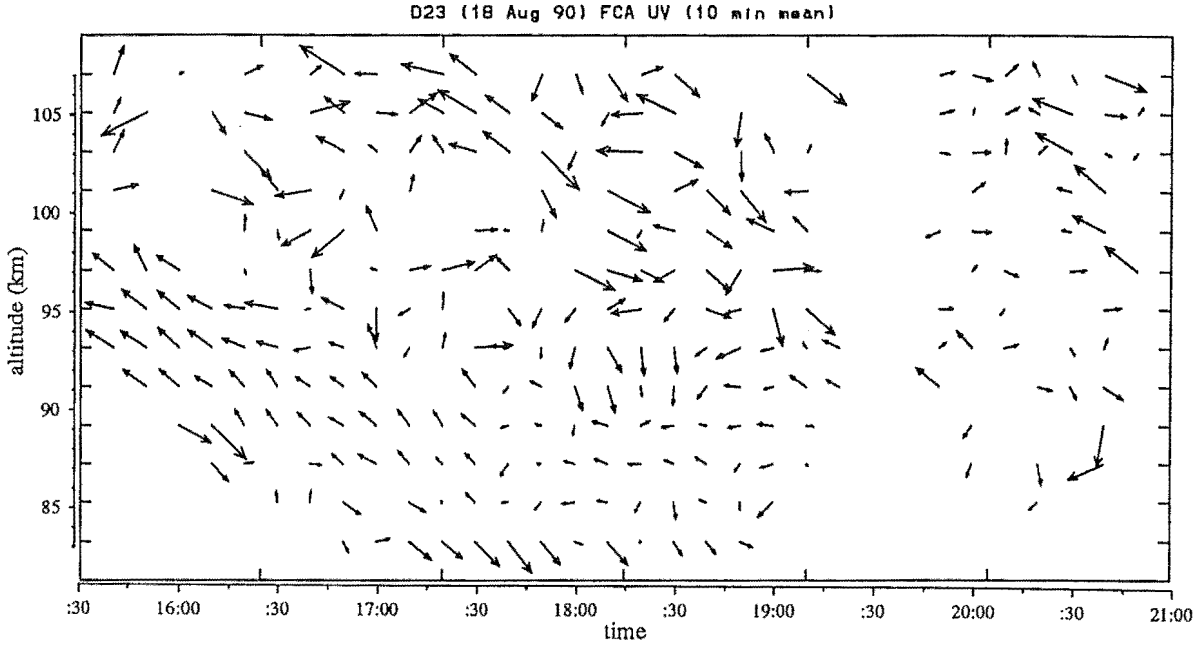

Figure D.3: **FCA true velocity, 18 August 1990,** 10 minute means. Largest vectors correspond to 100 ms^{-1}.

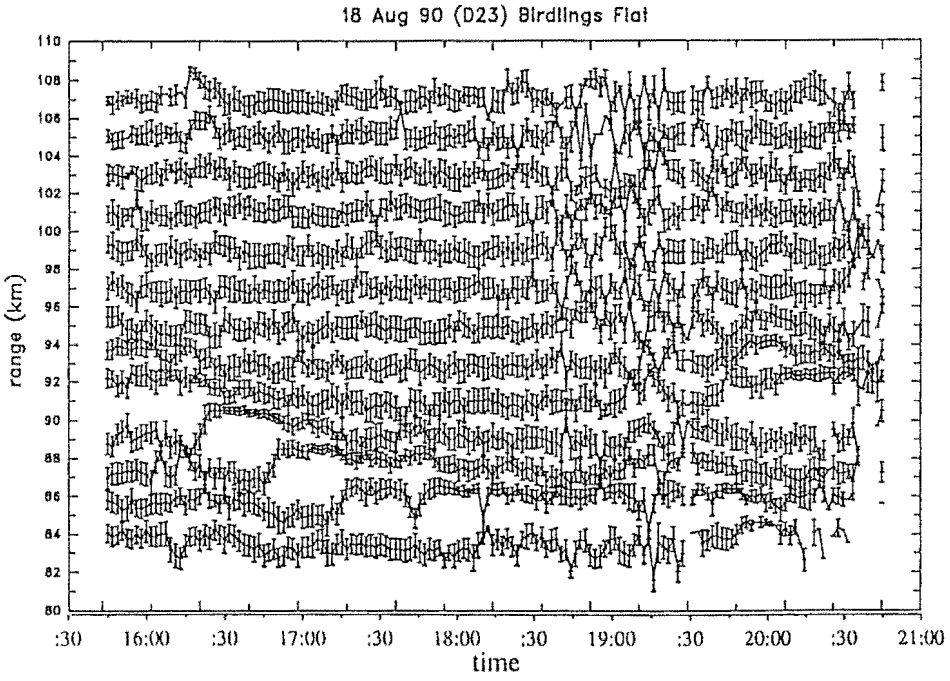

Figure D.4: **FDI range and scattering depth, 18 August 1990,** Birdlings Flat. The scattering depth is the full length of the error bars.

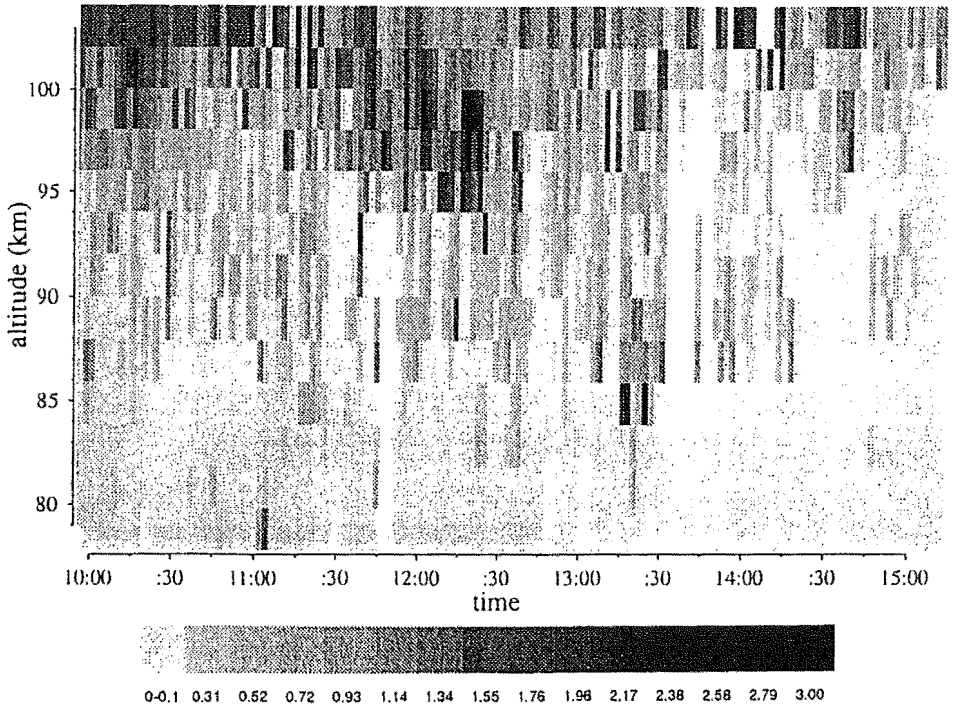

Figure D.5: **Rice parameters for 6 October 1990** at Birdlings Flat, determined using the method of [Hocking, 1987b].

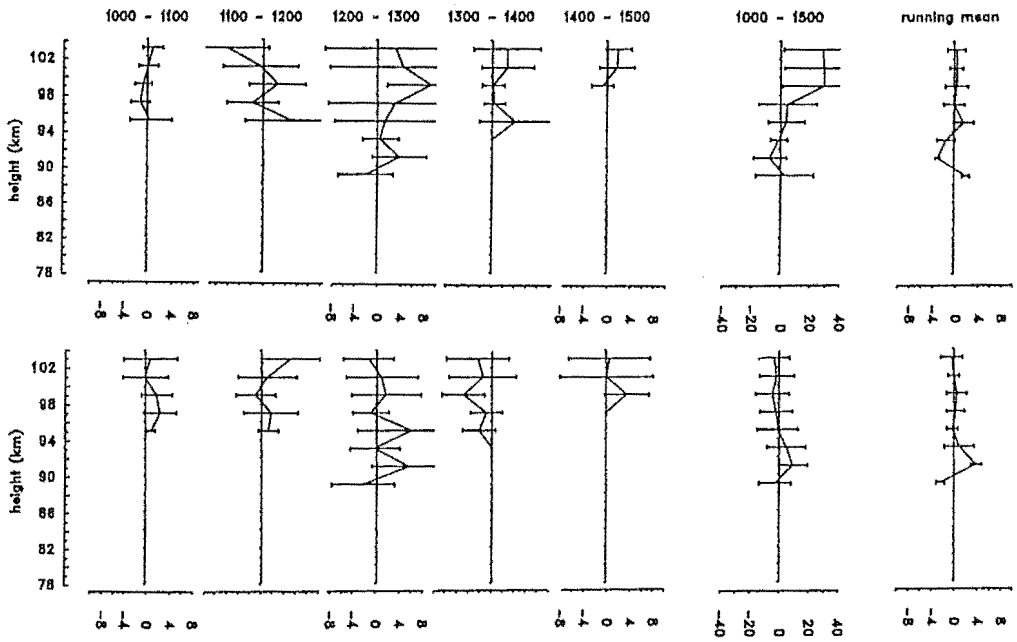

Figure D.6: **Momentum flux measurements** at Birdlings Flat on 6 October 1990, as found using three averaging periods. In the upper panel are profiles of the upward flux of zonal momentum $\overline{u'w'}$ and in the lower panel are profiles of the upward flux of meridional momentum $\overline{v'w'}$. The periods over which the fluxes were found are indicated above the $\overline{u'w'}$ profiles, the running mean being a one hour running mean over the five hour data set. The units are m^2s^{-2} and the error bars indicate standard deviations. As discussed in section 7.12.1, the vertical velocities used in this example are possibly erroneous.

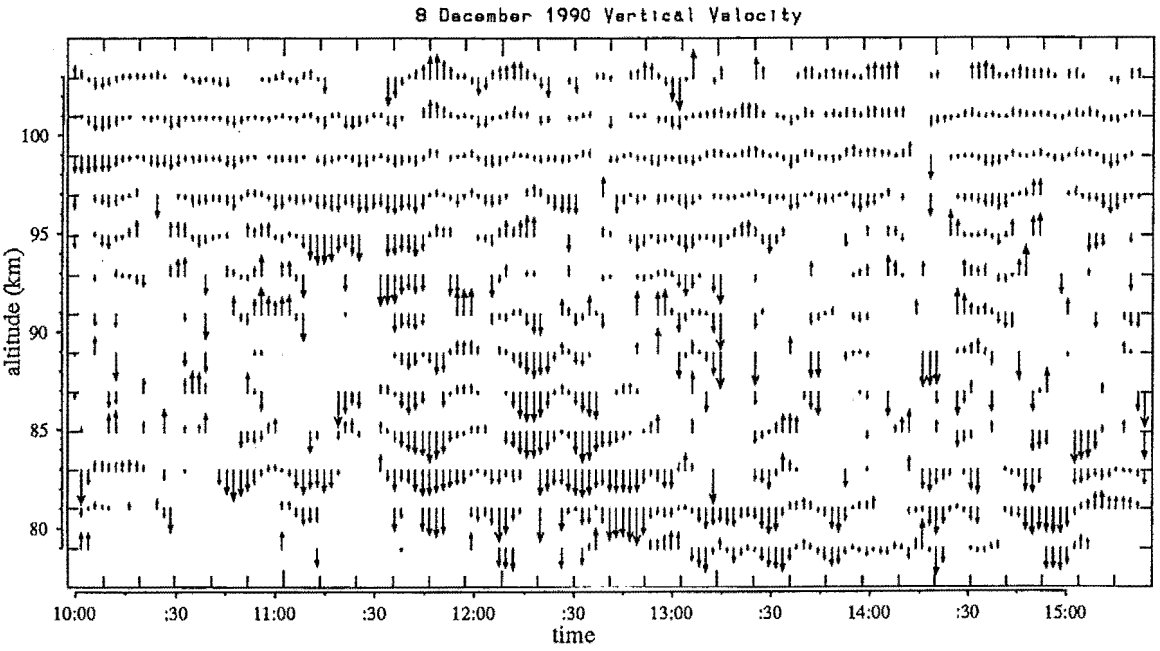

Figure D.7: **Vertical velocities, 8 December 1990** at Birdlings Flat (maximum vectors correspond to 4 ms^{-1}, quarter-half-quarter filtered).

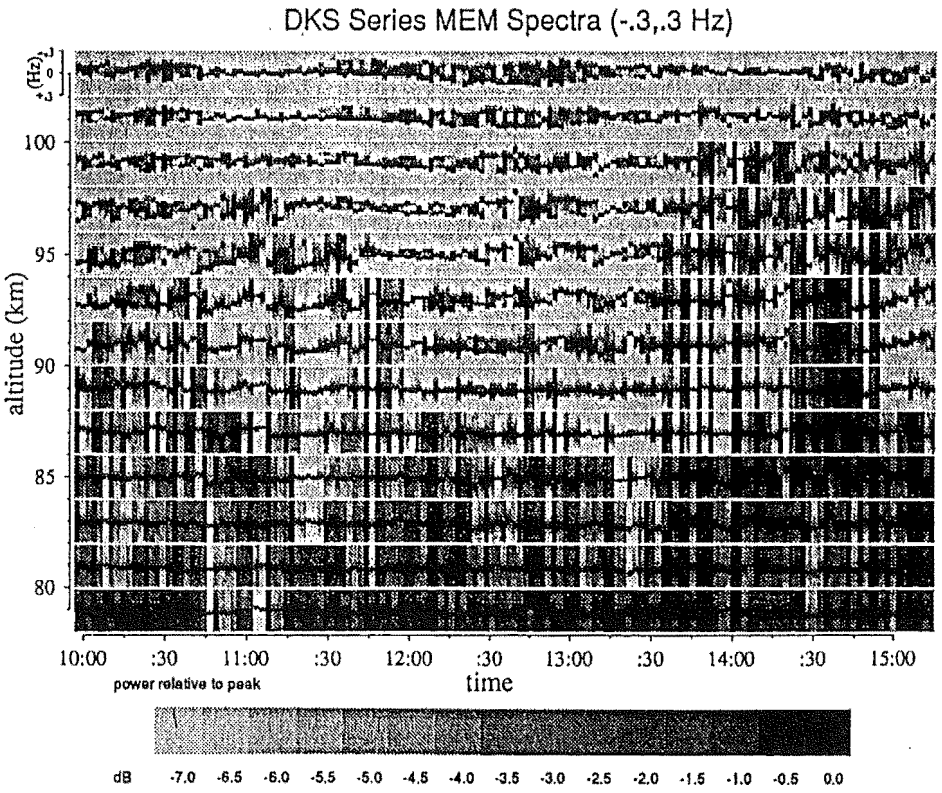

Figure D.8: **Sample MEM spectra on 6 October 1990.** Filter length 5.

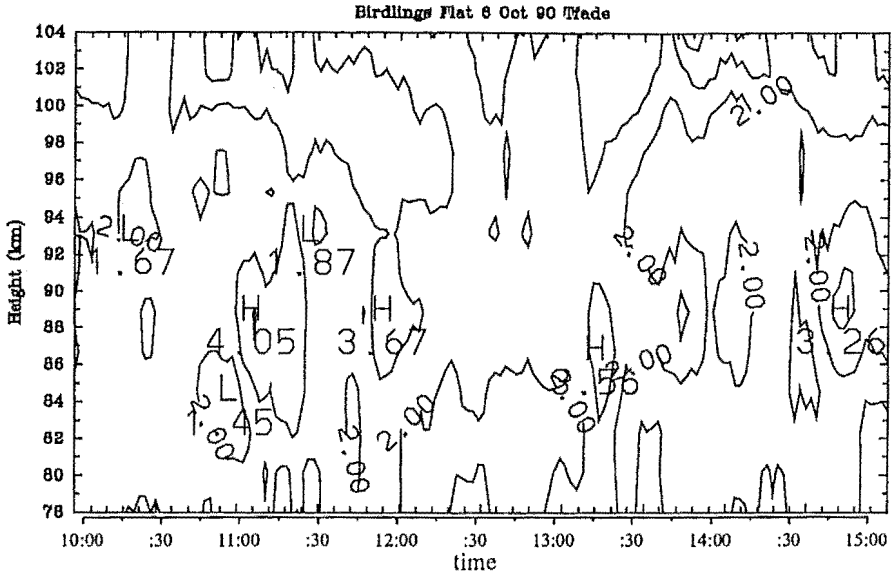

Figure D.9: **Fading time 6 October 1990**, 10 minute running mean, contour interval is one second.

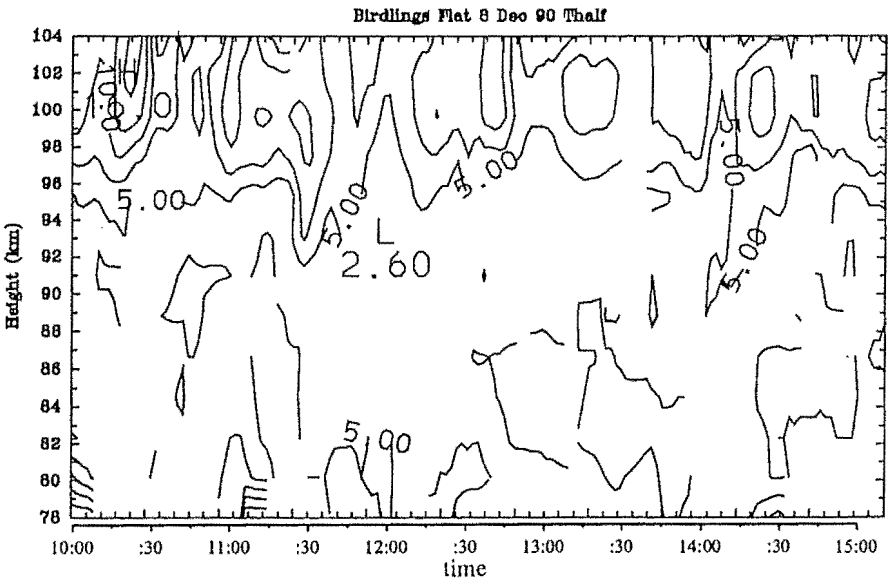

Figure D.10: **FCA $T_{\frac{1}{2}}$, 8 December 1990**, 10 minute running mean, contour interval is 2.5 seconds.

References

[Abbott, 1980] Abbott, R. H. (1980). The role of ALGOL 60 in computer education. *Computer Education*, (number 35):24–25.

[Ables, 1978] Ables, J. G. (1978). Maximum entropy spectral analysis. In [Childers, 1978], editor, *Modern Spectrum Analysis*, pages 23–33. IEEE press. (Reprinted from Astron. Astrophys. Suppl. Series, 15, 383-393, 1974).

[Adams et al., 1989] Adams, G. W., Brosnahan, J. W., and Johnson, R. E. (1989). Aspect sensitivity of 2.66-MHz radar returns from the mesosphere. *Radio Science*, 24:127–132.

[Adams et al., 1986] Adams, G. W., Brosnahan, J. W., Walden, D. C., and Nerney, S. F. (1986). Mesospheric observations using a 2.66-MHz radar as an imaging Doppler interferometer : Description and first results. *Journal of Geophysical Research*, 91A:1671–1683.

[Adams et al., 1985] Adams, G. W., Edwards, D. P., and Brosnahan, J. W. (1985). The imaging Doppler interferometer: Data analysis. *Radio Science*, 20:1481–1492.

[Andrews et al., 1987] Andrews, D. G., Holton, J. R., and Leovy, C. B. (1987). *Middle Atmosphere Dynamics*, volume 40 of *International Geophysics Series*. Academic Press, Orlando, Fl. 489p.

[Appleton, 1928] Appleton, E. V. (1928). Some notes on wireless methods of investigating the electrical structure of the upper atmosphere. I. *Proceedings of the Physical Society, London*, 41:43–59.

[Appleton and Barnett, 1925] Appleton, E. V. and Barnett, M. A. F. (1925). On some direct evidence for downward atmospheric reflection of electric rays. *Proceedings of the Royal Society, London*, A109:621–641.

[Atlas, 1990] Atlas, D., editor (1990). *Radar in Meteorology.* American Meteorological Society, Boston, Mass. (Battan Memorial and 40th Anniversary Radar Meteorology Conference, 1987.) 806p.

[Austin et al., 1969] Austin, G. L., Bennett, R. G. T., and Thorpe, M. R. (1969). The phase of waves partially reflected from the lower ionosphere. *Journal of Atmospheric and Terrestrial Physics*, 31:1099–1106.

[Austin and Manson, 1969] Austin, G. L. and Manson, A. H. (1969). On the nature of the irregularities that produce partial reflections of radio waves from the lower ionosphere (70-100km). *Radio Science*, 4:35–40.

[Awe, 1964] Awe, O. (1964). Errors in correlation between time series. *Journal of Atmospheric and Terrestrial Physics*, 26:1239–1255.

[Balsley and Riddle, 1984] Balsley, B. B. and Riddle, A. C. (1984). Monthly mean values of the mesospheric wind field over Poker Flat, Alaska. *Journal of the Atmospheric Sciences*, 41:2368–2375.

[Bendat and Piersol, 1986] Bendat, J. S. and Piersol, A. G. (1986). *Random Data: Analysis and Measurement Procedures.* Wiley, New York, second edition. 566p.

[Blackman and Tukey, 1958] Blackman, R. B. and Tukey, J. W. (1958). *The measurement of power spectra from the point of view of communications engineering.* Dover, New York. 190p.

[Blix, 1988] Blix, T. A. (1988). In situ studies of turbulence in the middle atmosphere by means of electrostatic ion probes. Technical report, Norwegian Defence Research Establishment, PO Box 25 - N-2007 Kjeller, Norway. Technical Report NDRE/PUBL-88/1002.

[Bloomfield, 1976] Bloomfield, P. (1976). *Fourier analysis of time series : An introduction.* Wiley, New York. 258p.

[Bolgiano, 1968] Bolgiano, Jr., R. (1968). The general theory of turbulence - turbulence in the atmosphere. In Rawer, K., editor, *Winds and turbulence in the stratosphere, mesosphere and ionosphere*, pages 371–400. North-Holland, Amsterdam. (NATO Advanced Study Institute, Lindau, Germany, 1966.) 421p.

[Bramley, 1951] Bramley, E. N. (1951). Diversity effects in spaced-aerial reception of ionospheric waves. *Proceedings of the IEEE*, 98(III)(51):19–25.

[Bremer and Singer, 1973] Bremer, J. and Singer, W. (1973). Mean D region electron density profiles derived by combination of rocket and radio wave propagation data. In Rawer, K., editor, *Methods of measurements and results of lower ionosphere structure*, pages 61–73. (COSPAR symposium.) 459p.

[Briggs, 1951] Briggs, B. H. (1951). An investigation of certain properties of the ionosphere by means of a rapid frequency-change experiment. *Proceedings of the Physical Society, London*, 64B:255–274.

[Briggs, 1968] Briggs, B. H. (1968). On the analysis of moving patterns in geophysics - I. Correlation analysis. *Journal of Atmospheric and Terrestrial Physics*, 30:1777–1788.

[Briggs, 1980] Briggs, B. H. (1980). Radar observations of atmospheric winds, and turbulence: A comparison of techniques. *Journal of Atmospheric and Terrestrial Physics*, 42:823–833.

[Briggs, 1984] Briggs, B. H. (1984). The analysis of spaced sensor records by correlation techniques. *Handbook for MAP*, 13:166–186. SCOSTEP.

[Briggs, 1992] Briggs, B. H. (1992). Radar measurements of aspect sensitivity of atmospheric scatterers using spaced-antenna correlation techniques. *Journal of Atmospheric and Terrestrial Physics*, 54(2):153–165.

[Briggs et al., 1969] Briggs, B. H., Elford, W. G., Felgate, D. G., Golley, M. G., Rossiter, D. E., and Smith, J. W. (1969). Buckland Park aerial array. *Nature*, 223:1321–1325.

[Briggs and Phillips, 1950] Briggs, B. H. and Phillips, G. J. (1950). A study of the horizontal irregularities of the ionosphere. *Proceedings of the Physical Society, London*, B63:907–923.

[Briggs et al., 1950] Briggs, B. H., Phillips, G. J., and Shinn, D. H. (1950). The analysis of observations on spaced receivers of the fading of radio signals. *Proceedings of the Physical Society, London*, B63:106–121.

[Briggs and Spencer, 1954] Briggs, B. H. and Spencer, M. (1954). Horizontal movements in the ionosphere. *Reports on Progress in Physics*, 17:245–280.

[Briggs and Vincent, 1973] Briggs, B. H. and Vincent, R. A. (1973). Some theoretical considerations on remote probing of weakly scattering irregularities. *Australian Journal of Physics*, 26:805–814.

[Briggs and Vincent, 1992] Briggs, B. H. and Vincent, R. A. (1992). Spaced-antenna analysis in the frequency domain. *Radio Science*, 27(2):117–129.

[Brigham, 1974] Brigham, E. O. (1974). *The fast Fourier transform.* Prentice-Hall, Englewood Cliffs, N.J. 252p.

[Brooks and Carruthers, 1953] Brooks, C. E. P. and Carruthers, N. (1953). *Handbook of statistical methods in meteorology.* Her Majesty's Stationery Office, London. (Meteorological Office of the Air Ministry). 412p.

[Brosnahan and Adams, 1990] Brosnahan, J. W. and Adams, G. W. (1990). The MAP-STAR Imaging Doppler Interferometer (IDI) radar: description and first results. *Journal of Geophysical Research.* (Submitted).

[Brown and Chapman, 1972] Brown, G. M. and Chapman, J. W. (1972). Full correlation ionospheric drift analysis for a general observing triangle. *Annales de Géophysique*, 28:349–356.

[Brown, 1986] Brown, W. O. J. (1986). MF radar measurement of mesospheric vertical winds. Master's thesis, Department of Physics, University of Canterbury. 85p.

[Brown, 1989] Brown, W. O. J. (1989). Antarctic middle/upper atmosphere HF radar programme (K055). *New Zealand Antarctic Record*, 9(3):30.

[Brown and Fraser, 1991] Brown, W. O. J. and Fraser, G. J. (1991). Radar interferometry on MF SA radar. In *Proceedings of the fifth workshop on technical and scientific aspects of MST radar*, pages 248–253. [Edwards, 1991].

[Budden, 1965] Budden, K. G. (1965). The theory of the correlation of amplitude fluctuations of radio signals at two frequencies, simultaneously scattered by the ionosphere. *Journal of Atmospheric and Terrestrial Physics*, 27:883–897.

[Budden, 1985] Budden, K. G. (1985). *The propagation of radio waves : The theory of radio waves of low power in the ionosphere and magnetosphere.* Cambridge University Press. 669p.

[Burg, 1978a] Burg, J. P. (1978a). Maximum entropy spectral analysis. In [Childers, 1978], editor, *Modern Spectrum Analysis*, pages 34–41. IEEE press. (Reprinted from Proceedings of the 37th Meeting of the Society of Exploration Geophysicists, 1967).

[Burg, 1978b] Burg, J. P. (1978b). A new analysis technique for time series data. In [Childers, 1978], editor, *Modern Spectrum Analysis*, pages 42–48. IEEE press. (Presented at the NATO Advanced Study Institute on Signal Processing with Emphasis on Underwater Acoustics, Aug.12-23, 1968.).

[Carter and Balsley, 1982] Carter, D. A. and Balsley, B. B. (1982). The summer wind field between 80 and 93 km observed by the MST radar at Poker Flat, Alaska, (65°N). *Journal of the Atmospheric Sciences*, 39:2905–2915.

[Chatfield, 1984] Chatfield, C. (1984). *The analysis of time series : an introduction.* Chapman and Hall, London, third edition. 286p.

[Childers, 1978] Childers, D. G., editor (1978). *Modern Spectrum Analysis.* IEEE Press. (A collection of 39 papers on MEM and MLM spectral analysis.) 334p.

[CIRA, 86] CIRA (86). COSPAR International Reference Atmosphere: 1986, Part II: Middle Atmosphere Models. *Advances in Space Research*, 10(12). COSPAR, (1990), edited by D. Rees, J. J. Barnett and K. Labitzke. 517p.

[Clemesha, 1963] Clemesha, B. R. (1963). The elongation of irregularities in the equatorial ionosphere. *Journal of Geophysical Research*, 68(9):2363–2366.

[Cummack and Cooper, 1986] Cummack, C. H. and Cooper, J. (1986). The classification of distorted-mirror reflections and its ionospheric modification due to the underlying ionization. *Journal of Atmospheric and Terrestrial Physics*, 48:51–59.

[Czechowsky et al., 1988] Czechowsky, P., Reid, I. M., and Rüster, R. (1988). VHF radar measurements of the aspect sensitivity of the summer polar mesopause echoes over Andenes (69°N,16°E), Norway. *Geophysical Research Letters*, 15(11):1259–1262.

[Davies, 1966] Davies, K. (1966). *Ionospheric radio propagation.* Dover, New York. 470p.

[Davies, 1990] Davies, K. (1990). *Ionospheric radio*, volume 31 of *IEE Electomagnetic Wave Series.* Peregrinus, London. 580p.

[Doviak and Zrnic, 1984] Doviak, R. J. and Zrnic, D. S. (1984). Reflection and scatter formula for anisotropically turbulent air. *Radio Science*, 19:325–336.

[Edwards, 1991] Edwards, B., editor (1991). *Proceedings of the fifth workshop on technical and scientific aspects of MST radar*, SCOSTEP Secretariat, University of Illinois. (Solar-Terrestrial Energy Program). Held at Department of Physics, The University College of Wales, Aberystwyth, U.K., August 1991.

[Farley et al., 1981] Farley, D. T., Ierkic, H. M., and Fejer, B. G. (1981). Radar interferometry: A new technique for studying plasma turbulence in the ionosphere. *Journal of Geophysical Research*, 86A:1467–1472.

[Flock and Balsley, 1967] Flock, W. L. and Balsley, B. B. (1967). VHF radar returns from the D region of the equatorial ionosphere. *Journal of Geophysical Research*, 72:5537–5541.

[Forbes, 1990] Forbes, J. M. (1990). Atmospheric tides between 80 km and 120 km. *Advances in Space Research*, 10(12):127–140. COSPAR.

[Franke et al., 1990] Franke, P. M., Thorsen, D., Champion, M., Franke, S. J., and Kudeki, E. (1990). Comparison of time- and frequency-domain techniques for wind velocity estimation using multiple-receiver MF radar data. *Geophysical Research Letters*, 17:2193–2196.

[Franke, 1990] Franke, S. J. (1990). Pulse compression and frequency domain interferometry with a frequency-hopped MST radar. *Radio Science*, 25:565–574.

[Fraser, 1965] Fraser, G. J. (1965). The measurement of atmospheric winds at altitudes of 64-120km using ground based radio equipment. *Journal of the Atmospheric Sciences*, 22:217–218.

[Fraser, 1984a] Fraser, G. J. (1984a). Partial reflection spaced antenna wind measurements. *Handbook for MAP*, 13:233–247. SCOSTEP.

[Fraser, 1984b] Fraser, G. J. (1984b). Summer circulation in the Antarctic middle atmosphere. *Journal of Atmospheric and Terrestrial Physics*, 46:143–146.

[Fraser, 1989] Fraser, G. J. (1989). Monthly mean winds in the mesosphere at 44S and 78S. *Pure and Applied Geophysics*, 130:291–301. In [Plumb and Vincent, 1989].

[Fraser and Khan, 1990] Fraser, G. J. and Khan, U. (1990). Semi-diurnal variations in the time scale of irregularities near the Antarctic summer mesopause. *Radio Science*, 25:997–1003.

[Fraser and Kochanski, 1970] Fraser, G. J. and Kochanski, A. (1970). Ionospheric drifts from 64-108 km altitudes at Birdlings Flat. *Annales de Géophysique*, 26:675–687.

[Fraser and Vincent, 1970] Fraser, G. J. and Vincent, R. A. (1970). A study of D-region irregularities. *Journal of Atmospheric and Terrestrial Physics*, 32:1591–1607.

[Fraser et al., 1989] Fraser, G. J., Vincent, R. A., Manson, A. H., Meek, C. E., and Clark, R. R. (1989). Inter-annual variability of tides in the mesosphere and lower thermosphere. *Journal of Atmospheric and Terrestrial Physics*, 51:555–567.

[Fritts, 1984] Fritts, D. C. (1984). Gravity wave saturation in the middle atmosphere : A review of theory and observations. *Reviews of Geophysics and Space Physics*, 22:275–308.

[Fritts, 1989] Fritts, D. C. (1989). A reveiw of gravity wave saturation processes, effects, and variability in the middle atmosphere. *Pure and Applied Geophysics*, 130:343–371. (In [Plumb and Vincent, 1989]).

[Fritts and Rastogi, 1985] Fritts, D. C. and Rastogi, P. K. (1985). Convective and dynamical instabilities due to gravity wave motions in the lower and middle atmosphere: Theory and observations. *Radio Science*, 20:1247–1277.

[Fritts and Vincent, 1987] Fritts, D. C. and Vincent, R. A. (1987). Mesospheric momentum flux studies at Adelaide, Australia: Observations and a gravity wave-tidal interaction model. *Journal of the Atmospheric Sciences*, 44(3):605–619.

[Fritts and Yuan, 1989] Fritts, D. C. and Yuan, L. (1989). Measurement of momentum fluxes near the summer mesopause at Poker Flat, Alaska. *Journal of the Atmospheric Sciences*, 46:2569–2579.

[Fukao, 1988] Fukao, S., editor (1988). *International School on Atmospheric Radar (ISAR), Lecture Notes.* Reprinted in MAP vol.30, 1989 (SCOSTEP Secretariat, University of Illinois). ISAR was hosted by the Radio Atmospheric Science Center, Kyoto University, Japan. 420p.

[Fukao et al., 1988a] Fukao, S., Sato, T., May, P. T., Tsuda, T., Kato, S., Inaba, M., and Kimura, I. (1988a). A systematic error in MST/ST radar wind measurement induced by a finite range volume effect, 1. observational results. *Radio Science*, 23:59–73.

[Fukao et al., 1988b] Fukao, S., Sato, T., Tsuda, T., Kato, S., Inaba, M., and Kimura, I. (1988b). VHF Doppler radar determination of the momentum flux in the upper troposphere and lower stratosphere: Comparison between the three- and four- beam methods. *Journal of Atmospheric and Oceanic Technology*, 5:57–69.

[Gage, 1990] Gage, K. S. (1990). Radar observations of the free atmosphere: Structure and dynamics. In [Atlas, 1990], editor, *Radar in meteorology*, chapter 28a, pages 534–565. American Meteorological Society, Boston.

[Gage et al., 1981] Gage, K. S., Balsley, B. B., and Green, J. L. (1981). Fresnel scattering model for the specular echoes observed by VHF radar. *Radio Science*, 16:1447–1453.

[Gage et al., 1985] Gage, K. S., Ecklund, W. L., and Balsley, B. B. (1985). A modified Fresnel scattering model for the parameterization of Fresnel returns. *Radio Science*, 20:1493–1501.

[Gardner and Pawsey, 1953] Gardner, F. F. and Pawsey, J. L. (1953). Study of the ionospheric D-region using partial reflections. *Journal of Atmospheric and Terrestrial Physics*, 3:321–344.

[Gerbier and Berenger, 1961] Gerbier, N. and Berenger, M. (1961). Experimental studies of lee waves in the French Alps. *Quarterly Journal of the Royal Meteorological Society*, 87:13–23.

[Goldstein, 1951] Goldstein, H. (1951). The fluctuations of clutter echoes. In Kerr, D. E., editor, *Propagation of short radio waves*, volume 13 of *MIT : Radiation Laboratory Series*, chapter 6:18-21, pages 550–587. McGraw-Hill, N.Y.

[Golley and Rossiter, 1970] Golley, M. G. and Rossiter, D. E. (1970). Some tests of methods of analysis of ionospheric drift records using an array of 89 aerials. *Journal of Atmospheric and Terrestrial Physics*, 32:1215–1233. 728p.

[Gregory, 1956] Gregory, J. B. (1956). Ionospheric reflections from heights below the E region. *Australian Journal of Physics*, 9:324–342.

[Gregory, 1961] Gregory, J. B. (1961). Ionospheric reflections below 50 kilometers during polar-cap absorption events. *Journal of Geophysical Research*, 66:2575–2577.

[Harris, 1978] Harris, F. J. (1978). On the use of windows for harmonic analysis with the discrete Fourier transform. *Proceedings of the IEEE*, 66:51–83.

[Hayashi, 1977] Hayashi, Y. (1977). Space-time power spectral analysis using the maximum entropy method. *Nihon Kishogakkai, Journal of the Meteorological Society of Japan*, 55:415–420.

[Hernandez, 1980] Hernandez, G. (1980). Measurement of thermospheric temperatures and winds by remote Fabry-Perot spectrometry. *Optical Engineering*, 19(4):518–531.

[Hines, 1960] Hines, C. O. (1960). Internal atmospheric gravity waves at ionospheric heights. *Canadian Journal of Physics*, 38:1441–1481. (Reproduced in [Hines and colleagues, 1974]).

[Hines, 1990a] Hines, C. O. (1990a). The saturation of gravity waves in the middle atmosphere. Part I: Critique of linear-instability theory. *Journal of the Atmospheric Sciences*, 48(11):1348–1359.

[Hines, 1990b] Hines, C. O. (1990b). The saturation of gravity waves in the middle atmosphere. Part II: Development of Doppler-spread theory. *Journal of the Atmospheric Sciences*, 48(11):1360–1379.

[Hines, 1990c] Hines, C. O. (1990c). The saturation of gravity waves in the middle atmosphere. Part III: Formation of the turbopause and of turbulent layers beneath it. *Journal of the Atmospheric Sciences*, 48(11):1380–1385.

[Hines and colleagues, 1974] Hines, C. O. and colleagues (1974). *The upper atmosphere in motion*, volume 18 of *Geophysical Monograph Series*. American Geophysical Union, Washington, D.C. (Collection of papers with annotations.) 1027p.

[Hines and Rao, 1968] Hines, C. O. and Rao, R. R. (1968). Validity of three-station methods of determining ionospheric motions. *Journal of Atmospheric and Terrestrial Physics*, 30:979–993.

[Hocking, 1983a] Hocking, W. K. (1983a). Mesospheric turbulence intensities measured with a HF radar at 35°S, II. *Journal of Atmospheric and Terrestrial Physics*, 45:103–114.

[Hocking, 1983b] Hocking, W. K. (1983b). On the extraction of atmospheric turbulence parameters from radar backscatter Doppler spectra - I. theory. *Journal of Atmospheric and Terrestrial Physics*, 45:89–102.

[Hocking, 1985] Hocking, W. K. (1985). Measurement of turbulent energy dissipation rates in the middle atmosphere by radar techniques: A review. *Radio Science*, 20:1403–1422.

[Hocking, 1987a] Hocking, W. K. (1987a). Radar studies of small scale structure in the upper middle atmosphere and lower ionosphere. *Advances in Space Research*, 7(10):327–338. COSPAR.

[Hocking, 1987b] Hocking, W. K. (1987b). Reduction of the effects of non-stationarity in studies of amplitude statistics of radio wave backscatter. *Journal of Atmospheric and Terrestrial Physics*, 49:1119–1131.

[Hocking, 1987c] Hocking, W. K. (1987c). Turbulence in the region 80-120 km. *Advances in Space Research*, 7(10):171–181. COSPAR.

[Hocking, 1989] Hocking, W. K. (1989). Target parameter estimation. *Handbook for MAP*, 30:228–268. (Also appears in [Fukao, 1988]).

[Hocking et al., 1990] Hocking, W. K., Bowhill, S. A., Labitzke, K., and Rycroft, M. J., editors (1990). *The Earth's middle atmosphere.* Advances in Space Research, COSPAR, volume 10(10).

[Hocking et al., 1989] Hocking, W. K., May, P. T., and Röttger, J. (1989). Interpretation, reliability and accuracies of parameters deduced by the spaced antenna method in middle atmosphere applications. *Pure and Applied Geophysics*, 130:571–604. In [Plumb and Vincent, 1989].

[Hocking and Röttger, 1983] Hocking, W. K. and Röttger, J. (1983). Pulse-length dependence of radar signal strengths for Fresnel backscatter. *Radio Science*, 18:1312–1324.

[Houghton, 1977] Houghton, J. T. (1977). *The Physics of Atmospheres.* Cambridge University Press, first edition. 203p.

[Howick, 1991] Howick, E. F. (1991). Atmospheric parameters from three-station radio-meteor data. Master's thesis, Department of Physics, University of Canterbury. 84p.

[Jenkins and Watts, 1968] Jenkins, G. M. and Watts, D. G. (1968). *Spectral analysis and its applications.* Holden-Day, San Francisco. 525p.

[Kanasewich, 1975] Kanasewich, E. R. (1975). *Time Sequence Analysis in Geophysics.* Uni. Alberta Press, Edmonton, second edition. 364p.

[Kay and Marple, 1981] Kay, S. M. and Marple, S. L. (1981). Spectrum analysis - A modern perspective. *Proceedings of the IEEE*, 69:1380–1419.

[Keeler and Passarelli, 1990] Keeler, R. J. and Passarelli, R. E. (1990). Signal processing for atmospheric radars. In [Atlas, 1990], editor, *Radar in meteorology*, chapter 20a, pages 199–229. American Meteorological Society, Boston.

[Kelleher, 1966] Kelleher, R. F. (1966). Some statistical properties of the ground diffraction patterns of vertically reflected radio waves. *Journal of Atmospheric and Terrestrial Physics*, 28:213–223.

[Khan, 1988] Khan, U. (1988). Seasonal and height dependence of turbulence in the middle atmosphere. Master's thesis, Department of Physics, University of Canterbury. 98p.

[Klostermeyer, 1986] Klostermeyer, J. (1986). Experiments with maximum entropy and maximum likelihood spectra of VHF radar signals. *Radio Science*, 21:731–736.

[Klostermeyer, 1989a] Klostermeyer, J. (1989a). Gravity waves and instabilities in the lower and middle atmosphere. *Handbook for MAP*, 30:269–298. (Also appears in [Fukao, 1988]).

[Klostermeyer, 1989b] Klostermeyer, J. (1989b). Maximum entropy estimation of Doppler shift and spectral width of VHF radar signals. *Radio Science*, 24:47–63.

[Kraus, 1988] Kraus, J. D. (1988). *Antennas.* McGraw-Hill, second edition. 892p.

[Krenek, 1977] Krenek, S. H. (1977). *A pulse compression radar system for high-resolution ionospheric sounding.* PhD thesis, Department of Physics, University of Canterbury. 202p.

[Kudeki and Stitt, 1987] Kudeki, E. and Stitt, G. R. (1987). Frequency domain interferometry: A high resolution radar technique for studies of atmospheric turbulence. *Geophysical Research Letters*, 14:198–201.

[Kudeki and Stitt, 1990] Kudeki. E. and Stitt, G. R. (1990). Frequency domain interferometry studies of mesospheric layers at Jicamara. *Radio Science*, 25:575–590.

[Kudeki et al., 1990] Kudeki, E., Surucu, F., and Woodman, R. F. (1990). Mesospheric wind and aspect sensitivity measurements at Jicamara using radar interferometry and poststatistics steering techniques. *Radio Science*, 25:595–612.

[Kudeki and Woodman, 1990] Kudeki, E. and Woodman, R. F. (1990). A poststatistics steering technique for MST radar applications. *Radio Science*, 25:591–594.

[Kuo et al., 1987] Kuo, F. S., Chen, C. C., Liu, S. I., Röttger, J., and Liu, C. H. (1987). Systematic behaviour of signal statistics of MST radar echoes from clear air and their interpretation. *Radio Science*, 22:1043–1052.

[Kwa, 1977] Kwa, E. (1977). The effects of ocean tides on antennae impedance. Master's thesis, Physics Department, University of Canterbury. 157p.

[Lawrence, 1990] Lawrence, B. N. (1990). *The Southern Hemisphere Middle Atmosphere : Climatology and Waves.* PhD thesis, Department of Physics, University of Canterbury. 263p.

[Lesicar and Hocking, 1992] Lesicar, D. and Hocking, W. K. (1992). Studies of seasonal behaviour of the shape of mesospheric scatterers using a 1.98 MHz radar. *Journal of Atmospheric and Terrestrial Physics*, 54(3/4):295–309.

[Lesicar et al., 1991] Lesicar, D., Vincent, R. A., and Hocking, W. K. (1991). Determination of the aspect sensitivity of mesospheric scatterers using MF radars at three sites. In *Proceedings of the fifth workshop on technical and scientific aspects of MST radar*, pages 113–115. [Edwards, 1991].

[Lindner, 1975a] Lindner, B. C. (1975a). The nature of D-region scattering of vertical incidence radio waves, I. Generalized statistical theory of diversity effects between spaced receiving antennas. *Australian Journal of Physics*, 28:163–170.

[Lindner, 1975b] Lindner, B. C. (1975b). The nature of D-region scattering of vertical incidence radio waves, II. Experimental observation using spaced antenna reception. *Australian Journal of Physics*, 28:171–184.

[Lindzen, 1981] Lindzen, R. S. (1981). Turbulence and stress owing to gravity wave and tidal breakdown. *Journal of Geophysical Research*, 86C:9707–9714.

[Liu et al., 1990] Liu, C. H., Röttger, J., Pan, C. J., and Franke, S. J. (1990). A model for spaced antenna observational mode for MST radars. *Radio Science*, 25(4):551–563.

[Lloyd et al., 1990] Lloyd, N., Manson, A. H., McEwen, D. J., and Meek, C. E. (1990). A comparison of middle atmosphere dynamics at Saskatoon (52°N, 107°W) as measured by a medium-frequency radar and a Fabry-Perot interferometer. *Journal of Geophysical Research*, 95(D6):7653–7660.

[Manson, 1965] Manson, A. H. (1965). *Electron densites in the lower ionosphere.* PhD thesis, Department of Physics, University of Canterbury. 145p.+supplement.

[Manson and Meek, 1991] Manson, A. H. and Meek, C. E. (1991). The effects of geomagnetic disturbances and atmospheric tides upon middle atmosphere winds and MF radar scatter at Saskatoon (52°N, 107°W, 61° geomagnetic). *Journal of Geophysical Research*, 96(D1):915–926.

[Manson et al., 1989] Manson, A. H., Meek, C. E., Teitelbaum, H., Vial, F., Schminder, R., Kürschner, D., Smith, M. J., Fraser, G. J., and Clark, R. R. (1989). Climatologies of semi-diurnal and diurnal tides in the middle atmosphere (70-110km) at middle latitudes (40 – 55°). *Journal of Atmospheric and Terrestrial Physics*, 51:579–593.

[Marple, 1987] Marple, S. L. (1987). *Digital spectral analysis with applications.* Prentice-Hall, Englewood Cliffs, N.J. 492p.

[May, 1988] May, P. T. (1988). Statistical errors in the determination of wind velocities with the spaced antenna technique. *Journal of Atmospheric and Terrestrial Physics*, 50:21–32.

[May, 1990] May, P. T. (1990). Spaced antenna versus Doppler radars: A comparison of techniques revisited. *Radio Science*, 25(6):1111–1119.

[McGregor, 1985] McGregor, J. A. (1985). *HF radar oceanography.* PhD thesis, Department of Physics, University of Canterbury. 333p.

[Meek, 1980] Meek, C. E. (1980). An efficient method for analysing ionospheric drifts data. *Journal of Atmospheric and Terrestrial Physics*, 42:835–839.

[Meek and Manson, 1987] Meek, C. E. and Manson, A. H. (1987). Mesospheric motions observed by simultaneous medium-frequency interferometer and spaced antenna experiments. *Journal of Geophysical Research*, 92D:5627–5639.

[Meek and Manson, 1992] Meek, C. E. and Manson, A. H. (1992). Angle-of-arrival oscillations in the mesosphere as seen by medium frequency (MF) radar. *Journal of Atmospheric and Terrestrial Physics*, 54(3/4):277–293.

[Meek et al., 1985] Meek, C. E., Reid, I. M., and Manson, A. H. (1985). Observations of mesospheric wind velocities 1. gravity waves horizontal scales and phase velocities determined from spaced wind observations. *Radio Science*, 20:1363–1382.

[Mitra, 1949] Mitra, S. N. (1949). A radio method of measuring winds in the ionosphere. *Proceedings of the IEEE*, 96:441–446.

[Munro, 1950] Munro, G. H. (1950). Travelling disturbances in the ionosphere. *Proceedings of the Royal Society, London*, A202:208–223.

[Muraoka et al., 1989] Muraoka, Y., Sugiyama, T., Sato, T., Tsuda, T., Fukao, S., and Kato, S. (1989). Interpretation of layered structure in mesospheric VHF echoes induced by an inertia gravity wave. *Radio Science*, 24:393–406.

[Murphy, 1984] Murphy, D. J. (1984). Vertical motions in the mesosphere. Master's thesis, Physics Department, University of Adelaide. 85p.

[Murphy, 1990] Murphy, D. J. (1990). *Measurements of energy and momentum in the mesosphere.* PhD thesis, Physics Department, University of Adelaide. 241p.

[Nakagami, 1960] Nakagami, M. (1960). The *m*-distribution - a general formula of intensity distribution of rapid fading. In Hoffman, W. C., editor, *Statistical methods of radio wave propagation*, pages 3–36. Pergamon Press, London. (Proceedings of a Symposium at UCLA, June 1958.) 334p.

[Otnes and Enochson, 1972] Otnes, R. K. and Enochson, L. (1972). *Digital time series analysis.* John Wiley and Sons, New York. 455p.

[Palmer et al., 1990a] Palmer, R. D., Woodman, R. F., Fukao, S., Larsen, M. F., Yamamoto, M., Tsuda, T., and Kato, S. (1990a). Frequency domain interferometry observations of tropo/stratospheric scattering layers using the MU radar : description and first results. *Geophysical Research Letters*, 17:2189–2192.

[Palmer et al., 1990b] Palmer, R. D., Woodman, R. F., Fukao, S., Tsuda, T., and Kato, S. (1990b). Three-antenna poststatistic steering using the MU radar. *Radio Science*, 25(6):1105–1110.

[Pawsey, 1935] Pawsey, J. L. (1935). Further investigations of the amplitude variations of downcoming wireless waves. *Proceedings of the Cambridge Philosophical Society*, 31:125–144.

[Pfister, 1971] Pfister, W. (1971). The wave-like nature of inhomogeneities in the E-region. *Journal of Atmospheric and Terrestrial Physics*, 33:999–1025.

[Phillips and Spencer, 1955] Phillips, G. J. and Spencer, M. (1955). The effects of anisometric amplitude patterns in the measurement of ionospheric drifts. *Proceedings of the Physical Society, London*, B68:481–492.

[Plumb and Vincent, 1989] Plumb, R. A. and Vincent, R. A., editors (1989). *Middle Atmosphere.* Pure and Applied Geophysics 130(2/3):149-616. (Also reprinted as separate collection).

[Press et al., 1986] Press, W. H., Flannery, B. P., Teukolsky, S. A., and Vetterling, W. H. (1986). *Numerical recipes: The art of scientific computing.* Cambridge, New York. 818p.

[Rastogi, 1989] Rastogi, P. K. (1989). Spectral and correlation analysis with applications to middle-atmosphere radars. *Handbook for MAP*, 30:184–227. (Also appears in [Fukao, 1988]).

[Rastogi, 1990] Rastogi, P. K. (1990). Signal processing and data analysis in middle atmosphere radar. *Radio Science*, 25:1071–1086.

[Rastogi and Holt, 1981] Rastogi, P. K. and Holt, O. (1981). On detecting reflections in presence of scattering from amplitude statistics with application to D-region partial reflections. *Radio Science*, 16:1431–1443.

[Ratcliffe, 1956] Ratcliffe, J. A. (1956). Some aspects of diffraction theory and their application to the ionosphere. *Reports on Progress in Physics*, 19:188–267.

[Rayleigh, 1894] Rayleigh (1894). *Theory of Sound.* MacMillan, New York, second edition. Baron Rayleigh, (John William Strutt). (Two volumes).

[Reid, 1983] Reid, G. C. (1983). The influence of electric fields on radar measurements of winds in the upper mesosphere. *Radio Science*, 18:1028–1034.

[Reid, 1986] Reid, I. M. (1986). Gravity wave motions in the upper middle atmosphere (60-110 km). *Journal of Atmospheric and Terrestrial Physics*, 48:1057–1072.

[Reid, 1990] Reid, I. M. (1990). Radar observations of stratified layers in the mesosphere and lower thermosphere (50-100 km). *Advances in Space Research*, 10(10):7–19. COSPAR.

[Reid and Vincent, 1987a] Reid, I. M. and Vincent, R. A. (1987a). Measurements of mesospheric gravity wave momentum fluxes and mean flow accelerations at Adelaide, Australia. *Journal of Atmospheric and Terrestrial Physics*, 49:443–460.

[Reid and Vincent, 1987b] Reid, I. M. and Vincent, R. A. (1987b). Measurements of the horizontal scales and phase velocities of short period mesospheric gravity waves at Adelaide, Australia. *Journal of Atmospheric and Terrestrial Physics*, 49:1033–1048.

[Rice, 1944] Rice, S. O. (1944). Mathematical analysis of random noise. *Bell System Technical Journal*, 23:282–332.

[Rice, 1945] Rice, S. O. (1945). Mathematical analysis of random noise. *Bell System Technical Journal*, 24:46–156.

[Röttger, 1981] Röttger, J. (1981). Investigations of lower and middle atmosphere dynamics with spaced antenna drifts radars. *Journal of Atmospheric and Terrestrial Physics*, 43:277–292.

[Röttger and Ierkic, 1985] Röttger, J. and Ierkic, H. M. (1985). Postset beam steering and interferometer applications of VHF radars to study winds, waves and turbulence in the lower and middle atmosphere. *Radio Science*, 20:1461–1480.

[Röttger and Larsen, 1990] Röttger, J. and Larsen, M. F. (1990). UHF/VHF radar techniques for atmospheric research and wind profiler applications. In [Atlas, 1990], editor, *Radar in meteorology*, chapter 21a, pages 235–281. American Meteorological Society, Boston.

[Sheen et al., 1985] Sheen, D. R., Liu, C. H., and Röttger, J. (1985). A study of signal statistics of VHF radar echoes from clear air. *Journal of Atmospheric and Terrestrial Physics*, 47:675–684.

[Smith, 1981] Smith, M. J. (1981). *Upper atmosphere circulation and wave motion.* PhD thesis, Department of Physics, University of Canterbury. 302p.

[Smith et al., 1987] Smith, S. A., Fritts, D. C., and VanZandt, T. E. (1987). Evidence of a saturated spectrum of atmospheric gravity waves. *Journal of the Atmospheric Sciences*, 44:1404–1410.

[Stitt and Bowhill, 1986] Stitt, G. R. and Bowhill, S. A. (1986). Improving range resolution with a frequency-hopping technique. *Handbook for MAP*, 20:448–457. SCOSTEP.

[Stitt and Franke, 1991] Stitt, G. R. and Franke, S. J. (1991). Frequency domain interferometry studies with the Urbana MF radar. In *Proceedings of the fifth workshop on technical and scientific aspects of MST radar*, pages 254–262. [Edwards, 1991].

[Stitt and Kudeki, 1991] Stitt, G. R. and Kudeki, E. (1991). Interferometric cross-spectral studies of mesospheric scattering layers. *Radio Science*, 26(3):783–799.

[Stubbs, 1973] Stubbs, T. J. (1973). The measurement of winds in the D-region of the ionosphere by the use of partially reflected radio waves. *Journal of Atmospheric and Terrestrial Physics*, 35:909–919.

[Stubbs, 1977] Stubbs, T. J. (1977). A study of ground diffraction pattern parameters associated with D-region partial reflections. *Journal of Atmospheric and Terrestrial Physics*, 39:589–594.

[Taylor, 1991] Taylor, A. D. (1991). *A Meteor Orbit Radar.* PhD thesis, Department of Physics, University of Canterbury. 429p.

[Titheridge, 1962] Titheridge, J. E. (1962). The stratification of the lower ionosphere. *Journal of Atmospheric and Terrestrial Physics*, 24:283–296.

[Tsuda, 1989] Tsuda, T. (1989). Data acquisition and processing. *Handbook for MAP*, 30:151–183. (Also appears in [Fukao, 1988]).

[Tsuda et al., 1986] Tsuda, T., Sato, T., Hirose, K., Fukao, S., and Kato, S. (1986). MU radar observations of the aspect sensitivity of backscattered VHF echo power in the troposphere and lower stratosphere. *Radio Science*, 21:971–980.

[Ulrych and Bishop, 1978] Ulrych, T. J. and Bishop, T. N. (1978). Maximum entropy spectral analysis and autoregressive decomposition. In [Childers, 1978], editor, *Modern Spectrum Analysis*, pages 54–71. IEEE press. (Reprinted from Rev. Geophysics and Space Phys., 13, 183-200, 1975).

[Uscinski, 1965] Uscinski, B. J. (1965). Theory of sweep frequency investigations of a randomly distributed ionosphere. *Journal of Atmospheric and Terrestrial Physics*, 27:873–882.

[Van Baelen et al., 1990] Van Baelen, J. S., Tsuda, T., Richmond, A. D., Avery, S. K., Kato, S., Fukao, S., and Yamamoto, M. (1990). Comparison of VHF Doppler beam swinging and spaced antenna observations with the MU radar: first results. *Radio Science*, 25:629–640.

[VanZandt, 1982] VanZandt, T. E. (1982). A universal spectrum of buoyancy waves in the atmosphere. *Geophysical Research Letters*, 9:575–578.

[VanZandt and Vincent, 1983] VanZandt, T. E. and Vincent, R. A. (1983). Is VHF Fresnel reflectivity due to low frequency buoyancy waves? *Handbook for MAP*, 9:78–80. SCOSTEP.

[Vincent and Belrose, 1978] Vincent, R. A. and Belrose, J. S. (1978). The angular distribution of radio waves partially reflected from the lower ionosphere. *Journal of Atmospheric and Terrestrial Physics*, 40:35–47.

[Vincent et al., 1987] Vincent, R. A., May, P. T., Hocking, W. K., Elford, W. G., Candy, B. H., and Briggs, B. H. (1987). First results with the Adelaide VHF radar: spaced

antenna studies of tropospheric winds. *Journal of Atmospheric and Terrestrial Physics*, 49:353–366.

[Vincent and Reid, 1983] Vincent, R. A. and Reid, I. M. (1983). HF Doppler measurements of mesospheric gravity wave momentum fluxes. *Journal of the Atmospheric Sciences*, 40:1321–1333.

[Vincent and Röttger, 1980] Vincent, R. A. and Röttger, J. (1980). Spaced antenna VHF radar observations of tropospheric velocities and irregularities. *Radio Science*, 15:319–335.

[Vincent et al., 1977] Vincent, R. A., Stubbs, T. J., Pearson, P. H. O., Lloyd, K. H., and Low, C. H. (1977). A comparison of partial reflection drifts with winds determined by rocket techniques. *Journal of Atmospheric and Terrestrial Physics*, 39:813–821.

[Von Biel, 1989] Von Biel, H. A. (1989). An investigation of the Antarctic mesosphere using partial reflections. *Planetary and Space Science*, 37:889–897.

[Von Biel, 1992] Von Biel, H. A. (1992). Ionisation in the Antarctic stratosphere. *Journal of Atmospheric and Terrestrial Physics*, 54(3/4):235–242.

[Welch, 1967] Welch, P. D. (1967). The use of fast Fourier transform for the estimation of power spectra: A method based on time averaging over short, modified periodograms. *IEEE Trans.Audio,Speech & Electro.*, AU-15:70–73. (Also in [Childers, 1978], p 17-20).

[Woodman and Chu, 1989] Woodman, R. F. and Chu, Y.-H. (1989). Aspect sensitivity measurements of VHF backscatter made with the Chung-Li radar: Plausible mechanisms. *Radio Science*, 24:113–125.

[Woodman and Guillen, 1974] Woodman, R. F. and Guillen, A. (1974). Radar observations of winds and turbulence in the stratosphere and mesosphere. *Journal of the Atmospheric Sciences*, 31:493–505.

[Wright and Fedor, 1969] Wright, J. W. and Fedor, L. S. (1969). The interpretation of ionospheric radio drifts measurements - II Kinesonde observations of microstructure and vertical motions in sporadic E. *Journal of Atmospheric and Terrestrial Physics*, 31:925–942.

[Wright and Pitteway, 1979] Wright, J. W. and Pitteway, M. L. V. (1979). Real-time data acquisition and interpretation capabilities of the Dynasonde: 1. Data acquisition and real-time display. *Radio Science*, 14:815–825.

Acknowledgements

First of all, I must express my appreciation to my supervisor, Dr Grahame Fraser, for his able guidance, helpful advice and constant encouragement. Thank you very much also to : Dr Bob Bennett for his role as acting supervisor, technical advice, tales of lore and for trying to teach me not to boldly split infinitives where none have been split before; Dr Harvey Cummack for the diffraction screen modelling and the many discussions on atmospheric physics, cycling and farming; Mr Graham Lees for the many hours of work at Birdlings Flat and for much technical, computing and general assistance; Dr Andre von Biel and Professor Jack Baggaley, particularly for assistance with Antarctic and sporadic E matters respectively; and especially to fellow students of SMART (Southern Middle Atmosphere Research Team!): Steve Smith, Andrew Taylor and Bryan Lawrence, for being around to help out with any tasks and to talk of many things. Thanks also to other passing students, particularly Steve Wood, John Welch, Usman Khan and Debbie Keep. The efforts of Steve Smith, Graham Lees, Bob Bennett and especially Grahame Fraser in proof reading are also greatly appreciated.

The financial support of the Department of Physics and Astronomy in various forms over the years is gratefully acknowledged as well as the Department's willingness in providing facilities for research of this nature, both at the University and at remote sites. The computing facilities used for the data processing and type setting (LaTeXand BIBTeX) in this work were supplied by the Department and by the Computer Services Centre of the University of Canterbury.

Much technical assistance for this project was provided by the Department's electronic workshop; thank you to Stephen Beuzenberg for building the synchronizers, multiple oscillator and various other items; to Ross Ritchie for the phase locked loop and also to Geoff Graham and Greg Haslett and other members of the workshop. Thank you also to Stephen Hemmingsen for the CAD plan of Birdlings Flat.

Logistical and operational support for the experiments at Scott Base was provided by the Antarctic Division of the Department of Scientific and Industrial Research and special appreciation is due to the staff of the 1988/89 season at Scott Base.

A big thank you to Deirdre and various other flatmates and to the Alley family for providing stable and friendly home environments.

Finally my sincerest gratitude goes to my parents, and to Stuart and Sarah, for all of their support, encouragement and patience throughout my studies.

Index

Citation Index

[Abbott, 1980], 40, 285
[Ables, 1978], 118, 285
[Adams et al., 1985], 18, 285
[Adams et al., 1986], 145, 146, 210, 285
[Adams et al., 1989], 78, 95, 247, 285
[Andrews et al., 1987], 2, 77–79, 81, 85, 194, 285
[Appleton, 1928], 5, 285
[Appleton and Barnett, 1925], 130, 285
[Atlas, 1990], 13, 77, 285
[Austin and Manson, 1969], 12, 286
[Austin et al., 1969], 24, 286
[Awe, 1964], 106, 286

[Balsley and Riddle, 1984], 197, 286
[Bendat and Piersol, 1986], 108, 286
[Blackman and Tukey, 1958], 117, 286
[Blix, 1988], 87, 286
[Bloomfield, 1976], 110, 286
[Bolgiano, 1968], 12, 91, 286
[Bramley, 1951], 10, 93, 186, 212, 247, 286
[Bremer and Singer, 1973], 3, 287
[Briggs, 1951], 20, 132, 287
[Briggs, 1968], 156, 287
[Briggs, 1980], 19, 287
[Briggs, 1984], 90, 93, 156, 158, 160, 163, 164, 166, 179, 204, 244, 287
[Briggs, 1992], 94, 96, 211, 248, 287
[Briggs and Phillips, 1950], 93, 287
[Briggs and Spencer, 1954], 153, 287
[Briggs and Vincent, 1973], 94, 211, 248, 287
[Briggs and Vincent, 1992], 141, 154, 288
[Briggs et al., 1950], 17, 102, 154, 156, 287
[Briggs et al., 1969], 19, 287
[Brigham, 1974], 111, 288
[Brooks and Carruthers, 1953], 99, 106, 288
[Brosnahan and Adams, 1990], 146, 288
[Brown, 1986], 24, 38, 64, 65, 288
[Brown, 1989], 49, 288
[Brown and Chapman, 1972], 21, 156, 166, 179, 180, 188, 288
[Brown and Fraser, 1991], 136, 288
[Budden, 1965], 133, 288
[Budden, 1985], 5, 6, 288
[Burg, 1978a], 118, 288
[Burg, 1978b], 118, 289

[Carter and Balsley, 1982], 84, 233, 289
[Chatfield, 1984], 108, 289
[Childers, 1978], 118, 119, 289
[CIRA, 86], 2–4, 180, 289
[Clemesha, 1963], 182, 289
[Cummack and Cooper, 1986], 180, 289
[Czechowsky et al., 1988], 92, 289

[Davies, 1966], 5, 47, 61, 289

[Davies, 1990], 5, 133, 289
[Doviak and Zrnic, 1984], 10, 138, 289

[Edwards, 1991], 13, 289

[Farley et al., 1981], 18, 122, 145, 290
[Flock and Balsley, 1967], 9, 290
[Forbes, 1990], 85, 197, 290
[Franke, 1990], 134–140, 246, 290
[Franke et al., 1990], 145, 200, 205, 210, 245, 290
[Fraser, 1965], 154, 186, 290
[Fraser, 1984a], 154, 290
[Fraser, 1984b], 47, 290
[Fraser, 1989], 2, 21, 24, 47, 180, 186, 244, 290
[Fraser and Khan, 1990], 85, 88, 90, 92, 185, 249, 290
[Fraser and Kochanski, 1970], 7, 155, 290
[Fraser and Vincent, 1970], 9, 24, 156, 290
[Fraser et al., 1989], 85, 291
[Fritts, 1984], 79, 81, 82, 88, 291
[Fritts, 1989], 78, 81, 84, 291
[Fritts and Rastogi, 1985], 81, 86, 291
[Fritts and Vincent, 1987], 237, 291
[Fritts and Yuan, 1989], 83, 238, 291
[Fukao, 1988], 13, 77, 291
[Fukao et al., 1988a], 19, 291
[Fukao et al., 1988b], 83, 237, 291

[Gage, 1990], 7, 8, 291
[Gage et al., 1981], 12, 292
[Gage et al., 1985], 12, 292
[Gardner and Pawsey, 1953], 8, 292
[Gerbier and Berenger, 1961], 80, 81, 292
[Goldstein, 1951], 103, 170, 292
[Golley and Rossiter, 1970], 182, 292
[Gregory, 1956], 8, 292
[Gregory, 1961], 47, 292

[Harris, 1978], 110, 292
[Hayashi, 1977], 119, 292
[Hernandez, 1980], 156, 292
[Hines, 1960], 78, 292
[Hines, 1990a], 84, 293
[Hines, 1990b], 84, 293
[Hines, 1990c], 84, 155, 293
[Hines and colleagues, 1974], 293
[Hines and Rao, 1968], 154, 293
[Hocking, 1983a], 19, 111, 113, 177, 178, 293
[Hocking, 1983b], 19, 89, 90, 149, 216, 247, 293
[Hocking, 1985], 87–89, 293
[Hocking, 1987a], 91, 95, 293
[Hocking, 1987b], 97, 98, 218, 293
[Hocking, 1987c], 88, 216, 247, 294
[Hocking, 1989], 8, 88, 91, 92, 94, 211, 248, 294
[Hocking and Röttger, 1983], 12, 294
[Hocking et al., 1989], 94, 106, 107, 154, 156, 239, 241, 242, 294
[Hocking et al., 1990], 2, 294
[Houghton, 1977], 77, 87, 294
[Howick, 1991], 24, 294

[Jenkins and Watts, 1968], 117, 294

[Kanasewich, 1975], 108, 119, 294
[Kay and Marple, 1981], 108, 111, 294
[Keeler and Passarelli, 1990], 108, 294
[Kelleher, 1966], 180, 294
[Khan, 1988], 88, 90, 184, 295
[Klostermeyer, 1986], 120, 295

[Klostermeyer, 1989a], 78, 295
[Klostermeyer, 1989b], 120, 295
[Kraus, 1988], 29, 295
[Krenek, 1977], 24, 27–29, 33, 38, 131, 295
[Kudeki and Stitt, 1987], 20, 134, 137, 138, 140, 175, 246, 295
[Kudeki and Stitt, 1990], 135, 137, 295
[Kudeki and Woodman, 1990], 148, 295
[Kudeki et al., 1990], 95, 295
[Kuo et al., 1987], 97, 99, 218, 220, 248, 295
[Kwa, 1977], 29, 64, 69, 295

[Lawrence, 1990], 194, 296
[Lesicar and Hocking, 1992], 93, 95, 212, 296
[Lesicar et al., 1991], 92, 95, 296
[Lindner, 1975a], 93, 212, 296
[Lindner, 1975b], 9, 93, 296
[Lindzen, 1981], 81, 296
[Liu et al., 1990], 13, 296
[Lloyd et al., 1990], 156, 296

[Manson, 1965], 3, 24, 296
[Manson and Meek, 1991], 8, 85, 296
[Manson et al., 1989], 85, 184, 297
[Marple, 1987], 108, 119, 120, 297
[May, 1988], 106, 154, 239–241, 297
[May, 1990], 19, 297
[McGregor, 1985], 24, 33, 38, 297
[Meek, 1980], 156, 297
[Meek and Manson, 1987], 18, 122, 142, 145, 146, 155, 206, 210, 245, 297
[Meek and Manson, 1992], 78, 297
[Meek et al., 1985], 83, 297
[Mitra, 1949], 17, 153, 297
[Munro, 1950], 78, 297
[Muraoka et al., 1989], 13, 297
[Murphy, 1984], 65, 298
[Murphy, 1990], 83, 87, 236–238, 298

[Nakagami, 1960], 97, 298

[Otnes and Enochson, 1972], 108, 298

[Palmer et al., 1990a], 135, 298
[Palmer et al., 1990b], 148, 298
[Pawsey, 1935], 153, 298
[Pfister, 1971], 18, 78, 105, 144, 145, 298
[Phillips and Spencer, 1955], 154, 156, 159, 298
[Plumb and Vincent, 1989], 2, 298
[Press et al., 1986], 99, 108, 123, 298

[Rastogi, 1989], 108, 299
[Rastogi, 1990], 108, 299
[Rastogi and Holt, 1981], 97, 299
[Ratcliffe, 1956], 10, 93, 96, 102, 299
[Rayleigh, 1894], 96, 299
[Reid, 1983], 8, 155, 299
[Reid, 1986], 83, 299
[Reid, 1990], 8, 91, 92, 215, 248, 299
[Reid and Vincent, 1987a], 83, 299
[Reid and Vincent, 1987b], 81, 83, 197, 299
[Rice, 1944], 96, 299
[Rice, 1945], 96, 299
[Röttger, 1981], 19, 149, 300
[Röttger and Ierkic, 1985], 148, 246, 300
[Röttger and Larsen, 1990], 134, 300

[Sheen et al., 1985], 98, 300
[Smith, 1981], 24, 184, 300
[Smith et al., 1987], 81, 82, 300

[Stitt and Bowhill, 1986], 134, 300
[Stitt and Franke, 1991], 136, 137, 221, 222, 300
[Stitt and Kudeki, 1991], 135, 300
[Stubbs, 1973], 156, 300
[Stubbs, 1977], 155, 182, 300

[Taylor, 1991], 24, 64, 301
[Titheridge, 1962], 9, 130, 301
[Tsuda, 1989], 44, 301
[Tsuda et al., 1986], 95, 301

[Ulrych and Bishop, 1978], 119, 120, 301
[Uscinski, 1965], 105, 133, 138, 301

[Van Baelen et al., 1990], 20, 301
[VanZandt, 1982], 84, 301
[VanZandt and Vincent, 1983], 13, 301
[Vincent and Belrose, 1978], 95, 301
[Vincent and Röttger, 1980], 103, 148, 173, 302
[Vincent and Reid, 1983], 79, 236, 302
[Vincent et al., 1977], 156, 302
[Vincent et al., 1987], 20, 155, 301
[Von Biel, 1989], 3, 47, 302
[Von Biel, 1992], 8, 47, 302

[Welch, 1967], 110, 302
[Woodman and Chu, 1989], 94, 302
[Woodman and Guillen, 1974], 7, 18, 104, 122, 302
[Wright and Fedor, 1969], 134, 302
[Wright and Pitteway, 1979], 133, 302

Subject Index

$d_{\frac{1}{2}}$, xiii, 163, 186, 211ff, 216, 217
σ_r, xiii, 137ff
$T_{\frac{1}{2}}$, xiii, 88, 90, 91, 93–95, **164**, 180, 184–186, 191, 211, 212, 215, 216ff
τ_{fad}, xiii, 94, 95, **103**, 106, 163–165, 186
θ_s, xiii, **91ff**, 135, 139, 211
$(V_c)_v$, 90, **164**, 166

A-scan, **14**, 24
A/D converters, Birdlings Flat, 35, 37, **41ff**
A/D converters, Scott Base, 52, **58ff**
acceptance criteria, FCA, **164ff**, 179
acceptance criteria, interferometry, **147ff**
airglow, 156
angular spread, 9, 93, 94, 207, 210
anisotropic diffraction pattern, 153, 154, **159ff**
Antarctic, 21, 47ff, 192, 194, 251ff
antenna, 14, 148
  Birdlings Flat, **28ff**, 149
  Scott Base, **51ff**, 52, 256
apparent velocity, 22, 153, **157ff**, 165, 180, 204, 246
Appleton equation, 5
Arrival Heights, **51ff**, 243, 251ff
aspect ratio, 91, 92
aspect sensitivity, xiii, 9, **91ff**, 135, 139, 140, 211ff, 216, 217, 227, 247ff
auto correlation functions, **103ff**, 157, 158, 170, 186
axial ratio, **163**, 166, 182, 206

balloon, 20, 155
beam broadening, 89, **90**, 94, 149, 211, 212, 247
beam width, 14, 29, 51
Birdlings Flat, **24ff**, 190, 243
Blackman Tukey spectral analysis, **117ff**, 176, 178, 245
Bragg scale, **88**, 89
Bragg scatter, 10, **11**
Brunt-Väisälä, 23, **79**, 86
Buckland Park, 19, 93, 98, 106, 113
buoyancy, 78, 79, 86, 89, 91

calibration, **62ff**, 243
  Birdlings Flat, 37, 198, 203
  Scott Base, 56
characteristic ellipse, **163**, 180
coherent integration, 167
coherent receivers, 16, 22, **33ff**, 108, 186ff, 245
comparison studies, 18, 155, 186ff, 200ff
  SAD & Doppler, 19
  SAD & interferometry, 145, 203ff
computer, Birdlings Flat, 40ff
computer, Scott Base, 52, 58ff
Coriolis effect, xiii, 80
correlation ellipse, 93, **160ff**, 166, 180, 183, 184, 206
correlation functions, **101ff**, 157ff, 158, 165, 166, 170ff, 186, 195, 245
COSPAR Reference Atmosphere, 2–4, 180, 289
critical frequency, **6**, 133
critical level, 82
cross correlation functions, **104**, 157, 158, 165, 173, 195, 239
cross spectrum, **141ff**, 198, 228

D-region, 1, 3, **4ff**, 130, 155
data logging, Birdlings Flat, 42ff, 169, 267ff
data logging, Scott Base, 58ff, 169, 267ff
Doppler beam swinging, **18ff**, 90, 95, 113, 155
Doppler shift, 88, 103, 113, 122, **126**, 150, 172, 177, 196, 228
  gravity waves, 79
Doppler sorting, **122**, 141, 198, 245
Doppler spectra, 176ff, 216
drifts experiment, **21**, 24, 47, 186ff

E-region, 1, 3, **4ff**, 132, 154, 155, 186, 218, 222
eddy dissipation rate, **87ff**, 216ff, 247
electron density, **3**, 4ff, 9, 12, 24, 47

F-region, **4ff**, 132, 154
Fabry-Perot interferometry , 156
fading time, xiii, 22, 23, 94, 98, **103**, 106, 113, 163–165, 172, 188, 211, 239
fast Fourier transform, xii, **110ff**, 176, 178
filter, 33, 45, 113, 119
Fourier analysis, **108ff**, 245
frequency correlation functions, **105**, 133, 137ff, 140, 174ff, 221
frequency domain interferometry, xii, 20, 23, 105, **130ff**, 150, 175, 220ff, 242, 245, 246
  aspect sensitivity, 93, 227
  calibration, 71ff, 244
frequency shift, 20, 23, 32, 43, 50, 131ff
Fresnel diffraction, 10
Fresnel reflection, 11, 249
Fresnel scatter, 11, **12ff**, 115, 249
Fresnel zone, 11
full correlation analysis, xii, 17, 22, 88, 90, 93, 102, 154, 155, **156ff**, 179ff, 244ff
  uncertainties, 106, 154, 239ff

Gaussian distribution, 67, 69, 74, 91, 95, 96ff, 111, 112, 137, 175, 203, 220
geomagnetic field effects, 5ff, 8, 85, 155, 182, 184
gravity waves, 2, 12, 13, 77, **78ff**, 154, 233ff
  inertio, 79, **80**, 85, 184, 197, 222, 249
  internal, 79
  saturation, **81ff**, 86, 88, 185

hypotenuse effect, 182

imaging Doppler interferometer, 145
incoherent receivers, **16**, 21, 38, 186ff, 245
inertial subrange, 86, 87, 91, 216
inertio gravity waves, 79, **80ff**, 85, 184, 197, 222, 249
interferometric velocity, 18, **144ff**, 155, 199ff, 245, 246
interferometry, 17, 18, 22, **125ff**
internal gravity waves, 79
ionosonde, 47, 133, 134
ionosphere, 1, **4ff**, 130, 153
isotropic diffraction pattern, 160

Jicamarca, 135

Kelvin-Helmholtz instabilities, 91, 92
Kennelly-Heaviside layer, 130
Kolmogoroff law, 87
kurtosis, 99, 220

least squares regression, 118, 128, 142, 145, 147, 157, 170, 180
linear-instability, 81, 84

magnetic field effects, 5ff, 8, 85, 155, 182, 184
magnetoionic theory, **5ff**
maximum entropy methods, xii, **118ff**, 176, 179, 245
meridional wind, xiii, 80, 233
mesosphere, **1ff**, 21, 77, 79–81, 83, 85–88, 91, 93, 154, 156, 197, 216
meteors, 13, 24, 64, 155
middle atmosphere, **1ff**, 77, 78, 85
  radar, **13ff**, 154
  scattering processes, **8ff**, 91ff, 96ff
moments, 99, 113, 120
momentum flux, xiii, **79**, 81–83, 236ff, 244
MST radar, xii, 13
MU radar, 20, 135

Nakagami distribution, **97ff**, 218ff, 248
noise, **103**, 138, 164, 170, 171, 173–175, 188
normalized time discrepancy, xii, 165
Nyquist frequency, 44, **110**, 113

orographic lee waves, 80
oscillator, 15, 23, 32ff, 50ff, 243
ozone, 2, 85

partial reflection, **7**, 8, 154
phase coherent, 16, 22, **33ff**, 38, 55, 108, 186, 245
phase locking, Birdlings Flat, **38ff**, 243
phase locking, Scott Base, **55ff**, 243
planetary waves, 77, 191, 194
plasma frequency, 5
Poker Flat, 8, 83, 84
polar diagram, 14, 28ff, 65, 94, 129, 134, 135, 148, 211
polar mesopause summer echo, 92
polar region, 8, 83, 85, 92, 155, 184, 239
polarimeter, 47ff, 251ff
postbeam steering, 95, **148ff**, 230ff, 246
pulse compression, 24, 130, **131**, 246

radar, 13ff, 21ff
  Doppler beam swinging, **18ff**, 90, 95, 113, 155
  frequency shift, 20, **130ff**
  spaced antennae, 14, **16ff**
radar volume, **14**, 15, 71, 134, 138, 139, 221, 226
radial velocity, xiii, **126**, 141, 145, 146, 172, 173, 196, 228
random velocity parameter, 90, **164**, 166
Rayleigh distribution, **96ff**, 218ff, 248
receivers, 14ff, 22, **33ff**, 186ff, 245
  characteristics - Birdlings Flat, 36
  characteristics - Scott Base, 52, 55
refractive index, **5ff**, 77, 85, 88, 155, 218
regression, 118, 128, 142, 145, 147, 157, 170, 180
Rice distribution, **96**, 218ff, 248

Saskatoon, 8, 156
scattering centre, **10**, 18, 122ff, 141ff, 145, 177, 195, 198, 199, 228, 245
scattering depth, xiii, 20, 132, 135, **137ff**, 175, 221ff, 246
scattering mechanisms, **8ff**, 91ff, 211, 249

scattering scales, **91ff**, 211ff, 247
Scott Base, 15, **47ff**, 192ff, 243, 251ff
signal distributions, **96ff**, 218ff, 248
signal power, **103**, 170, 171
signal to noise ratio, xii, **103**, 138, 147, 164, 170, 171, 189
skewness, 99
SOUSY radar, 148
spaced antennae drifts, xii, 17, **153ff**, 244
  experiment, **21**, 24, 47, 186ff
spaced antennae radar, 13, 14, **16ff**
spatial correlation function, 93, 94, 96, **159ff**, 182, 211
spatial domain interferometry, 18, 95, 107, **127ff**, 141, 144, 155, 194ff, 212, 242, 245
  calibration, 64ff, 244
spectral analysis, **107ff**, 176ff
  interferometry, **141**, 198, 228, 245
spectral broadening, 89, **90**
spectrum, Doppler, 176ff, 216
spectrum, turbulence, 86, 87
spectrum, wind fluctuations, 84, 233–235
specular reflection, **9ff**, 78, 88, 89, 91, 95, 96–98, 154, 215, 218, 227, 248
sporadic-E, **5**, 9, 12, 134
ST radar, xii, 13
standard error (correlation coefficient), 106
stratosphere, 1ff, 83, 135
synchronizer, Birdlings Flat, 38ff
synchronizer, Scott Base, 54, 57

temperature, 1ff, 12, 78, 79, 82, 85
thermosphere, 1ff, 21, 83, 86, 88, 154
tides, 8, **85**, 88, 184, 191, 218, 222, 249
time domain interferometry, 18, 126, 245
time series analysis, **101ff**
transmitter, Birdlings Flat, 27
transmitter, Scott Base, 49ff
troposphere, 1, 2, 83, 135, 155
true velocity, 22, **161ff**, 165, 180ff, 204ff, 211, 246
turbopause, 2ff, 86, 216
turbulence, 2, 7, 11, 12, 18, 77, 81, **85**, 185, 211, 247
  measurements, 88, 216

uncertainties, 198, **239ff**, 244
  correlation functions, **106**, 107
  FCA, 106, 154, **239**
  FDI, 242
  phase, **107**, 125, 241
  spatial domain interferometry, 107, 129, 198, 242
Urbana, 134, 136

velocity from interferometry, 18, **144ff**, 155, 199ff, 245, 246
vertical velocity, xiii, 24, 146, 148, 196ff, 244
virtual height, 7, 134

Wiener-Khintchine theorem, 101, 117
windows, **110ff**, 117, 167

zonal wind, xiii, 2, 4, 79, 80, 180, 184, 233